CHARLES UNIVERSITY

Faculty of Science

Department of Biochemistry

Mgr. František Filandr

Structural characterization of biotechnologically and medicinally important proteins

Strukturní charakterizace biotechnologicky a medicinálně významných proteinů

DOCTORAL THESIS

Supervisor: RNDr. Petr Man, Ph.D.

Prague 2020

Declaration

I declare that I have worked on this thesis under the guidance of my supervisor and that all sources of the previous knowledge are properly cited. No part of this work was used or will ever be used to obtain any other academic degree than Ph.D. from Charles University.

Prague .....

.....

Mgr. František Filandr

Declaration of authorship

I declare that Mgr. František Filandr contributed significantly to the experiments and to all scientific publications contained in this Ph.D. thesis. He performed most of the experiments, substantially contributed to their planning, and took a significant part in the primary data interpretation and their preparation for publication.

Prague .....

.....

RNDr. Petr Man, Ph.D.

Acknowledgements

Here, I would like to express my gratitude to all the people, who helped me and guided me throughout the years of my PhD study.

First and foremost, I would like to wholeheartedly thank my supervisor Petr Man, for his guidance and introduction to the scientific community. He often went out of his way to give me opportunities for growth and travel, always gave good advice when asked to and left me an unexpected and pleasant freedom and my own responsibility in the pursuit of this work.

I would also like to thank the whole group of Laboratory of Structural Biology and Cell Signalling for creating a good spirited environment, especially Zdeněk Kukačka for organizing great social events, Pavla Vaňková for her optimism and casual assistance, Petr Pompach for help with mass spectrometer, Petr Novák for his leadership and also former PhD student Alan Kádek for his initial tutoring and orderly notes that allowed me to seamlessly continue his work on the CDH/LPMO project.

Next, I would like to express my thanks to our collaborators Daniel Kracher, Roland Ludwig and other members of Biocatalysis & Biosensing Research Group at BOKU in Vienna, for productive cooperation and for allowing me to perform experiments in their lab and experience working in a foreign environment. I also grateful doc. Erik Sedlák for giving me the opportunity to contribute to the LOV2 research.

Finally, I would like to express my thanks to my parents Mária and František, for their endless support and motivating expectations, to my new-born daughter Stella for (usually) sleeping soundly on my home-office days during this year's covid-19 pandemic and my beloved wife Růžena for her patience, love and inspiring determination.

Abstract (in English)

A large number of biological processes depends on dynamics of protein structure and specific protein-protein and protein-ligand interactions occurring under specific native conditions in or outside of cells. Standard methods for protein structure analysis like x-ray crystallography, nuclear magnetic resonance or cryo-EM are able to obtain important atomic or near- atomic resolution protein structures, however these are usually a static snapshot of protein locked in a specific conformation and mostly in non-native conditions.

Structural mass spectrometry on the other hand, allows to describe protein structure dynamics, protein-protein and protein-ligand interactions and obtain inter- and intraprotein distance constraints between amino acid residues, all while working with proteins in their native conditions and needing only a fraction of sample.

In this work, hydrogen/deuterium exchange mass spectrometry (HDX-MS) and classical proteomic approaches were used together with other methods to analyse biotechnologically important proteins of fungal cellulolytic system lytic polysaccharide monooxygenase (LPMO) and cellobiose dehydrogenase (CDH) as well as plant-derived photosensitizer protein LOV2 with potential use in biologically targeted photodynamic therapy.

These methods allowed us to follow cellulolytic reaction of reduced LPMO even in heterogeneous solution of crystalline cellulose, obtaining insights into structural changes accompanying LPMO catalysis, mainly its notorious instability which was determined to be caused by oxidative modification of the protein, as well as verifying and structurally describing previously reported stabilisation of LPMO by suitable substrate. The recently speculated role of hydrogen peroxide as true LPMO cosubstrate was also confirmed.

Analysis of LOV2 protein then explained previously reported gradually increasing production of singlet oxygen upon protein irradiation as caused by a release of flavin cofactor into the solution, with interesting implications for biologically targeted photosensitizers.

Keywords: Structural mass spectrometry, hydrogen/deuterium exchange mass spectrometry (HDX-MS), lytic polysaccharide monooxygenase (LPMO), cellobiose dehydrogenase (CDH), oxidative modification, cellulose degradation, turbidimetry, photosensitizer, light oxygen and voltage sensing domain (LOV)

Abstrakt (in Czech)

Velké množství biologických procesů je závislé na strukturní dynamice proteinů a specifických protein-proteinových, nebo protein-ligandových interakcích závislých na specifických podmínkách uvnitř, či vně buněk. Analýza struktury proteinů klasickými metodami jako je rentgenová krystalografie, NMR, nebo nově cryo-EM poskytuje důležité struktury s atomárním rozlišením, avšak většinou ukazuje pouze statický obrázek bez detailů o dynamice, nebo transientních interakcích, a navíc často v nenativních podmínkách.

Tyto detaily může doplnit strukturní hmotnostní spektrometrie, která umí poskytnout informace o proteinové dynamice, interakcích proteinů s jinými molekulami a také o specifických meziatomových vzdálenostech v samotných proteinech, nebo mez interakčními partnery, to vše při relativně nativních podmínkách.

V této práci byla použita vodík/deuteriová výměna spojená s hmotnostní spektrometrií (HDX-MS), klasická proteomická analýza a turbidimetrie ke studiu biotechnologicky užitečných proteinů houbového celulolytického systému lytické polysacharidové monooxygenasy (LPMO) a celobiosadehydrogenasy (CDH) a rovněž fotosensitivní domény LOV2 pocházející z rostlinného fototropinu využitelné při fotodynamické terapii.

Pomocí těchto metod byla sledována celulolytická reakce katalyzovaná redukovaným enzymem LPMO v heterogenním roztoku mikrokrystalické celulosy a byly získány poznatky o změnách a dynamice struktury LPMO během reakce. Podstata destabilizace enzymu byla určena jako oxidativní degradace způsobená vedlejší reakcí hydroxidových radikálů generovaných aktivním centrem enzymu a byla rovněž strukturně popsána a vysvětlena stabilizace enzymu polysacharidovým substrátem. Byla rovněž potvrzena spekulovaná role H_2O_2 jako pravého kosubstrátu LPMO.

Analýza LOV2 pomohla vysvětlit dříve publikované zvýšení produkce singletového kyslíku ($^1O_2$) při dlouhodobém ozáření, které je způsobené uvolněním FMN kofaktoru s vysokou efektivitou produkce $^1O_2$ do roztoku po oxidativní modifikaci cysteinu v blízkosti kofaktoru v molekule proteinu.

Klíčová slova: strukturní hmotnostní spektrometrie, vodík deuteriová výměna, lytická polysacharidová monooxygenasa (LPMO), cellobiosa dehydrogenasa (CDH), oxidativní modifikace, rozklad cellulosy, turbidimetrie, fotosenzitivní protein, light oxygen and voltage sensing domain (LOV)

Table of contents:

Abbreviations

CDH	cellobiose dehydrogenase
*Nc*CDH	cellobiose dehydrogenase from Neurospora crassa
*Ch*CDH	cellobiose dehydrogenase from Crassicarpon hotsonii
LPMO	lytic polysaccharide monooxygenase
*Nc*LPMO	lytic polysaccharide monooxygenase from Neurospora crassa
CYT	N-terminal cytochrome domain from cellobiose dehydrogenase
DH	C-terminal dehydrogenase domain from cellobiose dehydrogenase
GOX	glucose oxidase
PASC	phosphoric acid swollen cellulose
GH61	glycosyl hydrolase family protein 61
ROS	reactive oxygen species
FAD	flavin adenine dinucleotide
FMN	flavin mononucleotide
IDET	interdomain electron transfer
IPET	interprotein electron transfer
PS	photosensitizer
LOV2	light, oxygen and voltage sensing domain 2
HDX-MS	hydrogen/deuterium exchange mass coupled with spectrometry
PTM	posttranslational modification
cryo-EM	cryogenic electron microscopy
LC	liquid chromatography
MS	mass spectrometry
ES	electrospray ionisation
MALDI	matrix-assisted laser desorption ionisation
FT-ICR	Fourier transform ion cyclotron resonance mass analyser
TOF	time-of-flight mass analyser
CCS	collisional cross-section
TWIM	traveling-wave ion mobility analyser
TIM	trapped ion mobility analyser
DTIM	drift-tube type ion mobility analyser
MS/MS	tandem mass spectrometry
ECD	electron-capture dissociation
ETD	electron-transfer dissociation
UVPD	ultraviolet photodissociation
TCEP	Tris(2-carboxyethyl)phosphine

1. Introduction

1.1. Protein Structure

To perform the variety of tasks proteins evolved to do, they come in myriad of shapes, sizes and functions. From functioning as a skeleton of a cell in the form of microtubule and microfibril network, or allowing photosynthetic organisms to consume and store solar energy and transform it into chemical bonds of hydrocarbons formed of CO_2, to forming complex protein machinery for copying and translating DNA, proteins play a crucial role in virtually every process in living organisms. The seeming omnipotence of proteins is a factor of combinatorics, since proteins are composed of 22 different amino acids, bearing hydroxyl, carboxyl, thiol, thioester, amide and other basic functional groups, linked by peptide bonds in a sequence encoded in genetic information of each cell (although only 20 are in fact specifically coded in DNA, two additional are incorporated by additional translation mechanisms). The different sequence of amino acids with different chemical properties in a polypeptide chain called *primary structure* is the main driving force behind protein shape and function and the amount of possible proteins allowed by 22 different amino acids is theoretically 22^n where *n* is the number of amino acid residues forming the protein. While this number is in reality substantially lower, since conserved or similar sequences often repeat throughout the evolution tree[1], it still allows for untold variety.

Suitable amino acids in a row can create a network of hydrogen bonds between carbonyl and secondary amino groups in peptide backbone, twisting the initial chain of amino acids into folded β-sheets (formed of individual β-strands), α-helixes and various turns, also assisted by side chain interactions and van der Waals forces (**Figure 1**, page 10)[2]. These more organized structures are called *secondary structure* and form basic elements of which the proteins are formed. The reduction in outward polarity often causes these secondary structures to form hydrophobic core of the enzyme while allowing more polar free strands to form the surface of the protein. The respective positioning and interactions of secondary structure elements manifests as the overall fold of the protein monomer called *tertiary structure*, turning the protein into shapes of globules, fibrils, or any other. These monomers formed of single polypeptide chain can in turn form complexes with themselves or with other proteins, with the resulting structure designated *as quaternary structure*, that often necessary for protein to be able to perform their complicated functions.

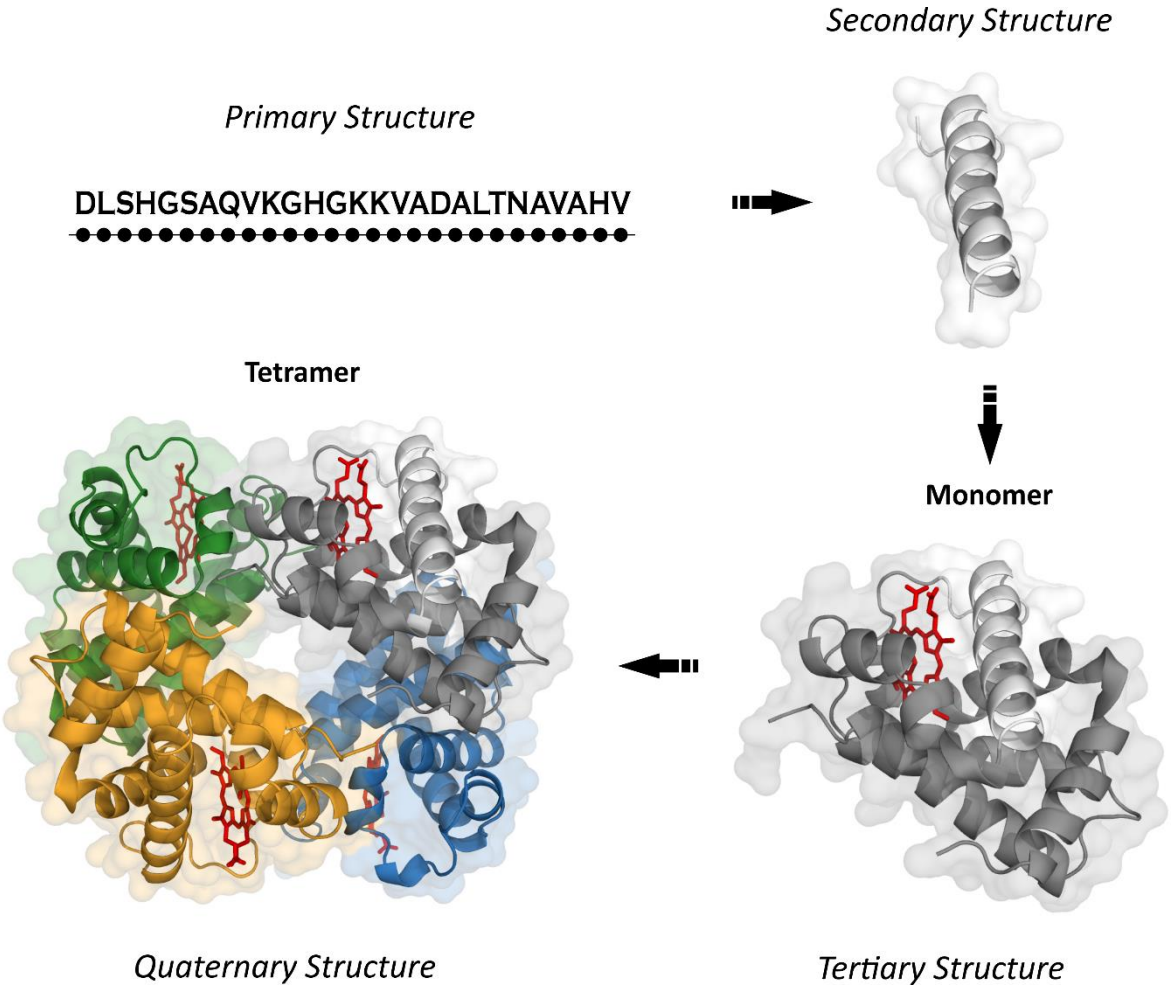

Figure 1: *Various levels of protein structure shown on deoxy haemoglobin tetramer (using structure 1A3N on PDB[2]).*

The function of the protein is tightly bound to its structure. Interactions of specific amino acid residues in a protein can form enzymatic active site, enabling the protein to catalyse chemical reactions using amino acid side chains as catalysts and several possible protein conformations may serve as functional switches. These function related structural changes may be induced by specific ligands or allosteric modulators and may involve discreet changes in specific region of protein, such as changes to the active site during catalysis or allosteric modulation activating or inhibiting enzymatic activity, or more profound changes to secondary or tertiary structure as for example in protein channels and transporters. The changes may also involve relative movements of whole domains as in fungal cellobiose dehydrogenase[3] or combination of many different changes.

Because structure of the protein is key to its function, random changes to protein structure can also easily cause deadly pathophysiology in what is called a proteinopathy. Single point mutations in proteins can lead to complete loss of function as is demonstrated in sickle-cell anemia[4]. Even wrong folding may by itself cause proteins to become toxic, as is the case in prion diseases, where misfolded version of naturally occurring protein aggregates and becomes toxic, while serving as a template for misfolding of other molecules[5,6]. In fact, other more common neurodegenerative diseases such as Alzheimer's disease can be considered a prion disease due to misfolding of tau protein[7] or amyloid peptides[8] also having templating properties[9]. These are not infectious however as the initial cause of misfolding is usually genetic in nature[10]. Understanding the function of a protein requires not only knowledge of precise three-dimensional structure of the protein but also of the dynamic structural changes occurring during protein function and interactions with other proteins or ligands.

1.2. Methods for Studying Protein Structure

In order to study molecules so diverse as proteins, plethora of methods was developed, that utilizes various physical and chemical properties of proteins. Some of the most commonly used are described in the following chapters, with a special focus on structural mass spectrometry, which is utilized in the experimental part of this thesis. The individual methodological approaches capture different views/snapshots of protein structure and dynamics and the recent trend lies in a combination of several techniques, called "integrative structural biology" which provides higher confidence in the postulated mechanisms and helps to sort out possible ambiguities. Here, structural mass spectrometry plays increasingly important role as it may complement the high-resolution snapshots by analysis of the dynamics and solution state of the protein(s) under investigation.

1.2.1. X-ray Crystallography

The X-ray crystallography is a high-resolution diffraction-based method capable of determining exact electron density and subsequently structure of a protein down to a resolution of 1Å. With the current number of protein crystal structures obtained by X-ray crystallography at PDB (http://www.rcsb.org/) standing well over 135 000, it is by far the most commonly used approach to elucidate protein structure[11]. Since the first protein structure obtained by X-ray crystallography was that of a sperm whale myoglobin published

already in 1958[12] at a resolution of 6Å, the method had a lot of time to mature. The basic concept of X-ray crystallography is obtaining a diffraction image of elastically scattering photons after they hit electrons of the crystallized sample with a wavelength close to the inter-atom distances in the sample[13]. While diffraction caused by single atoms is marginal, at specific angles, the atoms in crystal align and a constructive interference of diffracting photons creates characteristic patterns of black spots at a sensor. These spots are then analysed to reconstruct the electron density map of the sample, with the spatial distribution of the signals corresponding to shape and symmetry of sample crystal unit cell, and their intensities correspond to positions of individual atoms in the cell. Since all signal intensities are influenced by all atoms in the unit cell, it's not possible to solve only part of the structure[13]. The resulting electron density map is then refined by computational iteration to best fit the diffraction data[14] and interpreted in terms of individual atoms.

Although the exact structure of a protein is a crucial information when explaining its biological function and X-ray crystallography is a powerful tool for its determination, any protein crystallography is limited by its core premise, the need of a crystal of the examined molecule. The ability to crystallize depends on protein fold and flexible proteins with low amount of secondary structuralizing tend to crystalize poorly. Membrane proteins which need the lipidic phases to retain their correct biologically relevant structure[15] are problematic as well. While high-throughput methods for protein crystallization, including methods such as lipidic cubic phase for membrane proteins[16], has been developed, significant number of proteins still elude proper crystallization. Another factor that needs to be taken into account when interpreting crystal structure is the fact that a dynamic molecule is presented as a static object with the relative amount of dynamics in various regions of the protein only vaguely described by an atomic mean-square displacement (B factor)[17].

Very high protein concentration necessary for the crystallization as well as non-optimal pH and presence of additives and precipitants may also introduce non-native conformations and artefacts in the data, as well as being restrictive for proteins unable to be produced in such quantity or unstable at such concentrations[18,19]. New possibilities to look at protein dynamics emerged with the development of femtosecond X-ray free electron lasers (XFEL), which use highly brilliant photons produced by accelerators with magnetic oscillators to get a diffraction snapshot of analysed molecule before its vaporization due to the amount of energy absorbed. In this way, very small crystals or even single molecules can be analyzed[20].

1.2.2. Nuclear Magnetic Resonance

Nuclear magnetic resonance (NMR) is with more than 11 000 solved structures on PDB the second most commonly used high-resolution method for precise 3D structure determination of macromolecules[21]. NMR utilizes strong magnets to align spin-non-even nuclei of sample atoms (^{1}H, ^{13}C, ^{15}N and ^{31}P), which are then split between those aligning in the direction of the field (lower energy spin state) and those aligning against the field (higher energy spin state). The sample is subsequently irradiated with an electromagnetic radiation in radio range and this energy is absorbed at a specific resonant frequency by nuclei occupying lower spin state to excite to the higher spin state. The exact frequency absorbed, which corresponds to the precession frequency of a magnetic field created by nucleus spin called "Larmor frequency", depends on type of atom as well as its chemical surroundings, as electrons in the vicinity of the nucleus affect the energy gap between the spin states and this phenomenon is called "chemical shift". The chemical shift of each atom thus carries the information about neighbouring atoms and can be used to reconstruct the structure of the sample molecule. Because chemical shift causes the resonant frequency to change by only a very low margin in the range of ppm, having stronger magnetic field and thus energy gap between the spin states increases sensitivity significantly.

Modern instruments utilize pulsed Fourier transform NMR[22]. In this method, a very brief pulse of wider range high-power radio radiation, usually in specially devised sequences, is applied to the sample to excite all the nuclei of a given atom type. By aligning together, the precessing magnetic fields of nuclei sum up and create a net magnetization of a sample oscillating at specific Larmor frequencies of each atom type in the sample. This total oscillation is detected as an "echo", a decaying signal on a coil originally used to transmit the radio pulse. Fourier transform is subsequently used to separate individual frequencies from the compound waveform to create a spectrum.

Contrary to X-ray crystallography, NMR is analysing proteins in a solution and is able to describe their dynamics and interactions as well, albeit with some limitations[23]. First limiting factor is a protein size. With increasing protein size, broadening of spectral peaks and signal overlaps occur. Traditionally, NMR experiments were limited to 30-40 kDa proteins due to these reasons and while methods have been developed for analysis of larger proteins[24] enabling structural characterization of proteins and their complexes up to a size of 1 million Da[25], these require isotopic labelling of the sample protein and thus are not a

routine. Second limiting factor is protein concentration, solubility and stability requirements. NMR experiments often take days and require concentrations of 0.5 to 1 mM to obtain high quality spectra. Many proteins are not stable at such high concentration and need to be supplemented with higher ionic strengths or organic solvents. Taking all these facts into account, while NMR is considered more native than crystallographic approaches regarding protein conditions during analysis and is able to observe protein dynamics and specific structural changes it can still be complemented by analyses in more native conditions.

1.2.3. Cryogenic Electron Microscopy

Cryogenic electron microscopy (or Cryo-EM) is a type of transmission electron microscopy that utilizes vitrification - rapid freezing of sample in aqueous solution resulting in amorphous ice formation - to allow scanning of individual biological molecules, which would otherwise be destroyed by vacuum and radiation damage in the instrument[26]. It is an improvement over older three-dimensional reconstruction from electron microscopy (3D-EM), that utilizes 2D crystals, helical arrays or icosahedral viruses to provide rough 3D structure of their assembly, but is very limited in terms of resolution due to the need to stain and dehydrate the samples to withstand the conditions of the analysis and gain contrast[27].

Cryo-EM (and 3D-EM generally) generates 3D structures computationally from large number of 2D images corresponding to a projection of differently oriented molecule in the direction of the electron path. It has recently gathered a lot of attention with dramatic advancement in direct electron detectors and image processing algorithms leading to increase of resolution of obtained structures to less than 2Å[28,29] with ever smaller molecules being able to be observed. The method has been successfully used in structure or structural dynamics characterization of large ensembles like eukaryotic ribosome at 3Å resolution[30] and complexes of histone H1 and nucleosomes during the formation of chromatin fibres at resolution of 11Å[31], but also of relatively small multimeric proteins like TRPV1 ion channel at 3.4Å resolution[32], β-galactosidase at 2.2Å resolution[33]. Cryo-EM is still not able to identify more transient interactions and structures of small biomolecules, but recent sub 82 kDa structure of alcohol dehydrogenase at 2.7Å resolution proves, that the method is still developing and became now also usable in drug-target interaction identification[34].

1.2.4. Structural Mass Spectrometry

Structural mass spectrometry (MS) has seen rapid growth in recent years and became a hallmark of integrative structural biology. Structural MS is able to rapidly provide complex information about protein structure, from primary to tertiary, about protein dynamics, post-translational modifications (PTMs) and protein-protein and protein-ligand interactions. Importantly, while not able to provide complete 3D models of proteins, structural MS techniques work with much more "native" states of proteins compared to higher resolution techniques like x-ray crystallography or NMR, including working with heterogenous solutions, complex mixtures of proteins and their ligands all the while needing only a fraction of protein amount for analysis[35]. They thus complement high-resolution methods to provide additional dimension of information to static 3D structures.

1.2.4.1. Structural MS Principles

Mass spectrometry allows to measure exact mass of ionized analyte in the form of mass to charge ratio (m/z). While originally used mainly analytically for atoms and small molecules due to difficulties in creating gas-phase ions of larger mass, with the advent of "soft" ionization techniques, mainly electrospray ionization (ESI) coupled to liquid chromatography and matrix assisted laser desorption ionization (MALDI) more than two decades ago, analysis of larger biomolecules became possible. Both these techniques paved the way of classical proteomics into an invaluable tool of contemporary molecular biology, biochemistry and medicinally oriented research. However, the structural mass spectrometry relies mostly on ESI as it features more "gentle" ionization and can be readily coupled with separation techniques. ESI allows to transfer biomolecules from a solution to a gas phase in the form of rapidly evaporating droplets emitted by a highly charged capillary forming a characteristic Taylor cone, while giving them charge dependant on the size of the molecule without breaking their structure[36,37]. The dispersion is facilitated by droplets approaching Rayleigh limit, the maximum amount of charge a droplet of a certain size and composition can contain while still being stable, as they evaporate[38,39].

Two main protocols for protein structure analysis by mass spectrometry exist. The first one is "bottom-up" or "peptide-centric" approach, characterized by analysis of individual peptides from proteins of interest, usually from a solution, and obtaining information about protein primary structure and PTMs[40,41]. Techniques like covalent labelling, chemical cross-

linking and hydrogen-deuterium exchange allow to obtain a breath of additional information about protein structure and interactions from bottom-up analysis. The second one is "top-down" or "protein-centric" approach. This protocol is characterized by transferring the whole ionized proteins or their mixtures to the gas-phase, retaining their individual proteoform characteristics[42] and thus deducing information about their PTM heterogeneity[43], subunit composition and complex formation. This can be further combined with ion-mobility measurements to obtain collision cross sections of studied proteins or their complexes.

1.2.4.2. Native Mass Spectrometry and Ion Mobility

Native mass spectrometry allows for mass measurement of intact proteins and protein complexes with retained non-covalent interaction and PTMs upon their transfer from sample solution to vacuum of mass spectrometer. This is enabled first and foremost by precise tuning of instrument ion transfer, buffers and conditions of ESI to facilitate the most "gentle" ionization possible in order to not disrupt any quaternary structure of analysed proteins[44–46]. This also includes utilizing heated desolvation gas, accelerated voltage throughout the instrument and mild collisions with background gas to maintain the initial internal energy of ions and prevent their uncontrolled adiabatic expansion and subsequent freezing, when crossing from atmospheric pressure to vacuum in the instrument[47]. Modified ESI in the form of nanoflow electrospray ionization (nESI) proves especially useful in this regard, allowing better dispersion of the sample liquid, reduced sample flow and reducing the necessity of using non-native volatile compounds in buffers to assist evaporation[48] (**Figure 2**, page 17).

By adding additional energy to ions in the form of increased collisions in gas phase, either by increasing gas pressure or collision voltage throughout the ion transfer in the instrument, it is possible to observe selective dissociation or unfolding of proteins or protein complexes and in this way deduce more information about their structure and stability[49].

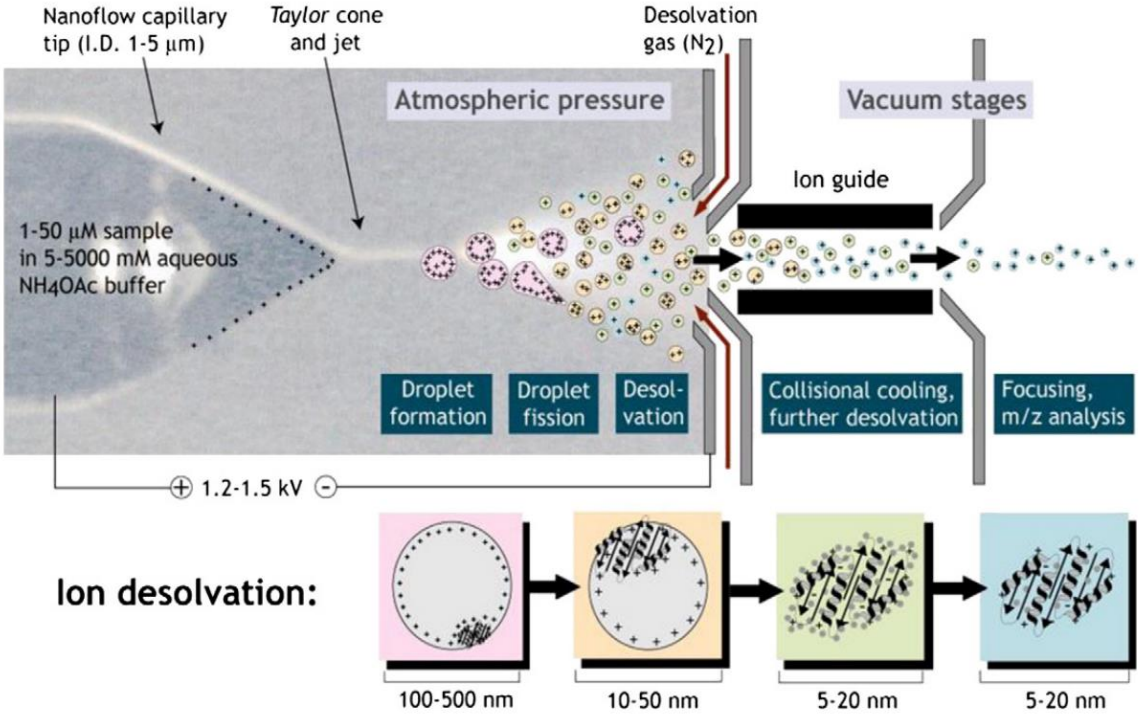

***Figure 2**: **Schematic representation of nESI ionization process.** Adapted from Konijnenberg et al. (2013).*

Ion mobility adds another dimension to native mass spectrometric analysis. In its simplest setup, ion mobility analyser consists of linear drift tube where ions are propelled by electric field against a flow or area of static inert gas[50]. Molecules drifting through the analyser separate according to their size and charge, as larger molecules undergo more collisions with the gas and are slowed down, while smaller or higher charged molecules drifting faster[48]. The parameter describing the ease with which the ion travels through the drift tube is referred to as "mobility" K_0 and is given by Mason-Schamp equation[50]:

$$K_0 = \frac{3ze}{16N\Omega}\left(\frac{2\pi}{\mu k_b T}\right)^{\frac{1}{2}}$$

where z is charge of analyte, N the number density of the drift gas, Ω the collisional cross section (CCS), μ the reduced mass of the ion, k_b the Boltzmann constant and T the temperature. Since the ion mobility drift tube is followed by mass spectrometric analyser, charge state and mass of each particle is measured and therefore CCS can be determined for each ion species. Improvements on the basic drift tube analyser include traveling wave ion mobility analyser (TWIM) and trapped ion mobility analyser (TIM)[51] (**Figure 3**, page 18).

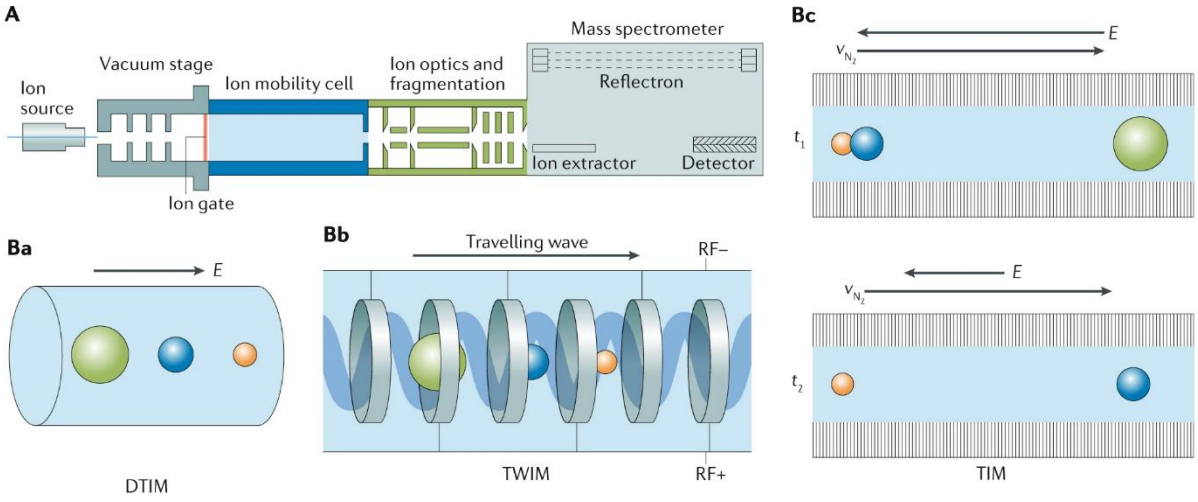

***Figure 3: Ion Mobility Mass Spectrometer Layout**: **A** - overview of an ion mobility-mass spectrometry instrument. **Ba** - drift-tube type ion mobility analyser (DTIM) with constant gas flow and uniform electric field, **Bb** - Travelling wave ion mobility (TWIM) analyser with travelling potential wave helping to separating analyte ions, **Bc** - Trapped Ion Mobility analyser (TIM) separating ions by selectively propelling them from an equilibrium state with electrostatic force in one direction and buffer gas flow in the opposite direction by gradual changes to the strength of applied electric field. Adapted from Kalenius et al. (2019).*

Because molecules in the drift tube tumble freely, the resulting CCS corresponds to orientation-averaged area interacting with the drift gas[52] and can be compared to theoretical models or known structures[53]. Combination of native MS and ion mobility can be used to elucidate heterogeneity, conformation stability, ligand binding strength or assembly pathways of protein multimers[54], complexes of proteins and nucleic acid such as CRISPR/Cas[55] and molecules as large as viral capsids[56,57] or ribosomes[58].

1.2.4.3. Covalent Labelling

Covalent labelling (CL) probes solvent accessible and reactive regions in proteins and through localized changes in extent of modification when comparing several protein states, deduces information about protein-protein or protein-ligand interactions or structural dynamics. The key feature is that these labels covalently modify amino acid side chains, creating irreversible mass changes which are then analysed usually by proteolytic digestion and LC-MS/MS analysis[59]. Since large number of protein complexes are mediated primarily by amino acid side chain interactions, covalent labelling can be very sensitive method for elucidation of these interactions. Additionally, utilizing very fast reaction kinetics of

hydroxyl or carbene radicals, CL can also be used to study protein folding reaction occurring on μsec timescales if performed properly[60,61].

Labelling reagents can be both specific to a given amino acid side chain or functional group, or non-specific, able to modify broader set of residues[62]. Specific reagents consist of large variety of chemicals with unique mechanisms of action for any given residue or functional group. Most common residue targets are those with carboxylic group[63], arginine[64], cysteine[65], histidine[66], lysine[67], tryptophan[68] or tyrosine[69]. Among the most commonly used non-specific reagents are hydroxyl radicals (•OH) produced usually by H_2O_2 photolysis or radiolysis of water[70,71] and targeting oxidizable amino acids like Cys, Met, Trp, Tyr and Phe, singlet carbenes produced by photolysis of precursors like 3-trifluromethyl-3-phenyldiarizine[72] and trifluoromethyl radicals (•CF3) produced by laser photolysis of triflinate[73], both of these able to insert into X-H bond (where X is C, O, N, or S) or diethylpyrocarbonate (DEPC) modifying nucleophilic amino acid side chains[74].

1.2.4.4. Chemical Cross-linking

Being technically a type of covalent labelling method, chemical cross-linking is a structural mass spectrometry method capable of obtaining distance constraints between various parts of protein, or between different proteins during their interaction. It is based on covalently labelling amino acid side chains with bifunctional reagents separated by a linker of a defined length. The labelling of two residues by the reagent will only occur if amino acid side chains in question are at any time during the reaction separated by a specific distance given by the linker length[75]. Thus by detecting the cross-linking products by a bottom-up analysis, it is possible to reconstruct these distances and utilize them for protein model refinement[19], for analysis of protein conformation and its changes[76] or to detect previously unknown interactions between analysed proteins[77].The most commonly used cross-linkers and amino-acid residues they react with are shown in **Table 1** on page 20[78].

CROSS-LINKER	SPACER LENGTH	RESIDUE REACTIVITY
BS3/DSS	11.4 Å	K, S, T, Y or N terminus to K, S, T, Y, or N terminus
DSSO	10.3 Å	K, S, T, Y or N terminus to K, S, T, Y, or N terminus
EDC	0 Å	D or E to K, S, T, Y or N terminus
DMTMM	Depends on variable dihydrazine spacer	D or E to D or E
SDA	3.4 Å	K, S, T, Y or N terminus to any amino acid residue

Table 1: Overview of most commonly used cross-linkers*. Spacer length and reactivity is also shown. Adapted from O'Reilly and Rappsilber (2019).*

However, not all cross-linkers necessarily happen to bind with both reactive groups to residues of interest. When we consider cross-linking a mixture of two presumably interacting proteins for a defined amount of time and then quenching the reaction, four possible cross-linking products may arise (**Figure 4**, page 21).

Type 0 (or Dead-end) cross-links are formed by binding of cross-linker to one residue while having the second functional group hydrolysed. This would be detected as a characteristic increase in mass of the peptide.

Type 1 (Intrapeptide or "Loop") cross-links are formed when two reactive residues are cross-linked by the reagent within one peptide. This would also be detected as a characteristic increase in mass of the peptide, different to the increase caused by dead-end cross-link due to the additional covalent bond.

Type 2 (Interpeptide) cross-links are formed when cross-linking reagent connects residues of two different peptides that can originate both from the same protein or from different proteins. Type 2 cross-links are detected as a mass signal corresponding to the sum of mass of two different peptides and a cross-linking reagent.

Type 0 cross-links only yield information about reactivity of residue to which cross-linker is bound and is therefore effectively serving only as a standard covalent label discussed in chapter 1.2.4.3. Type 1 and Type 2 cross-links provide distance constraints, either within one protein, or between different proteins, and can be used for protein model refinement, to detect changes to protein conformation under various conditions or provide information about protein-protein interaction and probable interaction interfaces.

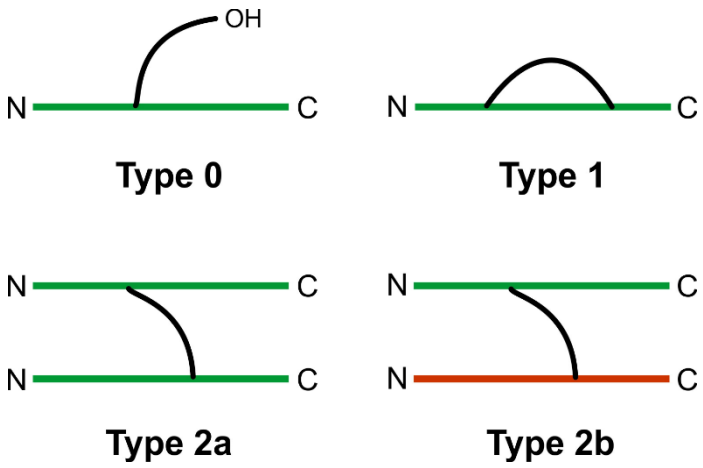

Table 4: Overview of possible forms of cross-linking product*. Type 0 - dead-end cross-link, Type 1- intrapeptide cross-link, Type 2a - interpeptide cross-link with both peptides originating from the same protein, Type 2b - interpeptide cross-link with each peptide originating from a different protein.*

To simplify detection of cross-linked peptides during LC-MS/MS analysis, which requires significant computing power due to the number of possible combinations of mass that need to be verified, isotopically labelled cross-linking reagents were developed. By incubating the sample with a mixture of "heavy" deuterium labelled and "light" cross-linker, each cross-linking product carrying the reagent will appear as a double peak in MS spectra with a characteristic difference that can be searched for[79]. Another improvement in cross-link detection are "MS-cleavable" cross-linkers, which yield characteristic product ions and constant mass changes during collision-induced dissociation in tandem MS analysis, further simplifying search for cross-link signals and their analysis in mass spectra[80].

The use isotopically labelled cross-linkers can also be used to conduct a quantitative analysis and compare two (or possibly more) protein states. Different samples are incubated with different isotopic variant of cross-linker and their proteolytic digests are mixed and analysed together. The characteristic double peaks indicating successful cross-linking are then still present and ratio of the two signals gives relative abundance of given cross-link formation in given sample. Information about differences in protein structure or different interaction kinetics can be obtained in this way[81].

In-vivo cross-linking presents the latest advancement[82], however problems with permeation of cross-linkers through cell plasmatic membrane and low abundancy of formed cross-links still make this approach inconvenient, although ingenious methods like genetically-encoded photoactivatable amino acid based cross-linkers are promising[83,84].

1.2.4.5. Hydrogen/deuterium exchange

Hydrogen/deuterium exchange coupled with mass spectrometry (HDX-MS) is a non-covalent labelling method capable of providing information about protein structure, its dynamics or interactions with other molecules. The method is based on the exchange of hydrogens in a protein for deuterium from solvent D_2O, and subsequent mass spectrometric analysis which detects increase in mass associated with the exchange. The rate of exchange is influenced by solvent accessibility of exchanging hydrogens and their possible hydrogen bonding and local conformational dynamics[85]. In folded proteins, the exchange can thus wary wildly on the timescales from minutes to months[86]. The measured rate of exchange in specific parts of protein over a time period can yield information about anything from protein structure and its dynamics[87] to protein-protein[88,89]or protein-ligand interactions[90]. The analysed sample can in principle be labelled in any ESI compatible solvent and even in heterogenic solution[91], giving the HDX-MS the advantage of using much more native conditions than higher-resolution structural methods like X-ray crystallography or NMR. This makes HDX-MS able to complement these methods and provide additional layer of information about dynamics and function of studied proteins. Since HDX-MS was used in this work, more details were included in this chapter compared to other structural mass spectrometry methods.

1.2.4.5.1. Hydrogen exchange in proteins - principles

The phenomenon of hydrogen/deuterium exchange in proteins was first described in 1954[92] when it was found, that hydrogens atoms in proteins can freely exchange for hydrogens from solution, detected by retention of deuterium on protein after incubation in D_2O. Different type of hydrogens in protein structure exchange at a different rate. Side chain hydrogens in carboxyl, hydroxyl, sulfhydryl and primary amine groups exchange rapidly, while hydrogens bonded to carbon atoms do not exchange at all. The middle ground are amide hydrogens of polypeptide backbone, which exchange at a convenient rate due to their involvement in structural hydrogen bonding, and their rate of exchange can be followed using suitable analytical methods (**Figure 5**, page 23)**.**

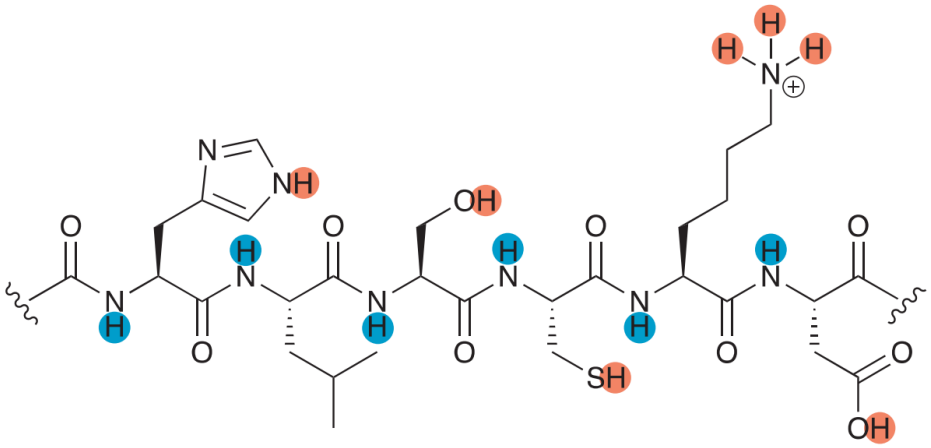

***Figure 5**: Different hydrogens in protein and their relative rate of exchange. Exchange of hydrogens in **orange** is usually too fast to be measurable. Exchange of amide hydrogens at the peptide bond in **blue** is happening on timescales of seconds to days and thus detectable. Adapted from Oganesyan et al. (2018).*

The rate constant for exchange of fully solvent-exposed backbone amide hydrogens is referred to as k_{ch} ("chemical" rate constant) and depends on neighbouring amino acid side chains, temperature and pH. The exchange of these hydrogens can be catalysed by both OH^- and H_3O^+ ions depending on pH of the solution. In aquatic solution, OH^- catalysed exchange dominates down to the pH of around 2.5, where H_3O^+ catalysis becomes higher due to protonation of the peptide group being the rate-limiting step of acidic catalysis[93]. The pH profile therefore shows a local minimum with OH^- catalysis in pH higher than at the rate minimum and H_3O^+ catalysis in pH lower (**Figure 6**, page 24)[94,95].

The influence of neighbouring amino acid side chains is mainly due to polar side chains rendering amide hydrogens more acidic and thus increasing OH^- catalysis rate involving proton abstraction while limiting H^+ catalysis dependent on protonation[96], however in common protein sequences, these sequence dependent changes to exchange kinetics are within a factor of 10 and therefore generally do not mask changes in exchange dependent on protein structure or hydrogen bonding[97].

Since hydrogens are exchanged for deuterium in HDX-MS experiments, the kinetics of exchange also differs slightly from pure hydrogen exchange mainly because of solvent kinetic isotope effect. This effect is caused by different effectivity of catalysis by either OH^- or OD^- due to each having a different basicity. The same effect also applies to acidic catalysis by H_3O^+ and D_3O^+[98]. The temperature affects the exchange rate according to traditional

Arrhenius equation, but it also influences protein fold and thus can change activation energy of the exchange at specific parts of the protein. This makes the effect of temperature on exchange rate non-logarithmic[86].

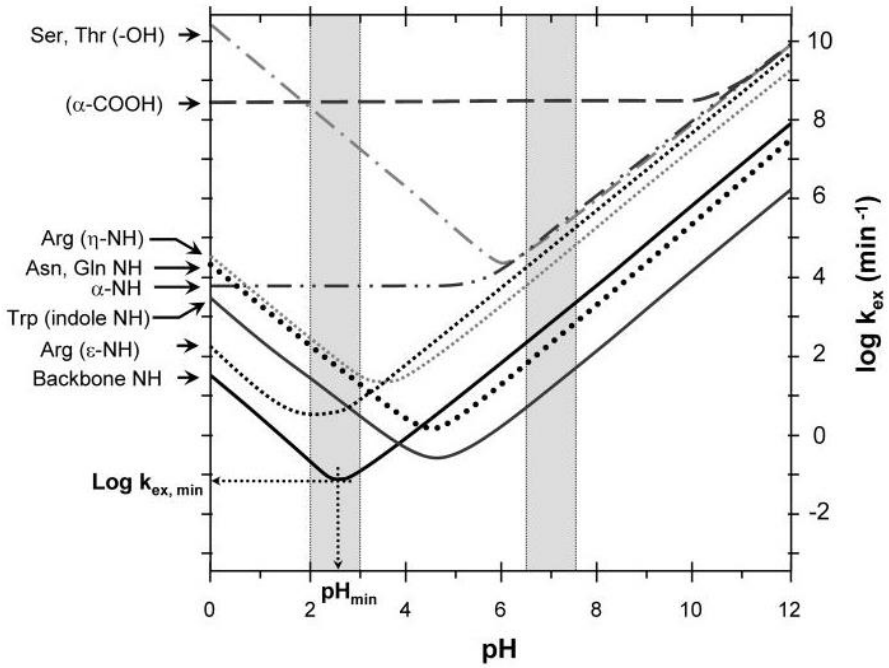

Figure 6: Dependance of rate of exchange of different hydrogens in protein on pH. *Hydrogens bonded directly to carbon atoms are now shown, as those do not exchange under normal conditions. Adapted from Morgan & Engen (2009).*

Usually though, hydrogens are not fully solvent-accessible and can also be involved in hydrogen bonding. Both factors contribute to a protection from exchange of the given amide hydrogen and a corresponding protection factor $P = k_{ch}/k_{HDX}$ was defined with k_{HDX} being the overall rate constant of deuteration reaction. The protection from exchange significantly affects the overall exchange rate as the P can be in the range of 10^6 in natively folded proteins[86]. That means the exchange events of these hydrogens are effectively dependent on conformational fluctuations of the protein, which make these hydrogens temporarily more prone to exchange, either by making them more accessible, or disrupting their hydrogen bonding. Some hydrogens are unable to exchange at all, until global unfolding of the protein occurs[99]. With the time period when hydrogen is exchangeable or unexchangeable denoted as "open" state and "closed" state respectively, following equation can be constructed for hydrogen/deuterium exchange[100]:

$$H_{closed} \underset{k_{cl}}{\overset{k_{op}}{\rightleftharpoons}} H_{open} \xrightarrow[D_2O]{k_{ch}} D_{open} \underset{k_{op}}{\overset{k_{cl}}{\rightleftharpoons}} D_{closed}$$

where k_{op} signifies the rate of opening and k_{cl} the rate of closing. When $k_{cl} >> k_{ch}$, there is only a small chance hydrogen will be exchanged with each opening and the increase in deuteration in the region of protein displaying this behaviour will be gradual with rate limiting step being the chemical rate of exchange. This seemingly bimolecular reaction kinetics was termed EX2 kinetics. On the other hand, when $k_{cl} << k_{ch}$, for each opening there is a high chance hydrogen will be exchanged. This effectively makes the deuteration profile non-gradual, with hydrogens displaying this behaviour being split into a population of hydrogens yet unexchanged and a second population which has already undergone the opening and became fully exchanged. This seemingly unimolecular reaction kinetics not dependent on rate of catalysis is termed EX1 kinetics[99,101] (**Figure 7**)[102].

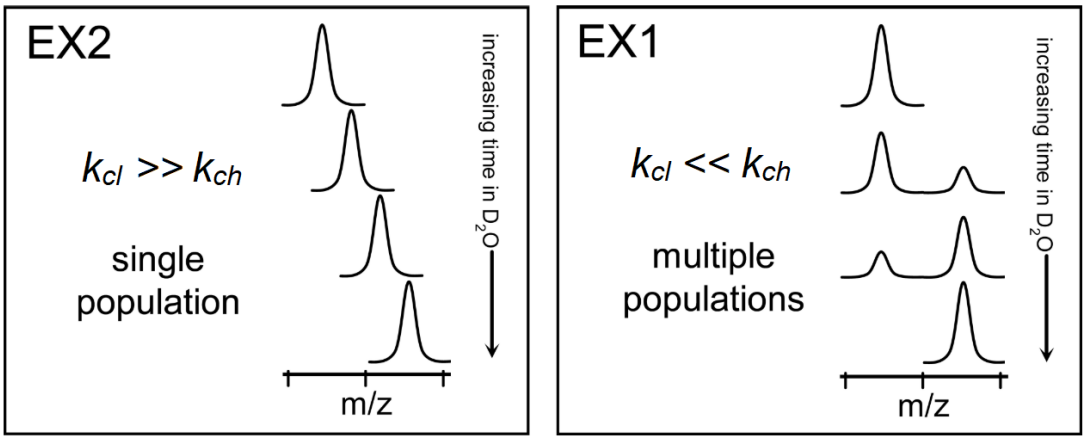

Figure 7: Schema of EX1 and EX2 deuteration kinetics. *Adapted from Engen et al. (2013).*

The EX2 kinetics is more common and is typically observed in structured regions of proteins. Changes in the gradual increase in deuteration also usually accompany transient and reversible protein-protein and protein-ligand interactions. EX1 kinetics on the other hand reveals alternate protein states or sudden structural changes like irreversible thermal unfolding or protein degradation, with a population of protein suddenly undergoing extensive deuteration. The type of kinetics observed can thus also give information about the structural dynamics of given region of protein.

1.2.4.5.2. HDX-MS workflow and analysis

Most HDX-MS experiments are done in *continuous labelling* mode (**Figure 8**)[103], where protein sample is incubated in typically 80-90% D_2O for various time intervals. The continuous increase in deuteration is observed and changes to the exchange under different conditions or in presence of different other molecules are detected. Time intervals can vary from seconds to days and the time of incubation is only limited by protein stability. After a set incubation time, the exchange reaction is "quenched" by adjusting pH to around 2.5 where the exchange is minimal and usually also rapidly frozen in liquid nitrogen to stop the exchange and avoid back-exchange of deuterium for hydrogen during subsequent analysis[103].

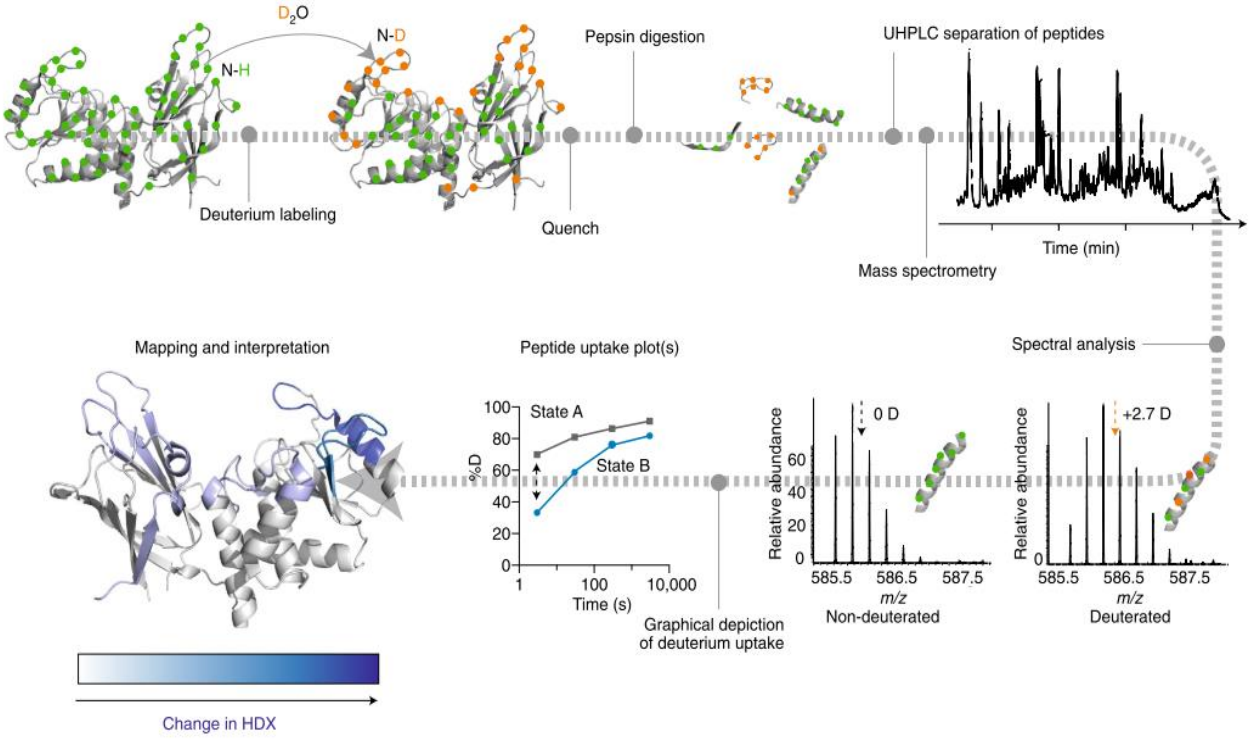

Figure 8: Schema of the common "bottom -up" HDX experiment. *Sample is incubated in D_2O and aliquots are taken at specific incubation times. Deuteration is stopped by lowering pH and temperature. Samples are subsequently analyzed by LC-MS after proteolytic cleavage, often done "online" with protease columns connected to LC-MS setup. Rate of deuteration is calculated from the average mass change of any given peptide. Adapted from (104).*

Another approach is *pulsed labelling*, in which unstable or conformation changing protein is incubated in H_2O based solvent for various time intervals and only labelled for a same short time period afterwards. This approach can give information about various protein states that occur during the incubation timeframe[104]. While the experiments are usually performed manually requiring significant time and labour investment, pipetting robots specially designed for HDX have been developed streamlining the process and increasing the reproducibility of deuteration significantly[105]. Even with pipetting robots however, the shortest possible deuteration times remained at around 10 seconds, where very dynamic and flexible regions of proteins already undergo full deuteration. Therefore, quench-flow systems were developed with D_2O dilution and subsequent quenching performed in a flow system enabling sub-second deuteration times[106] with recent advances also including 3D printed microfluidic chips[107].

The analysis of deuterated samples is usually done using a "bottom up" approach characterized by protease digestion of the sample and subsequent HPLC-ESI-MS. The deuteration is calculated from mass increase of peptides and spatial resolution therefore depends on proteolysis. Because the digestion needs to be performed under low pH, typical protease used is pepsin, which also has the advantage or relatively low specificity, creating overlapping peptides that enable to further increase the resolution by calculating deuteration of overlapping regions[108].

A range of alternative proteases was also developed specifically to allow digestion under HDX quench conditions[109,110]. To avoid using proteases altogether, an effort has also been made to adapt top-down mass spectrometry with ECD, ETD and UVPD[111] fragmentation techniques for analysis of deuterated proteins, with the advantage of limited hydrogen back-exchange and potentially higher spatial resolution[112,113].

1.3. Fungal Cellulolytic System – LPMO and CDH

The global rise in energy consumption, inevitable oil shortage and concerns regarding carbon dioxide production and its role in climate change all contribute to the effort to find alternative sources of both energy, and important chemicals that do not contribute to carbon dioxide production and are renewable. Since one of the perspective ways to obtain "clean" energy is the utilization of vast solar energy collector that is plant biomass, research into efficient saccharification of lignocellulosic matter is currently one of hot biotechnological topics. Through photosynthesis and plant growth, around 56.4 petagrams (10^{15} g) of carbon are annually siphoned from atmosphere and bound mainly in the form of polysaccharides composing wood[114]. However, wood is exceptionally resistant to biological degradation, which is currently the main bottleneck of utilization of wood for biofuel production[115,116].

Wood comprises of three main components: cellulose (40-45% of dry weight), hemicellulose (20-30% of dry weight) and lignin (15-25% of dry weight)[117]. Cellulose, while being a polysaccharide composed of β-(1→4) linked D-glucopyranose units and thus theoretically susceptible to hydrolases, displays remarkable resistance to biodegradation mostly due to its complex structure[115,118]. Two forms of cellulose exist, amorphous with tightly packed fibres forming parallel strands held together by hydrogen bonding, that aggregate into larger microfibrils, resulting in crystalline-like structures with flat surfaces completely inaccessible by standard hydrolytic enzymes dependant on binding of polysaccharide fibre into an active site cleft of the enzyme[115,118]. This recalcitrance of cellulose is largely assisted by hemicellulose, mainly xylan fibres. Xylan is a polymer composed of repeating β-(1→4) linked xylose units modified with acetyl and glucuronic acid side groups[119]. These fibres are responsible for both cross-linking of separate cellulose microfibrils, but also run along these microfibrils adding additional sterical protection to cellulose while being harder to degrade due to extensive modification of their surface[120,121]. Finally, additional structural integrity of wood is given by lignin, which is a cross-linked phenolic polymer biosynthesized by radical-catalysed polymerization with the assistance of various oxidative enzymes[122]. In contrast to other biopolymers such as proteins, saccharides or nucleic acids, lignin is undegradable by hydrolysis and boasts a densely packed structure sterically inaccessible by most enzymes, which makes it very resistant to biodegradation.

In order to efficiently process such biomass into simple saccharides or fuel, all these components must be degraded. In nature, wood decaying fungi belonging mainly to

Basidiomycetes and *Ascomycetes* are the primary contributors to degradation of wood and they employ specialized cellulolytic enzymatic systems to degrade and consume lignocellulose[118]. These specialized enzymes and their unique mode of action is now being heavily researched and used in biorefineries. Two of them are lytic polysaccharide monooxygenase (LPMO) and cellobiose dehydrogenase (CDH) (**Figure 9**). Structural aspects of these enzymes and their activity was studied in this work and represent good example of proteins, in which the dynamics of their structure heavily impact their function, and thus structural mass spectrometry is a suitable method for their study.

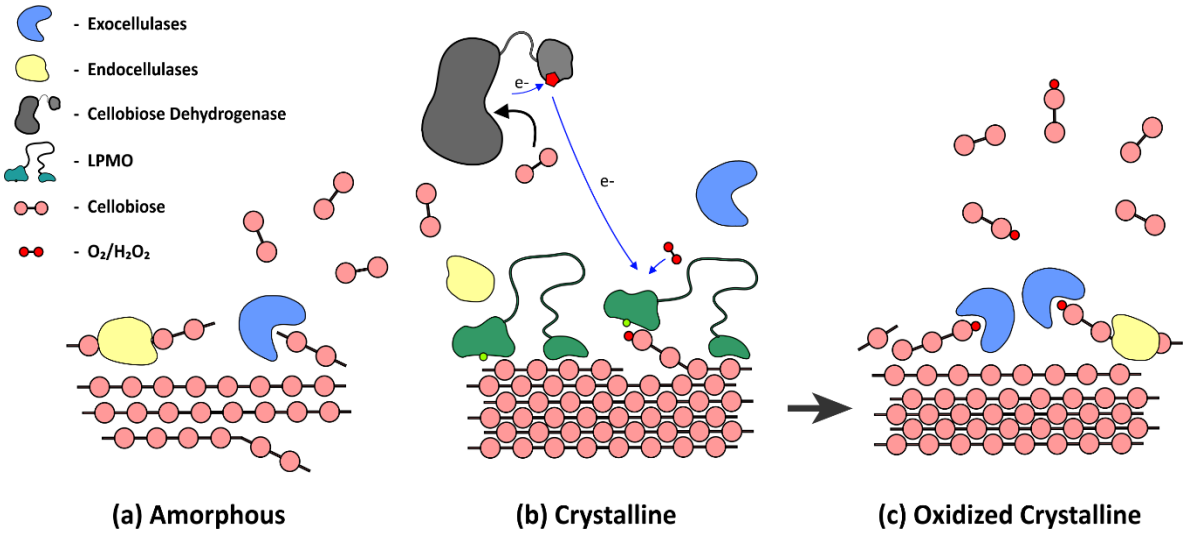

Figure 9: Schematic representation of fungal cellulolytic system employing CDH and LPMO. *Amorphous cellulose structures* ***(a)*** *are easily accessible by endo- and exocellulases and therefore are readily broken down into mono- and disaccharides. Crystalline cellulose* ***(b)*** *is however sterically hardly accessible and LPMO enzymes with flat catalytic sites are needed to oxidatively cleave these parts of cellulose to make them accessible* ***(c)****.*

1.3.1. Lytic Polysaccharide Monooxygenase

Lytic polysaccharide monooxygenases are cellulolytic copper-dependent redox enzymes, found mainly in bacteria[123] and fungi[124] but also in several other organisms[125,126], having their cellulose degradation enhancing properties first identified in 2010. Formerly an enigmatic enzyme family wrongly classified as glycosyl hydrolase family GH61, they were found to boost the effectivity of pre-treated corn stover hydrolysis by *T. reesei* cellulases[127]. Their mechanism of action was quickly found to be oxidative in nature and based on Fenton chemistry revolving around reduction of the active site copper ion, which subsequently binds

O_2 (or H_2O_2) to produce reactive oxygen species breaking down glycosidic bonds in polysaccharides and in light of this, they were reclassified as lytic polysaccharide monooxygenases[128–133]. The previous evidence for extracellular reactive oxygen species (ROS) production in fungi suspected to be connected to cellulose degradation was thus confirmed[134].

The LPMO active site is located on the flat surface of the protein and contains Cu^{+2} ion coordinated by histidines usually assisted by tyrosine in a conserved structural motif called histidine brace[135,136]. The flat surface enables the enzyme to bind on the surface of recalcitrant crystalline polysaccharide structures, which are otherwise inaccessible by standard exo- and endohydrolases[137]. Some LPMOs also carry carbohydrate binding modules (CBMs) on a flexible linker, which assist in substrate binding[138]. When reduced from Cu^{+2} to Cu^{+1} by either small-molecular reductants or its redox partner enzyme cellobiose dehydrogenase (chapter 1.2.3.2), LPMOs affinity to polysaccharide substrate, mediated by several aromatic residues surrounding the active site[139], is increased[140] and reduced copper ion binds either oxygen[141,142] or hydrogen peroxide[143,144] to produce ROS. These radicals are directed at either C1 or C4 position of β-(1→4) glycosidic bonds of polysaccharides, depending on the type of LPMO, causing oxidative cleavage of the bond[130,145]. If the cleavage happens close to the end of polysaccharide chain, oxidized oligosaccharides are released to the solution and if they are long enough, can be bound and cleaved by LPMO further[146]. As more examples of these enzymes were found, they were classified as Auxiliary Activity (AA) by CAZy database of carbohydrate active enzymes[147]. LPMOs were eventually found degrading chitin (AA11)[123,148], starch (AA13)[149], and various hemicelluloses (AA14-16)[150,151], giving them a broad substrate specifity in regards to lignocellulose depolymerisation.

While these enzymes are already utilized biotechnologically, they have a serious limitation in the form or low stability during catalysis and their application is challenging to optimize due to plethora of possible reactions occurring when mixing reductants, oxygen, hydrogen peroxide and not necessarily “clean” and precisely defined insoluble substrate[152]. This low stability was not researched thoroughly yet with only a handful of studies concerning thermal stability and possible structural changes during catalysis[140,153], however oxidative damage due to off-pathway catalytic processes is suspected to be involved[143].

The nature of the cosubstrate is also a topic of heated discussion, with increasing number

of reports stating that H_2O_2 is in fact the true cosubstrate and O_2 is only an intermediate, which would in fact make the enzyme peroxygenase and not monooxygenase[139,143,144,154,155]. This is in contrast to previous belief of O_2 being the polysaccharide substrate oxidizing cosubstrate of LPMO enzymes directly[3,142,156]. Thus, study of structural dynamics of LPMOs during catalysis and the nature of its cosubstrate are currently both an important topic to tackle.

1.3.2. Cellobiose Dehydrogenase

Cellobiose dehydrogenase (CDH; EC 1.1.99.18) is so far the only identified extracellular flavocytochrome[157]. It is composed of two functional domains: N-terminal cytochrome domain (CYT) harbouring heme *b* and C-terminal dehydrogenase domain (DH) containing flavin adenine dinucleotide (FAD) cofactor with a flexible linker connecting the two domains[3,158] and CDHIIA variants also containing family 1 CBM[159]. These enzymes are expressed in fungi alongside LPMOs and can form more than 2% of secreted cellulases in fungal secretomes[160]. Cellobiose or other small sugars including lactose and glucose[161] can be oxidized at the DH domain while reducing the FAD cofactor to $FADH_2$. Electrons from $FADH_2$ are then channelled in two one-electron steps to CYT domain via direct interdomain electron transfer (IET). Once at the CYT domain, electrons can be transferred to terminal acceptor, which is usually LPMOs active-site copper ion, reduction of which starts LPMOs oxidative depolarization of cellulose[3].

The IET is the crucial step in CDH function and dictates the rate at which CDH supplies electrons to other molecules[162]. It was found, that this transfer is occurring as a flip-flop mechanism during which CDHs separate domains alternate between a “closed” to “open” conformation using the flexible linker as a separator[158]. In closed conformation, domains get close enough for electron transfer to happen between FAD and heme *b*, which is followed by domain separation which positions CDH in an open conformation, where CYT domains heme *b* is facing away from CDH molecule and is free to pass the obtained electron[3]. Importantly, the electron can be transferred not only to LPMO molecule, but to any other molecule with suitable redox potential and even to the surface of electrode[161]. This has been utilized in the production of CDH based biosensors in the form of electrodes covered in immobilized CDH, which is able to detect selected saccharides and directly produce

electrical current proportional to the amount of saccharide present in the solution, albeit not linearly. The extent to which domains interact is largely governed by distribution of electrostatic charges on the interaction interfaces of the domains giving the protein specific pH optimum when domain repulsion is lowest[163–165].

Current research into CDH mostly revolves around study of interdomain electron transfer and rational engineering of the enzyme to modulate its pH optimum and other parameters to increase its viability in industrial biomass degradation and biosensor design[166–169].

1.4. Biological Photosensitisers

Photosensitizers (PS) are light absorbing compounds that produce specific reactive oxygen species (ROS) from oxygen upon irradiation with light of specific wavelength. They have found use in antimicrobial photodynamic inactivation (aPDI)[170], photodynamic therapy (PDT)[171] cancer treatment or in the study of cellular ROS mediated signalling[172]. Upon light irradiation, PS undergoes a transition to a singlet excited state and subsequently triplet excited state through intersystem crossing. Triplet state has relatively long lifetime and enables the PS to transfer energy to O_2 to produce singlet oxygen $^1O_2$ (so called type-II mechanism), or superoxide radical anion ($O_2•^-$) with the help of electron transfer from suitable neighbouring molecule (so called type-I mechanism). Superoxide anion can then undergo series of redox reaction and generate other ROS such as hydrogen peroxide (H_2O_2) or hydroxyl radical (OH•). Majority of photosensitisers are not selective to just one mechanism and produce a mixture of type-I and type-II products, with the ratio being influenced by PSs micro-environment.

Produced radicals, especially ^{1}O2 are highly reactive and induce oxidative modification of various macromolecules leading to cell death[173]. Using exogenous dyes as PS for PDT is not effective, due to inability to effectively target specific cells, general toxicity and limited pharmacokinetics. To address this issue, genetically encoded PS were developed. Majority of currently used and studied genetically encodable PSs are flavoproteins carrying FMN or FAD and derived from microbial and plant "light, oxygen and voltage sensing" (LOV) photoreceptor domains of phototropin[174].

The LOV photoreceptors, occurring in archaea, bacteria, fungi and plants are responsible for phototropism, chloroplast movement, circadian rhythms or general stress response, all of these physiological responses being driven by light or reactive oxygen species stimuli[175].

During the photocycle of LOV, the signal is transduced as a structural rearrangement of the domain following a formation of a covalent bond between conserved Cys residue in the active site of the protein and C4a atom of the present flavin isoalloxazine ring upon irradiation of FMN or FAD by blue light. Importantly, cysteine devoid variants were also reported showing higher levels of flavin radical species detected upon irradiation.

These proteins can also be fused to targeting sequences or antibodies, to direct them to specific cell compartments or cell types[171]. However, protein scaffold holding FMN limits the ROS production, so special proteins like miniSOG (mini Singlet Oxygen Generator) are engineered to increase the quantum yield of the ROS production[176]. Exact knowledge of protein structure and mechanistic details of ROS generation in natural photosensitizing domains are crucial for effective development of new photosensitizers and part of this thesis is aimed at structural and functional study of one such domain from *Avena sativa* – *As*LOV2[177].

2. Aims of the Thesis

The aim of this thesis was to explore structural aspects of different functional states of fungal enzymes CDH and LPMO involved in cellulose degradation and changes accompanying singlet oxygen generation by LOV2, using structural mass spectrometry methods.

The specific goals were:

- To characterize the interaction of cellobiose dehydrogenase and lytic polysaccharide monooxygenase
- To characterize structural stability of LPMO and structural changes accompanying LPMO inactivation during catalysis
- To obtain information about the nature of LPMO co-substrate
- To characterize changes occurring on *As*LOV2 during its light irradiation and production of reactive oxygen species

3. Methods

The publications included in this Ph.D. thesis provide a full description of all methods and experimental procedures used together with details necessary for their reproduction. Therefore, this chapter serves only to list experimental techniques used throughout the thesis.

List of used research methods:

- Protein sample preparation for MS analysis including enzymatic deglycosylation
- MS-based analysis of protein primary structure and post-translational modifications (MALDI-TOF, ESI-FTICR directly or in LC-MS and LC-MS/MS setup)
- MS analysis of oligosaccharides (MALDI-TOF)
- Hydrogen / deuterium exchange mass spectrometry
- Turbidimetric measurement of LPMO cellulolytic activity

4. Results and Discussion

The aim of this work was to analyse biotechnologically and medicinally important enzymes through the use of structural mass spectrometry. Three distinct enzymes were studied, lytic polysaccharide monooxygenase and cellobiose dehydrogenase, both part of the fungal extracellular cellulolytic system and *As*LOV2, plant derived photosensitizer. This section will thus be separated into two parts, first encompassing **Publication I, II and III** regarding CDH and LPMO and second, concerning *As*LOV2 and **Publication IV**.

4.1. Study of fungal cellulolytic enzymes LPMO and CDH

Fungal cellulolytic enzymes LPMO and CDH are heavily studied proteins, mainly due to their potential use in saccharification of lignocellulosic biomass and for biosensor production respectively. Current understanding of their activity is still insufficient mainly due to the complexity of the system involving ROS and insoluble substrates. Interaction of these enzymes occurring during the electron transfer from CDH to LPMO has remained rather elusive as well, mainly due to its transient nature. Moreover, LPMO is notoriously unstable, limiting its wider industrial use and research possibilities in its active reduced form. The exact aspects of this degradation/loss of activity have not been thoroughly examined either, with previous reports mainly focusing on structural differences between LPMO apo- and holoform and LPMO's overall thermal stability in relation to presence of cofactor and substrate[140,153], with only relatively brief mention of ROS induced damage[143]. The more structure-oriented studies were predominantly using X-ray crystallography or NMR and while providing excellent spatial resolution and describing the side chain mediated binding of polysaccharide substrate to LPMO, they do not provide information about structural aspects of its catalysis[178,179].

Structural mass spectrometry, and especially hydrogen/deuterium exchange can, however, analyse dynamics of protein structure even under such conditions and provide snapshots into effects occurring at various times of incubation, even though being lower resolution methods compared to X-ray crystallography or NMR. In this work, HDX-MS was utilized to shed more light on the interaction of CDH with LPMO, on structural changes occurring on the proteins during protein catalysis on a native substrate and explain its low stability in reducing conditions.

First step was the optimization of HDX protocol for these enzymes and exploring the interaction interface of LPMO and CDH, which was a matter of debate for some time. The main point of optimization was the selection of suitable protease for online digestion during LC-MS analysis and quench buffer composition, which both influence resulting sequence coverage. Mixed sample of deglycosylated *Neurospora crassa* LPMO9C (*Nc*LPMO9C) and *Neurospora crassa* CDH (*Nc*CDH-IIA) was analysed by LC-MS/MS after being processed as a standard HDX sample (with the difference of being dissolved in H_2O based buffer instead of D_2O) with different protease columns and varying composition of quench buffer used. Different Guanidine/Urea (denaturant) and TCEP (disulphide bond reduction) concentrations were tested. Final conditions with best sequence coverage were found to be a combination of immobilized Nepenthesin I and Rhizopuspepsin with a flow of 200 ul/min kept at 0 °C on a sample containing 4M Urea and 100 mM TCEP after quenching.

After the initial optimization, series of HDX-MS experiments utilizing mixtures of LPMO, CDH, cellobiose and cellulose were conducted, with the aim of detecting the interaction interfaces of CDH and LPMO during electron transfer from CDH to LPMO. Here several effects were observed, however none of them was clearly pointing to a defined interaction interface between CDH and LPMO. Quite encouragingly, weak signs of interaction under oxidized conditions when CDH and LPMO were mixed in the absence of substrate or reducing agents were found in the form of very decent structural relaxation around the LPMO's active site. However, no signs of similar effect or protection was observed on CDH. As the functional state, in which CDH is reduced after oxidizing its substrate, is expected to promote more frequent protein-protein contacts between CDH and LPMO, the conditions with cellulose or lactose added were followed. Unfortunately, even repeated experiments found only profound structural effects on both CDH cofactors arising from their reduction and no reliable additional interaction interface could be discerned. Nevertheless, these effects indicated that interdomain electron transfer is occurring and FAD is being reduced influencing the local structure (**Figure 10**, page 38). On the LPMO side, no additional protection was observed either and quite contrary, extensive increase in deuteration together with protein degradation was detected, which was studied further in **Publication I**.

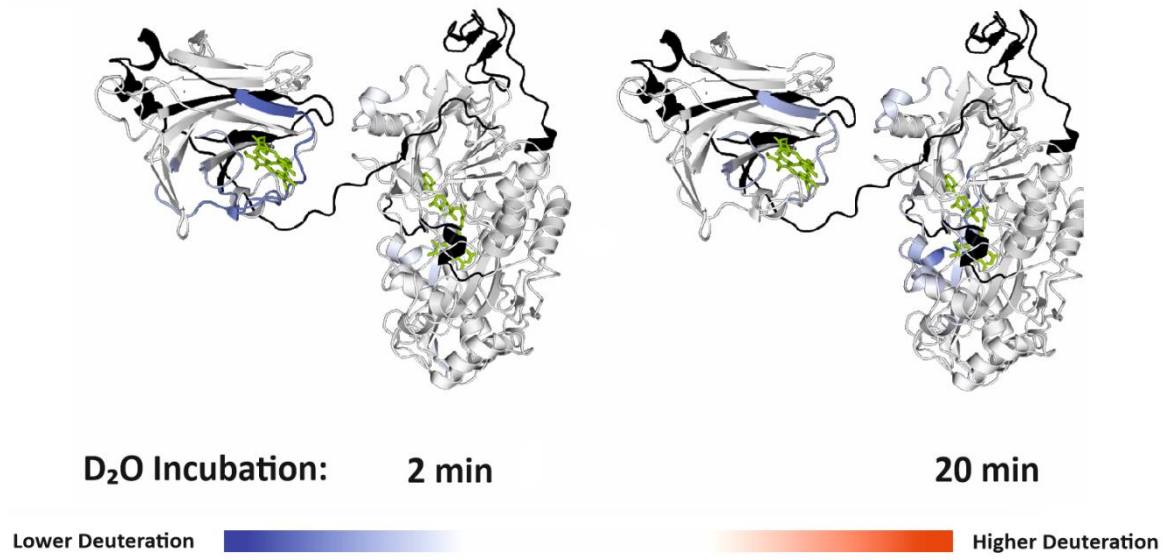

Figure 10: Effect of reduction of CDH by cellobiose measured by HDX-MS. *Protection from deuteration is apparent on the interaction interfaces of cytochrome and dehydrogenase domains. Black parts of the protein were not covered.*

Part of these results was utilized in **Publication III** which is discussed below and then concentrated on the structural dynamics of both enzymes separately. The CDH-LPMO cross-talk was further studied by collaborators using computational approaches combined with mutagenesis and enzyme assays and was recently published in *ACS Catalysis*[180].

The recent study published by Kádek et al. was also extended by a detailed analysis of wild-type and mutant CDH from *Crassicarpon hotsonii*. The mutations replaced four carboxylic residues on interdomain contact interface, which cause charge repulsion at higher pH in wild-type protein effectively eliminating IDET and thus enzyme activity, by lysine residues. This mutation causes shift in pH optimum and retained activity at higher pH. HDX-MS experiments with both glycosylated and deglycosylated *Ch*CDH were performed, showing that lower deuteration was present on interaction interfaces of the two domains when IDET was occurring, both in WT CDH at its optimal pH 5.4 and in the mutated "variant" CDH at pH 7.4, indicating domain contact. In samples of WT CDH at pH 5.4, only protection around the flavin cofactor was detected, pointing to the effect of reduction of DH domain without the effect of IDET. The hypothesis, that charge repulsion of the domains causes open-conformation state to be preferred and decreased IDET and enzyme activity, was thus confirmed. Interestingly, deglycosylated WT CDH also manifested some decrease in deuteration on the interaction interfaces indicating possibly retained activity at pH 7.4.

Since some of the glycosylation sites are close to the interaction interfaces of the two domains, this effect can be explained as some measure of interdomain contact regained even with charge repulsion, when steric hindrance caused by glycans is removed. These data are now being complemented with functional enzyme kinetic analyses and will form the basis of another publication.

4.1.1. Publication I

While studies on CDH-LPMO interaction at reducing conditions provided no decisive protein-protein interaction induced effects, massive increase in deuteration was detected for LPMO molecule at longer exchange times. It was hypothesized that this might be linked to previously suggested LPMO degradation by reactive oxygen species[181], therefore analysis of LPMO in this direction was conducted. Structural changes induced in LPMO upon reduction by ascorbic acid and in presence of polysaccharide substrate as well as changes resulting from the removal of copper ion, were observed under different temperatures to capture the progress of changes, occurring at different rate in different parts of protein.

Reduction of LPMO visualized by HDX-MS revealed two distinct effects. First one was manifesting as decrease in deuteration on peptides around the copper active site occurring at the very short time points. This effect is presumed to be connected to structural changes caused by reduction of copper ion, as similar effect was observed previously using circular dichroism[140]. The second effect was an extensive increase in deuteration progressing with time, starting at peptides around the active site and progressing to the rest of the molecule. This effect is probably the result of structural perturbation and subsequent unfolding caused by oxidative damage by ROS produced at the active site. A number of oxidative modifications predominantly on peptides around the active site, including oxidative peptide cleavages (**Figure 11**, page 40), was identified using LC-MS/MS analysis after incubating LPMO at the conditions of the HDX experiment. Significant (up to 10-fold) decrease in intensities of unmodified forms of affected peptide ions was also observed during the incubation of LPMO with ascorbate in the HDX-MS experiment.

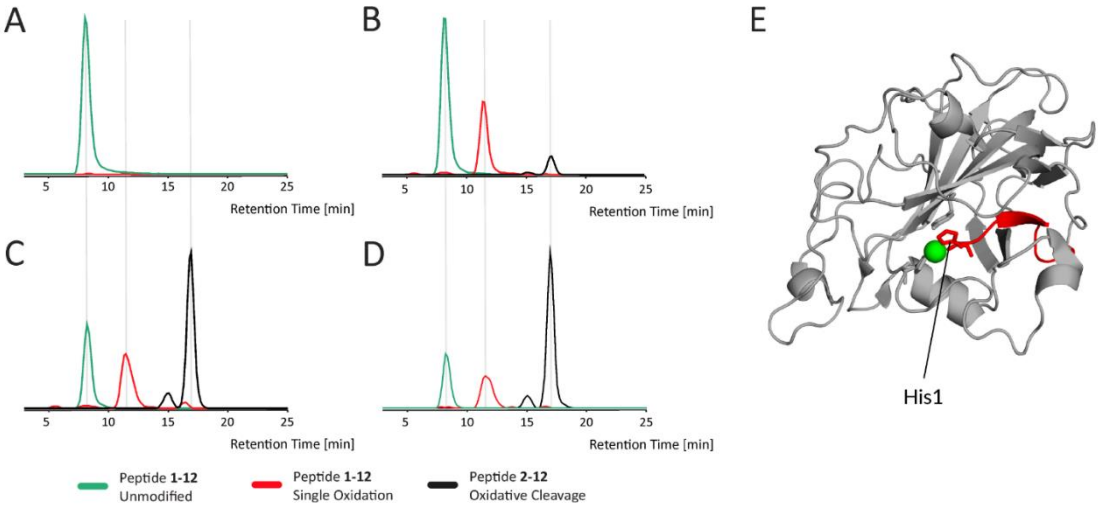

Figure 11. Monitoring kinetics of LPMO oxidative modifications by mass spectrometry. *Extracted ion chromatograms for the N-terminal LPMO peptide (1–12) that contains His1 residue involved in copper ion binding. LPMO were incubated (A) alone for 30 min, or with 5 mM ascorbic acid for (B) 10 min, (C) 20 min, (D) 30 min. Subsequently, it was digested with Asp-N and analyzed by LC-MS/MS. Chromatographic traces show a signal for unmodified (green), oxidized (+O1; red) and oxidatively cleaved (−His, +C1O1-H2; black) peptides. Localization of the peptide and the His residue is shown on a structure in (E). Copper ion is shown as green ball.*

It was previously reported, that cellulosic substrate increases thermal stability of LPMO[140]. To further probe the effect of substrate on the stability of LPMO, another HDX-MS experiment, now with increased temporal resolution, including LPMO with ascorbic acid and crystalline cellulose was performed (**Figure 12**, page 41). To remove the insoluble polysaccharide substrate from the reaction mixture before LC-MS analysis with as little hydrogen back exchange as possible, fast spin filtration step was added in-between quenching and freezing. This must be done thoroughly, since residue particles could clog and damage the HPLC-MS system with pressure sensitive protease column. As the sample is quenched by low-pH solution containing denaturants (0.5 M glycine pH 2.3, 4M Urea, 200 mM TCEP), the release of proteins from cellulosic substrate is also facilitated. The selection and testing of compatible spin filter chemistry was necessary as it was for example found that nylon based centrifugal filters leech a significant amount of contaminants to the sample and seriously affect the LC-MS analysis, which was later confirmed in the literature[182]. Polyvinylidene fluoride (PVDF) filters with pore diameter of 0.22 µM were found to be effective and inert and were used throughout the experiments.

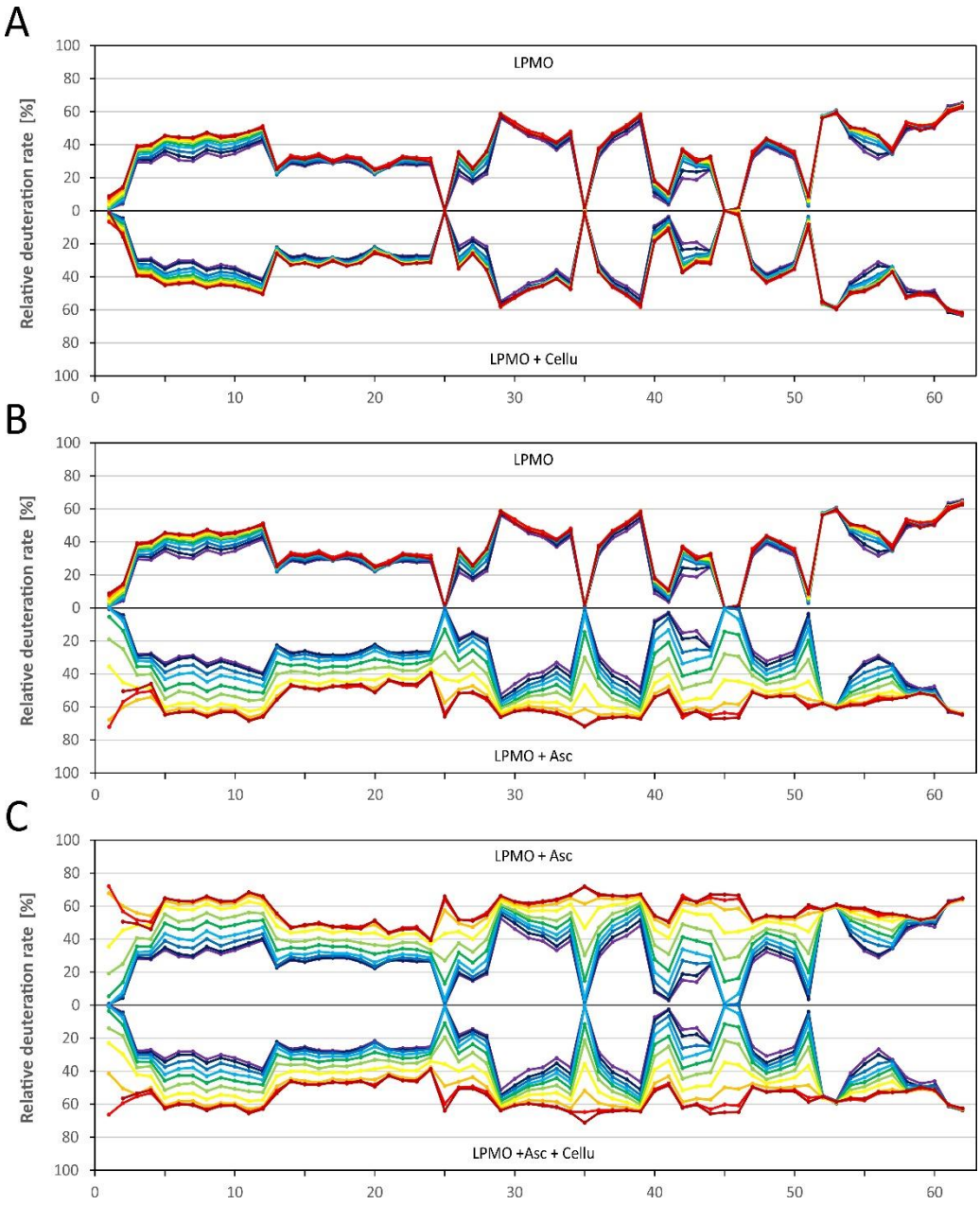

Figure 12: HDX-MS experiment featuring LPMO, ascorbic acid and crystalline cellulose. *Timepoints are 3, 5, 10, 15, 20, 25, 30, 35, 40 and 45 minutes and correspond to the colours starting at purple and ending with red according to sequence of colours in the visible light spectrum.*

In these experiments with cellulosic substrate included, the increase in deuteration upon LPMO reduction manifested on the same peptides as without cellulose, however the presence of substrate slowed down the onset of deuteration increase globally. It seems that, that the presence of suitable amount of cellulose substrate limits the oxidative damage incurred by the enzyme by absorbing bulk of the radicals created. Similar results obtained

with a different methodology were reported during preparation of manuscript [139].

In order to dissect the contribution of different effects in the above described experiments, experiments with apo form of LPMO were conducted to address the stabilization of the overall fold by active site copper ion and the effects of its removal, as active site copper loss may occur upon oxidative damage. These experiments and recent publication, however, showed that the copper remains bound for tens of minutes even at elevated temperature showing strong affinity to the protein[140]. The absence of copper ion was found to lower the overall thermal stability of LPMO, with the strongest effect centred at peptides immediately surrounding the active site. It can be concluded, that active-site copper ion is largely influencing the active site conformation, which is in line with its reported strong binding affinity. Within this study, new workflow based on HDX-MS that can be further used to study the effects of various LPMO reducing agents and substrates as well as mutant versions of LPMO with enhanced stability or catalytic properties was introduced.

4.1.2. Publication II

Our next effort went into gaining more information about the nature of LPMO cosubstrate, more precisely to confirm, whether H_2O_2 reported recently[143,154] is indeed a cosubstrate to LPMO or not, as the nature of the cosubstrate is currently a subject of heated discussion. Turbidimetry has been recently used to observe the cleavage of cellulosic substrate by LPMO[183]. During a stay in laboratory of Roland Ludwig in Vienna, this turbidimetric workflow was modified to a continuous measurement in a tempered spectrophotometer with a magnetic stirrer. In this way, it was possible to measure LPMO activity under various conditions in real time. While ascorbic acid is widely used as a reductant in LPMO activity assays, it also slowly produces H_2O_2. The activity of LPMO with an increasing concentration of ascorbic acid, all of which are presumed to be saturating, was examined. The increase in activity proportional to the amount of ascorbic acid present was observed and when catalase was also present, binding of LPMO to cellulose was retained (reduction dependant), but the cellulolytic activity was severely limited (**Figure 13A**, page 43). Interestingly, catalase also reduced LPMO activity when its natural redox partner CDH was employed as a reductant showing a role of H_2O_2 in native conditions.

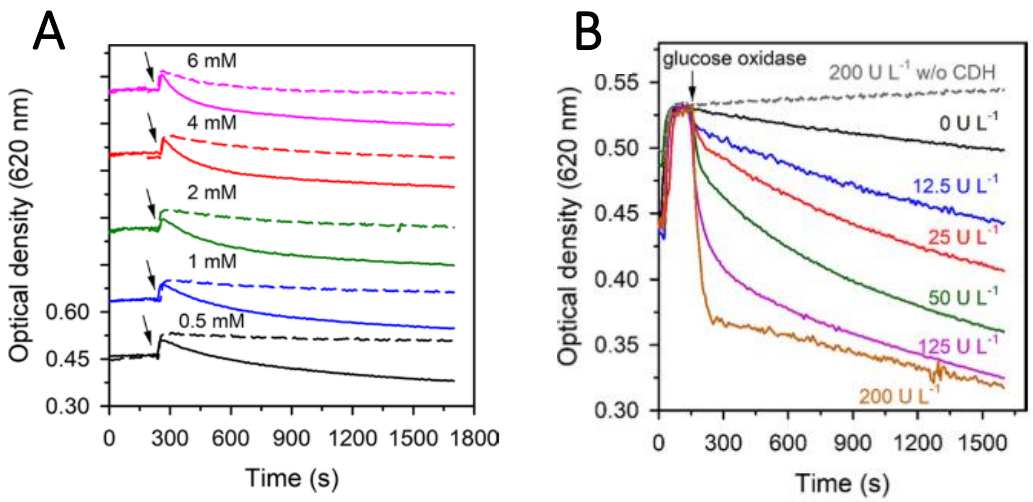

Figure 13: Turbidimetry measurement of LPMO activity with various concentrations of ascorbic acid or GOX. *A) Ascorbic acid addition. Time of addition of ascorbic acid is indicated by black arrow. Initial increase in absorbance is caused by binding of LPMO to the substrate. Gradual decrease of absorbance from that point corresponds to the activity of LPMO. Dashed lines represent identical reactions with the addition of 2000 U/ml catalase. B) GOX addition. Time of addition of GOX is indicated by black arrow. Reduction is facilitated by small amount (0.5 µM) CDH.*

To test the LPMO activity upon addition of raw H_2O_2 into the reaction, glucose oxidase (GOX) was employed as a source of gradually generated H_2O_2 (**Figure 13B**). The activity was found to be proportional to the amount of GOX added and levelled off with very high amount of GOX. That is probably due to oxidative damage incurred by LPMO, as was observed in **Publication I**. There were some concerns, whether H_2O_2 doesn't facilitate a different mechanism of action from O_2-based cellulose degradation by LPMO. To verify that oxidative oligosaccharide products are indeed formed, MALDI-MS measurements of desalted reaction mixtures were performed on FT-ICR mass spectrometer in Prague. These have shown that oxidized oligosaccharides with the length of 3 to 6 are produced in larger quantity when H_2O_2 is added to the reaction.

Electrochemical measurements of H_2O_2 consumption were also performed **(Figure 4 – Publication II)** and showed that H_2O_2 is only consumed when reduced LPMO is present in the reaction mixture and no consumption was detected with unreduced LPMO or with cellulosic substrate alone.

4.1.3. Publication III

The focus of this work, currently under review in *ASC Catalysis,* is the investigation of the two electron transfer steps in *Neurospora crassa* CDH, interdomain electron transfer (IDET) between CYT domain and DH domain and interprotein electron transfer (IPET) from CYT domain to the final electron acceptor. The driving force of IDET is the redox potential between heme *b* of the CYT domain and FAD of DH domain. High variability observed in CYT domains and linkers compared to DH domains in various CDH proteins suggested an evolutionary adaptation to various redox partners with the universal DH domain electron source. To study the effect of various CYT domains and linkers on IDET and IPET, chimeric proteins consisting of various swapped domains from *Nc*CDHIIA and *Nc*CDHIIB were produced and their properties were analysed electrochemically, by molecular docking.

Kinetic measurements showed, that there are differences in presteady-state reduction rates of FAD by cellobiose between the different DH domains, but no additional effect was observed by CYT domain swapping. Chimeric CDH proteins showed shifted pH optimum (**Figure 15**) and reduced IDET rates and modelling of domain contact showed that domain edge-to-edge distance is the key factor in effective IDET, and low-surface complementarity and longer linker causes the protein to prefer open conformation with domains further apart. Thus, it can be concluded, that the rate of IDET is less dependent on electrochemical potential between the cofactors and more dependent on the structural dynamics of respective CYT and DH domains.

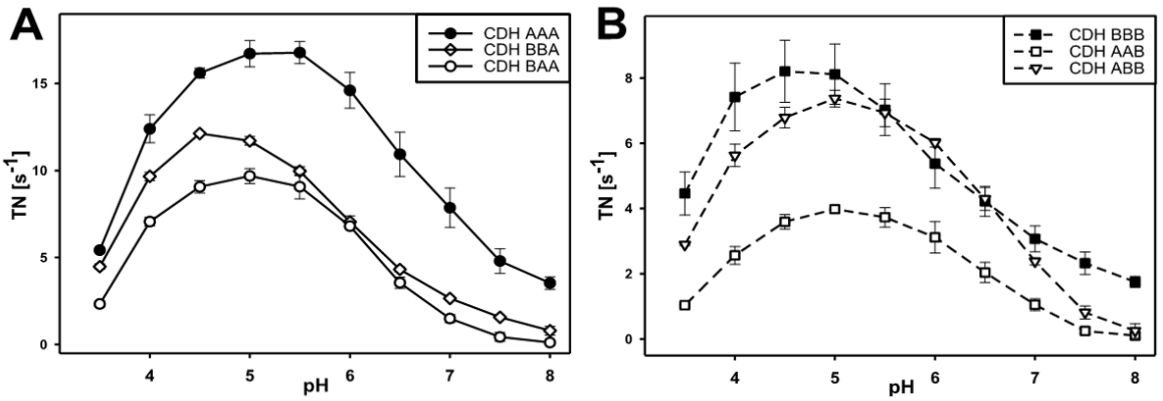

Figure 15: Effects of domain swapping on IDET. *A, pH optima of cytochrome c turnover numbers for wild-type and chimeric CDHs with DH domain from NcCDHIIA. B, pH optima of cytochrome c turnover numbers for wild-type and chimeric CDHs with DH domain from NcCDHIIB.*

Data from previous HDX-MS measurements of the interaction of non-chimeric *Nc*CDHIIA with *Nc*LPMO9C was utilized in this study and it shows (**Figure 16**), that the interaction is only affecting peptides in the vicinity of the active site, disproving previous theory of interaction occurring on the opposite side of the protein on a conserved[129].

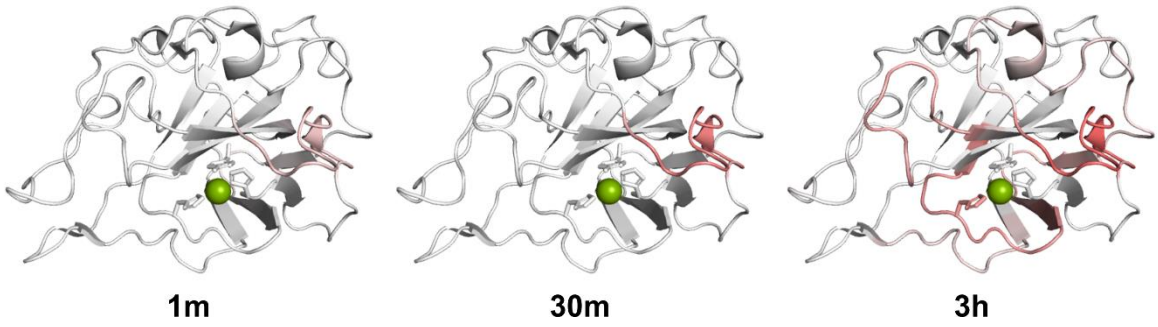

Figure 16: HDX-MS of interaction of NcCDHIIA and NcLPMO9C. *The interaction was observed in oxidized state due to protein degradation occurring in reducing conditions. Structural perturbance was detected on the LPMO in the vicinity of the active site copper ion, indicating direct contact of active sites of CDH and LPMO. No other effect was observed anywhere on the protein.*

Measurement of the IPET rate between WT and chimeric CDH and *Nc*LPMO9C was also performed and showed that just as for IDET, the rate determining step for IPET is not the redox potential difference between LPMO and CYT, but rather the rate at which CDH forms the open conformation with reduced CYT ready to transfer electrons to the acceptor as chimeric CDH proteins more prone to being in the open conformation showed higher IPET rates over wild-type CDHs.

4.1.4. Summary of LPMO and CDH studies

From all the results obtained in **Publication I**, **II and III** it can be concluded, that H_2O_2 is indeed needed for the cellulose breakdown by LPMO to occur and O_2, previously thought as being prime cosubstrate of LPMO, is probably just an intermediate, that needs to be first reduced to H_2O_2 to be utilized by LPMO. Probable mechanism of such LPMO reaction was published very recently[139,148,155] and correlates well with findings both from **Publication I** and **Publication II**. According to this mechanism, LPMO is first reduced in a "priming reduction". Reduced LPMO is able to bind both O_2 and H_2O_2. When O_2 is bound by reduced

LPMO, it is transformed to H_2O_2 and released while LPMO is oxidized during and unable to further utilize it. Another reduced LPMO molecule can, however, bind this H_2O_2 and break it down to form hydroxyl radicals (OH•) in the same manner as was demonstrated before for proteins and solutions containing copper ions[184,185]. When these hydroxyl radicals are formed on LPMO bound to cellulosic substrate, they attack nearby glycosidic bond and facilitate oxidative cellulose breakdown. When these radicals are formed on LPMO not bound to substrate, they react with the enzyme itself, causing oxidative damage and inactivation, both by oxidizing key amino acid side chains facilitating substrate binding[139], and by causing oxidative peptide bond cleavages **(Figure 5, Publication I)**. For effective industrial utilization of LPMO, it is therefore crucial to carefully maintain saturation of LPMO with substrate to eliminate futile side reaction causing protein degradation, while keeping suitable amount of H_2O_2 present to increase the rate of cellulose breakdown in comparison to only using O_2.

Results from **Publication III** then show, that main factors influencing both the IDET and IPET are relative domain flexibility and domain surface complementarity, as CDH variants with longer linkers and lower surface complementarity show increased IPET rate at the expense of IDET rate and vice-versa. The recent data on the mutant version of CDH (not published yet) showed way toward enzyme that can exert its electron transfer activity even at physiological pH and that it functions more efficiently if the aberrant hyperglycosylation is removed. Therefore, there are now experiments underway aiming at the production of these enzymes in other producing cells than *Pichia*.

These findings show, how the function of CDH depends on its structure and its dynamics and are important for engineering of CDH proteins with desired characteristics for biosensor production or industrial cellulose saccharification.

4.2. Study of oxidative processes on *As*LOV2

LOV2 domain from *Avena sativa* phototropin 1 protein (*As*LOV2) is a photosensitizer containing FMN and producing reactive singlet oxygen ($^1O_2$) upon light irradiation. It has been found for similar photosensitizer miniSOG (80% primary structure identity), that continuous irradiation gradually increases the quantum yield of $^1O_2$ production, while causing oxidative modification of amino acid residues surrounding the FMN. The increase in quantum yield is however not fully explained. Study of this gradual quantum yield

increase was thus conducted with *As*LOV2 as model protein. This work was done in collaboration with the group of assoc. prof. Erik Sedlák from the Center for Interdisciplinary Biosciences in Košice.

4.2.1. Publication IV

To study the production of $^1O_2$ by *As*LOV2, wild-type and variant with conserved active-site cysteine C450 replaced by alanine, resulting in limited photoswitching ability and presumably higher flavin radical generation, was used.

The measurement of $^1O_2$ phosphorescence showed gradual increase in $^1O_2$ production upon irradiation of both *As*LOV2 wt and *As*LOV2 C450A. Complementary measurement of FMN fluorescence then showed both shift in wavelength and increase in fluorescence upon protein irradiation indicating release of FMN from the protein to the solution. This effect was more prominent in wild-type protein, with ~1.6-fold increase in FMN fluorescence

	Mod.	wt-N [%]	mut-N [%]	wt-I [%]	mut-I [%]	mut-I - mut-N / wt-I - wt-N
F415:	+O1	0.0	0.0	2.8	3.8	1.4
P420	-C1O1	0.0	0.0	19.3	19.8	1.0
P423/426	-C1O1	0.0	0.3	11.1	14.7	1.3
F429	+O1	0.0	1.0	19.0	21.5	1.1
C450	+O2/+O3	-	-	82.5	-	*
F452/P456	+O1	0.0	0.0	0.1	0.2	2.0
P456	-C1O1	0.0	0.0	0.3	1.0	3.0
Y483	+O1	0.0	0.0	3.5	3.7	1.1
F490/W491	+O1	1.1	1.6	18.4	16.3	0.9
W491	-C1O1	0.0	0.0	7.9	7.4	0.9
M499	+O1	10.0	9.8	29.5	44.0	1.8
Y508	+O1	0.0	0.2	1.2	1.0	0.7
M530	+O1	0.6	0.0	6.1	11.7	2.1

Table 2: ***List of oxidation products and their extent of oxidation (intensity of oxidatively modified peptide) in all studied protein forms – wild-type (wt) and C450A (mut) before (N) and after (I) irradiation. Column*** *Mod shows the elemental composition of the modification (oxidation: +O1, +O2 or +O3; Trp to kynurenine: -C1+O1; Pro to pyrrolidone: -C1O1). When it was not possible to clearly assign oxidation to one specific residue, two possibly affected residues are listed in the first column. The last column highlights the fold change in oxidation between C450A and wt forms. In case of C450 oxidation (marked in the last column with an asterisk) such comparisons were not possible due to generation of different peptides upon oxidation and due to mutation. The intensity of oxidized form was indirectly deduced from intensity decrease of the intact, unoxidized Asp-N generated peptide.*

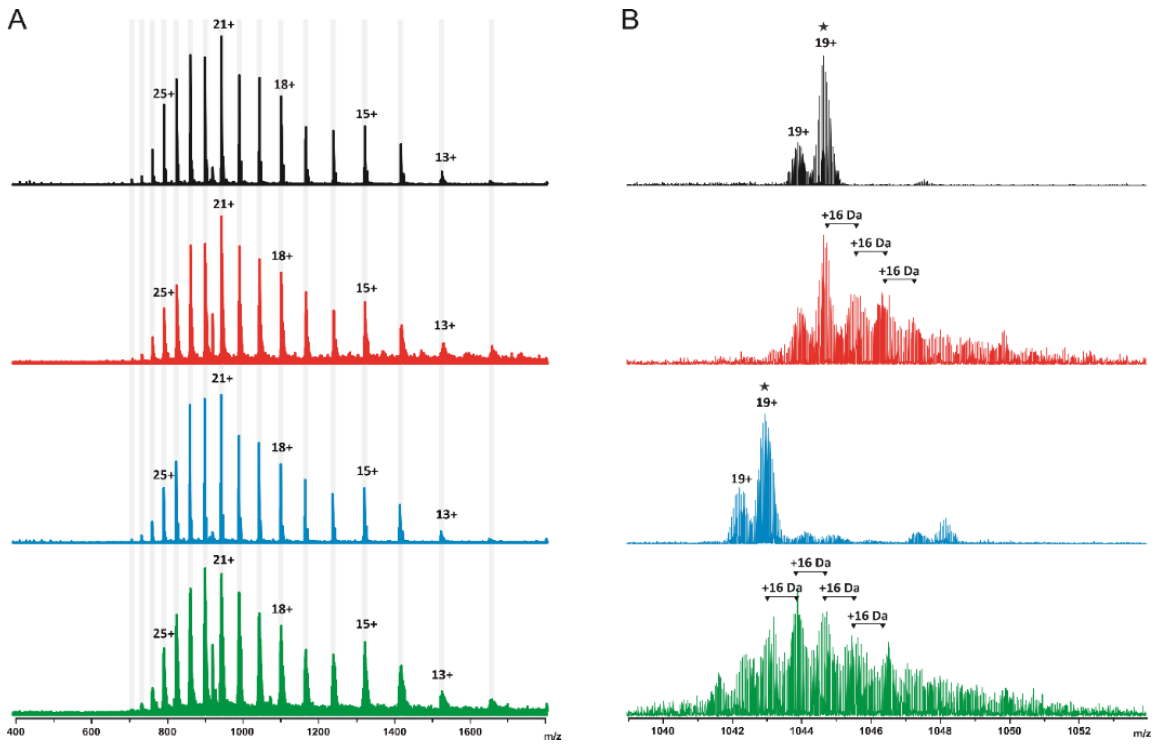

Figure 17: Analysis of intact proteins by nESI-FT-ICR MS. A *– from top to bottom - broad band spectra of wild-type AsLOV2 before (**black**) and after (**red**) irradiation and of C450A form before (**blue**) and after (**green**) irradiation. Panel **B** with zoom on the charge state 19+ demonstrates much higher modification extent in the C450A variant than in the wild-type AsLOV2.*

detected for *As*LOV2 C450A variant and ~2.6-fold increase detected for *As*LOV2 wt. Since the protein matrix surrounding the FMN decreases the quantum yield of FMN $^1O_2$ production by quenching the excited triplet state of FMN and restricting the oxygen diffusion to the isoalloxazine ring, release of FMN from the protein would explain the increased $^1O_2$ production detected by $^1O_2$ phosphorescence. To help explain the release of FMN from the protein, both bottom-up (**Table 2**) and top-down (**Figure 17**) mass spectrometry was employed to analyse structural changes to *As*LOV2 wt and *As*LOV2 C450A variant upon irradiation. A range of oxidative modifications was found on the protein with more extensive modification globally was detected in *As*LOV2 wt protein, with highest increase in mutant form concentrated in the area close to the FMN (F452, P456). Cystein 450 of *As*LOV2 wt was also found to be extensively oxidized upon irradiation, but the extent of modification could not be compared as it is missing in the mutant form. Overall, the same residues are generally modified in both *As*LOV2 wt and *As*LOV2 C450A, with the *As*LOV2 C450A having higher extent of oxidation.

Overall, the results point to a higher release of FMN from *As*LOV2 wt upon irradiation, which increases the overall production of $^1O_2$ over time. Seemingly contrary to the increase in ROS generated, higher extent of oxidation was detected in C450A form. However, while free FMN in solution shows higher quantum yield, the FMN retained on protein in C450A generates radicals located directly next to the detected modified residues which could increase their extent of oxidation. Simulation of the modification of C450 then shows, that transformation of -SH functional group to -SO_2 which was detected in wt protein by mass spectrometry, creates sterical clash, that forces the FMN out of the protein (**Figure 18**). This explains the lower release of FMN to the solution in mutant form, where this cysteine is missing.

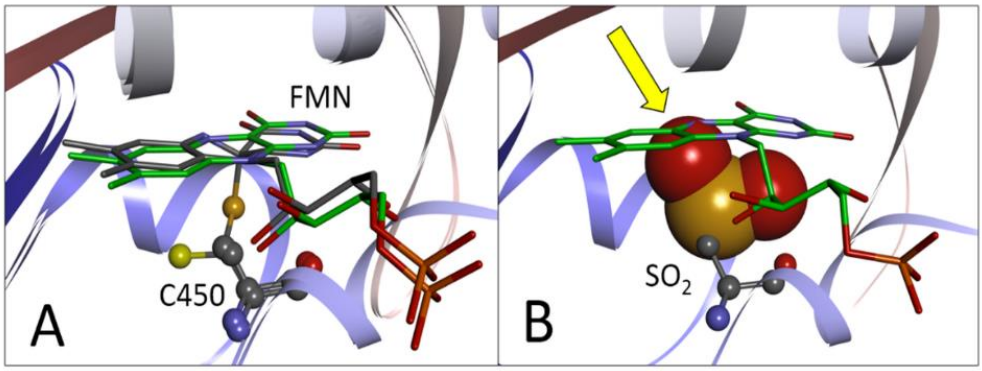

Figure 18: A) *Superposition of PDB ID: 2w0u (FMN with green carbons) and PDB ID: 2v0w (FMN bound to Cys450 with grey-coloured carbons).* ***B)*** *-SH to -SO_2^- substitution in C450 with marked atomic clash of the generated structure.*

These details of *As*LOV2 $^1O_2$ production and release of FMN to the solution may be utilized to design more efficient genetically encoded photosensitizers based on LOV domains. The addition of suitable oxidizable amino acids like methionine or cysteine close to the FMN can facilitate its release upon irradiation, while the protein scaffold can be modified to target specific tissues or cells for photodynamic therapy.

5. Summary

The goal of this thesis was to contribute to the research of medicinally and biotechnologically important enzymes using methods of structural mass spectrometry. Following results, included in three publications and two manuscripts, were obtained during the study of fungal cellulolytic enzymes lytic polysaccharide monooxygenase and cellobiose dehydrogenase and natural photosensitizer *As*LOV2:

- Structural changes to *Nc*LPMO9c during its catalysis, namely reduction of its active site copper ion and subsequent degradation, were observed using HDX-MS
- Primary cause of the loss of activity and degradation of *Nc*LPMO9c during catalysis was identified as oxidative modification and peptide bond cleavage using standard proteomics and peptide intensity observation during HDX-MS
- Protective effect of substrate on *Nc*LPMO9c was detected using HDX-MS in heterogenous mixture of *Nc*LPMO9c and crystalline cellulose
- Hydrogen peroxide was confirmed as a cosubstrate to *Nc*LPMO9c using turbidimetric and chronoamperometric measurements of reaction mixtures containing *Nc*LPMO9c, phosphoric acid swollen cellulose and various hydrogen peroxide generation systems, as all reaction were inhibited by catalase and activity was proportional to the amount of hydrogen peroxide added
- The rate of IDET and IPET in CDH was found to be strongly dependant on relative movement of CYT and DH domains of CDH and their structural complementarity. CDHs with less compatible domain interaction interfaces and longer linker resulting in higher preference for open conformation show higher IPET and lower IDET rates and vice versa.
- Oxidative modification of C450 in *As*LOV2 was found to be responsible for release of FMN to the solution upon extended protein irradiation, causing increase in the production of singlet oxygen

List of Publications

Publications directly supporting this thesis:

1. **Filandr, F.**, Kavan, D., Kracher, D., Laurent, C. V. F. P., Ludwig, R., Man, P. & Halada, P. Structural Dynamics of Lytic Polysaccharide Monooxygenase during Catalysis. *Biomolecules* 10, 242 (2020). Doi:10.3390/biom10020242

2. **Filandr, F.**, Man, P., Halada, P., Chang, H., Ludwig, R. & Kracher, D. The H2O2-dependent activity of a fungal lytic polysaccharide monooxygenase investigated with a turbidimetric assay. *Biotechnol. Biofuels* 13, 1–13 (2020). doi:10.1186/s13068-020-01673-4

3. Petrenčáková, M., **Filandr, F.**, Hovan, A., Yassaghi, G., Man, P., Kožár, T., Schwer, M. S., Jancura, D., Plückthun, A., Novák, P., Miškovský, P., Bánó, G. & Sedlák, E. Photoinduced damage of AsLOV2 domain is accompanied by increased singlet oxygen production due to flavin dissociation. *Sci. Rep.* 10, 1–15 (2020). doi: 10.1038/s41598-020-60861-2

4. Felice A.K.G., Schuster C., Kadek, A., **Filandr F.**, Laurent, C.V.F.P., Scheiblbrandner, S., Schwaiger, L., Schachinger, F., Kracher, D., Sygmund, C., Man, P., Halada, P., Oostenbrink, C. & Ludwig, R. Chimeric cellobiose dehydrogenases reveal the function of cytochrome domain mobility for the electron transfer to lytic polysaccharide monooxygenase. ***ACS Catal****., under review.*

Other publications by author:

5. Kalabova, D., **Filandr, F**., Alblova, M., Petrvalska, O., Horvath, M., Man, P., Obsil, T. & Obsilova, V. 14-3-3 protein binding blocks the dimerization interface of caspase-2. *FEBS J.* febs.15215 (2020). doi:10.1111/febs.15215

Bibliography

1. Levitt, M. Growth of novel protein structural data. *Proc. Natl. Acad. Sci.* **104,** 3183–3188 (2007).
2. Tame, J. R. H. & Vallone, B. The structures of deoxy human haemoglobin and the mutant Hb Tyrα42His at 120 K. *Acta Crystallogr. Sect. D Biol. Crystallogr.* **56,** 805–811 (2000).
3. Tan, T.-C., Kracher, D., Gandini, R., Sygmund, C., Kittl, R., Haltrich, D., Hällberg, B. M., Ludwig, R. & Divne, C. Structural basis for cellobiose dehydrogenase action during oxidative cellulose degradation. *Nat. Commun.* **6,** 7542 (2015).
4. Ingram, V. M. Abnormal human haemoglobins. *Biochim. Biophys. Acta* **28,** 539–545 (1958).
5. Prusiner, S. B. Nobel Lecture: Prions. *Proc. Natl. Acad. Sci.* **95,** 13363–13383 (1998).
6. Prusiner, S. B. Creutzfeldt-Jakob Disease And Scrapie Prions. *Alzheimer Dis. Assoc. Disord.* **3,** 52–78 (1989).
7. Goedert, M., Spillantini, M. G. & Crowther, R. A. Tau Proteins and Neurofibrillary Degeneration. *Brain Pathol.* **1,** 279–286 (1991).
8. Hardy, J. & Allsop, D. Amyloid deposition as the central event in the aetiology of Alzheimer's disease. *Trends Pharmacol. Sci.* **12,** 383–388 (1991).
9. Meyer-Luehmann, M. Exogenous Induction of Cerebral -Amyloidogenesis Is Governed by Agent and Host. *Science (80-.).* **313,** 1781–1784 (2006).
10. Williamson, J., Goldman, J. & Marder, K. S. Genetic Aspects of Alzheimer Disease. *Neurologist* **15,** 80–86 (2009).
11. Burley, S. K., Berman, H. M., Bhikadiya, C., Bi, C., Chen, L., Di Costanzo, L., Christie, C., Dalenberg, K., Duarte, J. M., Dutta, S., Feng, Z., Ghosh, S., Goodsell, D. S., Green, R. K., Guranović, V., Guzenko, D., Hudson, B. P., Kalro, T., Liang, Y., Lowe, R., Namkoong, H., Peisach, E., Periskova, I., Prlić, A., Randle, C., Rose, A., Rose, P., Sala, R., Sekharan, M., Shao, C., Tan, L., Tao, Y.-P., Valasatava, Y., Voigt, M., Westbrook, J., Woo, J., Yang, H., Young, J., Zhuravleva, M. & Zardecki, C. RCSB Protein Data Bank: biological macromolecular structures enabling research and education in fundamental biology, biomedicine, biotechnology and energy. *Nucleic Acids Res.* **47,** D464–D474 (2019).
12. Kendrew, J. C., Bodo, G., Dintzis, H. M., Parrish, R. G., Wyckoff, H. & Phillips, D. C. A Three-Dimensional Model of the Myoglobin Molecule Obtained by X-Ray Analysis. *Nature* **181,** 662–666 (1958).
13. Wlodawer, A., Minor, W., Dauter, Z. & Jaskolski, M. Protein crystallography for non-crystallographers, or how to get the best (but not more) from published macromolecular structures. *FEBS J.* **275,** 1–21 (2008).
14. Engh, R. A. & Huber, R. Accurate bond and angle parameters for X-ray protein structure refinement. *Acta Crystallogr. Sect. A Found. Crystallogr.* **47,** 392–400 (1991).
15. Holcomb, J., Spellmon, N., Zhang, Y., Doughan, M., Li, C. & Yang, Z. Protein crystallization: Eluding the bottleneck of X-ray crystallography. *AIMS Biophys.* **4,** 557–575 (2017).
16. Li, D., Boland, C., Walsh, K. & Caffrey, M. Use of a Robot for High-throughput Crystallization of Membrane Proteins in Lipidic Mesophases. *J. Vis. Exp.* 1–8 (2012). doi:10.3791/4000
17. Halle, B. Flexibility and packing in proteins. *Proc. Natl. Acad. Sci.* **99,** 1274–1279 (2002).
18. McPherson, A. & Gavira, J. A. Introduction to protein crystallization. *Acta Crystallogr. Sect. F Struct. Biol. Commun.* **70,** 2–20 (2014).
19. Rozbesky, D., Man, P., Kavan, D., Chmelik, J., Cerny, J., Bezouska, K. & Novak, P. Chemical Cross-Linking and H/D Exchange for Fast Refinement of Protein Crystal Structure. *Anal. Chem.* **84,** 867–870 (2012).
20. Chapman, H. N. X-Ray Free-Electron Lasers for the Structure and Dynamics of Macromolecules. *Annu. Rev. Biochem.* **88,** 35–58 (2019).

21. Burley, S. K., Berman, H. M., Bhikadiya, C., Bi, C., Chen, L., Di Costanzo, L., Christie, C., Dalenberg, K., Duarte, J. M., Dutta, S., Feng, Z., Ghosh, S., Goodsell, D. S., Green, R. K., Guranović, V., Guzenko, D., Hudson, B. P., Kalro, T., Liang, Y., Lowe, R., Namkoong, H., Peisach, E., Periskova, I., Prlić, A., Randle, C., Rose, A., Rose, P., Sala, R., Sekharan, M., Shao, C., Tan, L., Tao, Y.-P., Valasatava, Y., Voigt, M., Westbrook, J., Woo, J., Yang, H., Young, J., Zhuravleva, M. & Zardecki, C. RCSB Protein Data Bank: biological macromolecular structures enabling research and education in fundamental biology, biomedicine, biotechnology and energy. *Nucleic Acids Res.* **47,** D464–D474 (2019).
22. Farrar, T. C. in *Transform Tech. Chem.* **154,** 199–226 (Springer US, 1978).
23. Marion, D. An Introduction to Biological NMR Spectroscopy. *Mol. Cell. Proteomics* **12,** 3006–3025 (2013).
24. Pervushin, K., Riek, R., Wider, G. & Wüthrich, K. Attenuated T2 relaxation by mutual cancellation of dipole–dipole coupling and chemical shift anisotropy.pdf. *Proc. Natl. Acad. Sci. U. S. A.* **94,** 12366–12371 (1997).
25. Fernandez, C. TROSY in NMR studies of the structure and function of large biological macromolecules. *Curr. Opin. Struct. Biol.* **13,** 570–580 (2003).
26. Nogales, E. & Scheres, S. H. W. Cryo-EM: A Unique Tool for the Visualization of Macromolecular Complexity. *Mol. Cell* **58,** 677–689 (2015).
27. Saxton, W. O., Baumeister, W. & Hahn, M. Three-dimensional reconstruction of imperfect two-dimensional crystals. *Ultramicroscopy* **13,** 57–70 (1984).
28. Cheng, Y. Single-Particle Cryo-EM at Crystallographic Resolution. *Cell* **161,** 450–457 (2015).
29. Schröder, R. R. Advances in electron microscopy: A qualitative view of instrumentation development for macromolecular imaging and tomography. *Arch. Biochem. Biophys.* **581,** 25–38 (2015).
30. Ben-Shem, A., Garreau de Loubresse, N., Melnikov, S., Jenner, L., Yusupova, G. & Yusupov, M. The Structure of the Eukaryotic Ribosome at 3.0 A Resolution. *Science (80-.).* **334,** 1524–1529 (2011).
31. Song, F., Chen, P., Sun, D., Wang, M., Dong, L., Liang, D., Xu, R.-M., Zhu, P. & Li, G. Cryo-EM Study of the Chromatin Fiber Reveals a Double Helix Twisted by Tetranucleosomal Units. *Science (80-.).* **344,** 376–380 (2014).
32. Liao, M., Cao, E., Julius, D. & Cheng, Y. Structure of the TRPV1 ion channel determined by electron cryo-microscopy. *Nature* **504,** 107–112 (2013).
33. Bartesaghi, A., Merk, A., Banerjee, S., Matthies, D., Wu, X., Milne, J. L. S. & Subramaniam, S. 2.2 A resolution cryo-EM structure of -galactosidase in complex with a cell-permeant inhibitor. *Science (80-.).* **348,** 1147–1151 (2015).
34. Herzik, M. A., Wu, M. & Lander, G. C. High-resolution structure determination of sub-100 kDa complexes using conventional cryo-EM. *Nat. Commun.* **10,** 1032 (2019).
35. Allison, T. M. & Bechara, C. Structural mass spectrometry comes of age: new insight into protein structure, function and interactions. *Biochem. Soc. Trans.* **47,** 317–327 (2019).
36. Yamashita, M. & Fenn, J. B. Electrospray ion source. Another variation on the free-jet theme. *J. Phys. Chem.* **88,** 4451–4459 (1984).
37. Fenn, J., Mann, M., Meng, C., Wong, S. & Whitehouse, C. Electrospray ionization for mass spectrometry of large biomolecules. *Science (80-.).* **246,** 64–71 (1989).
38. Taflin, D. C., Ward, T. L. & Davis, E. J. Electrified droplet fission and the Rayleigh limit. *Langmuir* **5,** 376–384 (1989).
39. Kebarle, P. & Verkerk, U. H. Electrospray: From ions in solution to ions in the gas phase, what we know now. *Mass Spectrom. Rev.* **28,** 898–917 (2009).
40. Chait, B. T. Mass Spectrometry: Bottom-Up or Top-Down? *Science (80-.).* **314,** 65–66 (2006).

41. Bantscheff, M., Schirle, M., Sweetman, G., Rick, J. & Kuster, B. Quantitative mass spectrometry in proteomics: a critical review. *Anal. Bioanal. Chem.* **389,** 1017–1031 (2007).
42. Smith, L. M. & Kelleher, N. L. Proteoforms as the next proteomics currency. *Science (80-.).* **359,** 1106–1107 (2018).
43. Ben-Nissan, G., Belov, M. E., Morgenstern, D., Levin, Y., Dym, O., Arkind, G., Lipson, C., Makarov, A. A. & Sharon, M. Triple-Stage Mass Spectrometry Unravels the Heterogeneity of an Endogenous Protein Complex. *Anal. Chem.* **89,** 4708–4715 (2017).
44. Robinson, C. V. Finding the right balance - a personal journey from individual proteins to membrane-embedded motors. *FEBS J.* **279,** 663–677 (2012).
45. Li, H., Nguyen, H. H., Ogorzalek Loo, R. R., Campuzano, I. D. G. & Loo, J. A. An integrated native mass spectrometry and top-down proteomics method that connects sequence to structure and function of macromolecular complexes. *Nat. Chem.* **10,** 139–148 (2018).
46. Gabelica, V. & Marklund, E. Fundamentals of ion mobility spectrometry. *Curr. Opin. Chem. Biol.* **42,** 51–59 (2018).
47. Gabelica, V. & Pauw, E. De. Internal energy and fragmentation of ions produced in electrospray sources. *Mass Spectrom. Rev.* **24,** 566–587 (2005).
48. Konijnenberg, A., Butterer, A. & Sobott, F. Native ion mobility-mass spectrometry and related methods in structural biology. *Biochim. Biophys. Acta - Proteins Proteomics* **1834,** 1239–1256 (2013).
49. Hyung, S.-J., Robinson, C. V. & Ruotolo, B. T. Gas-Phase Unfolding and Disassembly Reveals Stability Differences in Ligand-Bound Multiprotein Complexes. *Chem. Biol.* **16,** 382–390 (2009).
50. Kanu, A. B., Dwivedi, P., Tam, M., Matz, L. & Hill, H. H. Ion mobility-mass spectrometry. *J. Mass Spectrom.* **43,** 1–22 (2008).
51. Kalenius, E., Groessl, M. & Rissanen, K. Ion mobility–mass spectrometry of supramolecular complexes and assemblies. *Nat. Rev. Chem.* **3,** 4–14 (2019).
52. Bush, M. F., Hall, Z., Giles, K., Hoyes, J., Robinson, C. V. & Ruotolo, B. T. Collision Cross Sections of Proteins and Their Complexes: A Calibration Framework and Database for Gas-Phase Structural Biology. *Anal. Chem.* **82,** 9557–9565 (2010).
53. Politis, A., Stengel, F., Hall, Z., Hernández, H., Leitner, A., Walzthoeni, T., Robinson, C. V & Aebersold, R. A mass spectrometry–based hybrid method for structural modeling of protein complexes. *Nat. Methods* **11,** 403–406 (2014).
54. Gessel, M. M., Wu, C., Li, H., Bitan, G., Shea, J.-E. & Bowers, M. T. Aβ(39–42) Modulates Aβ Oligomerization but Not Fibril Formation. *Biochemistry* **51,** 108–117 (2012).
55. van Duijn, E., Barbu, I. M., Barendregt, A., Jore, M. M., Wiedenheft, B., Lundgren, M., Westra, E. R., Brouns, S. J. J., Doudna, J. A., van der Oost, J. & Heck, A. J. R. Native Tandem and Ion Mobility Mass Spectrometry Highlight Structural and Modular Similarities in Clustered-Regularly-Interspaced Shot-Palindromic-Repeats (CRISPR)-associated Protein Complexes From Escherichia coli and Pseudomonas aeruginosa. *Mol. Cell. Proteomics* **11,** 1430–1441 (2012).
56. Uetrecht, C., Versluis, C., Watts, N. R., Wingfield, P. T., Steven, A. C. & Heck, A. J. R. Stability and Shape of Hepatitis B Virus Capsids In Vacuo. *Angew. Chemie Int. Ed.* **47,** 6247–6251 (2008).
57. Uetrecht, C., Barbu, I. M., Shoemaker, G. K., van Duijn, E. & Heck, A. J. R. Interrogating viral capsid assembly with ion mobility–mass spectrometry. *Nat. Chem.* **3,** 126–132 (2011).
58. McKay, A. R., Ruotolo, B. T., Ilag, L. L. & Robinson, C. V. Mass Measurements of Increased Accuracy Resolve Heterogeneous Populations of Intact Ribosomes. *J. Am. Chem. Soc.* **128,** 11433–11442 (2006).

59. Mendoza, V. L. & Vachet, R. W. Probing protein structure by amino acid-specific covalent labeling and mass spectrometry. *Mass Spectrom. Rev.* **28,** 785–815 (2009).
60. Vahidi, S. & Konermann, L. Probing the Time Scale of FPOP (Fast Photochemical Oxidation of Proteins): Radical Reactions Extend Over Tens of Milliseconds. *J. Am. Soc. Mass Spectrom.* **27,** 1156–1164 (2016).
61. Gau, B. C., Sharp, J. S., Rempel, D. L. & Gross, M. L. Fast Photochemical Oxidation of Protein Footprints Faster than Protein Unfolding. *Anal. Chem.* **81,** 6563–6571 (2009).
62. Limpikirati, P., Liu, T. & Vachet, R. W. Covalent labeling-mass spectrometry with non-specific reagents for studying protein structure and interactions. *Methods* **144,** 79–93 (2018).
63. Akashi, S., Shirouzu, M., Terada, T., Ito, Y., Yokoyama, S. & Takio, K. Characterization of the structural difference between active and inactive forms of the Ras protein by chemical modification followed by mass spectrometric peptide mapping. *Anal. Biochem.* **248,** 15–25 (1997).
64. Akinsiku, O. T., Yu, E. T. & Fabris, D. Mass spectrometric investigation of protein alkylation by the RNA footprinting probe kethoxal. *J. Mass Spectrom.* **40,** 1372–81 (2005).
65. Apuy, J. L., Chen, X., Russell, D. H., Baldwin, T. O. & Giedroc, D. P. Ratiometric pulsed alkylation/mass spectrometry of the cysteine pairs in individual zinc fingers of MRE-binding transcription factor-1 (MTF-1) as a probe of zinc chelate stability. *Biochemistry* **40,** 15164–75 (2001).
66. Glocker, M. O., Borchers, C., Fiedler, W., Suckau, D. & Przybylski, M. Molecular Characterization of Surface Topology in Protein Tertiary Structures by Amino-Acylation and Mass Spectrometric Peptide Mapping. *Bioconjug. Chem.* **5,** 583–590 (1994).
67. Novak, P., Kruppa, G. H., Young, M. M. & Schoeniger, J. A top-down method for the determination of residue-specific solvent accessibility in proteins. *J. Mass Spectrom.* **39,** 322–8 (2004).
68. Hassani, O., Mansuelle, P., Cestele, S., Bourdeaux, M., Rochat, H. & Sampieri, F. Role of lysine and tryptophan residues in the biological activity of toxin VII (Ts gamma) from the scorpion Tityus serrulatus. *Eur. J. Biochem.* **260,** 76–86 (1999).
69. Leite, J. F. & Cascio, M. Probing the topology of the glycine receptor by chemical modification coupled to mass spectrometry. *Biochemistry* **41,** 6140–8 (2002).
70. Chea, E. E. & Jones, L. M. Modifications generated by fast photochemical oxidation of proteins reflect the native conformations of proteins. *Protein Sci.* **27,** 1047–1056 (2018).
71. Kiselar, J. G. & Chance, M. R. Future directions of structural mass spectrometry using hydroxyl radical footprinting. *J. Mass Spectrom.* **45,** 1373–1382 (2010).
72. Manzi, L., Barrow, A. S., Scott, D., Layfield, R., Wright, T. G., Moses, J. E. & Oldham, N. J. Carbene footprinting accurately maps binding sites in protein–ligand and protein–protein interactions. *Nat. Commun.* **7,** 13288 (2016).
73. Cheng, M., Zhang, B., Cui, W. & Gross, M. L. Laser-Initiated Radical Trifluoromethylation of Peptides and Proteins: Application to Mass-Spectrometry-Based Protein Footprinting. *Angew. Chemie - Int. Ed.* **56,** 14007–14010 (2017).
74. Miles, E. W. in *Methods Enzymol.* **47,** 431–442 (1977).
75. Sinz, A. Cross-Linking/Mass Spectrometry for Studying Protein Structures and Protein–Protein Interactions: Where Are We Now and Where Should We Go from Here? *Angew. Chemie Int. Ed.* **57,** 6390–6396 (2018).
76. Young, M. M., Tang, N., Hempel, J. C., Oshiro, C. M., Taylor, E. W., Kuntz, I. D., Gibson, B. W. & Dollinger, G. High throughput protein fold identification by using experimental constraints derived from intramolecular cross-links and mass spectrometry. *Proc. Natl. Acad. Sci.* **97,** 5802–5806 (2000).
77. Iacobucci, C., Götze, M. & Sinz, A. Cross-linking/mass spectrometry to get a closer view on protein interaction

networks. *Curr. Opin. Biotechnol.* **63,** 48–53 (2020).

78. O'Reilly, F. J. & Rappsilber, J. Cross-linking mass spectrometry: methods and applications in structural, molecular and systems biology. *Nat. Struct. Mol. Biol.* **25,** 1000–1008 (2018).
79. Ihling, C., Schmidt, A., Kalkhof, S., Schulz, D. M., Stingl, C., Mechtler, K., Haack, M., Beck-Sickinger, A. G., Cooper, D. M. F. & Sinz, A. Isotope-labeled cross-linkers and fourier transform ion cyclotron resonance mass spectrometry for structural analysis of a protein/peptide complex. *J. Am. Soc. Mass Spectrom.* **17,** 1100–1113 (2006).
80. Müller, M. Q., Dreiocker, F., Ihling, C. H., Schäfer, M. & Sinz, A. Cleavable cross-linker for protein structure analysis: Reliable identification of cross-linking products by tandem MS. *Anal. Chem.* **82,** 6958–6968 (2010).
81. Fischer, L., Chen, Z. A. & Rappsilber, J. Quantitative cross-linking/mass spectrometry using isotope-labelled cross-linkers. *J. Proteomics* **88,** 120–128 (2013).
82. Agou, F. & Véron, M. in *Protein-Protein Interact. Methods Appl. Second Ed.* (eds. Meyerkord, C. L. & Fu, H.) **1278,** 391–405 (Springer New York, 2015).
83. Yang, B., Tang, S., Ma, C., Li, S.-T., Shao, G.-C., Dang, B., DeGrado, W. F., Dong, M.-Q., Wang, P. G., Ding, S. & Wang, L. Spontaneous and specific chemical cross-linking in live cells to capture and identify protein interactions. *Nat. Commun.* **8,** 2240 (2017).
84. Pham, N. D., Parker, R. B. & Kohler, J. J. Photocrosslinking approaches to interactome mapping. *Curr. Opin. Chem. Biol.* **17,** 90–101 (2013).
85. Marcsisin, S. R. & Engen, J. R. Hydrogen exchange mass spectrometry: what is it and what can it tell us? *Anal. Bioanal. Chem.* **397,** 967–972 (2010).
86. Englander, S. W. & Kallenbach, N. R. Hydrogen exchange and structural dynamics of proteins and nucleic acids. *Q. Rev. Biophys.* **16,** 521–655 (1983).
87. Möller, I. R., Slivacka, M., Nielsen, A. K., Rasmussen, S. G. F., Gether, U., Loland, C. J. & Rand, K. D. Conformational dynamics of the human serotonin transporter during substrate and drug binding. *Nat. Commun.* **10,** 1687 (2019).
88. Trcka, F., Durech, M., Vankova, P., Chmelik, J., Martinkova, V., Hausner, J., Kadek, A., Marcoux, J., Klumpler, T., Vojtesek, B., Muller, P. & Man, P. Human Stress-inducible Hsp70 Has a High Propensity to Form ATP-dependent Antiparallel Dimers That Are Differentially Regulated by Cochaperone Binding. *Mol. Cell. Proteomics* **18,** 320–337 (2019).
89. Harrison, R. A. & Engen, J. R. Conformational insight into multi-protein signaling assemblies by hydrogen–deuterium exchange mass spectrometry. *Curr. Opin. Struct. Biol.* **41,** 187–193 (2016).
90. Vankova, Salido, Timson, Man & Pey. A Dynamic Core in Human NQO1 Controls the Functional and Stability Effects of Ligand Binding and Their Communication across the Enzyme Dimer. *Biomolecules* **9,** 728 (2019).
91. Filandr, F., Kavan, D., Kracher, D., Laurent, C. V. F. P., Ludwig, R., Man, P. & Halada, P. Structural Dynamics of Lytic Polysaccharide Monooxygenase during Catalysis. *Biomolecules* **10,** 242 (2020).
92. Hvidt, A. & Linderstrøm-Lang, K. Exchange of hydrogen atoms in insulin with deuterium atoms in aqueous solutions. *Biochim. Biophys. Acta* **14,** 574–575 (1954).
93. Englander, S. W. & Poulsen, A. Hydrogen-tritium exchange of the random chain polypeptide. *Biopolymers* **7,** 379–393 (1969).
94. Bai, Y., Milne, J. S., Mayne, L. & Englander, S. W. Primary structure effects on peptide group hydrogen exchange. *Proteins Struct. Funct. Genet.* **17,** 75–86 (1993).
95. Morgan, C. R. & Engen, J. R. Investigating Solution-Phase Protein Structure and Dynamics by Hydrogen Exchange Mass Spectrometry. *Curr. Protoc. Protein Sci.* **58,** 1–23 (2009).

96. Woodward, C. K. & Rosenberg, A. Oxidized RNAse As A Protein Model Having No Contribution To The Hydrogen Exchange Rate From Conformational Restrictions. *Proc. Natl. Acad. Sci.* **66,** 1067–1074 (1970).

97. Molday, R. S., Englander, S. W. & Kallen, R. G. Primary structure effects on peptide group hydrogen exchange. *Biochemistry* **11,** 150–158 (1972).

98. Connelly, G. P., Bai, Y., Jeng, M.-F. & Englander, S. W. Isotope effects in peptide group hydrogen exchange. *Proteins Struct. Funct. Genet.* **17,** 87–92 (1993).

99. Ferraro, D. M., Lazo, N. D. & Robertson, A. D. EX1 Hydrogen Exchange and Protein Folding,. *Biochemistry* **43,** 3756–3756 (2004).

100. Konermann, L., Tong, X. & Pan, Y. Protein structure and dynamics studied by mass spectrometry: H/D exchange, hydroxyl radical labeling, and related approaches. *J. Mass Spectrom.* **43,** 1021–1036 (2008).

101. Weis, D. D., Wales, T. E., Engen, J. R., Hotchko, M. & Ten Eyck, L. F. Identification and Characterization of EX1 Kinetics in H/D Exchange Mass Spectrometry by Peak Width Analysis. *J. Am. Soc. Mass Spectrom.* **17,** 1498–1509 (2006).

102. Engen, J. R., Wales, T. E., Chen, S., Marzluff, E. M., Hassell, K. M., Weis, D. D. & Smithgall, T. E. Partial cooperative unfolding in proteins as observed by hydrogen exchange mass spectrometry. *Int. Rev. Phys. Chem.* **32,** 96–127 (2013).

103. Masson, G. R., Burke, J. E., Ahn, N. G., Anand, G. S., Borchers, C., Brier, S., Bou-assaf, G. M., Engen, J. R., Englander, S. W., Faber, J., Garlish, R., Griffin, P. R., Gross, M. L., Guttman, M., Hamuro, Y., Klinman, J. P., Konermann, L., Man, P., Mayne, L., Pascal, B. D., Reichmann, D., Skehel, M., Snijder, J., Strutzenberg, T. S., Underbakke, E. S., Wintrode, P. L., Zhang, Z., Zheng, J., Schriemer, D. C. & Rand, K. D. Recommendations for performing, interpreting and reporting hydrogen deuterium exchange mass spectrometry (HDX-MS) experiments. *Nat. Methods* **16,** (2019).

104. Xiao, H. Mapping protein energy landscapes with amide hydrogen exchange and mass spectrometry: I. A generalized model for a two-state protein and comparison with experiment. *Protein Sci.* **14,** 543–557 (2005).

105. Burkitt, W. & Connor, G. O. Assessment of the repeatability and reproducibility of hydrogen / deuterium exchange mass spectrometry measurements y. 3893–3901 (2008). doi:10.1002/rcm

106. Rist, W., Rodriguez, F., Jørgensen, T. J. D. & Mayer, M. P. Analysis of subsecond protein dynamics by amide hydrogen exchange and mass spectrometry using a quenched-flow setup. 626–632 (2005). doi:10.1110/ps.041098305

107. Svejdal, R. R., Dickinson, E. R., Sticker, D., Kutter, J. P. & Rand, K. D. Thiol-ene microfluidic chip for performing hydrogen / deuterium exchange of proteins at sub-second timescales. (2018). doi:10.1021/acs.analchem.8b03050.

108. Gessner, C., Steinchen, W., Bédard, S., J. Skinner, J., Woods, V. L., Walsh, T. J., Bange, G. & Pantazatos, Di. P. Computational method allowing Hydrogen-Deuterium Exchange Mass Spectrometry at single amide Resolution. *Sci. Rep.* **7,** 3789 (2017).

109. Yang, M., Hoeppner, M., Rey, M., Kadek, A., Man, P. & Schriemer, D. C. Recombinant Nepenthesin II for Hydrogen/Deuterium Exchange Mass Spectrometry. *Anal. Chem.* **87,** 6681–6687 (2015).

110. Kadek, A., Mrazek, H., Halada, P., Rey, M., Schriemer, D. C. & Man, P. Aspartic Protease Nepenthesin-1 as a Tool for Digestion in Hydrogen/Deuterium Exchange Mass Spectrometry. *Anal. Chem.* **86,** 4287–4294 (2014).

111. Mistarz, U. H., Bellina, B., Jensen, P. F., Brown, J. M., Barran, P. E. & Rand, K. D. UV Photodissociation Mass Spectrometry Accurately Localize Sites of Backbone Deuteration in Peptides. *Anal. Chem.* **90,** 1077–1080 (2018).

112. Rand, K. D., Adams, C. M., Zubarev, R. A., Jørgensen, T. J. D. & Uppsala, S.-. Electron Capture Dissociation

Proceeds with a Low Degree of Intramolecular Migration of Peptide Amide Hydrogens. 1341–1349 (2008). doi:10.1021/ja076448i

113. Pan, J., Han, J., Borchers, C. H. & Konermann, L. Hydrogen / Deuterium Exchange Mass Spectrometry with Top-Down Electron Capture Dissociation for Characterizing Structural Transitions of a 17 kDa Protein. 12801–12808 (2009). doi:10.1021/ja904379w.

114. Field, C. B. Primary Production of the Biosphere: Integrating Terrestrial and Oceanic Components. *Science (80-.).* **281,** 237–240 (1998).

115. Beckham, G. T., Matthews, J. F., Peters, B., Bomble, Y. J., Himmel, M. E. & Crowley, M. F. Molecular-Level Origins of Biomass Recalcitrance: Decrystallization Free Energies for Four Common Cellulose Polymorphs. *J. Phys. Chem. B* **115,** 4118–4127 (2011).

116. Himmel, M. E., Ding, S.-Y., Johnson, D. K., Adney, W. S., Nimlos, M. R., Brady, J. W. & Foust, T. D. Biomass Recalcitrance: Engineering Plants and Enzymes for Biofuels Production. *Science (80-.).* **315,** 804–807 (2007).

117. Viikari, L., Suurnäkki, A., Grönqvist, S., Raaska, L. & Ragauskas, A. in *Encycl. Microbiol.* 80–94 (Elsevier, 2009). doi:10.1016/B978-012373944-5.00123-1

118. Payne, C. M., Knott, B. C., Mayes, H. B., Hansson, H., Himmel, M. E., Sandgren, M., Ståhlberg, J. & Beckham, G. T. Fungal Cellulases. *Chem. Rev.* **115,** 1308–1448 (2015).

119. Scheller, H. V. & Ulvskov, P. Hemicelluloses. *Annu. Rev. Plant Biol.* **61,** 263–289 (2010).

120. Wierzbicki, M. P., Maloney, V., Mizrachi, E. & Myburg, A. A. Xylan in the Middle: Understanding Xylan Biosynthesis and Its Metabolic Dependencies Toward Improving Wood Fiber for Industrial Processing. *Front. Plant Sci.* **10,** 1–29 (2019).

121. Marriott, P. E., Gómez, L. D. & McQueen-Mason, S. J. Unlocking the potential of lignocellulosic biomass through plant science. *New Phytol.* **209,** 1366–1381 (2016).

122. Frei, M. Lignin: Characterization of a Multifaceted Crop Component. *Sci. World J.* **2013,** 1–25 (2013).

123. Vaaje-Kolstad, G., Westereng, B., Horn, S. J., Liu, Z., Zhai, H., Sørlie, M. & Eijsink, V. G. H. An Oxidative Enzyme Boosting the Enzymatic Conversion of Recalcitrant Polysaccharides. *Science (80-.).* **330,** 219–222 (2010).

124. Quinlan, R. J., Sweeney, M. D., Lo Leggio, L., Otten, H., Poulsen, J.-C. N. J.-C. N. J.-C. N., Johansen, K. S., Krogh, K. B. R. M., Jørgensen, C. I., Tovborg, M., Anthonsen, A., Tryfona, T., Walter, C. P., Dupree, P., Xu, F., Davies, G. J., Walton, P. H., Jorgensen, C. I., Tovborg, M., Anthonsen, A., Tryfona, T., Walter, C. P., Dupree, P., Xu, F., Davies, G. J. & Walton, P. H. Insights into the oxidative degradation of cellulose by a copper metalloenzyme that exploits biomass components. *Proc. Natl. Acad. Sci.* **108,** 15079–15084 (2011).

125. Chiu, E., Hijnen, M., Bunker, R. D., Boudes, M., Rajendran, C., Aizel, K., Oliéric, V., Schulze-Briese, C., Mitsuhashi, W., Young, V., Ward, V. K., Bergoin, M., Metcalf, P. & Coulibaly, F. Structural basis for the enhancement of virulence by viral spindles and their in vivo crystallization. *Proc. Natl. Acad. Sci.* **112,** 3973–3978 (2015).

126. Sabbadin, F., Hemsworth, G. R., Ciano, L., Henrissat, B., Dupree, P., Tryfona, T., Marques, R. D. S., Sweeney, S. T., Besser, K., Elias, L., Pesante, G., Li, Y., Dowle, A. A., Bates, R., Gomez, L. D., Simister, R., Davies, G. J., Walton, P. H., Bruce, N. C. & McQueen-Mason, S. J. An ancient family of lytic polysaccharide monooxygenases with roles in arthropod development and biomass digestion. *Nat. Commun.* **9,** 1–12 (2018).

127. Harris, P. V., Welner, D., McFarland, K. C., Re, E., Navarro Poulsen, J.-C., Brown, K., Salbo, R., Ding, H., Vlasenko, E., Merino, S., Xu, F., Cherry, J., Larsen, S. & Lo Leggio, L. Stimulation of Lignocellulosic Biomass Hydrolysis by Proteins of Glycoside Hydrolase Family 61: Structure and Function of a Large, Enigmatic Family. *Biochemistry* **49,** 3305–3316 (2010).

128. Phillips, C. M., Beeson, W. T., Cate, J. H. & Marletta, M. A. Cellobiose Dehydrogenase and a Copper-Dependent Polysaccharide Monooxygenase Potentiate Cellulose Degradation by Neurospora crassa. *ACS Chem. Biol.* **6,** 1399–1406 (2011).

129. Li, X., Beeson, W. T., Phillips, C. M., Marletta, M. A. & Cate, J. H. D. Structural Basis for Substrate Targeting and Catalysis by Fungal Polysaccharide Monooxygenases. *Structure* **20,** 1051–1061 (2012).

130. Beeson, W. T., Phillips, C. M., Cate, J. H. D. & Marletta, M. A. Oxidative Cleavage of Cellulose by Fungal Copper-Dependent Polysaccharide Monooxygenases. *J. Am. Chem. Soc.* **134,** 890–892 (2012).

131. Westereng, B., Agger, J. W., Horn, S. J., Vaaje-Kolstad, G., Aachmann, F. L., Stenstrøm, Y. H. & Eijsink, V. G. H. Efficient separation of oxidized cello-oligosaccharides generated by cellulose degrading lytic polysaccharide monooxygenases. *J. Chromatogr. A* **1271,** 144–152 (2013).

132. Martinez, A. T. How to break down crystalline cellulose. *Science (80-.).* **352,** 1050–1051 (2016).

133. Sygmund, C., Kracher, D., Scheiblbrandner, S., Zahma, K., Felice, A. K. G., Harreither, W., Kittl, R. & Ludwig, R. Characterization of the two Neurospora crassa cellobiose dehydrogenases and their connection to oxidative cellulose degradation. *Appl. Environ. Microbiol.* **78,** 6161–6171 (2012).

134. Cohen, R., Jensen, K. A., Houtman, C. J. & Hammel, K. E. Significant levels of extracellular reactive oxygen species produced by brown rot basidiomycetes on cellulose. *FEBS Lett.* **531,** 483–488 (2002).

135. Aachmann, F. L., Sorlie, M., Skjak-Braek, G., Eijsink, V. G. H. & Vaaje-Kolstad, G. NMR structure of a lytic polysaccharide monooxygenase provides insight into copper binding, protein dynamics, and substrate interactions. *Proc. Natl. Acad. Sci.* **109,** 18779–18784 (2012).

136. Hemsworth, G. R., Taylor, E. J., Kim, R. Q., Gregory, R. C., Lewis, S. J., Turkenburg, J. P., Parkin, A., Davies, G. J. & Walton, P. H. The Copper Active Site of CBM33 Polysaccharide Oxygenases. *J. Am. Chem. Soc.* **135,** 6069–6077 (2013).

137. Eibinger, M., Ganner, T., Bubner, P., Rošker, S., Kracher, D., Haltrich, D., Ludwig, R., Plank, H. & Nidetzky, B. Cellulose surface degradation by a lytic polysaccharide monooxygenase and its effect on cellulase hydrolytic efficiency. *J. Biol. Chem.* **289,** 35929–35938 (2014).

138. Courtade, G., Forsberg, Z., Heggset, E. B., Eijsink, V. G. H. & Aachmann, F. L. The carbohydrate-binding module and linker of a modular lytic polysaccharide monooxygenase promote localized cellulose oxidation. *J. Biol. Chem.* (2018). doi:10.1074/jbc.RA118.004269

139. Loose, J. S. M., Arntzen, M. Ø., Bissaro, B., Ludwig, R., Eijsink, V. G. H. & Vaaje-Kolstad, G. Multipoint Precision Binding of Substrate Protects Lytic Polysaccharide Monooxygenases from Self-Destructive Off-Pathway Processes. *Biochemistry* **57,** 4114–4124 (2018).

140. Kracher, D., Andlar, M., Furtmüller, P. G. & Ludwig, R. Active-site copper reduction promotes substrate binding of fungal lytic polysaccharide monooxygenase and reduces stability. *J. Biol. Chem.* **293,** 1676–1687 (2018).

141. Frandsen, K. E. H., Simmons, T. J., Dupree, P., Poulsen, J.-C. N., Hemsworth, G. R., Ciano, L., Johnston, E. M., Tovborg, M., Johansen, K. S., von Freiesleben, P., Marmuse, L., Fort, S., Cottaz, S., Driguez, H., Henrissat, B., Lenfant, N., Tuna, F., Baldansuren, A., Davies, G. J., Lo Leggio, L. & Walton, P. H. The molecular basis of polysaccharide cleavage by lytic polysaccharide monooxygenases. *Nat. Chem. Biol.* **12,** 298–303 (2016).

142. Kjaergaard, C. H., Qayyum, M. F., Wong, S. D., Xu, F., Hemsworth, G. R., Walton, D. J., Young, N. A., Davies, G. J., Walton, P. H., Johansen, K. S., Hodgson, K. O., Hedman, B. & Solomon, E. I. Spectroscopic and computational insight into the activation of O2 by the mononuclear Cu center in polysaccharide monooxygenases. *Proc. Natl. Acad. Sci.* **111,** 8797–8802 (2014).

143. Bissaro, B., Røhr, Å. K., Müller, G., Chylenski, P., Skaugen, M., Forsberg, Z., Horn, S. J., Vaaje-Kolstad, G. &

Eijsink, V. G. H. Oxidative cleavage of polysaccharides by monocopper enzymes depends on H2O2. *Nat. Chem. Biol.* **13,** 1123–1128 (2017).

144. Kuusk, S., Bissaro, B., Kuusk, P., Forsberg, Z., Eijsink, V. G. H. H., Sørlie, M. & Väljamäe, P. Kinetics of H 2 O 2 -driven degradation of chitin by a bacterial lytic polysaccharide monooxygenase. *J. Biol. Chem.* **293,** 523–531 (2018).
145. Bennati-Granier, C., Garajova, S., Champion, C., Grisel, S., Haon, M., Zhou, S., Fanuel, M., Ropartz, D., Rogniaux, H., Gimbert, I., Record, E. & Berrin, J.-G. Substrate specificity and regioselectivity of fungal AA9 lytic polysaccharide monooxygenases secreted by Podospora anserina. *Biotechnol. Biofuels* **8,** 90 (2015).
146. Isaksen, T., Westereng, B., Aachmann, F. L., Agger, J. W., Kracher, D., Kittl, R., Ludwig, R., Haltrich, D., Eijsink, V. G. H. & Horn, S. J. A C4-oxidizing Lytic Polysaccharide Monooxygenase Cleaving Both Cellulose and Cello-oligosaccharides. *J. Biol. Chem.* **289,** 2632–2642 (2014).
147. Levasseur, A., Drula, E., Lombard, V., Coutinho, P. M. & Henrissat, B. Expansion of the enzymatic repertoire of the CAZy database to integrate auxiliary redox enzymes. *Biotechnol. Biofuels* **6,** 1–14 (2013).
148. Bissaro, B., Streit, B., Isaksen, I., Eijsink, V. G. H., Beckham, G. T., DuBois, J. L. & Røhr, Å. K. Molecular mechanism of the chitinolytic peroxygenase reaction. *Proc. Natl. Acad. Sci.* 201904889 (2020). doi:10.1073/pnas.1904889117
149. Vu, V. V., Beeson, W. T., Span, E. A., Farquhar, E. R. & Marletta, M. A. A family of starch-active polysaccharide monooxygenases. *Proc. Natl. Acad. Sci.* **111,** 13822–13827 (2014).
150. Agger, J. W., Isaksen, T., Varnai, A., Vidal-Melgosa, S., Willats, W. G. T., Ludwig, R., Horn, S. J., Eijsink, V. G. H. & Westereng, B. Discovery of LPMO activity on hemicelluloses shows the importance of oxidative processes in plant cell wall degradation. *Proc. Natl. Acad. Sci.* **111,** 6287–6292 (2014).
151. Couturier, M., Ladevèze, S., Sulzenbacher, G., Ciano, L., Fanuel, M., Moreau, C., Villares, A., Cathala, B., Chaspoul, F., Frandsen, K. E., Labourel, A., Herpoël-Gimbert, I., Grisel, S., Haon, M., Lenfant, N., Rogniaux, H., Ropartz, D., Davies, G. J., Rosso, M.-N., Walton, P. H., Henrissat, B. & Berrin, J.-G. Lytic xylan oxidases from wood-decay fungi unlock biomass degradation. *Nat. Chem. Biol.* **14,** 306–310 (2018).
152. Eijsink, V. G. H., Petrovic, D., Forsberg, Z., Mekasha, S., Røhr, Å. K., Várnai, A., Bissaro, B. & Vaaje-Kolstad, G. On the functional characterization of lytic polysaccharide monooxygenases (LPMOs). *Biotechnol. Biofuels* **12,** 58 (2019).
153. Singh, R. K., Blossom, B. M., Russo, D. A., van Oort, B., Croce, R., Jensen, P. E., Felby, C. & Bjerrum, M. J. Thermal unfolding and refolding of a lytic polysaccharide monooxygenase from Thermoascus aurantiacus. *RSC Adv.* **9,** 29734–29742 (2019).
154. Müller, G., Chylenski, P., Bissaro, B., Eijsink, V. G. H. & Horn, S. J. The impact of hydrogen peroxide supply on LPMO activity and overall saccharification efficiency of a commercial cellulase cocktail. *Biotechnol. Biofuels* **11,** 209 (2018).
155. Jones, S. M., Transue, W. J., Meier, K. K., Kelemen, B. & Solomon, E. I. Kinetic analysis of amino acid radicals formed in H2O2 -driven Cu I LPMO reoxidation implicates dominant homolytic reactivity. *Proc. Natl. Acad. Sci.* **117,** 11916–11922 (2020).
156. Kim, S., Stahlberg, J., Sandgren, M., Paton, R. S. & Beckham, G. T. Quantum mechanical calculations suggest that lytic polysaccharide monooxygenases use a copper-oxyl, oxygen-rebound mechanism. *Proc. Natl. Acad. Sci.* **111,** 149–154 (2014).
157. Zamocky, M., Ludwig, R., Peterbauer, C., Hallberg, B., Divne, C., Nicholls, P. & Haltrich, D. Cellobiose Dehydrogenase – A Flavocytochrome from Wood-Degrading, Phytopathogenic and Saprotropic Fungi. *Curr. Protein Pept. Sci.* **7,** 255–280 (2006).

158. Harada, H., Onoda, A., Uchihashi, T., Watanabe, H., Sunagawa, N., Samejima, M., Igarashi, K. & Hayashi, T. Interdomain flip-flop motion visualized in flavocytochrome cellobiose dehydrogenase using high-speed atomic force microscopy during catalysis. *Chem. Sci.* **8,** 6561–6565 (2017).

159. Harreither, W., Sygmund, C., Augustin, M., Narciso, M., Rabinovich, M. L., Gorton, L., Haltrich, D. & Ludwig, R. Catalytic Properties and Classification of Cellobiose Dehydrogenases from Ascomycetes. *Appl. Environ. Microbiol.* **77,** 1804–1815 (2011).

160. Phillips, C. M., Iavarone, A. T. & Marletta, M. A. Quantitative Proteomic Approach for Cellulose Degradation by Neurospora crassa. *J. Proteome Res.* **10,** 4177–4185 (2011).

161. Ludwig, R., Ortiz, R., Schulz, C., Harreither, W., Sygmund, C. & Gorton, L. Cellobiose dehydrogenase modified electrodes: advances by materials science and biochemical engineering. *Anal. Bioanal. Chem.* **405,** 3637–3658 (2013).

162. IGARASHI, K., MOMOHARA, I., NISHINO, T. & SAMEJIMA, M. Kinetics of inter-domain electron transfer in flavocytochrome cellobiose dehydrogenase from the white-rot fungus Phanerochaete chrysosporium. *Biochem. J.* **365,** 521–526 (2002).

163. Kracher, D., Zahma, K., Schulz, C., Sygmund, C., Gorton, L. & Ludwig, R. Inter-domain electron transfer in cellobiose dehydrogenase: modulation by pH and divalent cations. *FEBS J.* **282,** 3136–3148 (2015).

164. Kadek, A., Kavan, D., Felice, A. K. G., Ludwig, R., Halada, P. & Man, P. Structural insight into the calcium ion modulated interdomain electron transfer in cellobiose dehydrogenase. *FEBS Lett.* **589,** 1194–1199 (2015).

165. Kadek, A., Kavan, D., Marcoux, J., Stojko, J., Felice, A. K. G., Cianférani, S., Ludwig, R., Halada, P. & Man, P. Interdomain electron transfer in cellobiose dehydrogenase is governed by surface electrostatics. *Biochim. Biophys. Acta - Gen. Subj.* **1861,** 157–167 (2017).

166. Kracher, D., Forsberg, Z., Bissaro, B., Gangl, S., Preims, M., Sygmund, C., Eijsink, V. G. H. & Ludwig, R. Polysaccharide oxidation by lytic polysaccharide monooxygenase is enhanced by engineered cellobiose dehydrogenase. *FEBS J.* **287,** 897–908 (2020).

167. Tuoriniemi, J., Gorton, L., Ludwig, R. & Safina, G. Determination of the Distance Between the Cytochrome and Dehydrogenase Domains of Immobilized Cellobiose Dehydrogenase by Using Surface Plasmon Resonance with a Center of Mass Based Model. *Anal. Chem.* **92,** 2620–2627 (2020).

168. Meneghello, M., Al-Lolage, F. A., Ma, S., Ludwig, R. & Bartlett, P. N. Studying Direct Electron Transfer by Site-Directed Immobilization of Cellobiose Dehydrogenase. *ChemElectroChem* **6,** 700–713 (2019).

169. Scheiblbrandner, S. & Ludwig, R. Cellobiose dehydrogenase: Bioelectrochemical insights and applications. *Bioelectrochemistry* **131,** 107345 (2020).

170. Endres, S., Wingen, M., Torra, J., Ruiz-González, R., Polen, T., Bosio, G., Bitzenhofer, N. L., Hilgers, F., Gensch, T., Nonell, S., Jaeger, K.-E. & Drepper, T. An optogenetic toolbox of LOV-based photosensitizers for light-driven killing of bacteria. *Sci. Rep.* **8,** 15021 (2018).

171. Serebrovskaya, E. O., Edelweiss, E. F., Stremovskiy, O. A., Lukyanov, K. A., Chudakov, D. M. & Deyev, S. M. Targeting cancer cells by using an antireceptor antibody-photosensitizer fusion protein. *Proc. Natl. Acad. Sci. U. S. A.* **106,** 9221–9225 (2009).

172. Westberg, M., Bregnhøj, M., Etzerodt, M. & Ogilby, P. R. Temperature Sensitive Singlet Oxygen Photosensitization by LOV-Derived Fluorescent Flavoproteins. *J. Phys. Chem. B* **121,** 2561–2574 (2017).

173. Robertson, C. A., Evans, D. H. & Abrahamse, H. Photodynamic therapy (PDT): A short review on cellular mechanisms and cancer research applications for PDT. *J. Photochem. Photobiol. B Biol.* **96,** 1–8 (2009).

174. Salomon, M., Christie, J. M., Knieb, E., Lempert, U. & Briggs, W. R. Photochemical and mutational analysis of the FMN-binding domains of the plant blue light receptor, phototropin. *Biochemistry* **39,** 9401–9410 (2000).

175. Zoltowski, B. D. & Gardner, K. H. Tripping the Light Fantastic: Blue-Light Photoreceptors as Examples of Environmentally Modulated Protein−Protein Interactions. *Biochemistry* **50,** 4–16 (2011).

176. Torra, J., Lafaye, C., Signor, L., Aumonier, S., Flors, C., Shu, X., Nonell, S., Gotthard, G. & Royant, A. Tailing miniSOG: structural bases of the complex photophysics of a flavin-binding singlet oxygen photosensitizing protein. *Sci. Rep.* **9,** 2428 (2019).

177. Petrenčáková, M., Filandr, F., Hovan, A., Yassaghi, G., Man, P., Kožár, T., Schwer, M.-S., Jancura, D., Plückthun, A., Novák, P., Miškovský, P., Bánó, G. & Sedlák, E. Photoinduced damage of AsLOV2 domain is accompanied by increased singlet oxygen production due to flavin dissociation. *Sci. Rep.* **10,** 4119 (2020).

178. Courtade, G., Wimmer, R., Røhr, Å. K., Preims, M., Felice, A. K. G., Dimarogona, M., Vaaje-Kolstad, G., Sørlie, M., Sandgren, M., Ludwig, R., Eijsink, V. G. H. & Aachmann, F. L. Interactions of a fungal lytic polysaccharide monooxygenase with β-glucan substrates and cellobiose dehydrogenase. *Proc. Natl. Acad. Sci.* **113,** 5922–5927 (2016).

179. Bodenheimer, A. M., O'Dell, W. B., Oliver, R. C., Qian, S., Stanley, C. B. & Meilleur, F. Structural investigation of cellobiose dehydrogenase IIA: Insights from small angle scattering into intra- and intermolecular electron transfer mechanisms. *Biochim. Biophys. Acta - Gen. Subj.* **1862,** 1031–1039 (2018).

180. Breslmayr, E., Laurent, C. V. F. P., Scheiblbrandner, S., Jerkovic, A., Heyes, D. J., Oostenbrink, C., Ludwig, R., Hedison, T. M., Scrutton, N. S. & Kracher, D. Protein Conformational Change Is Essential for Reductive Activation of Lytic Polysaccharide Monooxygenase by Cellobiose Dehydrogenase. *ACS Catal.* **10,** 4842–4853 (2020).

181. Kracher, D., Scheiblbrandner, S., Felice, A. K. G., Breslmayr, E., Preims, M., Ludwicka, K., Haltrich, D., Eijsink, V. G. H. & Ludwig, R. Extracellular electron transfer systems fuel cellulose oxidative degradation. *Science (80-.).* **352,** 1098–1101 (2016).

182. Tran, J. C. & Doucette, A. A. Cyclic polyamide oligomers extracted from nylon 66 membrane filter disks as a source of contamination in liquid chromatography/mass spectrometry. *J. Am. Soc. Mass Spectrom.* **17,** 652–656 (2006).

183. Hansson, H., Karkehabadi, S., Mikkelsen, N., Douglas, N. R., Kim, S., Lam, A., Kaper, T., Kelemen, B., Meier, K. K., Jones, S. M., Solomon, E. I. & Sandgren, M. High-resolution structure of a lytic polysaccharide monooxygenase from Hypocrea jecorina reveals a predicted linker as an integral part of the catalytic domain. *J. Biol. Chem.* jbc.M117.799767 (2017). doi:10.1074/jbc.M117.799767

184. Gutteridge, J. M. C. & Wilkins, S. Copper salt-dependent hydroxyl radical formation. Damage to proteins acting as antioxidants. *BBA - Gen. Subj.* **759,** 38–41 (1983).

185. Mann, S. I., Heinisch, T., Ward, T. R. & Borovik, A. S. Peroxide Activation Regulated by Hydrogen Bonds within Artificial Cu Proteins. *J. Am. Chem. Soc.* **139,** 17289–17292 (2017).

Attached Publications

ARTICLE I

Filandr, F., Kavan, D., Kracher, D., Laurent, C. V. F. P., Ludwig, R., Man, P. & Halada, P.

Structural Dynamics of Lytic Polysaccharide Monooxygenase during Catalysis.

Biomolecules **10,** 242 (2020).

My contribution: *planning and conducting experiments (hydrogen/deuterium exchange mass spectrometry, LC-MS/MS analysis of oxidative modifications), data analysis & interpretation, manuscript writing, figure design*

biomolecules

MDPI

Article

Structural Dynamics of Lytic Polysaccharide Monooxygenase during Catalysis

Frantisek Filandr [1,2], Daniel Kavan [1], Daniel Kracher [3], Christophe V.F.P. Laurent [3], Roland Ludwig [3], Petr Man [1,*] and Petr Halada [1,*]

[1] Institute of Microbiology of the CAS, Division BioCeV, Prumyslova 595, 252 50 Vestec, Czech Republic; frantisek.filandr@biomed.cas.cz (F.F.); kavan@biomed.cas.cz (D.K.)

[2] Department of Biochemistry, Faculty of Science, Charles University, Hlavova 2030/8, 128 43 Prague 2, Czech Republic

[3] Biocatalysis and Biosensing Research Group, Department of Food Science and Technology, BOKU—University of Natural Resources and Life Sciences, Muthgasse 18, 1190 Vienna, Austria; danielkracher@boku.ac.at (D.K.); christophe.laurent@boku.ac.at (C.V.F.P.L.); roland.ludwig@boku.ac.at (R.L.)

* Correspondence: pman@biomed.cas.cz (P.M.); halada@biomed.cas.cz (P.H.)

Received: 15 January 2020; Accepted: 31 January 2020; Published: 5 February 2020

Abstract: Lytic polysaccharide monooxygenases (LPMOs) are industrially important oxidoreductases employed in lignocellulose saccharification. Using advanced time-resolved mass spectrometric techniques, we elucidated the structural determinants for substrate-mediated stabilization of the fungal LPMO9C from *Neurospora crassa* during catalysis. LPMOs require a reduction in the active-site copper for catalytic activity. We show that copper reduction in *Nc*LPMO9C leads to structural rearrangements and compaction around the active site. However, longer exposure to the reducing agent ascorbic acid also initiated an uncoupling reaction of the bound oxygen species, leading to oxidative damage, partial unfolding, and even fragmentation of *Nc*LPMO9C. Interestingly, no changes in the hydrogen/deuterium exchange rate were detected upon incubation of oxidized or reduced LPMO with crystalline cellulose, indicating that the LPMO-substrate interactions are mainly side-chain mediated and neither affect intraprotein hydrogen bonding nor induce significant shielding of the protein surface. On the other hand, we observed a protective effect of the substrate, which slowed down the autooxidative damage induced by the uncoupling reaction. These observations further complement the picture of structural changes during LPMO catalysis.

Keywords: lytic polysaccharide monooxygenase; lignocellulose degradation; hydrogen/deuterium exchange mass spectrometry; oxidative amino acid modification; peptide bond cleavage; reactive oxygen species

1. Introduction

Plant-biomass is a major source of renewable energy in the form of biofuels and bio-produced chemicals, but the recalcitrance of lignocellulose is a major obstacle to cost-effective saccharification. Fungal copper-dependent lytic polysaccharide monooxygenases (LPMOs, EC 1.14.99.53, - 56) have been found to boost the overall effectiveness of lignocellulolytic secretomes in the decomposition of insoluble recalcitrant polysaccharide structures [1]. Initially described in bacteria in 2010 [2], LPMOs have since been identified in fungi and insects and have been classified by the curators of the carbohydrate-active enzyme (CAZy) database (www.cazy.org) into several auxiliary activity (AA) families [3]. Fungal LPMOs have so far been classified as AA9 (activity on soluble and insoluble beta-

glucans), AA11 (chitin-active), AA13 (starch-active) [4], AA14 (xylan-active) [5], AA15, and AA16 [6]. LPMOs differ from common endo- and exo-glycosyl hydrolases by employing an oxidative mechanism to cleave glycosidic bonds in polysaccharides, such as cellulose, hemicellulose, starch or chitin, to produce access points for exo-acting hydrolases. After prolonged incubation, they also release soluble oligosaccharide products [7–10]. The ability to cleave polymers is enabled by a characteristic, flat binding-site consisting of aromatic and hydrophilic amino acids for the interaction with sugar moieties. An exposed active-site copper is held in place by a conserved, "histidine brace" motif [11–13]. These structural features enable LPMOs to attack polysaccharide surfaces inaccessible to hydrolases [13,14].

The catalytic mechanism of LPMOs is still under investigation, but several cornerstones of LPMO catalysis have been elucidated. The first step in the catalytic cycle is the reduction of the Cu(II) in the catalytic site to Cu(I), either by small molecular reductants [15–17], such as ascorbic acid (Asc) or gallic acid or by the fungal redox enzyme cellobiose dehydrogenase (CDH) [18]. CDH most likely requires the dissociation of LPMO from the substrate in order to contact the otherwise buried copper center of LPMO [19]. The reduction of the copper ion is also accompanied by a conformational change in LPMO, as was observed by using NMR [20] or electronic circular dichroism [21], and it also increases the affinity to its carbohydrate substrate [21,22]. As co-substrate for the LPMO reaction, either O_2 [23] or H_2O_2 [24] have been suggested. Whether the binding and reduction in an oxygen species happen preferentially in the free or substrate-bound state is not settled, but a recent publication suggests that hydrogen peroxide can access the active side of substrate-bound LPMO [25]. The catalytically competent LPMO abstracts hydrogens from its polysaccharide substrate and thereby breaks the glycosidic bond [23,26,27]. Oxidation on both C1 and C4 positions of the polysaccharide substrate was reported, with different resulting products. C1 oxidation leads to the formation of a lactone which spontaneously hydrolyzes into gluconic acid, while C4 oxidation forms a C4 ketone that hydrolyzes into a gemdiol in aqueous solution [7,27,28]. Several studies have shown that H_2O_2 increased the reaction rate relative to O_2 by an order of magnitude [24,29,30] while the measured affinity of LPMO for H_2O_2 was in the micromolar range [24,29]. The proposed reaction mechanism based on H_2O_2 as cosubstrate would also require only one electron to initiate the catalytic reaction, which aligns well with CDH's capability of transferring single electrons via its cytochrome domain. Several studies reported that the presence of H_2O_2-scavengers, such as peroxidase or catalase, inhibited the LPMO reaction, which implies that H_2O_2 is required for the LPMO reaction [21,24,30]. By providing a mix of different H_2O_2 and O_2 isotopes, Bissaro et al. showed that the oxygen atom inserted into the LPMO reaction products originated from the H_2O_2 [24]. A recent paper showed that potentially both O_2 and H_2O_2 can serve as co-substrates for LPMO, resulting in polysaccharide oxidative cleavage, but concluded that different molecular mechanisms are probably employed [30].

LPMOs were reported to be notoriously unstable under non-optimal reaction conditions. Especially, the observed higher catalytic rates in the presence of H_2O_2 were accompanied by a rapid inactivation of LPMO [30]. Employing LPMO in a commercial cellulase cocktail using industrially relevant substrates, therefore, requires fine-tuning of the reaction rate by controlling the H_2O_2 supply [31]. The observed instability was mainly attributed to autoxidative damage caused by oxygen radicals released from the active site, which lead to the oxidation of amino acids surrounding and forming the active site of LPMO [21,24,32]. The apparent T_m of the fungal LPMO9C from *Neurospora crassa* decreased from 61.5 ± 0.4 °C to 48.8 ± 1.1 °C when the active site copper was reduced by Asc. Under these conditions, H_2O_2 accumulates via the oxidation of O_2 by Asc [33,34]. In addition, the reduced LPMO may also generate low amounts of H_2O_2 through an uncoupling reaction [35]. In the presence of suitable substrates, however, the apparent T_m of *Nc*LPMO9C remained relatively unchanged at 60.4 ± 0.5 °C [21]. The stabilization of reduced LPMO by the substrate can be explained by the prevention of freely diffusing oxygen radicals due to the catalytic reaction [36], which may also consume the generated H_2O_2.

In addition to autooxidative damage, another form of destabilization was observed upon removal of the active site copper, e.g., by incubation of LPMO with an excess of the metal chelator - ethylenediaminetetraacetic acid (EDTA) [21,37]. Several studies showed reduced temperature

stability of copper-depleted LPMOs [21,38]. For example, removal of copper reduced the apparent T_m of *Nc*LPMO9C from 61.5 to 52.7 °C [21], which indicates that the histidine brace motif and the presence of the copper ion stabilize the overall protein fold. The thermal stability of the apoenzyme was unaffected by the presence of reducing agents and substrates, showing that an intact active site is required for substrate recognition and catalysis. While it is possible that the loss of the active-site copper ion contributes to the initial LPMO destabilization following active-site reduction and subsequent oxidation, it was demonstrated that the vast majority of LPMO molecules retained the copper ion upon unfolding.

In this work, we study the destabilizing effect of reducing agent and copper ion removal on *Nc*LPMO9C in temporal and structural detail by hydrogen/deuterium exchange mass spectrometry (HDX-MS). We also investigate the stabilizing effect of carbohydrate substrates during catalysis. The employed HDX-MS methods are well suited for the detection of structural changes involving the rearrangement of hydrogen bonds and changes in solvent accessibility in proteins, and they allow studying heterogeneous reactions with insoluble components, as long as they can be quickly removed before MS analysis. This is crucial for studying LPMOs, as their typical natural substrates, e.g., cellulose, are inherently insoluble. We observed a significant increase in peptide solvent accessibility throughout the LPMO molecule when incubated with a reducing agent, starting at peptides close to the copper ion active site and then propagating further. This effect was found to be slowed down in the presence of cellulose. Removal of the active site copper ion caused a temperature-induced unfolding beginning at lower temperatures, which affected the histidine brace peptides first and then propagated to the rest of the molecule upon longer incubation times.

Thus far, amino acid modifications resulting from autooxidative damage of LPMOs have only been reported in bacterial LPMOs [24]. We, therefore, aimed to verify that the same modifications occur in fungal LPMOs. Using LC-MS/MS analysis, we show that various oxidative alterations of peptides located around the copper active site occurred in a fungal LPMO. Oxidative peptide bond cleavages and, thus, direct degradation of the protein was detected for the first time in a fungal LPMO. The peptide signal intensity observed in our HDX-MS experiments provides a measure of the given peptide abundance. We observed a decrease in the intensity for unmodified peptides located in the vicinity of the active-site, indicating their cleavage or modification.

2. Materials and Methods

2.1. Protein Samples

Expression and purification of *Neurospora crassa* LPMO9C (*Nc*LPMO9C) were performed according to a published protocol [35]. NcLPMO9C was recombinantly expressed in *Pichia pastoris* X-33 cells under control of the methanol-dependent alcohol oxidase (AOX) promoter and chromatographically purified to homogeneity. Specific activity of 5.50 U g^{-1} was determined by using the Amplex Red assay [35], with the total protein concentration being determined by the Bradford protein assay. This value is close to the reported specific activity of *Nc*LPMO9C of 5.57 U g^{-1} [35].

2.2. Hydrogen/Deuterium Exchange Mass Spectrometry (HDX-MS)

*Nc*LPMO9C ("holo", 2 μM) or *Nc*LPMO9C copper-depleted by overnight incubation with 10 mM EDTA ("apo", 2 μM) was pre-incubated at 35, 50, or 65 °C in 50 mM sodium acetate buffer, pH 6.0. Dilution into D2O deuteration buffer (50 mM sodium acetate, pD 6.0) was done 10-fold, and aliquots containing 100 pmol of *Nc*LPMO9C were removed at different time points. Deuteration of *Nc*LPMO9C alone or in the presence of 5 mM Asc, 4 mg mL^{-1} microcrystalline cellulose, or both Asc and microcrystalline cellulose was performed. These additives were added to the deuteration buffer prior to mixing with the LPMO sample. The microcrystalline cellulose was centrifuged and washed several times with a deuterated buffer to remove H_2O and soluble oligosaccharides prior to use. Deuterium exchange in aliquoted samples was immediately stopped by mixing the sample 1:1 with quenching solution (200 mM tris (2-carboxyethyl) phosphine (TCEP), 8 M urea, 1 M glycine, pH 2.3). The sample was subsequently flash-filtered for 20 s using spin filter tubes (Ultrafree-MC GV,

polyvinylidene fluoride (PVDF) 0.22 μm, Merck, Darmstadt, Germany) to remove insoluble cellulose fibers and then rapidly frozen in liquid nitrogen. Sampling, filtering, and freezing took precisely 90 s for every sample. For the peptide mapping of non-deuterated control samples, the same protocol was used with the difference of using H_2O-based buffer instead of a D_2O-based buffer.

2.3. HPLC/ESI-FT-ICR-MS Analysis of HDX Samples

Samples were stored at −80 °C, quickly thawed before the LC-MS analysis, and then injected into an in-house build LC system maintained at a stable temperature of 0 °C to minimize the deuterium back-exchange. The digestion took place on columns with immobilized proteases (rhizopuspepsin, nepenthesin I, made in-house [39,40]) using 0.4% formic acid (FA) in water as an eluent at a flow-rate of 200 μL min^{-1} (LC-20AD HPLC pump, Shimadzu, Tokyo, Japan). The resulting peptides were subsequently trapped and desalted on a peptide microtrap (Optimize Technologies, Oregon City, OR, USA). The whole digestion and desalting procedure took precisely 3 min. Desalted peptides were eluted with an acetonitrile gradient (HPLC system Agilent 1200, Agilent Technologies, Waldbronn, Germany) on a reversed-phase analytical column (ZORBAX 300SB-C18, 0.5 × 35 mm, 3.5 μm, Agilent Technologies, Waldbronn, Germany) where they were further separated. The eluting gradient from 5–35% B lasted for 5 min and was followed by a quick change to 95% B and subsequent column re-equilibration. Solvents were A: 0.4% FA, 2% acetonitrile (ACN) in water, and B: 0.4% FA, 95% ACN in water. The flow through the column was kept at 20 μL min^{-1}. The column was interfaced with an electrospray ionization (ESI) source of the Fourier transform ion cyclotron resonance mass spectrometer (15T-solariX XR FT-ICR, Bruker Daltonics, Bremen, Germany). Peptide mapping was performed in a positive data-dependent MS/MS broadband mode, where each MS scan was followed by six MS/MS scans of the most abundant peptides found in the previous MS scan, which underwent collision-induced fragmentation. Deuterated samples were analyzed in the LC-MS mode.

2.4. Oxidative Modification Analysis

*Nc*LPMO9C was incubated at 50 °C in 50 mM sodium acetate buffer, pH 6.0, alone, or in combination with 5 mM Asc. Samples were taken in 10-min intervals for up to 30 min. The reaction was stopped by the addition of EDTA (10 mM final concentration) to chelate LPMO's copper ion. Methionine (25 mM final concentration) was added to scavenge existing ROS. Protein samples were digested using trypsin or AspN proteases after pH adjustment to 8.8 with TRIS buffer (80 mM final concentration). Trypsin was added in a 1:100 ratio (protease:LPMO; *w*:*w*), AspN was added in a 1:300 ratio (protease:LPMO; *w*:*w*). Disulfide bonds in the samples were reduced by a 30-min incubation with 5 mM TCEP and alkylated by a 30 min incubation with 10 mM iodoacetamide in the dark at 22 °C. The pH of the samples was adjusted to acidic pH (< 2) by adding 4% trifluoroacetic acid (TFA) to stop the protease reaction. Subsequently, the samples were analyzed using HPLC/ESI-FT-ICR-MS using binding and elution solutions A and B (A: 0.1% FA, 2% ACN in water, B: 0.1% FA, 95% ACN in water) at a constant flow rate of 10 μL min^{-1}, with online desalting on a reversed-phase trap column (ZORBAX 300SB-C18 5 μm, 0.3 × 5 mm, Agilent Technologies, Santa Clara, CA, USA), separation on an analytical column (ZORBAX 300SB-C18, 0.3 × 150 mm, 3.5 μm, Agilent Technologies, Santa Clara, CA, USA) and elution during a 15 min linear gradient to 25% solution B.

2.5. Data Processing

Obtained LC-MS/MS data were processed by DataAnalysis 4.1 (Bruker Daltonics, Billerica, MA, USA) and then searched by MASCOT (Matrix Science, London, UK) in ProteinScape 4 (Bruker Daltonics, Billerica, MA, USA) against a database containing the *Nc*LPMO9C sequence as well as sequences of rhizopuspepsin and nepenthesin-1 as false positives/controls. Data processing combined approaches described previously [41,42]. For HDX-MS peptide mapping the no-enzyme search with no modification included was performed. Two search rounds were done—one with precursor and fragment accuracies 3 ppm and 0.05 Da, respectively. Another one, where the parent ion mass accuracy window was wider—1000 ppm and the results with errors above 3 ppm were

discarded. Hits with ion scores below 20 were checked manually for fragment ion assignments and also for mass uniqueness within the *Nc*LPMO9c sequence and for isotope pattern fit. Oxidation data were also searched with multiple rounds of searches. PEAKS algorithm (Bioinformatics Solutions, Waterloo, ON, Canada) was used first to asses all possible modifications and then the data were re-searched using MASCOT. Here, the search employed small errors (3 ppm and 0.05 Da for precursor and fragments, respectively) and enzyme specificity (trypsin or Asp-N). Cys carbamidomethylation was set as fixed modification. Variable modifications were selected on the basis of PEAKS searches and included: single (+15.995) and double (+31.999) oxidation of Met, Trp, His, Tyr, Pro; His->Asp oxidative breakdown (− 22.032); oxidative peptide bond cleavage (−0.985/+25.979). All assignments were verified manually to double-check the site of oxidation. Protein purity was assessed by searching the LC-MS/MS from HDX-MS mapping and unmodified samples from oxidation analysis against NCBInr database. HDX-MS data were plotted using the DrawMap script, part of MSTools [43]. LC-MS HDX data were processed by using the in-house software DeutEx (unpublished). Deuteration levels of individual peptides at each time point were calculated. Peptides with overlapping regions were used to calculate the number of exchanged deuterium atoms to increase spatial resolution. This software was also used to calculate the peptide abundance changes as changes in MS intensity under various conditions. Data were modeled on the known crystal structure of the catalytic domain of *Nc*LPMO9C [44].

3. Results

A recent report from Kracher et al. described the interaction of the fungal *Nc*LPMO9C with various substrates, the enhancement of substrate binding upon active-site copper reduction, and the protective/stabilizing role of substrates on LPMO under reducing conditions. Spectroscopic techniques, such as circular dichroism, indicated conformational changes in the LPMO upon active-site copper reduction and copper depletion but did not provide insight into the structural details of the various *Nc*LPMO9C states [38,45]. In order to gain accurate structurally resolved answers underlying these phenomena, we performed a systematic hydrogen/deuterium (H/D) exchange study, which allowed us to extend the previous conclusions.

In the first step, we optimized the HDX-MS workflow, which included tuning of digestion conditions and rapid separation of proteins from the insoluble substrate during the post-labeling step. In our previous studies, which focused on cellobiose dehydrogenase, an enzyme closely cooperating with LPMO during the cellulolytic activity, we showed that strong reducing and denaturing conditions are required for efficient digestion. As these enzymes are adapted to a harsh extracellular environment, it is not surprising that LPMO digestion required denaturation. However, in contrast to the previously used guanidine hydrochloride, we switched to urea, which provided similar sequence coverage but avoided adverse effects on LC analysis. In addition, from the studies published so far, it is evident that in contrast to guanidine hydrochloride, even a high concentration of urea has much less deleterious or even enhancing effects on the protease activity [46–48]. We also tested various proteolytic setups (protease columns, flow rates) with serial coupling of nepenthesin-1 and rhizopuspepsin columns operated at 200 μL min^{-1}, providing the best sequence coverage and spatial resolution. Finally, we had to cope with the heterogeneous, insoluble substrate (microcrystalline cellulose) present in the sample. We found the use of 0.45 μm spin filters as an optimal solution, adding approximately 50 s to the sample processing time while ensuring complete removal of insoluble matter. The harsh denaturing conditions also prevented possible adherence of LPMO to the substrate via its interaction surface and/or carbohydrate-binding module (CBM). The additional post-quench time of 90 s was also required to achieve the reduction in the disulfide bonds in *Nc*LPMO9C. We observed that raising the TCEP concentration or prolonging the incubation time did not lead to more efficient digestion and, therefore, we used the lowest possible TCEP concentration and reduction time. As a result, we fully covered the catalytic domain (except for residues 41–44) and the CBM. The linker peptide connecting the catalytic domain to the CBM (residues 225–309) could not be resolved due to its high and heterogeneous O-glycosylation (Figure S1).

With the optimized workflow, we performed an initial set of HDX-MS measurements in which we focused on several factors. First, building upon the data from Kracher et al., we looked at the effect of high temperature on the free, oxidized LPMO and its apo form prepared by EDTA treatment. Here, the exchange was followed at 35, 50, and 65 °C, and the HDX kinetics covered time points at 0.33, 2, 20, 120, and 360 min. A summary of selected HDX data is provided in the protection plots in Figure 1. While this presentation focuses on the catalytic domain and representative exchange times only, we provide full data covering the whole LPMO sequence, including the CBM and all exchange times in the form of mirror plots (Figure S2) [43]. Peptides in mirror plots are represented on the *X*-axis by their "midpoint" value, which is calculated as an average value between the N- and C- terminal residue sequence position of a given peptide and thus allows for easy and reproducible sorting of the overlapping peptides generated and analyzed in the HDX-MS experiment.

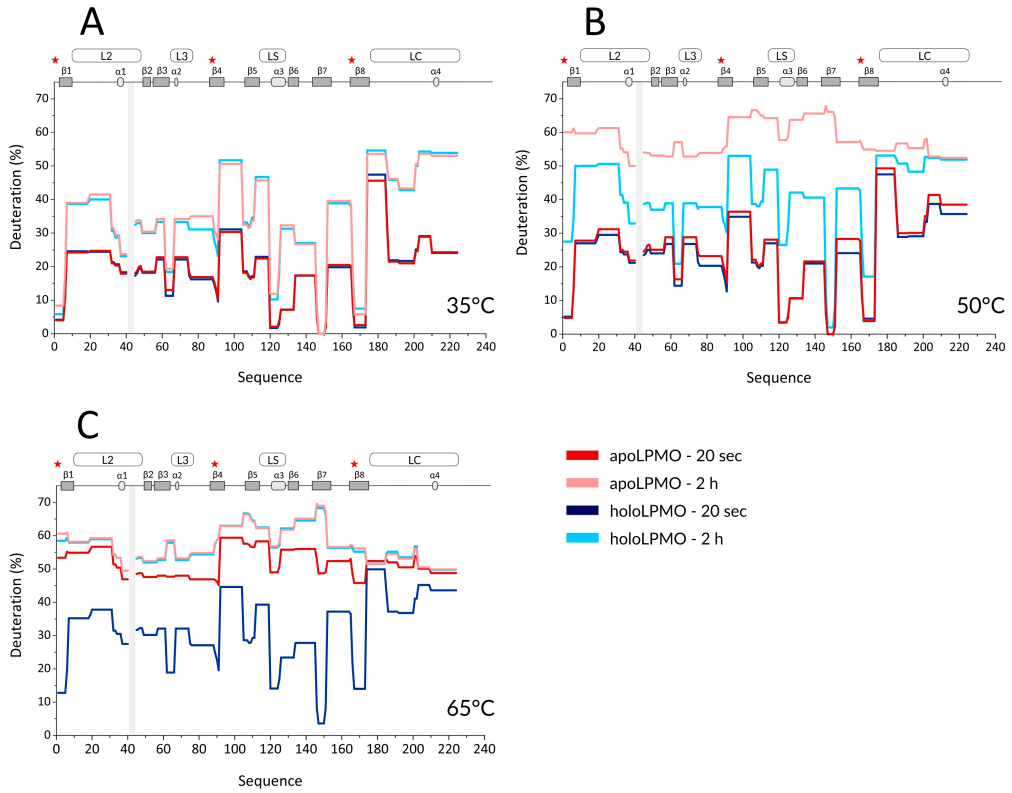

Figure 1. Selected hydrogen/deuterium (H/D) exchange kinetic profiles of holo- and apo-*Nc*LPMO9C at three different temperatures. Protection plots showing deuteration of *Nc*LPMO9C apo- (red tones) and holoenzyme (blue tones) at (**A**) 35 °C, (**B**) 50 °C, and (**C**) 65 °C and at two exchange times of 20 s (dark colors) and 2 h (light colors). Secondary structure elements and positions of loops are shown on the top of each graph. Shaded boxes illustrate gaps in the sequence coverage. The visualization covers the catalytic domain and part of the linker connecting the catalytic domain to the CBM. Asterisk denotes positions of the histidine brace residues (His1, His88, and Tyr166).

Since we observed no difference induced by cofactor absence or active site copper reduction at the CBM (Figure S2) and we missed a large part of the linker, we avoided these structural features in Figures 1 and 2. It should be stressed that the intrinsic exchange rate was influenced by the temperature and, thus, the data acquired at different temperatures are not directly comparable. We, therefore, plotted these data separately (Figure 1A–C). However, normalization using correction factors calculated based on the Arrhenius equation can be applied to compensate for the different exchange rates. The exchange rate at 50 °C was multiplied by a factor of 3.628 and those at 65 °C by 11.739, which led to normalization to the lowest temperature of the dataset (35 °C). How this affects the data interpretation is shown in several selected deuterium uptake curves (Figure S3). From these graphs, it can be inferred that the deuterium uptake curves of the LPMO holoenzyme obtained at 35

°C and at 50 °C were either fully or partially overlapping for the whole protein and differences between these two temperatures could be seen only after longer exchange times (> 20 min). The main differences were observed in peptides covering the histidine brace residues (His1, His88, and Tyr166) or the closely neighboring regions. This shows that even at 50 °C, the structural integrity of *Nc*LPMO9C was well preserved, and only weak destabilization occurred around the active site. In contrast, at 65 °C, the majority of the uptake curves had a much steeper slope, reaching equilibrium deuteration already after 2 min of exchange, except for unstructured and freely accessible regions (regions/peptides 92–104, 174–185, 201–224. and the CBM: 310–343). These observations clearly show that structural destabilization at 65 °C was strongly accelerated when compared with the lower temperatures. These trends were further amplified (Figure S2) when the copper was removed from the active site using EDTA treatment. When incubating the apoprotein at 35 °C, the LPMO was slightly perturbed around the active site as the deuteration increase could be observed for the peptides covering the copper-binding residues (Figures 1A and S3). Interestingly, virtually no difference was detected for the region around Tyr166 (see peptides 152–165 and 166–173 in Figure S3—black and grey curves). The importance of the copper ion on the overall structure stabilization is demonstrated by a significant structure opening at elevated temperatures. At 50 °C, the apo-protein was much more accessible for deuteration (Figures 1B and S3), and this was further enhanced at the highest temperature monitored (65 °C) where the protein was readily deuterated even after 20 s of deuteration (Figures 1C, S2C, and S3). To position these effects onto the structure, we colored the LPMO structure using the difference in HDX between the apo- and holoenzyme (Figure S4), which illustrates the destabilization of the protein core upon copper ion removal.

Next, we performed HDX experiments targeting effects induced by ascorbic acid (Asc). To allow for time-resolved analysis of the effect of LPMO reduction, we added Asc at the same time when the deuteration was started. To be able to compare the results to holo- and apo-form experiments, the reduction by Asc was also followed at three different temperatures (35, 50, and 65 °C). Key data are shown in the form of protection plots in Figure 2, while the whole dataset was visualized using mirror plots (Figure S5). The most obvious change observed at 35 °C was a generally higher deuteration of the reduced LPMO at longer incubation times (> 2 h, Figure 2A—the lightest colors). This was observed for peptides covering β1 (including the N-terminus with His1), loop L2, β2, β3-α2 linker (in L3), β5, α3 in LS, β6, β7, β8 (including Tyr166), and the middle part of loop LC. Interestingly, no such effects were detected for peptides covering the third His brace residue, His83. The protection plots showed that the peptides covering His83 were slightly less deuterated in the presence of Asc and at longer incubation times. Besides the above-described effects detected at longer time scales (> 2 h), there were also indications of lower deuteration of the reduced enzyme at earlier time points (Figure 2A-light and dark colors). However, these differences were small and cannot be considered as significant without further supporting observations. Such additional validation was obtained through inspection of data acquired at 50 °C (Figures 2B and S5B). Here, the lower deuteration at 20 s and 2 min in the presence of Asc was more obvious and manifested through the peptides covering the His brace residues, including His83. Lower deuteration was also observed in neighboring peptides (e.g., L2, LS with α3, N-term part of β6, β7) or parts distant from the active site (e.g., β2, β4-β5, N-term part of LC) of *Nc*LPMO9C. On the other hand, the destabilizing effect of Asc was observed as a much higher deuteration occurring already after 20 min of exchange/reduction. Intriguingly, we observed a significant decrease in deuteration at longer incubation times beyond 2 h, which was specific for certain peptides, including the His brace residues (Figures S5 and S6A).

We observed such unusual effects if protein degradation or precipitation occurred during the H/D experiment. Indeed, an inspection of the summed up peak intensity plots of the individual peptides (alternative data visualization in DeutEx, Figure S6B) showed a signal decrease that correlated with the trend of deuteration decrease. Hence, we conclude that at 50 °C and in the presence of Asc, LPMO is likely oxidized and/or degraded, which leads to the signal loss. At 65 °C, the effects induced by copper ion reduction were fading, and the only prominent event we observed was degradation after longer reduction/deuteration times (Figures 2C and S5C). This is likely due to the destabilization of LPMO at this temperature, which we also detected for oxidized LPMO.

However, considering that we still detected signal loss on peptides close to the active site even at 65 °C (see Figure S5C), we speculate that even at this temperature, the copper ion could remain bound to the His brace and the enzyme at least partially exerts its activity. To put the Asc-induced effect into a structural perspective, the difference in deuteration between reduced and oxidized *Nc*LPMO9C was plotted onto the structure (Figure S7).

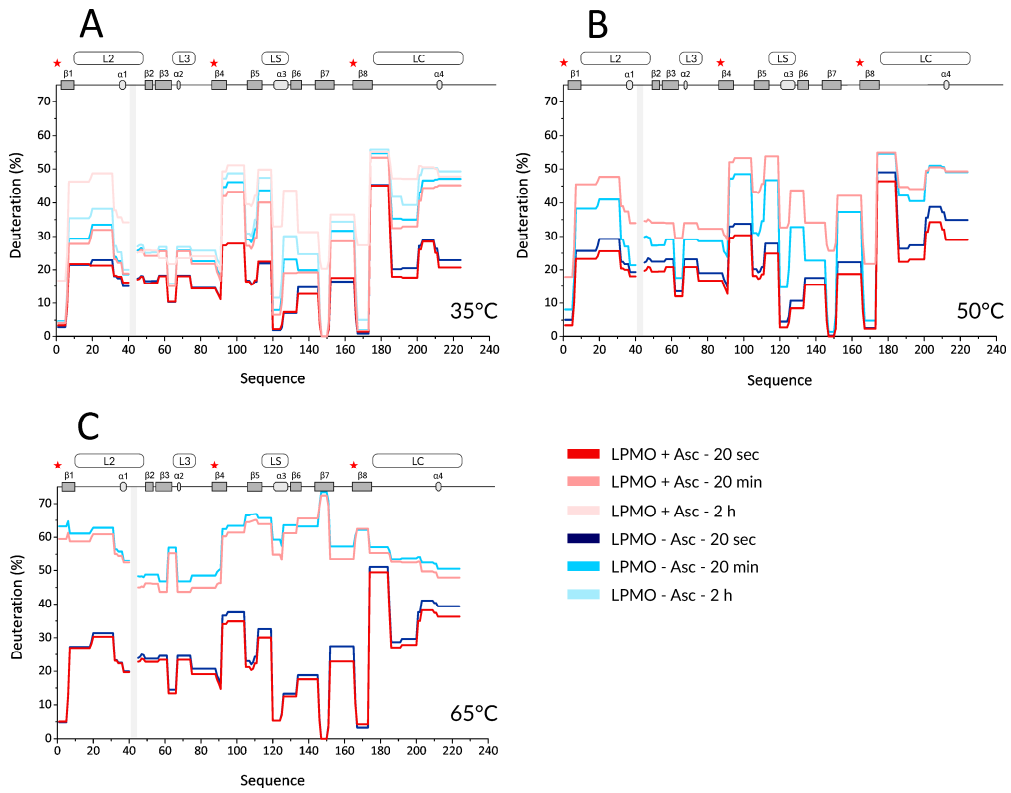

Figure 2. Selected H/D exchange kinetics profiles of oxidized and Asc-reduced *Nc*LPMO9C at three different temperatures. Protection plots showing deuteration of the Asc-reduced (red) and the oxidized (blue) form of *Nc*LPMO9C at (**A**) 35 °C, (**B**) 50 °C, and (**C**) 65 °C. Three exchange times of 20 s (dark colors), 20 min (lighter colors), and 2 h (the lightest colors) are shown for 35 °C (**A**), whereas (**B**) and (**C**) display only the two shorter times (20 s and 20 min, respectively). Secondary structure elements and positions of loops are shown on the top of each graph. Shaded boxes illustrate gaps in the sequence coverage. The visualization covers the catalytic domain and part of the linker. Asterisk denotes positions of the histidine brace residues (His1, His88, and Tyr166).

Based on these data, we then set up the final experiment. A temperature of 50 °C was chosen, as the kinetics of H/D changes were slow at 35 °C and, on the other hand, the protein was significantly perturbed at 65 °C. In addition, given the autooxidative damage detected in the experiments with Asc, the maximum exchange time was reduced to 45 min. We increased the temporal resolution of these experiments by collecting a higher number of samples and focused on the substrate binding and its protective role on the LPMO. The experimental conditions included oxidized and Asc-reduced LPMO, either alone in solution or mixed with microcrystalline cellulose. Representative HDX data are shown in the form of protection plots in Figure 3, and the whole dataset is shown as mirror plots in Figure S8. The profile of the oxidized LPMO was virtually indistinguishable from that obtained in the presence of cellulose, which implies that there is no tight binding that would alter the H/D exchange of the protein (Figure 3: black vs. green and Figure S8A). Similar to previous experiments, reduction by Asc led to two distinct effects (Figure 3—black vs. red and Figure S8B).

First, lower deuteration was detected for reduced LPMO on the peptides covering the His brace and the neighboring regions, mainly L2, L3, and its extension to β4, LS, and LC. This effect lasted

until 10–15 min of deuteration. Second, the difference in deuteration between oxidized and reduced LPMO vanished after 15–20 min, and the reduced LPMO became more deuterated at later time points. This was likely linked to the oxidation-induced LPMO damage, which, after 35 min, also led to an apparent decrease in the deuteration of the His brace-covering peptides. Finally, the trends observed for free, reduced LPMO were also observed when cellulose was added.

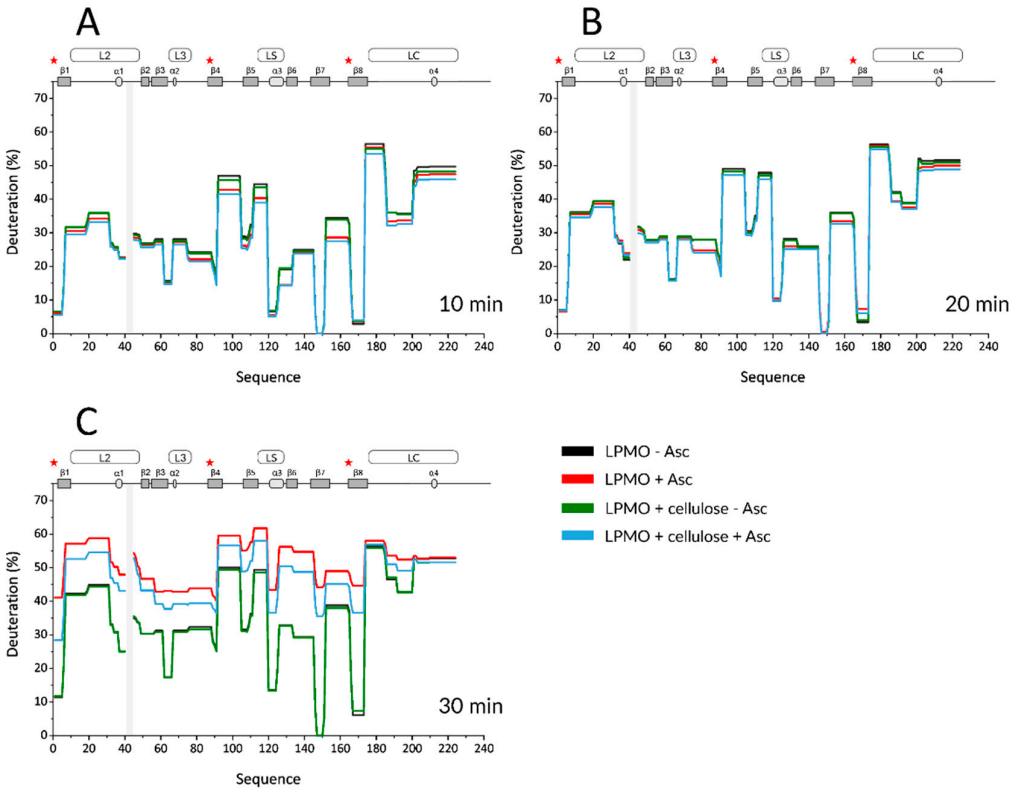

Figure 3. Selected H/D exchange kinetics profiles of oxidized and Asc-reduced *Nc*LPMO9C in the presence of microcrystalline cellulose. Protection plots showing deuteration profiles of oxidized (black) and Asc-reduced (red) *Nc*LPMO9C alone or in presence of cellulose (green and purple, respectively) at three deuteration times—3 min (**A**), 10 min (**B**), and 30 min (**C**). The exchange was followed at 50 °C and reduction with Asc was induced at the same time as deuteration. Secondary structure elements and positions of loops are shown on the top of each graph. Shaded boxes illustrate gaps in the sequence coverage. The visualization covers the catalytic domain and part of the linker. Asterisk denotes positions of the histidine brace residues (His1, His88, and Tyr166).

Although it was shown that LPMO binds to microcrystalline cellulose under reducing conditions, albeit weakly compared to more amorphous phosphoric acid swollen cellulose (PASC) [21], we observed no decrease in deuteration in the first data points due to the presence of cellulose. However, the transition point at which the reduced protein switched from a more protected to a more deuterated state was shifted, indicating that oxidation and degradation are slowed down due to the protective role of the cellulose substrate. The last data points of the kinetics showed a deuteration decrease (described above for free reduced LPMO), which can be considered as an indicator of protein degradation. This effect was observed for both the free and cellulose-bound and Asc-reduced LPMO, which shows that the autooxidative damage at a certain point overrode the protective effect of the cellulose. We also observed protection from exchange on the CBM upon cellulose addition. This effect is not affected by the presence of Asc and justifies the binding of LPMO to the substrate. However, the extent of this protection was very small and at the border of significance. All these effects were visualized on the LPMO structure (Figure 4—selected time points and Figure S9—whole dataset, excluding oxidized LPMO conditions where no difference was detected).

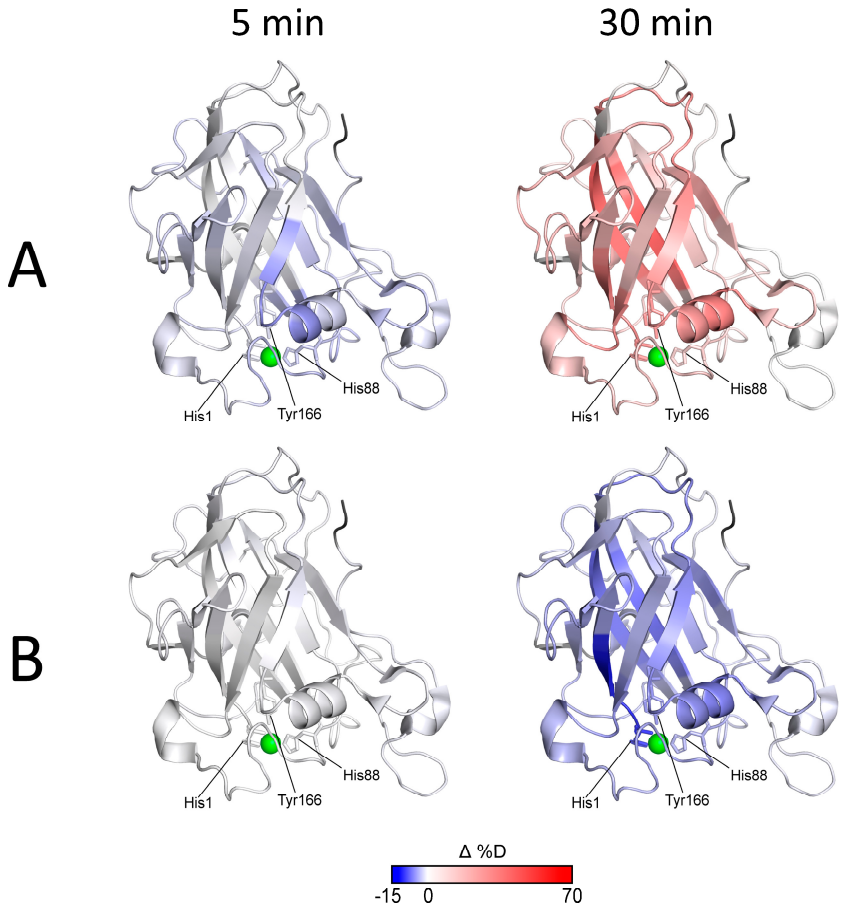

Figure 4. Visualization of effects exerted by Asc-reduction and cellulose binding on the structure of NcLPMO9C. Structure of NcLPMO9C (pdb: 4D7U) was colored according to the differences in deuteration. (**A**) Asc-reduction effects—deuteration of free reduced LPMO was subtracted from deuteration of the free oxidized form and the structure was colored according to these differences. (**B**) protective effect of cellulose binding/presence—deuteration levels of Asc-reduced LPMO were subtracted from the levels of LPMO reduced in the presence of cellulose. Two exchange times of 5 min and 30 min (also indicated above the structures) are shown. The full dataset covering 3 min to 35 min of incubation is shown in Figure S9. The blue-white-red gradient covers the range from –15% to 70% with white at 0%. Histidine brace residues His1, His88 and Tyr166 are labeled and their side chains are shown as sticks. Active site copper ion is shown as green ball.

The effects of Asc reduction (protection/lower deuteration) and subsequent autooxidative damage to LPMO (higher deuteration) are evident from the blue-to-red transition shown in Figures 4A and S9A. Figures 4B and S9B show that the expected tighter LPMO binding to cellulose did not cause detectable alterations in the HDX kinetics and that only protection from autooxidative damage could be captured using HDX-MS. It should be noted that this protective effect aligned well with the timing of increased oxidative damage (detectable after 15 min of exchange/reduction) and was diminished after 30 min when oxidative damage prevailed. Oxidation and/or degradation and the protective effect of the cellulose were also supported by the plots following signal intensity throughout the experiment. These are shown in Figure S10 together with the respective deuterium uptake plots for the peptides covering the His brace and several representative parts of the protein structure. It is evident that in cases where the deuteration drop occurred during the last time points, the signal intensity also decreased (Figure S10A,B). The protective effect of the cellulose substrate under reducing conditions then manifested as slower deuteration, and it also slowed-down the degradation. The structural and spatial dependences of these effects could be deduced from the localization of the peptides on the *Nc*LPMO9C structure. Here, it is evident that the proximity of peptides to the catalytic center was the major factor behind the signal loss (amino acid oxidation extent, Figure S10C).

In order to verify that the mechanism underlying signal loss and deuteration decrease is indeed protein oxidation caused by reactive oxygen species generated by the reduced LPMO, we searched for oxidized versions of the peptides detected in HDX-MS. However, this approach was largely unsuccessful, with only a few significant hits. This can be demonstrated by peptide 1–6 (Figure S11) for which the singly oxidized version (oxidation of His1, part of the His brace) was found. The deuterium uptake (Figure S11A) had a different shape when compared with the unmodified peptide and increased rapidly starting from the early time-points on. In addition, the time-dependent signal intensity (Figure S11B) showed the opposite trend. While the unmodified peptide vanished, the intensity of the oxidized peptide increased, showing that the oxidation was ongoing throughout the experiment.

A detailed description of oxidative modifications in LPMO was done using a classical proteomic bottom-up approach based on the digestion of the protein with specific proteases. *Nc*LPMO9C was subjected to reduction using Asc, and protein samples were taken at different incubation times and digested using Trypsin or Asp-N proteases. The breakdown products were analyzed by LC-MS/MS, followed by a database search and manual validation. Due to the sheer amount of variability in oxidative modifications present, we only focused on the most abundant peptide forms, which yielded intense fragment spectra of sufficient quality to verify the modification type and residue position. An overview of the identified oxidative modifications is provided in Table S1**.** The analysis confirmed that similar to a previous report on *Sc*LPMOC [24], *Nc*LPMO9C underwent extensive autocatalyzed oxidation in the presence of Asc. When searching our dataset, we found not only known oxidative modifications of amino acid side chains but also generally overlooked peptide bond cleavages [49,50]. These peptide bond cleavages result in either +25,980 Da or -1,030 Da mass changes in the N-terminus of resulting shorter cleaved peptides and -30,010 Da or -0,985 Da mass change in the C-terminus, depending on the cleavage mechanism. An example shown in Figure 5 shows the extracted ion chromatograms of various forms of the N-terminal peptide bearing His1 (part of His brace), which belongs to a group of rapidly oxidized regions undergoing further oxidation-induced events, such as oxidative cleavage.

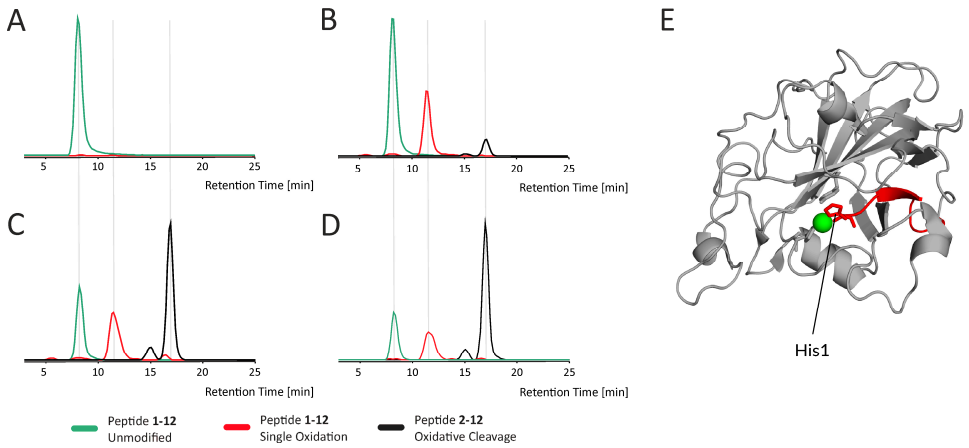

Figure 5. Monitoring kinetics of LPMO oxidative modifications by mass spectrometry. Extracted ion chromatograms for the N-terminal LPMO peptide (1–12) that contains His1 residue involved in copper ion binding. LPMO were incubated (**A**) alone for 30 min, or with 5 mM ascorbic acid for (**B**) 10 min, (**C**) 20 min, (**D**) 30 min. Subsequently, it was digested with Asp-N and analyzed by LC-MS/MS. Chromatographic traces show a signal for unmodified (green), oxidized (+O1; red) and oxidatively cleaved (−His, +C1O1-H2; black) peptides. The data clearly shows how the relative amount of the singly oxidized form increases, followed by oxidative cleavage, while the relative intensity of the unmodified peptide is decreasing. Localization of the peptide and the His residue is shown on a structure in (**E**). Copper ion is shown as green ball.

Generally, the extent and kinetics of oxidation depended on the proximity of the peptide to the catalytic center and on the amino-acid composition of the peptide, as shown in Figure S12. It is apparent from both Figures S10 and S12 that residues close to the active site were oxidized faster than those located on the opposite side of the protein.

4. Discussion

Previous reports described thermal aspects of LPMO stability in relation to its cofactor and substrates [21,45]. Other publications focused on the structural differences between the apo- and the holoenzyme and substrate binding effects. These employed protein X-ray crystallography or NMR providing excellent spatial resolution and detailed answers about key amino acids and their side chains involved in these interactions. Here, we employed hydrogen/deuterium exchange, which is a lower-resolution structural biology method but offers a more detailed view on the dynamics of thermal- and ROS-induced destabilization of proteins. It also complements the crystallography and NMR data by allowing the monitoring of different conditions not easily amenable by either of the two classical techniques. We also employed hydrogen/deuterium exchange to follow the deactivation of reduced LPMO in a time-dependent manner. Thereby, we shed light on the nature of the destabilization, which is important in the context of effective industrial utilization of LPMOs.

Our first experiment aimed to elucidate the structural differences between the apo- and holo-forms of *Nc*LPMO9C and their stability at different temperatures. A previous NMR study followed the titration of the apoLPMO by Cu^{2+} and provided evidence about changes mainly at the copper coordinating residues and their surroundings [20]. Other studies based on thermal unfolding assays then showed that the absence of the copper ion results in structural unfolding occurring at lower temperatures when compared to the holo form [21–38]. Using HDX-MS, we further extended these findings by providing spatially resolved data on *Nc*LPMO9C. We selected three temperatures representing important points on the *Nc*LPMO9C unfolding pathway. At 35 °C, a very mild structure perturbation was detected (Figures 1A and S4A). Slightly higher deuteration of the apo form was detected for peptides covering His1, His83, and Tyr166 after 2 h of incubation. Kinetics of deuteration varied between the individual amino acids forming the His brace. Changes in His83 manifested mostly between 2 and 20 min of deuteration, while changes in His1 and Tyr166 were observed only

at longer deuteration times between 2 and 6 h (Figure S3). This is likely related to the location of these residues in the protein structure. His1 and Tyr166 are both linked to the core beta-sandwich, which could result in slower deuteration despite the fact that both amino acids are solvent-exposed. In contrast, His83 is positioned in the loop L3 connecting helices 3 and 4 and is thus less protected from an exchange. At 50 °C, the crucial role of the copper ion in the stabilization of the overall protein fold manifested (Figures 1B and S4B). Detected deuteration differences were similar to those at 35 °C, albeit much more pronounced, mainly in regions covering the histidine brace residues (especially His1 and Tyr166) but also for regions 61–66, 120–125, and 146–151. These segments are either forming the beta-sandwich core (146–151) or are positioned close to the catalytic center (61–66, 120–125). Interestingly, the region 105–111, which is distant from the catalytic center, showed a high degree of perturbation as well, which suggests the overall "disassembly" of the LPMO core upon removal of the copper ion. Finally, we observed that the highest employed temperature of 65 °C leads to very rapid deuteration of both LPMO states with slower kinetics present in the holo-form (Figures 1C and S3). This indicates that the copper ion was probably still bound to the enzyme, as was previously observed for fungal and bacterial LPMOs [21,38].

The function of LPMOs depends on the reduction state of their active-site metal ion. The reduction and subsequent catalytic activity, however, leads to rapid inactivation of the enzyme in the absence of suitable substrates. This inactivation was attributed to the formation of oxygen radicals and subsequent oxidative modifications of amino acid residues lining the active site [19,22,28]. Here, the accompanying structural changes were investigated through another set of HDX-MS experiments, and the oxidation pathways were further explored by LC-MS/MS analyses. Among the three temperatures followed in this experiment, 50 °C was the most informative temperature since the differences at 35 °C were only observable after long incubation times and both states (oxidized and reduced) were highly perturbed at a higher temperature of 65 °C (Figures 2 and S5). Two types of changes in the Asc-reduced LPMO structure could be observed at 50 °C (Figures 2 and S6). At short incubation times, we observed a low deuteration of peptides covering the histidine brace motif and of some of the loops surrounding the active site (Figure S7). This change in structure could be responsible for the increased affinity of the reduced LPMO to the polysaccharide substrate [21]. Similar loops were also found to be responsible for substrate binding of a bacterial LPMO [20] and could correspond to structural changes observed in *Nc*LPMO9C using circular dichroism [21]. A second important observation was an extensive increase in deuteration of reduced *Nc*LPMO9C at longer incubation times. Deuteration started on peptides bearing the histidine brace residues and propagated to the rest of the molecule during the incubation time. At a temperature of 50 °C, even the innermost parts of the protein were highly deuterated after 30 min, clearly showing enzyme unfolding and probably partial protein degradation. Therefore, we concluded that the optimal conditions to follow the Asc-induced reduction and LPMO substrate binding are best represented by 50 °C and shorter incubation/deuteration times, likely not exceeding 1 hr.

Based on these findings, we set up the final experiment in which the protein was followed in its oxidized and reduced state either in solution or bound to a substrate. Finer sampling clearly supported the conclusions of the previous experiment, which showed that Asc reduction (Figures 4A, S9A and S10) caused a lower deuteration at shorter incubation times, transitioning towards increased deuteration at longer incubation times. Finally, we observed signal loss events in amino acids localized mostly around the histidine brace. Inclusion of microcrystalline cellulose as a substrate showed no deuteration effects under oxidizing conditions, which agrees well with the previous findings [21]. However, when the cellulose was added to the reduced LPMO, a protective effect was detected via slower deuteration. As can be seen in Figures 3C, S9A and S10, the substrate failed to stop the destructive pathways at some point (time > 35min), and the oxidation-driven LPMO damage overrode the protective abilities of the cellulose. This can likely be attributed to the weaker binding of *Nc*LPMO9C to crystalline cellulose when compared to amorphous substrates, such as PASC [21]. However, it should be noted that our initial trials with PASC provided poorly reproducible results (data not shown) and, thus, we switched to crystalline cellulose. Interestingly, we failed to observe any further decrease in deuteration induced by substrate binding. This can be

again attributed to the weaker binding of the LPMO to microcrystalline cellulose. However, another and more likely reason might be the inability of the H/D exchange approach to capture these interactions since they are side chain mediated, and the HDX targets back-bone amides only [51,52]. The same reasoning could explain the negligible effect of crystalline cellulose on CBM. It is known from the literature that CBM binding to cellulose surface is mediated via side chains of aromatic residues [53,54]. Since the overall fold of CBM is highly compact, it is not likely that side-chain mediated cellulose-binding may induce significant changes in CBM hydrogen bonding or solvent protection detectable by HDX-MS. Hence, while we repeatedly detected Asc-independent protection of the CBM in the presence of cellulose, the effect was at the level of insignificance. Nevertheless, our experiments clearly demonstrate that the substrate protects the enzyme from degradation and that this protective effect correlates well with the mechanism through which the enzyme is structurally perturbed in its free, Asc-reduced form (compare Figure S9A,B). This protection can be due to either scavenging of the reactive species, LPMO reoxidation, or active-site protection due to substrate binding.

An additional effect we observed throughout the experiments with Asc-reduced LPMO was a time-dependent decrease in signal intensity for peptides around the active site or nearby loops. Loss of peptide signal intensity can result from the modification of some of its amino acids, leading to mass shifts and, thus, to the vanishing of the peptide from HDX-MS analysis. Such effects were used as an indirect measure of oxidative peptide modification by Loose at al. [34]. In addition to the signal intensity loss, we here attempted to identify increases in signal intensity of oxidatively modified peptides. This approach was largely unsuccessful with the reported example (Figure S11) being the only unambiguous one. It should be stressed that looking for oxidatively modified peptides in HDX-MS data is not ideal for several reasons. First, the nonspecific proteases (here a combination of nepenthesin I and rhizopuspepsin) create many overlapping peptides that cause signal intensity splitting. Second, oxidative modifications are often heterogeneous and create a variety of subsequent reaction products adding variations to the multiple peptides covering each region. Finally, the signal intensity is further decreased due to deuteration, which usually widens the isotopic structure of the peptide ions. These combined effects make all but the most common peptide forms undetectable. We, therefore, used a separate LC-MS/MS analysis step to obtain detailed information about protein modifications occurring in Asc-treated LPMO digested by either trypsin or Asp-N. This approach also helped to verify that the introduced oxidative modifications caused the observed decrease in signal intensity. However, in contrast to results obtained with *Sc*LPMO10C by Bissaro et al., we were not able to get a comprehensive list of all modifications, since *Nc*LPMO9C was not amenable by any typical proteomic-based proteolysis approach [24]. Even the use of two different proteases (trypsin and Asp-N) failed to provide fragments of reasonable size covering the entire protein sequence or at least the catalytic unit. Instead of relying on a pure search engine scoring, we performed manual validation of the MS/MS assignments and listed only those modifications where the exact oxidation position could be deciphered. This may also lead to a shortening of the list of modified residues. However, even with a less comprehensive listing, we provide clear proof that the *Nc*LPMO9C is extensively oxidized on many sites (Table S1). Besides the oxidations and the known subsequent products of the oxidation pathways, we also found prominent oxidation leading to peptide bond cleavages. These were mainly located on amino acids close to the active site (Table S1). These peptide cleavages have been identified before in other proteins [32,33], but are not very well-known and have not been connected to LPMO oxidative damage so far. Using extracted ion chromatograms from our LC-MS/MS data, we also followed the abundance of oxidatively modified peptides during incubation of LPMO with ascorbic acid (Figures 5 and S12). These data show a clear increase in the level of protein oxidation over time, resulting also in peptide bond cleavages, as illustrated by peptide H1-A12 in Figure 5. In addition, there is a clear dependency between the level of oxidation at particular sites and their proximity to the active site. We highlight this in Figure S12, where side chains containing amino acids prone to oxidation are shown as sticks. Considering their surface accessibility and the rate of oxidation, which can be inferred from the extracted ion chromatograms, it is clear that the driving factor affecting the extent of oxidation in Asc-reduced LPMO is the proximity to the active

center, specifically the involvement in copper ion binding (compare peptides. 94–109 and 22–45 versus 58–84).

5. Conclusions

Our results describe the degradation of LPMO in structural detail and confirm that the increase in stability of LPMO caused by the presence of substrate is based on the decrease in oxidative damage incurred to the enzyme over time. The developed methodological setup marks the way towards more systematic structural studies, in which the stabilizing or destabilizing effects of larger sets of substrates, reductants, and cosubstrates can be effectively probed. Such studies may help to guide the rational design of cellulose-active enzymes leading to more efficient substrate binding to increase the lifetime of enzymes used in industrial settings.

Supplementary Materials: The following are available online at www.mdpi.com/xxx/s1. Figure S1: Peptide map showing the sequence coverage of *Nc*LPMO9C after serial nepenthesin-1 / rhizopuspepsin digestion, Figure S2: *Nc*LPMO9C structural changes induced by the temperature, Figure S3: Selected examples of deuterium uptake curves for holo-/apo- *Nc*LPMO9C after temperature correction, Figure S4: Destabilization of the *Nc*LPMO9C by active site copper removal as observed by HDX-MS comparison of holo- and apoenzymes, Figure S5: *Nc*LPMO9C structural changes induced by reduction with ascorbic acid at different temperatures, Figure S6: Ascorbic acid reduction causes a range of effects in HDX kinetics and a signal loss, Figure S7: The effect of ascorbic acid-mediated copper ion reduction mapped on the structure of *Nc*LPMO9C, Figure S8: The effects of the reduction of *Nc*LPMO9C by Asc and cellulose-binding in the oxidized and Asc-reduced states, Figure S9: The effects of *Nc*LPMO9C ascorbic acid reduction and cellulose-binding of the Asc-reduced LPMO visualized on the protein structure, Figure S10: Detailed monitoring of ascorbic acid reduction and its effects on HDX kinetics and signal loss, Figure S11: Oxidation induced by copper ion reduction detected in the HDX dataset, Figure S12: Monitoring of the signal intensity increase of modified peptides. Table S1: Manually verified modifications and cleavages on amino acids in LPMO recorded by MS/MS.

Author Contributions: Conceptualization, P.M., D.K. (Daniel Kracher), F.F.; methodology, F.F., D.K. (Daniel Kavan), P.M.; software, D.K. (Daniel Kavan); validation, F.F., D.K. (Daniel Kavan), P.M.; formal analysis, F.F., D.K. (Daniel Kavan), P.M.; investigation, F.F., D.K. (Daniel Kavan), D.K. (Daniel Kracher), C.V.F.P.L., P.M.; resources, D.K. (Daniel Kavan), D.K. (Daniel Kracher), C.V.F.P.L.; data curation, F.F., D.K. (Daniel Kavan), P.M.; writing—original draft preparation, F.F. and P.M.; writing—review and editing, F.F., D.K. (Daniel Kavan), D.K. (Daniel Kracher), C.V.F.P.L., R.L., P.H., P.M.; visualization, F.F., D.K. (Daniel Kavan), P.M.; supervision, P.M., P.H., R.L.; project administration, P.H., R.L.; funding acquisition, P.H., R.L., D.K. (Daniel Kracher). All authors have read and agreed to the published version of the manuscript.

Funding: Financial support from CSF (16-34818L) and the Austrian Science Fund (projects I 2385-N28, W1224 and J-4154) is gratefully acknowledged. Access to MS facilities was enabled through EU/MEYS support—CZ.1.05/1.1.00/02.0109; LQ1604 and LM2015043 CIISB. F.F. also acknowledges SVV260427/2019.

Conflicts of Interest: The authors declare no conflict of interest. The funders had no role in the design of the study; in the collection, analyses, or interpretation of data; in the writing of the manuscript, or in the decision to publish the results.

References

1. Chylenski, P.; Bissaro, B.; Sørlie, M.; Røhr, A.K.; Várnai, A.; Horn, S.J.; Eijsink, V.G.H. Lytic polysaccharide monooxygenases in enzymatic processing of lignocellulosic biomass. *ACS Catal.* **2019**, *9*, 4970–4991, doi:10.1021/acscatal.9b00246.
2. Vaaje-Kolstad, G.; Westereng, B.; Horn, S.J., Liu, Z.; Zhai, H.; Sørlie, M.; Eijsink, V.G.H. An oxidative enzyme boosting the enzymatic conversion of recalcitrant polysaccharides. *Science* **2010**, *330*, 219–222, doi:10.1126/science.1192231.
3. Levasseur, A.; Drula, E.; Lombard, V.; Coutinho, P.M.; Henrissat, B. Expansion of the enzymatic repertoire of the CAZy database to integrate auxiliary redox enzymes. *Biotechnol. Biofuels* **2013**, *6*, 1–14, doi:10.1186/1754-6834-6-41.
4. Vu, V.V.; Beeson, W.T.; Span, E.A.; Farquhar, E.R.; Marletta, M.A. A family of starch-active polysaccharide monooxygenases. *Proc. Natl. Acad. Sci. USA* **2014**, *111*, 13822–13827, doi:10.1073/pnas.1408090111.

5. Couturier, M.; Ladevèze, S.; Sulzenbacher, G.; Ciano, L.; Fanuel, M.; Moreau, C.; Villares, A.; Cathala, B.; Chaspoul, F.; Frendsen, K.E.; et al. Lytic xylan oxidases from wood-decay fungi unlock biomass degradation. *Nat. Chem. Biol*. **2018**, *14*, 306–310, doi:10.1038/nchembio.2558.
6. Sabbadin, F.; Hemsworth, G.R.; Ciano, L.; Henrissat, B.; Dupree, P.; Tryfona, T.; Marques, R.D.S.; Sweeney, S.T.; Besser, K.; Elias, L.; et al. An ancient family of lytic polysaccharide monooxygenases with roles in arthropod development and biomass digestion. *Nat. Commun.* **2018**, *9*, 756, doi:10.1038/s41467-018-03142-x.
7. Isaksen, T.; Westereng, B.; Aachmann, F.L.; Agger, J.W.; Kracher, D.; Kittl, R.; Ludwig, R.; Haltrich, D.; Eijsink, V.G.H.; Horn, S.J. A C4-oxidizing lytic polysaccharide monooxygenase cleaving both cellulose and cello-oligosaccharides. *J. Biol. Chem.* **2014**, *289*, 2632–2642, doi:10.1074/jbc.M113.530196.
8. Quinlan, R.J.; Sweeney, M.D.; Lo Leggio, L.; Otten, H.; Poulsen, J.N.; Johansen, K.S.; Krogh, K.B.R.M.; Jørgensen, C.I.; Tovborg, M.; Anthonsen, A.; et al. Insights into the oxidative degradation of cellulose by a copper metalloenzyme that exploits biomass components. *Proc. Natl. Acad. Sci. USA* **2011**, *108*, 15079–15084, doi:10.1073/pnas.1105776108.
9. Westereng, B.; Ishida, T.; Vaaje-Kolstad, G.; Wu, M.; Eijsink, V.G.H.; Igarashi, K.; Samejima, M.; Ståhlberg, J.; Horn, S.J.; Sandgren, M. The putative endoglucanase PcGH61D from *Phanerochaete chrysosporium* is a metal-dependent oxidative enzyme that cleaves cellulose. *PLoS ONE* **2011**, *6*, e27807, doi:10.1371/journal.pone.0027807.
10. Tan, T.; Kracher, D.; Gandini, R.; Sygmund, C.; Kittl, R.; Haltrich, D.; Hällberg, B.M.; Ludwig, R.; Divne, C. Structural basis for cellobiose dehydrogenase action during oxidative cellulose degradation. *Nat. Commun.* **2015**, *6*, 7542, doi:10.1038/ncomms8542.
11. Harris, P.V.; Welner, D.; McFarland, K.C.; Re, E.; Poulsen, J.N.; Brown, K.; Salbo, R.; Ding, H.; Vlasenko, E.; Merino, S.; et al. Stimulation of lignocellulosic biomass hydrolysis by proteins of glycoside hydrolase family 61: Structure and function of a large, enigmatic family. *Biochemistry* **2010**, *49*, 3305–3316, doi:10.1021/bi100009p.
12. Danneels, B.; Tanghe, M.; Joosten, H.; Gundinger, T.; Spadiut, O.; Stals, I.; Desmet, T. A quantitative indicator diagram for lytic polysaccharide monooxygenases reveals the role of aromatic surface residues in *Hj*LPMO9A regioselectivity. *PLoS ONE* **2017**, *12*, e0178446, doi:10.1371/journal.pone.0178446.
13. Frandsen, K.E.H.; Poulsen, J.N.; Tandrup, T.; Lo Leggio, L. Unliganded and substrate bound structures of the cellooligosaccharide active lytic polysaccharide monooxygenase Ls AA9A at low pH. *Carbohydr. Res*. **2017**, *448*, 187–190, doi:10.1016/j.carres.2017.03.010.
14. Li, X.; Beeson, W.T.; Phillips, C.M.; Marletta, M.A.; Cate, J.H.D. Structural basis for substrate targeting and catalysis by fungal polysaccharide monooxygenases. *Structure* **2012**, *20*, 1051–1061, doi:10.1016/j.str.2012.04.002.
15. Kracher, D.; Scheiblbrandner, S.; Felice, A.K.; Breslmayr, E.; Preims, M.; Ludwicka, K.; Haltrich, D.; Eijsink, V.G.; Ludwig, R. Extracellular electron transfer systems fuel cellulose oxidative degradation. *Science* **2016**, *352*, 1098–1101, doi:10.1126/science.aaf3165.
16. Frommhagen, M.; Mutte, S.K.; Westphal, A.H.; Koetsier, M.J.; Hinz, S.W.A.; Visser, J.; Vincken, J.P.; Weijers, D., van Berkel, W.J.H.; Gruppen, H.; et al. Boosting LPMO-driven lignocellulose degradation by polyphenol oxidase-activated lignin building blocks. *Biotechnol. Biofuels* **2017**, *10*, 121, doi:10.1186/s13068-017-0810-4.
17. Loose, J.S.; Forsberg, Z.; Kracher, D.; Scheiblbrandner, S.; Ludwig, R.; Eijsink, V.G.; Vaaje-Kolstad, G. Activation of bacterial lytic polysaccharide monooxygenases with cellobiose dehydrogenase. *Protein Sci.* **2016**, *25*, 2175–2186, doi:10.1002/pro.3043.
18. Phillips, C.M.; Beeson, W.T.; Cate, J.H.; Marletta, M.A. Cellobiose dehydrogenase and a copper-dependent polysaccharide monooxygenase potentiate cellulose degradation by *Neurospora crassa*. *ACS Chem. Biol.* **2011**, *6*, 1399–1406, doi:10.1021/cb200351y.
19. Courtade, G.; Wimmer, R.; Røhr, Å.K.; Preims, M.; Felice, A.K.; Dimarogona, M.; Vaaje-Kolstad, G.; Sørlie, M.; Sandgren, M.; Ludwig, R.; Eijsink, V.G.; et al. Interactions of a fungal lytic polysaccharide monooxygenase with β-glucan substrates and cellobiose dehydrogenase. *Proc. Natl. Acad. Sci. USA* **2016**, *113*, 5922–5927, doi:10.1073/pnas.1602566113.
20. Aachmann, F.L.; Sorlie, M.; Skjak-Braek, G.; Eijsink, V.G.H.; Vaaje-Kolstad, G. NMR structure of a lytic polysaccharide monooxygenase provides insight into copper binding, protein dynamics, and substrate interactions. *Proc. Natl. Acad. Sci. USA* **2012**, *109*, 18779–18784, doi:10.1073/pnas.1208822109.

21. Kracher, D.; Andlar, M.; Furtmüller, P.G.; Ludwig, R. Active-site copper reduction promotes substrate binding of fungal lytic polysaccharide monooxygenase and reduces stability. *J. Biol. Chem.* **2018**, *293*, 1676–1687, doi:10.1074/jbc.RA117.000109.
22. Hangasky, J.A.; Marletta, M.A. A random-sequential kinetic mechanism for polysaccharide monooxygenases. *Biochemistry* **2018**, *57*, 3191–3199, doi:10.1021/acs.biochem.8b00129.
23. Beeson, W.T.; Phillips, C.M.; Cate, J.H.D.; Marletta, M.A. Oxidative cleavage of cellulose by fungal copper-dependent polysaccharide monooxygenases. *J. Am. Chem. Soc.* **2012**, *134*, 890–892, doi:10.1021/ja210657t.
24. Bissaro, B.; Røhr, Å.K.; Müller, G.; Chylenski, P.; Skaugen, M.; Forsberg, Z.; Horn, S.J.; Vaaje-Kolstad, G.; Eijsink, V.G.H. Oxidative cleavage of polysaccharides by monocopper enzymes depends on H_2O_2. *Nat. Chem. Biol.* **2017**, *13*, 1123–1128, doi:10.1038/nchembio.2470.
25. Bissaro, B.; Streit, B.; Isaksen, I.; Eijsink, V.G.H.; Beckham, G.T.; DuBois, J.L.; Røhr, Å.K. Molecular mechanism of the chitinolytic peroxygenase reaction. *Proc. Natl. Acad. Sci. USA* **2020**, *117*, 1504–1513, doi:10.1073/pnas.1904889117.
26. Kim, S.; Stahlberg, J.; Sandgren, M.; Paton, R.S.; Beckham, G.T. Quantum mechanical calculations suggest that lytic polysaccharide monooxygenases use a copper-oxyl, oxygen-rebound mechanism. *Proc. Natl. Acad. Sci. USA* **2014**, *111*, 149–154, doi:10.1073/pnas.1316609111.
27. Bennati-Granier, C.; Garajova, S.; Champion, C.; Grisel, S.; Haon, M.; Zhou, S.; Fanuel, M.; Ropartz, D.; Rogniaux, H.; Gimbert, I.; et al. Substrate specificity and regioselectivity of fungal AA9 lytic polysaccharide monooxygenases secreted by *Podospora anserina*. *Biotechnol. Biofuels* **2015**, *8*, 90, doi:10.1186/s13068-015-0274-3.
28. Walton, P.H.; Davies, G.J. On the catalytic mechanisms of lytic polysaccharide monooxygenases. *Curr. Opin. Chem. Biol.* **2016**, *31*, 195–207, doi:10.1016/j.cbpa.2016.04.001.
29. Kuusk, S.; Bissaro, B.; Kuusk, P.; Forsberg, Z.; Eijsink, V.G.H.; Sørlie, M.; Väljamäe, P. Kinetics of H_2O_2 -driven degradation of chitin by a bacterial lytic polysaccharide monooxygenase. *J. Biol. Chem.* **2018**, *293*, 523–531, doi:10.1074/jbc.M117.817593.
30. Hangasky, J.A.; Iavarone, A.T.; Marletta, M.A. Reactivity of O_2 versus H_2O_2 with polysaccharide monooxygenases. *Proc. Natl. Acad. Sci. USA* **2018**, *115*, 4915–4920, doi:10.1073/pnas.1801153115.
31. Müller, G.; Chylenski, P.; Bissaro, B.; Eijsink, V.G.H.; Horn, S.J. The impact of hydrogen peroxide supply on LPMO activity and overall saccharification efficiency of a commercial cellulase cocktail. *Biotechnol. Biofuels* **2018**, *11*, 209, doi:10.1186/s13068-018-1199-4.
32. Loose, J.S.M.; Arntzen, M.Ø.; Bissaro, B.; Ludwig, R.; Eijsink, V.G.H.; Vaaje-Kolstad, G. Multipoint precision binding of substrate protects lytic polysaccharide monooxygenases from self-destructive off-pathway processes. *Biochemistry* **2018**, *57*, 4114–4124, doi:10.1021/acs.biochem.8b00484.
33. Scarpa, M.; Stevanato, R.; Viglino, P., Rigo, A. Superoxide ion as active intermediate in the autoxidation of ascorbate by molecular oxygen. Effect of superoxide dismutase. *J. Biol. Chem*. **1983**, *258*, 6695–6697.
34. Bissaro, B.; Várnai, A.; Røhr, Å.K.; Eijsink, V.G.H. Oxidoreductases and reactive oxygen species in conversion of lignocellulosic biomass. Microbiol. *Mol. Biol. Rev.* **2018**, *82*, e00029-18, doi:10.1128/MMBR.00029-18.
35. Kittl, R.; Kracher, D.; Burgstaller, D.; Haltrich, D.; Ludwig, R. Production of four *Neurospora crassa* lytic polysaccharide monooxygenases in *Pichia pastoris* monitored by a fluorimetric assay. *Biotechnol. Biofuels* **2012**, *5*, 79, doi:10.1186/1754-6834-5-79.
36. Span, E.A.; Suess, D.L.M.; Deller, M.C.; Britt, R.D.; Marletta, M.A. The role of the secondary coordination sphere in a fungal polysaccharide monooxygenase. *ACS Chem. Biol.* **2017**, *12*, 1095–1103, doi:10.1021/acschembio.7b00016.
37. Gregory, R.C.; Hemsworth, G.R.; Turkenburg, J.P.; Hart, S.J.; Walton, P.H.; Davies, G.J. Activity, stability and 3-D structure of the Cu^{II} form of a chitin-active lytic polysaccharide monooxygenase from *Bacillus amyloliquefaciens*. *Dalt. Trans*. **2016**, *45*, 16904–16912, doi:10.1039/c6dt02793h.
38. Sugimoto, H.; Nakajima, Y.; Motoyama, A.; Katagiri, E.; Watanabe, T.; Suzuki, K. Unfolding of CBP21, a lytic polysaccharide monooxygenase, without dissociation of its copper ion cofactor. *Biopolymers* **2019**, *111*, e23339, doi:10.1002/bip.23339.
39. Kadek, A.; Mrazek, H.; Halada, P.; Rey, M.; Schriemer, D.C.; Man, P. Aspartic protease nepenthesin-1 as a tool for digestion in hydrogen/deuterium exchange mass spectrometry. *Anal. Chem.* **2014**, *86*, 4287–4294, doi:10.1021/ac404076j.

40. Rey, M.; Man, P.; Brandolin, G.; Forest, E.; Pelosi, L. Recombinant immobilized rhizopuspepsin as a new tool for protein digestion in hydrogen/deuterium exchange mass spectrometry. *Rapid Commun. Mass Spectrom.* **2009**, *23*, 3431–3438, doi:10.1002/rcm.4260.
41. Hsieh, E.J.; Hoopmann, M.R.; MacLean, B.; MacCoss, M.J. Comparison of database search strategies for high precursor mass accuracy MS/MS data. *J. Proteome Res.* **2010**, *9*, 1138–1143, doi:10.1021/pr900816a.
42. Trcka, F.; Durech, M.; Vankova, P.; Chmelik, J.; Martinkova, V.; Hausner, J.; Kadek, A.; Marcoux, J.; Klumpler, T.; Vojtesek, B.; et al. Human Stress-inducible Hsp70 Has a High Propensity to Form ATP-dependent Antiparallel Dimers That Are Differentially Regulated by Cochaperone Binding. *Mol. Cell. Proteomics* **2019**, *18*, 320–337, doi:10.1074/mcp.RA118.001044.
43. Kavan, D.; Man, P. MSTools—Web based application for visualization and presentation of HXMS data. *Int. J. Mass Spectrom.* **2011**, *302*, 53–58, doi:10.1016/j.ijms.2010.07.030.
44. Borisova, A.S.; Isaksen, T.; Dimarogona, M.; Kognole, A.A.; Mathiesen, G.; Várnai, A.; Røhr, Å.K.; Payne, C.M.; Sørlie, M.; Sandgren, M.; Eijsink, V.G. Structural and functional characterization of a lytic lolysaccharide monooxygenase with broad substrate specificity. *J. Biol. Chem.* **2015**, *290*, 22955–22969, doi:10.1074/jbc.M115.660183.
45. Singh, K.R.; Blossom, B.M.; Russo, D.A.; van Oort, B.; Croce, R.; Jensen, P.E.; Felbyb, C.; Bjerrum, M.J. Thermal unfolding and refolding of a lytic polysaccharide monooxygenase from *Thermoascus aurantiacus*. *RSC Adv.* **2019**, *9*, 29734–29742, doi:10.1039/C9RA05920B.
46. Yang, M.; Hoeppner, M.; Rey, M.; Kadek, A.; Man, P.; Schriemer, D.C. Recombinant nepenthesin II for hydrogen/deuterium exchange mass spectrometry. *Anal. Chem.* **2015**, *87*, 6681–6687, doi:10.1021/acs.analchem.5b00831.
47. Kadek, A.; Tretyachenko, V.; Mrazek, H.; Ivanova, L.; Halada, P.; Rey, M.; Schriemer, D.C.; Man, P. Expression and characterization of plant aspartic protease nepenthesin-1 from *Nepenthes gracilis*. *Protein Expr. Purif.* **2014**, *95*, 121–128, doi:10.1016/j.pep.2013.12.005.
48. Tsiatsiani, L.; Akeroyd, M.; Olsthoorn, M.; Heck, A.J.R. *Aspergillus niger* prolyl endoprotease for hydrogen–deuterium exchange mass spectrometry and protein structural studies. *Anal. Chem.* **2017**, *89*, 7966–7973, doi:10.1021/acs.analchem.7b01161.
49. Uchida, K.; Kato, Y.; Kawakishi, S. A novel mechanism for oxidative cleavage of prolyl peptides induced by the hydroxyl radical. *Biochem. Biophys. Res. Commun.* **1990**, *169*, 265–271, doi:10.1016/0006-291x (90)91463-3.
50. Garrison, W.M. Reaction mechanisms in the radiolysis of peptides, polypeptides, and proteins. *Chem. Rev.* **1987**, *87*, 381–398, doi:10.1021/cr00078a006.
51. Frandsen, K.E.; Simmons, T.J.; Dupree, P.; Poulsen, J.C.; Hemsworth, G.R.; Ciano, L.; Johnston, E.M.; Tovborg, M.; Johansen, K.S.; von Freiesleben, P.; et al. The molecular basis of polysaccharide cleavage by lytic polysaccharide monooxygenases. *Nat. Chem. Biol.* **2016**, *12*, 298–303, doi:10.1038/nchembio.2029.
52. Vaaje-Kolstad, G.; Forsberg, Z.; Loose, J.S.; Bissaro, B.; Eijsink, V.G. Structural diversity of lytic polysaccharide monooxygenases. *Curr. Opin. Struct. Biol.* **2017**, *44*, 67–76, doi:10.1016/j.sbi.2016.12.012.
53. Beckham, G.T.; Matthews, J.F.; Bomble, Y.J.; Bu, L.; Adney, W.S.; Himmel, M.E.; Nimlos, M.R., Crowley, M.F. Identification of amino acids responsible for processivity in a Family 1 carbohydrate-binding module from a fungal cellulase. *J. Phys. Chem. B* **2010**, *114*, 1447–1453, doi:10.1021/jp908810a.
54. Griffo, A.; Rooijakkers, B.J.M.; Hähl, H.; Jacobs, K.; Linder, M.B.; Laaksonen, P. Binding Forces of Cellulose Binding Modules on Cellulosic Nanomaterials. *Biomacromolecules* **2019**, *20*, 769–777, doi:10.1021/acs.biomac.8b01346.

© 2020 by the authors. Licensee MDPI, Basel, Switzerland. This article is an open access article distributed under the terms and conditions of the Creative Commons Attribution (CC BY) license (http://creativecommons.org/licenses/by/4.0/).

ARTICLE II

Filandr, F., Man, P., Halada, P., Chang, H., Ludwig, R. & Kracher, D.

The H_2O_2-dependent activity of a fungal lytic polysaccharide monooxygenase investigated with a turbidimetric assay.

Biotechnol. Biofuels **13**, 37 (2020)

My contribution: *performing experiments (turbidimetric measurements of LPMO activity, MALDI-MS analysis of product oligosaccharides), data analysis & interpretation, figure design*

Biotechnology for Biofuels

RESEARCH Open Access

The H_2O_2-dependent activity of a fungal lytic polysaccharide monooxygenase investigated with a turbidimetric assay

Frantisek Filandr[1,2,3], Petr Man[1], Petr Halada[1], Hucheng Chang[3], Roland Ludwig[3] and Daniel Kracher[3,4*]

Abstract

Background: Lytic polysaccharide monooxygenases (LPMOs) are copper-dependent redox enzymes that cleave recalcitrant biopolymers such as cellulose, chitin, starch and hemicelluloses. Although LPMOs receive ample interest in industry and academia, their reaction mechanism is not yet fully understood. Recent studies showed that H_2O_2 is a more efficient cosubstrate for the enzyme than O_2, which could greatly affect the utilization of LPMOs in industrial settings.

Results: We probe the reactivity of LPMO9C from the cellulose-degrading fungus *Neurospora crassa* with a turbidimetric assay using phosphoric acid-swollen cellulose (PASC) as substrate and H_2O_2 as a cosubstrate. The measurements were also followed by continuous electrochemical H_2O_2 detection and LPMO reaction products were analysed by mass spectrometry. Different systems for the in situ generation of H_2O_2 and for the reduction of LPMO's active-site copper were employed, including glucose oxidase, cellobiose dehydrogenase, and the routinely used reductant ascorbate.

Conclusions: We found for all systems that the supply of H_2O_2 limited LPMO's cellulose depolymerization activity, which supports the function of H_2O_2 as the relevant cosubstrate. The turbidimetric assay allowed rapid determination of LPMO activity on a cellulosic substrate without the need for time-consuming and instrumentally elaborate analysis methods.

Keywords: Lytic polysaccharide monooxygenase, Cellobiose dehydrogenase, Glucose oxidase, Hydrogen peroxide, Cellulose, *Neurospora crassa*

Background

LPMOs (CAZy AA9–11, 13–16) are copper-dependent redox enzymes that employ a redox reaction to cleave and decrystallize recalcitrant biopolymers [1, 2]. LPMO activity has been demonstrated in biomass-degrading bacteria [3], fungi [4] and, as of recently, also in firebrat (*Thermobia domestica*) [5], insect poxvirus [6] and the fern *Tectaria macrodonta* [7]. The substrate scope of LPMOs includes cellulose [8], in some cases soluble cello-oligosaccharides [9], chitin [3], starch [10] and various hemicelluloses [9, 11–13].

Since their discovery in 2010 [3], LPMOs have received ample attention in basic and applied research due to their synergistic interaction with hydrolytic enzymes [14, 15]. However, the insoluble nature of their substrates complicates the use of routine biochemical analysis methods, which typically require homogenous conditions. Furthermore, LPMOs depend on a steady supply of electrons and a cosubstrate while generating a complex array of oxidation products that necessitate specialized equipment for

*Correspondence: danielkracher@boku.ac.at
[3] Biocatalysis and Biosensing Research Group, Department of Food Science and Technology, BOKU-University of Natural Resources and Life Sciences, Muthgasse 18, 1190 Vienna, Austria
Full list of author information is available at the end of the article

© The Author(s) 2020. This article is licensed under a Creative Commons Attribution 4.0 International License, which permits use, sharing, adaptation, distribution and reproduction in any medium or format, as long as you give appropriate credit to the original author(s) and the source, provide a link to the Creative Commons licence, and indicate if changes were made. The images or other third party material in this article are included in the article's Creative Commons licence, unless indicated otherwise in a credit line to the material. If material is not included in the article's Creative Commons licence and your intended use is not permitted by statutory regulation or exceeds the permitted use, you will need to obtain permission directly from the copyright holder. To view a copy of this licence, visit http://creativecommons.org/licenses/by/4.0/. The Creative Commons Public Domain Dedication waiver (http://creativecommons.org/publicdomain/zero/1.0/) applies to the data made available in this article, unless otherwise stated in a credit line to the data.

analysis. As a result, key questions on the LPMO catalytic cycle and kinetics, including the cosubstrate preference, await experimental clarification [16].

Despite their widespread distribution and their diverse substrate specificities, all known LPMOs share a highly conserved active site which includes a dyad of histidines coordinating a single Cu(II) atom [4, 17]. LPMO requires an external electron donor and an oxygen-containing cosubstrate for catalysis [16]. In fungi, electron-donating systems for LPMOs include a variety of phenols released during lignocellulose degradation [18, 19]. The fungal flavocytochrome cellobiose dehydrogenase (CDH) directly reduces the copper centre of LPMOs [20, 21]. Synergies with other fungal redox enzymes such as polyphenol oxidases [22], laccases [23] or oxidoreductases of the GMC-oxidoreductase family [24] were previously shown to provide a range of potential electron-donating systems for LPMOs through the release or recycling of phenolic lignin breakdown products. Potential electron-donating systems in other organisms, e.g. in bacteria or insects, await identification.

Reduced LPMOs are reported to utilize either O_2 [3, 25] or H_2O_2 [26] as a cosubstrate, resulting in a monooxygenase or peroxygenase reaction, respectively. The outcome of both reactions is the regioselective insertion of an oxygen atom at the C1 [4] or C4 [9] carbon of the glycosidic linkage, which destabilizes and breaks the bond [17, 27]. Recent kinetic studies of bacterial [26, 28] and fungal LPMOs [29] showed that turnover numbers with H_2O_2 as cosubstrate exceeded those obtained with O_2 by two orders of magnitude. A drawback of the peroxygenase reaction is the susceptibility of LPMOs for oxidative damage in the absence of substrate, or at high H_2O_2 concentrations [26, 30]. It was argued that the lower turnover with O_2 could protect LPMO from such oxidation reactions and thus extend the operational stability to longer time-scales [29]. Despite several studies [4, 25, 26, 28, 29], it is still disputed whether O_2 or H_2O_2 is preferred as cosubstrate in a natural environment. Here, it is worth noting that a number of GMC-oxidoreductases secreted by fungi also provide a steady H_2O_2 supply required for peroxidases involved in biomass degradation [31]. This includes CDH, which was shown to possess a weak oxidase activity [32] that can provide sufficient amounts of H_2O_2 for LPMO catalysis [33].

Typically, activity measurements for LPMOs rely on the identification of soluble, oxidized oligosaccharides, which are liberated by the LPMO [34]. Such studies are complicated by the array of possible oxidation products and the lack of suitable standards (e.g. C4-oxidized oligosaccharides). If C4-oxidizing LPMOs are used in combination with CDH, also doubly oxidized products occur, since CDH efficiently oxidizes the reducing end of soluble oligosaccharides [9]. Such analyses also miss the introduced carboxylic groups, resulting in aldonic acids in the insoluble fraction of the substrate, which make up a considerable fraction of the total reaction products (see e.g. [33]). Kuusk et al. [28] previously reported a detailed kinetic analysis of the chitin-active, bacterial LPMO CBP21 using ^{14}C-labelled chitin. This procedure allowed for the sensitive detection of reaction products independent of their oxidation. A recently introduced activity assay for LPMOs is based on the colourimetric detection of a pyrocatechol violet–Ni^{2+} complex, which enabled quantifying the number of aldonic acids on the substrate generated by LPMO [35]. A drawback of this procedure is the inability to detect the activity of C4-oxidizing LPMOs, which do not introduce aldonic acids into the substrate. In homogenous solution, LPMO activity can be readily detected based on the quantification of H_2O_2 released in a futile side reaction that occurs in the absence of substrate [9, 36]. LPMOs also oxidize 2,6-dimethoxyphenol in the presence of peroxide and reducing equivalents, which results in the formation of the dimerization product coerulignone that can be quantified spectroscopically [37]. While these homogeneous assays may be used as a proxy for LPMO activity, they do not allow analysing reaction kinetics with native, heterogeneous LPMO substrates. To date, there is still the need for universal and easy-to-apply methods that enable measuring the time-dependent LPMO activity without specialized equipment.

Here, we employ a turbidimetric assay using a cellulose solution to examine the peroxygenase activity of the fungal, C4-oxidizing LPMO9C from the model fungus *Neurospora crassa.*

Results

LPMO activity monitored by a turbidimetric assay

Turbidimetry has been recently employed to screen the cellulolytic activity of a fungal LPMO towards phosphoric acid-swollen cellulose (PASC), which represents a disordered, amorphous form of cellulose. This screening assay measured the decrease in the optical density of the substrate after a defined incubation time of 360 min at 50 °C in microwell plates [38]. Here, we adapt this procedure into a continuous, turbidimetric assay to measure the time-dependent conversion of PASC by a cellulose-active LPMO.

Initially, we established the relation between PASC concentration and the loss of transmitted light intensity. The optical attenuation was linear up to a concentration of 1.4 mg mL^{-1} PASC (Fig. 1a). These measurements were performed under constant stirring to prevent the settling of particles in the suspension. In the standard assay, we employed a concentration of PASC (0.8 mg mL^{-1}) that

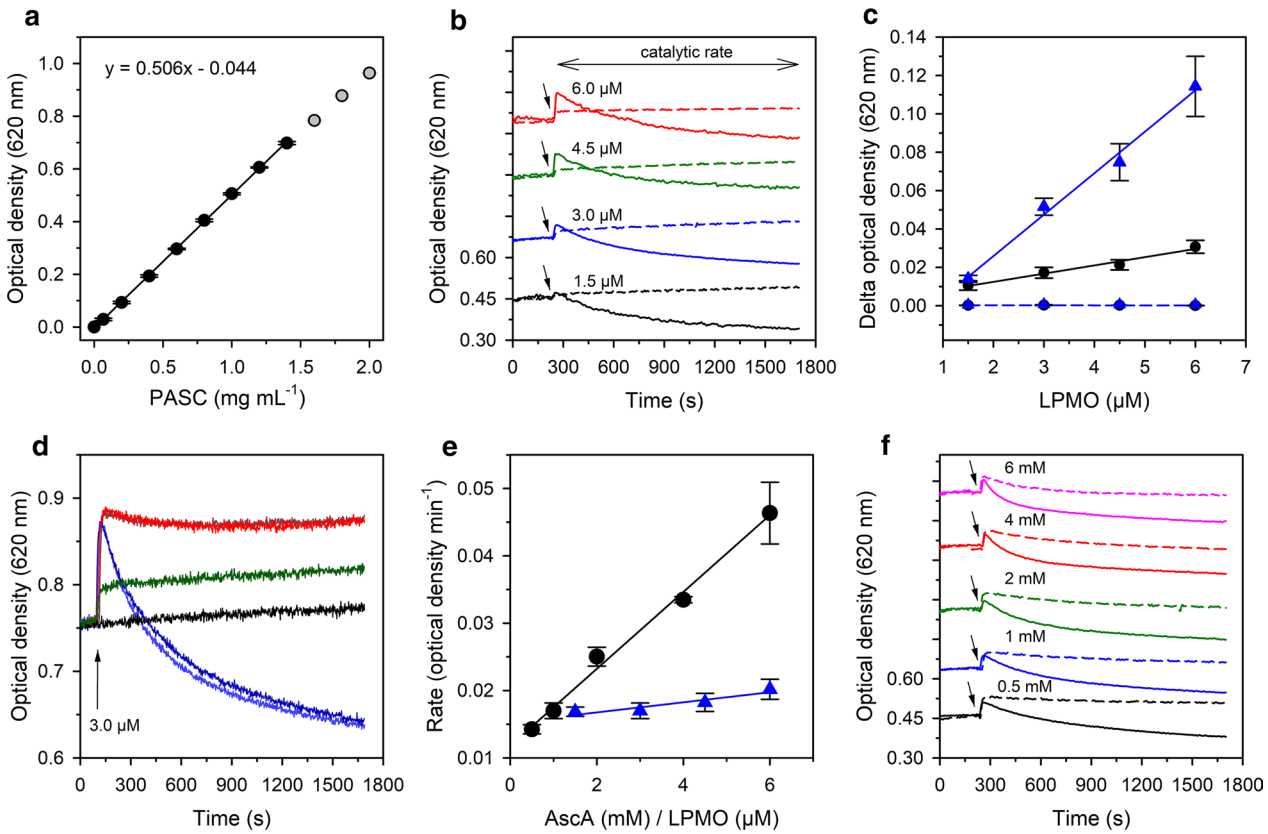

Fig. 1 Activity of LPMO with ascorbate as reductant. **a** Calibration curve showing the relation between PASC concentration and the turbidity. Assays were performed in 50 mM sodium phosphate buffer, pH 6.0, at 30 °C. The equation for the linear range (0–1.4 mg mL^{-1} PASC) is given. **b** Time-dependent turbidity changes of a 0.8 mg mL^{-1} PASC solution incubated with various LPMO concentrations in the presence (solid lines) and absence (dashed lines) of 1 mM ascorbate. LPMO concentrations are specified above the traces. LPMO and ascorbate were added simultaneously to the assay (black arrows). Traces are vertically shifted by the same increment for better visibility. The extent of the catalytic reaction is indicated by an arrow above the graphs. **c** Absorbance changes observed in **b** upon titration of LPMO to PASC in the presence (blue triangles) or absence (black circles) of ascorbate. Dashed lines indicate the addition of LPMO to a buffer solution without PASC in the presence (blue triangles) or absence (black circles) of 1 mM ascorbate. Note that the curves coincide because no apparent changes in optical density were observed. **d** Degradation of PASC by LPMO measured in an anaerobic glove box. PASC (0.6 mg mL^{-1}) was mixed with 3 µM *Nc*LPMO9C in the absence (green curve) or presence of 2 mM ascorbate (dark and light red curves). For comparison, the experiment was performed under the same conditions (3 µM LPMO and 2 mM ascorbate) under aerobic conditions (dark and light blue curves). A control containing only PASC (0.6 mg mL^{-1}) is shown as a black curve. Note that for technical reasons a different photometer had to be used for this experiment. The equation for the linear range of the calibration curve (0–1 mg mL^{-1} PASC) was 1.16x + 0.03. The black arrow indicates the addition of LPMO and/or ascorbate. **e** Reaction rates determined from the initial slopes of the reactions shown in **b** (blue triangles) and **f** (black circles). **f** Reaction of LPMO (3 µM) with various concentrations of ascorbate (solid lines). The arrows indicate the addition of LPMO and ascorbate concentrations are specified above the traces. Identical reactions carried out in the presence of catalase (2000 U mL^{-1}) are indicated as colour-coded dashed lines

provided a stable baseline and a low background signal from the light scattering of larger substrate particles in the suspension. The molar concentration of PASC was 24.7 µM assuming an average chain length of 200 glucose units [39]. However, the particle distribution of PASC is not homogenous, which affects the depolymerization kinetics as discussed later. The reaction was started by injecting an LPMO-containing stock solution, which also contained the reducing agent. In experiments using H_2O_2 as the cosubstrate, the stock solution was added before addition of the H_2O_2. The optical density of the PASC suspension was continuously monitored at a wavelength of 620 nm, which was previously used for the turbidimetric measurement of cellulase activity [40].

Binding of LPMO to PASC

In the following experiments, we employed LPMO9C from *Neurospora crassa* (*Nc*LPMO9C; UniProt accession number Q7SHI8), which is active on cellulose, hemicelluloses and soluble oligosaccharides [9, 11, 41].

This LPMO contains a family 1 carbohydrate-binding module (CBM1) which is fused to the catalytic domain via a lengthy linker peptide of 82 amino acids. In the first set of experiments, we employed 1 mM ascorbate, which is a commonly used concentration in LPMO conversion assays. The assay was started after 240 s by the addition of a relatively high concentration of LPMO (3 µM) to achieve a fast assay. Unexpectedly, this led to an instant increase in optical density within the mixing time (Fig. 1b). For both the reduced and the oxidized *Nc*LPMO9C, the optical density increased linearly with the enzyme concentration, but the observed increase was approximately three times higher for the reduced LPMO (Fig. 1c). The same increase in optical density was also observed when mixing ascorbate and LPMO under anaerobic conditions, demonstrating that this phase represents a non-catalytic reaction (Fig. 1d). Control experiments in the absence of PASC did not show detectable absorbance changes for all employed LPMO concentrations.

The fact that the reduced LPMO showed a higher increase in optical density than its oxidized form under both aerobic and anaerobic conditions suggests that the rapid initial increase in optical density is due to improved substrate binding. Previous binding experiments demonstrated a higher substrate affinity of *Nc*LPMO9C to PASC when the active site was in the reduced state [42]. In this study, the presence of ascorbate increased both the binding affinity and the binding capacity to PASC approximately twice [42]. A similar observation was made for the binding of LPMO9E from *Myceliophthora thermophila* to soluble oligosaccharides [43]. The binding of different substrate chains by the catalytic domain and the CBM1 under reducing conditions may lead to a "cross-linking" of PASC fibres and may thereby increase the optical density.

Ascorbate-driven LPMO activity

Following the initial, very rapid increase in optical density, a second phase showing an attenuation of the signal was observed in assays containing LPMO and ascorbate (Fig. 1b). The decrease in optical density indicates the degradation of the PASC by the LPMO. To confirm catalysis, we mixed *Nc*LPMO9C with ascorbate in an anaerobic glove box (Fig. 1d) in the absence of any oxygen species. We observed the first phase of the reaction (binding of the LPMO to PASC), but found that the second, catalytic phase was completely suppressed. In the following, LPMO activity is expressed as the relative change in optical density per min. The rates were calculated from the linear slopes of the catalytic phase to avoid substrate depletion at the end of the experiment. An important and unexpected observation from these experiments is that almost similar reaction rates were obtained for different LPMO concentrations (Fig. 1e, blue triangles). The observed uncoupling of catalyst concentration and reaction rate—a fourfold increase of enzyme concentration correlated to a 25% increase of the activity—points towards a rate-limiting factor in the overall reaction. One reason could be the concentration of the reductant ascorbate, which was applied in a 1 mM concentration. We, therefore, varied the ascorbate concentration for 3 µM *Nc*LPMO9C (Fig. 1f). Initial rates calculated from these batch conversions demonstrated a strong correlation between activity and ascorbate concentration (Fig. 1e, black circles). A previous study that employed the bacterial *Sm*LPMO10A and chitin as the substrate showed a clear dependency of the LPMO reaction rate on the reductant concentration, with an apparent K_M for ascorbate of 2 µM [44]. However, it is also well documented that ascorbate can reduce O_2 to H_2O_2 under commonly employed reaction conditions [24, 28]. Thus, providing a higher ascorbate concentration in the assays is likely to release higher amounts of H_2O_2, which can act as a cosubstrate for LPMO. To test whether the availability of H_2O_2 was the rate-limiting factor in the measurements, we replicated the activity assays in the presence of catalase (final concentration: 2000 U mL^{-1} at pH 6) to scavenge most of the formed H_2O_2. Under these conditions, we still observed the initial increase in optical density upon addition of LPMO, indicating that substrate binding of the LPMO was not compromised by the catalase. However, the subsequent catalytic reaction was clearly, but not fully suppressed in the presence of catalase (Fig. 1f, dashed lines).

Interaction of *Nc*LPMO9C with *Nc*CDHIIA

We also initiated LPMO activity with cellobiose dehydrogenase (CDH), which is a proposed native interaction partner of LPMOs in wood-decaying fungi [20, 24]. CDHs oxidize cellobiose or soluble cello-oligosaccharides in an FAD-dependent reaction and reduce the LPMO active site via a dedicated, flexible cytochrome domain [21]. Reduced CDHs also have a low, FAD-dependent oxidase activity [45, 46], which can support LPMO activity through the slow release of H_2O_2 [33]. We used *Nc*CDHIIA (UniProt accession number Q7RXM0), the main secreted CDH in *N. crassa* [47], to activate *Nc*LPMO9C in the PASC turbidity assays (Fig. 2a). The activity of LPMO in this reaction setup was strictly dependent on the presence of cellobiose as CDH substrate (Additional file 1: Figure S1). *Nc*CDHIIA in combination with cellobiose induced moderate LPMO activity, which was dependent on the applied *Nc*CDHIIA concentration. The observed rates were approximately one order of magnitude lower than those obtained with ascorbate as

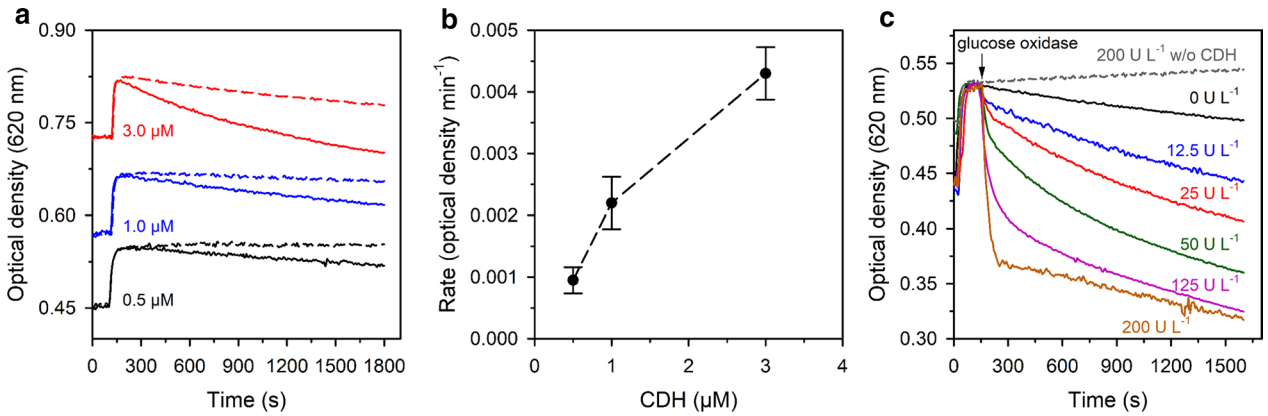

Fig. 2 LPMO activity in the presence of CDH and glucose oxidase. **a** Solid lines indicate the time-dependent absorbance changes of a 0.8 mg mL^{-1} PASC solution in presence of 3 μM LPMO and 0.5, 1.0 or 3.0 μM *Nc*CDHIIA. Reactions were carried out in 50 mM potassium phosphate buffer, pH 6.0. The same reactions were carried out in presence of 2000 U mL^{-1} catalase (colour-coded dashed lines). Traces were vertically shifted for better visibility. **b** Reaction rates of PASC degradation of the reactions shown in **a**. **c** LPMO activity in the presence of 0.5 μM *Nc*CDHIIA and various indicated activities of glucose oxidase (GOX). The volumetric activity of GOX was determined as described in the "Methods" section. All samples contained 10 mM glucose and 10 mM lactose as a substrate for GOX and CDH, respectively, and were carried out at 30 °C in 50 mM sodium phosphate buffer, pH 6.0. In control experiments, *Nc*CDHIIA (grey dashed line) or GOX (black line) were avoided

LPMO-reductant (Figs. 2b vs 1e). Catalase (2000 U mL^{-1}) completely inhibited the reaction at a low, 0.5 μM concentration of *Nc*CDHIIA, while at higher concentrations a weak LPMO activity was observed, possibly reflecting the incomplete H_2O_2 removal by the catalase. The obvious inhibition of the turbidimetric PASC assay by catalase at low CDH concentrations indicates that H_2O_2 was predominantly used as cosubstrate by *Nc*LPMO9C. Since both *Nc*LPMO9C and *Nc*CDHIIA feature a CBM1 that binds to cellulose, the spatial proximity of the two enzymes during catalysis, which is required for the electron transfer between both enzymes, may also provide a locally increased H_2O_2 concentration in the vicinity of the heterogeneous substrate.

To further probe the effect of H_2O_2 on CDH-driven LPMO activity, we used commercial glucose oxidase (GOX) from *Aspergillus niger* for the in situ generation of H_2O_2. GOX in combination with glucose and LPMO did not lead to changes in the optical density (Fig. 2c), demonstrating that an LPMO-specific reductant is required to induce activity. For LPMO reduction a low, 0.5 μM concentration of *Nc*CDHIIA in combination with 10 mM cellobiose was added. Under these conditions, the addition of GOX led to a rate enhancement that depended on the applied GOX activity and, therefore, also on the amount of produced H_2O_2. At high GOX activities, a fast, initial attenuation of the optical density was followed by a slower phase of signal decay. This indicates a rapid deactivation of *Nc*LPMO9C at high GOX concentrations, possibly due to H_2O_2-induced oxidation of the copper-coordinating amino acids [26]. Such deactivation effects were recently observed for a bacterial LPMO, which was rapidly deactivated when the H_2O_2 supply exceeded the enzyme's capability to convert the cosubstrate [33]. The pronounced rate acceleration upon addition of GOX in the presence of a low, 0.5 μM concentration of *Nc*CDHIIA indicated that not the availability of reducing equivalents, but the H_2O_2 concentration was the rate-limiting factor in these reactions.

To verify that the observed increase in activity upon H_2O_2 addition detected by turbidimetry corresponds to the formation of oxidized oligosaccharide products, MALDI-MS measurements were performed on the soluble fraction of the reaction mixtures. The formation of products was followed in reactions containing PASC, LPMO, CDH and lactose and in related reactions spiked several times with H_2O_2 during the course of the incubation (Fig. 3). C4 oxidized products, which are typical products of the *Nc*LPMO9C reaction [9], were detected in the form of sodium adducts of C4 ketones and geminal diols. Small amounts of native (unoxidized) oligosaccharides, e.g. Glc3, Glc4 and Glc5, were also present in control samples containing only PASC, CDH and lactose. Such products may also occur during the LPMO action due to a weak hydrolytic background [48]. While absolute quantitation cannot be achieved by MALDI-MS, the changes in the ratio of unoxidized and oxidized oligosaccharides between the individual conditions clearly indicated the boosting effect of H_2O_2 on the action of *Nc*LPMO9C (Fig. 3b–d).

The high resolving power and high mass accuracy of the FT-ICR MS allowed us to unambiguously assign

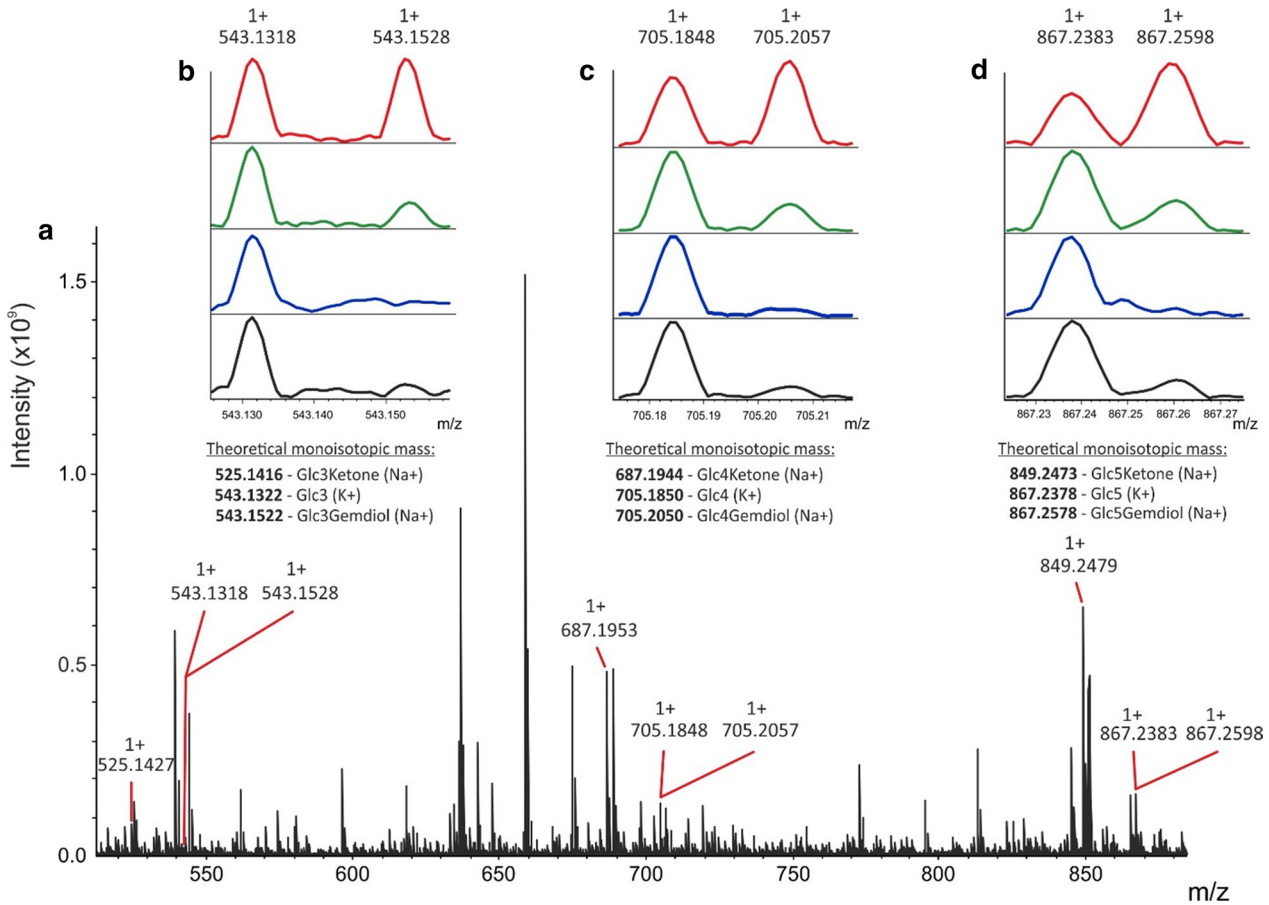

Fig. 3 MALDI-MS analysis of oxidized oligosaccharide products. Reactions containing 10 mg mL^{-1} PASC, 3 µM LPMO, 0.1 µM CDH, 1 mM lactose and H_2O_2 (120 µM final concentration added in four batches of 30 µM over 30 min) were analysed under different conditions using MALDI-MS. **a** Overview of selected parts of the MALDI-MS spectra obtained from samples containing all components (PASC, CDH, lactose, LPMO and H_2O_2) showing various oligosaccharide products. **b**–**d** Details of selected product spectra under four conditions: PASC with oxidized LPMO (black line), PASC with oxidized LPMO and H_2O_2 (blue line), PASC with CDH, lactose and LPMO (green line) and PASC with CDH, lactose, LPMO and H_2O_2 (red line). Addition of H_2O_2 led to a notable, relative increase in C4-oxidized products compared to the unoxidized forms of the analysed oligosaccharides. All oligosaccharides and their oxidized products were detected as sodium or potassium adducts. Shown are also the theoretical monoisotopic masses of all analysed reaction products. Peaks with no labels are matrix adducts or other, non-carbohydrate based, background signals

different carbohydrate molecules and their adduct state. For example, we were able to clearly distinguish between Glc(n)(K+) and Glc(n)Gemdiol(Na^+) adducts, which differ only by 0.02 Da. The mass measurements can also provide indirect proof whether the LPMO generates C1 or C4 oxidized products. C1 oxidation leads to the formation of sugar lactones, which undergo conversion into aldonic acids. The acidic products are then preferentially detected in the form of salt (sodium or potassium), charged by an additional alkali metal cation (Na^+ or K^+) [27, 34]. On the other hand, C4 oxidizing LPMOs create keto/gemdiol forms, which are not forming salts and are present only as single alkali metal cation charged masses. Since we have not detected aldonic acids in any of the reaction mixtures and only detected gemdiols, we can conclude that the *Nc*LPMO9C indeed generated C4 oxidation products.

The peroxygenase reactivity of LPMO

To determine the H_2O_2 consumption rate by LPMO, we tested the reactivity of *Nc*LPMO9C with H_2O_2 by titrating aliquots of H_2O_2 to reactions containing 0.8 mg mL^{-1} PASC, 3 µM LPMO and 2 mM ascorbate. In these experiments, H_2O_2 was added to the reaction every 90 s using three different concentrations (20, 40 or 80 µM per addition). The total change in the reaction volume due to the addition of H_2O_2 was less than 3% in all assays. The addition of H_2O_2 to reduced LPMO caused an immediate

decrease in optical density, which points towards a fast consumption of H_2O_2. This reaction was much faster than the reference reaction without H_2O_2 (Fig. 4a). The substrate conversion rate could not be determined because it was as fast or faster than the mixing time of the cuvette (ca. 10 s). However, doubling the amount of added H_2O_2 also doubled the observed change in optical density. For all titrations, approximately 350–400 µM of H_2O_2 was required to reach maximal observable changes, corresponding to approximately 0.2 units of optical density. Addition of H_2O_2 or LPMO beyond this lower limit did not induce further changes in the optical density of the PASC suspension. Control experiments in which either LPMO or reductant were omitted did not show any changes in the optical density of the PASC suspension (Additional file 1: Figure S2). Likewise, the titration of H_2O_2 to oxidized *Nc*LPMO9C had no observable effect on the optical density of the PASC (Additional file 1: Figure S2).

To correlate the observed substrate degradation with the cosubstrate consumption, we followed the depletion of H_2O_2 using electrochemical detection of H_2O_2 (Fig. 4b). These assays were carried out at a larger volume of 12 mL in a stirred electrochemical cell to avoid exceeding consumption of H_2O_2 by the electrode. Titration of 40 µM H_2O_2 to reactions containing only PASC or only LPMO showed a stable, H_2O_2 concentration-dependent decrease of the measured current. The addition of H_2O_2 to oxidized LPMO resulted in slightly lower currents, indicating H_2O_2 depletion through a background reaction. Under these conditions, no turbidimetric changes of PASC were observed (Additional file 1: Figure S2) showing that this futile reaction did not induce observable catalytic events. The addition of H_2O_2 to reactions containing 2 mM ascorbate (Fig. 4b, magenta line) led to a slow depletion of H_2O_2, possibly via reduction of the H_2O_2 [49, 50]. Upon titration of H_2O_2 to a reaction containing ascorbate, LPMO and PASC, no detectable increase in the H_2O_2 concentration was observed, showing that H_2O_2 was rapidly consumed in this experiment (Fig. 4b, red line). This is a clear indication that the consumption of the cosubstrate by the system occurred within the response time of the electrochemical sensor, which was approximately 3 s. After 9 H_2O_2 additions, corresponding to a total added H_2O_2 concentration of 360 µM, a built-up of H_2O_2 was observed. This concentration coincides with the required H_2O_2 concentration that induced maximal changes in optical density of PASC in degradation assays carried out under comparable conditions (Fig. 4a, red line). Doubling the concentration of added H_2O_2 to 80 µM per addition (Fig. 4b, blue line) resulted in notable signal spikes after 4–5 additions (320–400 µM), which compares well to the experiments shown in Fig. 4a which employed the same H_2O_2 addition rate. Taken together, these experiments demonstrate fast consumption of H_2O_2 by an LPMO-dependent reaction and connect the observed absorbance changes to the consumption of H_2O_2. The visual change that

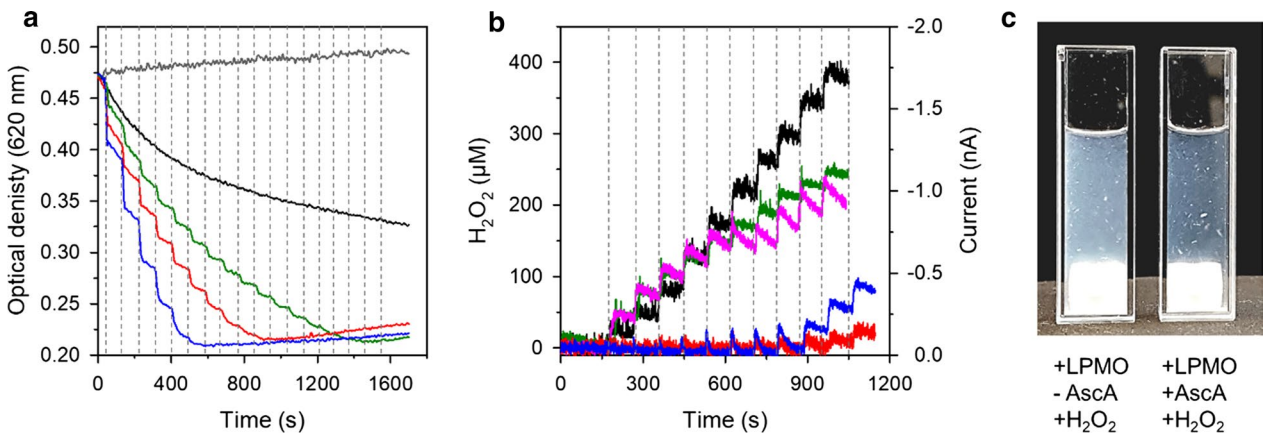

Fig. 4 Effect of H_2O_2 on the degradation of PASC by LPMO. **a** Sequential titration of 20 µM (green line), 40 µM (red line) or 80 µM (blue line) H_2O_2 to a solution containing 0.8 mg mL^{-1} PASC, 3 µM LPMO and 2 mM ascorbate. The background reaction of LPMO in the presence (black line) or absence (grey line) of 2 mM ascorbate. **b** Time-dependent, electrochemical measurement of H_2O_2. All reactions were carried out at a volume of 12 mL under constant stirring at 30 °C and contained 0.8 mg mL^{-1} PASC in 50 mM sodium phosphate buffer, pH 6.0. Vertical dotted lines indicate the addition of fresh H_2O_2 which was added approximately every 90 s in aliquots of 40 µM. Shown is the addition of H_2O_2 to PASC (black line); PASC and 3 µM LPMO (green line); PASC and 2 mM ascorbate (magenta line); PASC, 2 mM ascorbate and 3 µM LPMO (red line). In an additional experiment, PASC, 2 mM ascorbate and 3 µM LPMO was supplemented with 80 µM H_2O_2 per addition (blue line). **c** Degradation of 0.8 mg mL^{-1} PASC by 3 µL LPMO. H_2O_2 (40 µM) was sequentially added to the samples every 90 s in presence or absence of 2 mM ascorbate. The total amount of added H_2O_2 was 400 µM

accompanied the degradation of PASC by LPMO upon titration with 40 µM H_2O_2 is shown in Fig. 4c. The images suggest that, to a large extent, *Nc*LPMO9C preferentially targeted finely dispersed, amorphous PASC while bigger particles remained largely intact at the end of the reaction. The heterogeneity of the substrate may also explain why the reaction levelled off at a certain optical density.

Substrate binding of LPMO during H_2O_2-mediated PASC degradation

To gain further insight into the binding of LPMO to PASC, we monitored the fraction of free *Nc*LPMO9C during the titration of reduced LPMO with 10 aliquots of 40 µM H_2O_2. Samples of 50 µL were regularly withdrawn from this reaction and the supernatants analysed by SDS-PAGE after centrifugation (Fig. 5a). Incubation of LPMO with PASC in absence of reductant reduced the concentration of soluble LPMO by 50%, indicating binding of the other 50% of LPMO to the substrate. Addition of ascorbate to this reaction instantly increased the fraction of bound enzyme to 71%. This compares well to the observed changes in optical density in Fig. 1b, which showed a higher signal change for the reduced LPMO when compared to the oxidized enzyme. The fraction of free enzyme gradually increased upon titration with H_2O_2 (Fig. 5a). Quantitative assessment of PASC by weight determination (Fig. 5b) showed that notable substrate degradation occurred only in samples containing ascorbate together with LPMO. Addition of H_2O_2 to this mixture led to a notably higher PASC degradation than observed in the presence of ascorbate alone. In this reaction, approximately 20% of the PASC initially present in the assay was solubilized by the LPMO. In the same reaction, the optical density of PASC decreased by ca. 45% (from 0.47 to 0.21 optical density at 620 nm). Thus, part of the observed absorbance changes may be a result of PASC modification rather than solubilization, e.g. via the introduction of oxidized ends, or the release of insoluble oligomers. Results obtained from bacterial or fungal LPMOs previously showed that only approximately 50% of the total introduced oxidized ends were found on soluble oligomers, while the remaining modifications occurred on the insoluble fraction [33].

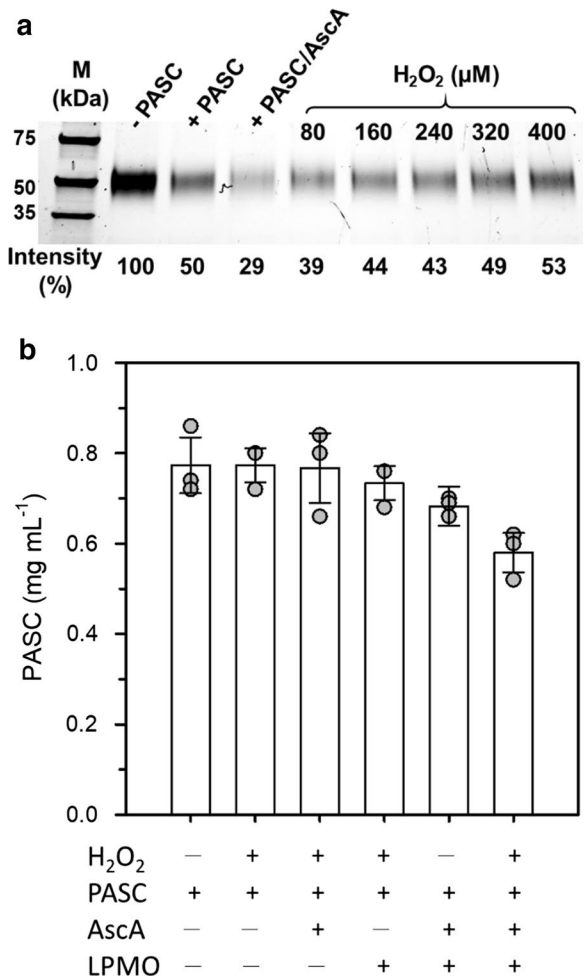

Fig. 5 Binding of *Nc*LPMO9C to PASC and substrate degradation during H_2O_2-mediated PASC degradation. **a** SDS-PAGE analysis of supernatants obtained from titration of reduced *Nc*LPMO9C with aliquots of 40 µM H_2O_2 (Fig. 4a, red line). Three µM LPMO was incubated for 10 min in buffer solution ("-PASC") or together with 0.8 mg mL^{-1} PASC ("+PASC"). To the latter reaction mix, ascorbate was added to a final concentration of 2 mM ("+PASC/AscA"), and titration with H_2O_2 in aliquots of 40 µM was performed. The intensity (in %) denotes the intensities of the bands relative to those of *Nc*LPMO9C incubated in buffer solution. Intensities were calculated with the Image Lab Software Suite (BioRad). All reactions were carried out in 50 mM potassium phosphate buffer, pH 6.0. The SDS-PAGE analysis was repeated twice with the error being within 5%. **b** Weight determination of PASC in different control experiments. The total concentration of H_2O_2 added to the samples was 400 µM, which was added in aliquots of 40 µM every 90 s (as shown in Fig. 4a, red line). All assays were performed in 3 mL quartz cuvettes at 30 °C and under constant stirring. For each data point shown, 2 reactions containing 2.5 mL of sample solution were pooled, centrifuged and washed twice with deionized water. The dry weight of PASC in each reaction mix was determined after drying the sample at 55 °C to a constant weight (ca. 16 h of incubation)

Discussion

A growing body of evidence demonstrates that LPMOs use H_2O_2 as cosubstrate with a much higher catalytic efficiency than O_2 [26, 28, 44, 51]. While the cosubstrate preference of LPMOs in their native environments is still debated [29] the efficient peroxygenase reactivity may be beneficial in industrial settings to achieve faster biomass depolymerization [52].

The activity of LPMOs is typically assessed in the presence of an about 1 mM concentration of ascorbate, which reduces the active-site copper and initiates the oxidative degradation of the substrate. Several recent publications, however, raised the question whether the observed activity is due to an O_2-dependent monooxygenase reaction, or, at least partially, depends on the H_2O_2 that is slowly released by the reaction of oxygen with the reductant ascorbate [26, 31, 44]. In addition, reduced LPMOs in solution may also release low H_2O_2 concentrations via an uncoupling reaction [36]. Results obtained with the turbidimetric assay support an H_2O_2-dependent LPMO activity. First, we observed that the rate of *Nc*LPMO9C increased linearly with the concentration of ascorbate. While we cannot exclude experimentally that the assays may not have been carried out under saturating ascorbate concentrations, a recent study showed that the bacterial LPMO10A from *Serratia marcescens* had an apparent K_M-value of 2 µM for ascorbate [44]. Even if the K_M-value of *Nc*LPMO9C for ascorbate would be 50-times higher, the high 0.5–6 mM ascorbate concentration present in our assays should still provide sufficiently saturating conditions to achieve maximal turnover. The reduction of the active site by ascorbate is not the rate-limiting step in the overall LPMO reaction at high ascorbate concentrations [53] and providing more reducing equivalents should not exert a boosting effect on the LPMO catalysis. From experiments with the H_2O_2 scavenger catalase, we conclude that the H_2O_2 generated from the oxidation reaction of O_2 by ascorbate is preferentially used as cosubstrate by the *Nc*LPMO9C for the degradation of the cellulose substrate. Stability measurements of ascorbate conducted under the same reaction conditions used in this study (50 mM phosphate buffer, pH 6, and 30 °C) showed that a concentration of 1 mM ascorbate depleted within 100 min of incubation (Figure S10 in Ref. [24]), forming H_2O_2 and dehydroascorbic acid as the degradation products.

We also found that the reaction of LPMO with the native electron donor cellobiose dehydrogenase depended on the presence of H_2O_2. The CDH/LPMO system was sensitive to the presence of catalase, which is in good agreement with a previous report showing that a CDH variant with enhanced oxygen reactivity was more efficient in initiating the activity of a bacterial LPMO [33]. In this study, the measured LPMO reaction rates corresponded to the rate of H_2O_2 formation by CDH, while the electron transfer from CDH to LPMO was not rate-limiting. Here, we confirm and extend this observation by demonstrating that the same effects occur when using a CDH together with an LPMO from the same organism (*N. crassa*) during the degradation of a cellulosic substrate. Experiments using a low amount (0.5 µM) of CDH showed that the LPMO reaction rate could be tuned by the addition of glucose oxidase/glucose, indicating that reductive activation of the LPMO by CDH was not rate-limiting.

Also, it should be noted that the high CDH concentrations (0.5–3 µM) employed in our assays aimed at visualizing degradation effects within the assay time of ~30 min, but may not reflect conditions encountered in vivo. Quantitative secretome analysis of the fungus *N. crassa* previously showed that *Nc*CDHIIA constituted only a minor fraction of the proteins detected under cellulolytic conditions (2.4% or 0.28 µmol g^{-1} secretome) [54]. In comparison, the 3 LPMOs identified in this study together made up 14.6% of the total secretome, corresponding to 5.23 µmol g^{-1} secretome. This indicates that a 15- to 20-fold lower concentration of CDH is used by the fungus to support LPMO activity.

Overall, the herein used assay procedure allows a rapid determination of LPMO activity under heterogeneous conditions. We reason that the limits of our assay were largely determined by substrate depletion due to the modification or depolymerization of PASC. Conversion experiments carried out at different H_2O_2 feeding rates all converged at a similar optical density (Fig. 4a). However, the addition of fresh PASC, ascorbate or H_2O_2 at the end of the assays (after addition of 400 µM H_2O_2) did not induce notable absorbance changes of the PASC solution (Additional file 1: Figure S3). We, therefore, conclude that a limitation of binding sites on PASC and oxidative damage of the unbound LPMO [26] are the limiting factors of this assay procedure.

Conclusions

Lytic polysaccharide monooxygenases employ a unique redox mechanism to degrade recalcitrant polysaccharides. To date, there is still an ongoing dispute whether O_2 or H_2O_2 is the preferred cosubstrate of the enzyme. Using different reducing systems, including the native reductase cellobiose dehydrogenase, we here show that the depolymerization of a cellulosic substrate by *Nc*LPMO9C depends on the supply of H_2O_2. Furthermore, we introduce an easy-to-apply assay for lytic polysaccharide monooxygenases that employs an insoluble cellulose substrate.

Methods

Enzymes and chemicals

Cellobiose dehydrogenase IIA (CDHIIA) and lytic polysaccharide monooxygenase 9C (LPMO9C) from

N. crassa were recombinantly produced in *Pichia pastoris* X-33 cells as previously reported [55]. Purification was done by sequential hydrophobic interaction chromatography (HIC) and anion exchange chromatography (AIEX) [36, 55]. The purity of the enzymes was verified by SDS-PAGE and activity assays.

CDH activity was measured spectrophotometrically by monitoring the reduction of the FAD-dependent electron acceptor dichlorophenol indophenol (DCIP, $\varepsilon_{520} = 6.8\ mM^{-1}\ cm^{-1}$) or the heme *b*-dependent chromogen cytochrome *c* (cyt *c*, $\varepsilon_{550} = 19.6\ mM^{-1}\ cm^{-1}$). Assays had a total volume of 1 mL and contained 30 mM lactose as CDH substrate along with 300 µM DCIP or 20 µM cyt *c* in 50 mM potassium phosphate buffer, pH 6.0. One unit of CDH activity was defined as the amount of enzyme that reduced 1 µmol of the electron acceptor per min under the given assay conditions.

Catalase from *Corynebacterium glutamicum* and FAD-dependent glucose oxidase from *A. niger* were obtained from Sigma Aldrich and used without additional purification. Catalase activity was assayed by monitoring the decrease of 40 mM H_2O_2 at a wavelength of 240 nm ($\varepsilon_{240} = 43.6\ M^{-1}\ cm^{-1}$ [56]). Assays had a total volume of 1 mL and were performed at 30 °C in 50 mM potassium phosphate buffer, pH 6.0. One unit of catalase activity was defined as the amount of enzyme consuming 1 µmol H_2O_2 per min.

Glucose oxidase activity was assayed with a peroxidase-coupled assay using ABTS [2,2′-azinobis(3-ethylbenzthiazolinesulfonic acid)] ($\varepsilon_{420} = 36\ mM^{-1}\ cm^{-1}$) as the chromogenic substrate. Assays had a total volume of 1 mL and contained 10 mM glucose, 10 mM ABTS and 7 U mL^{-1} horseradish peroxidase II (Sigma Aldrich) in 50 mM potassium phosphate buffer, pH 6.0. One unit of glucose oxidase activity was defined as the amount of enzyme necessary for the generation of 1 µmol of H_2O_2 per min.

Preparation of phosphoric acid-swollen cellulose (PASC)

Phosphoric acid-swollen cellulose (PASC) was prepared by dissolving 8 g of microcrystalline cellulose (20–160 µm) in 200 mL of ice-cold 85% (v/v) phosphoric acid. The solution was stirred for 1 h at 4 °C. After removing undissolved cellulose, 1.8 L of ice-cold HQ-water was added to induce the precipitation of PASC. The precipitate was washed on a vacuum pump with deionized water (ca. 2.0 L), with 2 L of a 2 M sodium bicarbonate solution and finally with 50 mM potassium phosphate buffer, pH 6.0, until a constant pH was measured. Before utilization, PASC was homogenized with a disperser (Ultra Turrax, Ika).

Turbidimetric measurement of PASC and determination of LPMO activity

LPMO activity was measured based on the decrease of the optical density of a PASC suspension upon degradation [40]. The optical density of PASC was determined at 620 nm using a temperature-controlled, single-beam UV–visible spectrophotometer (U-3000, Hitachi) with a built-in magnetic stirrer. The measurement setup consisted of a quartz cuvette with 3 mL volume containing a 6 mm cross-shaped magnetic stirrer. The cuvette was filled with 2.5 mL of the PASC suspension and was placed in a temperature-controlled UV–Vis spectrometer (Hitachi U-3000). The stirrer speed was set to an angular frequency of approximately 50 rad s^{-1} and the PASC suspension was equilibrated within the instrument for 10 min at 30 °C. The time to achieve uniform mixing in the cuvette was approximately 10 s. The linear relation between the PASC concentration and its optical density at 620 nm was verified between 0 and 1.4 mg PASC mL^{-1} (Fig. 1a). Standard activity assays contained 0.8 mg mL^{-1} PASC and 3 µM of LPMO. Reducing agents for LPMO were ascorbate, or *Nc*CDHIIA together with 10 mM cellobiose. All assays were performed at 30 °C unless stated otherwise. Control experiments were performed by adding only ascorbate or *Nc*LPMO9C to PASC. The activity was assessed based on the initial, linear decrease in optical density by fitting the data to a linear equation. PASC degradation experiments in absence of oxygen were performed in an anaerobic glove box (Whitley DG250, Don Whitley Scientific) which was continuously flushed with a nitrogen/hydrogen mixture (99:1). Residual oxygen traces were removed by a palladium catalyst and the generated water vapour captured by silica gel. Measurements were performed on an Agilent 8453 UV–visible spectrophotometer equipped with a magnetic stirrer. During all measurements, the temperature inside the glove box was maintained at 25 ± 1 °C by an external thermostat.

Matrix-assisted laser desorption/ionization mass spectrometry (MALDI-MS) analysis

MALDI-MS analysis was performed on a Bruker SolariX 15T FT-ICR mass spectrometer. PASC was washed two times with 250 mM sodium acetate, centrifuged at 2000×*g* for three minutes, and resuspended in 25 mM TRIS, pH 6.0, at a concentration of 10 mg mL^{-1}. *Nc*CDHIIA (0.1 µM), lactose (1 mM) and *Nc*LPMO9C (3 µM) were added to a total reaction volume of 500 µL. The reaction mixture was incubated for 30 min at 30 °C under constant shaking. H_2O_2 was added to a concentration of 30 µM (5 µL of a 3 mM H_2O_2 stock solution) at the start of the incubation and after 10, 20 and 30 min resulting

in a total added concentration of 120 μM H_2O_2 at the end of the experiment. Samples were taken at the end of the incubation, desalted using a porous graphitic carbon resin (HyperCarb, Thermo Fisher Scientific) in a pipette tip (washed with water and eluted with 50% ACN) and were spotted (1.5 μL) on a MALDI plate in a 10, 20 and 60 μg μL^{-1} DHB matrix in 30% ACN (1.5 μL). Measured values are a sum of 1500 laser shots randomly distributed across the sample spot. Results are only shown for 20 μg μL^{-1} matrix that yielded the highest intensities of the products.

Electrochemical measurements

Chronoamperometric measurements were performed in a water-jacketed electrochemical cell filled with 12 mL of sample solution connected to a water bath (Julabo F12, Germany) using an Autolab PGSTAT204 potentiostat (Metrohm, Netherlands). A standard three-electrode configuration employed a platinum disk microelectrode with a diameter of 100 μm as the working electrode, an Ag/AgCl electrode as the reference electrode and a platinum coiled wire as the auxiliary electrode (BAS Inc.). Prior to all measurements, the phosphate buffer solution (50 mM, pH 6.0) containing 0.8 mg mL^{-1} PASC, 2 mM ascorbate and 3 μM *Nc*LPMO9C was degassed by bubbling with nitrogen for 20 min and subsequently protected by applying a nitrogen atmosphere during the whole measurements. A potential of −0.15 V was applied to detect H_2O_2. When the background current reached a stable signal, the freshly prepared and degassed H_2O_2 sample was injected into the PASC suspension through an FEP tube (diameter 0.15 mm) connected to a 1-mL syringe (SGE Analytical Science). All measurements were conducted at 30.0 ± 0.2 °C and a magnetic stirrer operated at an angular frequency of approximately 50 rad s^{-1} provided convective transport. The data were collected at 0.5 s^{-1} and corrected for the background current.

Supplementary information

Supplementary information accompanies this paper at https://doi.org/10.1186/s13068-020-01673-4.

Additional file 1: Figure S1. Incubation of 3 μM LPMO and 0.8 mg mL^{-1} PASC with CDH at concentrations of 0.5 μM (red) 1 μM (blue) or 3 μM (green) in absence of cellobiose. Black line: 3 μM CDH and 10 mM cellobiose in absence of LPMO. All reactions were carried out under constant stirring at 30 °C in 50 mM sodium phosphate buffer, pH 6.0. **Figure S2.** Titration of oxidized LPMO (3 μM) and 0.8 mg mL^{-1} PASC with 20 μM (green), 40 μM (red) or 80 μM (blue) H_2O_2 (solid lines). Dashed, coloured lines show the titration of 2 mM ascorbate and 0.8 mg mL^{-1} PASC with 20 μM (green), 40 μM (red) or 80 μM (blue) H_2O_2. The vertical dashed lines indicate the addition of H_2O_2. The arrow indicates the addition of LPMO (solid lines) or 2 mM ascorbate (dashed lines). All reactions were carried out under constant stirring at 30 °C in 50 mM sodium phosphate buffer, pH 6.0. **Figure S3.** Titration of LPMO (3 μM) and 0.8 mg mL^{-1} PASC with 40 μM H_2O_2. The vertical dashed lines indicate the addition of H_2O_2. The arrow indicates the addition of fresh PASC which was either added alone (green line) or simultaneously with 1 mM ascorbate (AscA, black line). The blue line indicates the addition of ascorbate (1 mM). All reactions were carried out under constant stirring at 30 °C in 50 mM sodium phosphate buffer, pH 6.0.

Abbreviations

LPMO: Lytic polysaccharide monooxygenase; CDH: Cellobiose dehydrogenase; CBM: Carbohydrate-binding module; PASC: Phosphoric acid-swollen cellulose; ANS: 8-Anilinonaphthalene-1-sulfonic acid; EDTA: Ethylenediaminetetraacetic acid; DHB: 2,5-Dihydroxybenzoic acid; TCEP: Tris(2-carboxyethyl)phosphine; MC: Microcrystalline cellulose; ECD: Electronic circular dichroism; MS: Mass spectrometry; MALDI: Matrix-assisted laser desorption/ionization; FT-ICR: Fourier-transform ion cyclotron resonance.

Acknowledgements

The authors thank E. Breslmayr for valuable discussions and input.

Authors' contributions

DK conceptualised the study; FF and DK performed the turbidimetric assays; HC performed electrochemical measurements; FF, PM and PH performed mass spectrometry; DK, RL, PM, FF and PH interpreted and analysed experimental data; RL and DK wrote the final version of the manuscript. All authors read and approved the final manuscript.

Funding

The project was supported by the Austrian Science Fund FWF through grants J4154 (D.K.), I2385-N28 (R.L.), the ERC Consolidator Grant OXIDISE (grant agreement Nr. 726396, R.L.) and the Czech Science Foundation through grant 16-34818L (P.H.). MS instrument access was enabled through EU/MEYS funding: CZ.1.05/1.1.00.02.0109 and LM2015043 CIISB.

Availability of data and materials

The datasets used and/or analysed during the current study are available from the corresponding author on reasonable request.

Ethics approval and consent to participate

Not applicable.

Consent for publication

All authors have seen and approved the manuscript before submission to *Biotechnology for Biofuels*.

Competing interests

The authors declare that they have no competing interests.

Author details

[1] BioCeV-Institute of Microbiology, The Czech Academy of Sciences, Prumyslova 595, 252 50 Vestec, Czech Republic. [2] Faculty of Science, Charles University, Hlavova 2030/8, 128 43 Prague 2, Czech Republic. [3] Biocatalysis and Biosensing Research Group, Department of Food Science and Technology, BOKU-University of Natural Resources and Life Sciences, Muthgasse 18, 1190 Vienna, Austria. [4] The University of Manchester, Manchester Institute of Biotechnology, Manchester M1 7DN, UK.

Received: 12 December 2019 Accepted: 1 February 2020
Published online: 05 March 2020

References

1. Johansen KS. Discovery and industrial applications of lytic polysaccharide mono-oxygenases. Biochem Soc Trans. 2016;44:143–9. https://doi.org/10.1042/BST20150204.
2. Müller G, Várnai A, Johansen KS, et al. Harnessing the potential of LPMO-containing cellulase cocktails poses new demands on processing conditions. Biotechnol Biofuels. 2015;8:187. https://doi.org/10.1186/s13068-015-0376-y.

3. Vaaje-Kolstad G, Westereng B, Horn SJ, et al. An oxidative enzyme boosting the enzymatic conversion of recalcitrant polysaccharides. Science (80). 2010;330:219–22. https://doi.org/10.1126/science.1192231.
4. Quinlan RJ, Sweeney MD, Lo Leggio L, et al. Insights into the oxidative degradation of cellulose by a copper metalloenzyme that exploits biomass components. Proc Natl Acad Sci. 2011;108:15079–84. https://doi.org/10.1073/pnas.1105776108.
5. Sabbadin F, Hemsworth GR, Ciano L, et al. An ancient family of lytic polysaccharide monooxygenases with roles in arthropod development and biomass digestion. Nat Commun. 2018. https://doi.org/10.1038/s41467-018-03142-x.
6. Chiu E, Hijnen M, Bunker RD, et al. Structural basis for the enhancement of virulence by viral spindles and their in vivo crystallization. Proc Natl Acad Sci. 2015;112:3973–8. https://doi.org/10.1073/pnas.1418798112.
7. Yadav SK, Archana, Singh R, et al. Insecticidal fern protein Tma12 is possibly a lytic polysaccharide monooxygenase. Planta. 2019;249:1987–96. https://doi.org/10.1007/s00425-019-03135-0.
8. Forsberg Z, Vaaje-kolstad G, Westereng B, et al. Cleavage of cellulose by a cbm33 protein. Protein Sci. 2011;20:1479–83. https://doi.org/10.1002/pro.689.
9. Isaksen T, Westereng B, Aachmann FL, et al. A C4-oxidizing lytic polysaccharide monooxygenase cleaving both cellulose and cello-oligosaccharides. J Biol Chem. 2014;289:2632–42. https://doi.org/10.1074/jbc.M113.530196.
10. Vu VV, Beeson WT, Span EA, et al. A family of starch-active polysaccharide monooxygenases. Proc Natl Acad Sci. 2014;111:13822–7. https://doi.org/10.1073/pnas.1408090111.
11. Agger JW, Isaksen T, Varnai A, et al. Discovery of LPMO activity on hemicelluloses shows the importance of oxidative processes in plant cell wall degradation. Proc Natl Acad Sci. 2014;111:6287–92. https://doi.org/10.1073/pnas.1323629111.
12. Frommhagen M, Sforza S, Westphal AH, et al. Discovery of the combined oxidative cleavage of plant xylan and cellulose by a new fungal polysaccharide monooxygenase. Biotechnol Biofuels. 2015;8:101. https://doi.org/10.1186/s13068-015-0284-1.
13. Couturier M, Ladevèze S, Sulzenbacher G, et al. Lytic xylan oxidases from wood-decay fungi unlock biomass degradation. Nat Chem Biol. 2018;14:306–10. https://doi.org/10.1038/nchembio.2558.
14. Harris PV, Welner D, McFarland KC, et al. Stimulation of lignocellulosic biomass hydrolysis by proteins of glycoside hydrolase family 61: structure and function of a large, enigmatic family. Biochemistry. 2010;49:3305–16. https://doi.org/10.1021/bi100009p.
15. Langston JA, Shaghasi T, Abbate E, et al. Oxidoreductive cellulose depolymerization by the enzymes cellobiose dehydrogenase and glycoside hydrolase 61. Appl Environ Microbiol. 2011;77:7007–15. https://doi.org/10.1128/AEM.05815-11.
16. Meier KK, Jones SM, Kaper T, et al. Oxygen activation by Cu LPMOs in recalcitrant carbohydrate polysaccharide conversion to monomer sugars. Chem Rev. 2018;118:2593–635. https://doi.org/10.1021/acs.chemrev.7b00421.
17. Walton PH, Davies GJ. On the catalytic mechanisms of lytic polysaccharide monooxygenases. Curr Opin Chem Biol. 2016;31:195–207. https://doi.org/10.1016/j.cbpa.2016.04.001.
18. Westereng B, Cannella D, Wittrup Agger J, et al. Enzymatic cellulose oxidation is linked to lignin by long-range electron transfer. Sci Rep. 2016;5:18561. https://doi.org/10.1038/srep18561.
19. Martinez AT. How to break down crystalline cellulose. Science (80). 2016;352:1050–1. https://doi.org/10.1126/science.aaf8920.
20. Phillips CM, Beeson WT, Cate JH, et al. Cellobiose dehydrogenase and a copper-dependent polysaccharide monooxygenase potentiate cellulose degradation by *Neurospora crassa*. ACS Chem Biol. 2011;6:1399–406. https://doi.org/10.1021/cb200351.
21. Tan T-C, Kracher D, Gandini R, et al. Structural basis for cellobiose dehydrogenase action during oxidative cellulose degradation. Nat Commun. 2015;6:7542. https://doi.org/10.1038/ncomms8542.
22. Frommhagen M, Mutte SK, Westphal AH, et al. Boosting LPMO-driven lignocellulose degradation by polyphenol oxidase-activated lignin building blocks. Biotechnol Biofuels. 2017;10:121. https://doi.org/10.1186/s13068-017-0810-4.
23. Brenelli L, Squina FM, Felby C, et al. Laccase-derived lignin compounds boost cellulose oxidative enzymes AA9. Biotechnol Biofuels. 2018;11:10. https://doi.org/10.1186/s13068-017-0985-8.
24. Kracher D, Scheiblbrandner S, Felice AKG, et al. Extracellular electron transfer systems fuel cellulose oxidative degradation. Science (80). 2016;352:1098–101. https://doi.org/10.1126/science.aaf3165.
25. Kjaergaard CH, Qayyum MF, Wong SD, et al. Spectroscopic and computational insight into the activation of O_2 by the mononuclear Cu center in polysaccharide monooxygenases. Proc Natl Acad Sci U S A. 2014;111:8797–802. https://doi.org/10.1073/pnas.1408115111.
26. Bissaro B, Røhr ÅK, Müller G, et al. Oxidative cleavage of polysaccharides by monocopper enzymes depends on H_2O_2. Nat Chem Biol. 2017;13:1123–8. https://doi.org/10.1038/nchembio.2470.
27. Forsberg Z, Sørlie M, Petrović D, et al. Polysaccharide degradation by lytic polysaccharide monooxygenases. Curr Opin Struct Biol. 2019;59:54–64. https://doi.org/10.1016/j.sbi.2019.02.015.
28. Kuusk S, Bissaro B, Kuusk P, et al. Kinetics of H_2O_2-driven degradation of chitin by a bacterial lytic polysaccharide monooxygenase. J Biol Chem. 2018;293:523–31. https://doi.org/10.1074/jbc.M117.817593.
29. Hangasky JA, Iavarone AT, Marletta MA. Reactivity of O_2 versus H_2O_2 with polysaccharide monooxygenases. Proc Natl Acad Sci U S A. 2018;115:4915–20. https://doi.org/10.1073/pnas.1801153115.
30. Petrović DM, Bissaro B, Chylenski P, et al. Methylation of the N-terminal histidine protects a lytic polysaccharide monooxygenase from auto-oxidative inactivation. Protein Sci. 2018;27:1636–50. https://doi.org/10.1002/pro.3451.
31. Bissaro B, Várnai A, Røhr ÅK, et al. Oxidoreductases and reactive oxygen species in conversion of lignocellulosic biomass. Microbiol Mol Biol Rev. 2018. https://doi.org/10.1128/mmbr.00029-18.
32. Sygmund C, Santner P, Krondorfer I, et al. Semi-rational engineering of cellobiose dehydrogenase for improved hydrogen peroxide production. Microb Cell Fact. 2013;12:38. https://doi.org/10.1186/1475-2859-12-38.
33. Kracher D, Forsberg Z, Bissaro B, et al. Polysaccharide oxidation by lytic polysaccharide monooxygenase is enhanced by engineered cellobiose dehydrogenase. FEBS J. 2019. https://doi.org/10.1111/febs.15067.
34. Westereng B, Arntzen M, Agger JW, et al. Analyzing activities of lytic polysaccharide monooxygenases by liquid chromatography and mass spectrometry. Methods in molecular biology. New York: Humana press; 2017. p. 71–92. https://doi.org/10.1007/978-1-4939-6899-2_7.
35. Wang D, Li J, Wong ACYY, et al. A colorimetric assay to rapidly determine the activities of lytic polysaccharide monooxygenases. Biotechnol Biofuels. 2018;11:215. https://doi.org/10.1186/s13068-018-1211-z.
36. Kittl R, Kracher D, Burgstaller D, et al. Production of four *Neurospora crassa* lytic polysaccharide monooxygenases in *Pichia pastoris* monitored by a fluorimetric assay. Biotechnol Biofuels. 2012;5:79. https://doi.org/10.1186/1754-6834-5-79.
37. Breslmayr E, Hanžek M, Hanrahan A, et al. A fast and sensitive activity assay for lytic polysaccharide monooxygenase. Biotechnol Biofuels. 2018;11:1–13. https://doi.org/10.1186/s13068-018-1063-6.
38. Hansson H, Karkehabadi S, Mikkelsen N, et al. High-resolution structure of a lytic polysaccharide monooxygenase from *Hypocrea jecorina* reveals a predicted linker as an integral part of the catalytic domain. J Biol Chem. 2017;292:19099–109. https://doi.org/10.1074/jbc.M117.799767.
39. Zhang YHP, Lynd LR. Determination of the number-average degree of polymerization of cellodextrins and cellulose with application to enzymatic hydrolysis. Biomacromolecules. 2005;6:1510–5. https://doi.org/10.1021/bm049235j.
40. Enari T-M, Niku-Paavola M-L. Nephelometric and turbidometric assay for cellulase. Methods in enzymology. New York: Academic Press; 1988. p. 117–26.
41. Borisova AS, Isaksen T, Dimarogona M, et al. Structural and functional characterization of a lytic polysaccharide monooxygenase with broad substrate specificity. J Biol Chem. 2015;290:22955–69. https://doi.org/10.1074/jbc.M115.660183.
42. Kracher D, Andlar M, Furtmüller PG, et al. Active-site copper reduction promotes substrate binding of fungal lytic polysaccharide monooxygenase and reduces stability. J Biol Chem. 2018;293:1676–87. https://doi.org/10.1074/jbc.RA117.000109.
43. Hangasky JA, Marletta MA. A random-sequential kinetic mechanism for polysaccharide monooxygenases. Biochemistry. 2018;57:3191–9. https://doi.org/10.1021/acs.biochem.8b00129.

44. Kuusk S, Kont R, Kuusk P, et al. Kinetic insights into the role of the reductant in H_2O_2-driven degradation of chitin by a bacterial lytic polysaccharide monooxygenase. J Biol Chem. 2019;294:1516–28. https://doi.org/10.1074/jbc.RA118.006196.
45. Pricelius S, Ludwig R, Lant NJ, et al. In situ generation of hydrogen peroxide by carbohydrate oxidase and cellobiose dehydrogenase for bleaching purposes. Biotechnol J. 2011;6:224–30. https://doi.org/10.1002/biot.201000246.
46. Wilson MT, Hogg N, Jones GD. Reactions of reduced cellobiose oxidase with oxygen. Is cellobiose oxidase primarily an oxidase? Biochem J. 1990;270:265–7. https://doi.org/10.1042/bj2700265.
47. Znameroski EA, Coradetti ST, Roche CM, et al. Induction of lignocellulose-degrading enzymes in *Neurospora crassa* by cellodextrins. Proc Natl Acad Sci. 2012;109:6012–7. https://doi.org/10.1073/pnas.1118440109.
48. Westereng B, Agger JW, Horn SJ, et al. Efficient separation of oxidized cello-oligosaccharides generated by cellulose degrading lytic polysaccharide monooxygenases. J Chromatogr A. 2013;1271:144–52. https://doi.org/10.1016/j.chroma.2012.11.048.
49. Lowry JP, O'Neill RD. Homogeneous mechanism of ascorbic acid interference in hydrogen peroxide detection at enzyme-modified electrodes. Anal Chem. 1992;64:453–6. https://doi.org/10.1021/ac00028a022.
50. Deutsch JC. Ascorbic acid oxidation by hydrogen peroxide. Anal Biochem. 1998;255:1–7. https://doi.org/10.1006/ABIO.1997.2293.
51. Müller G, Chylenski P, Bissaro B, et al. The impact of hydrogen peroxide supply on LPMO activity and overall saccharification efficiency of a commercial cellulase cocktail. Biotechnol Biofuels. 2018;11:209. https://doi.org/10.1186/s13068-018-1199-4.
52. Chylenski P, Bissaro B, Sørlie M, et al. Lytic polysaccharide monooxygenases in enzymatic processing of lignocellulosic biomass. ACS Catal. 2019;9:4970–91. https://doi.org/10.1021/acscatal.9b00246.
53. Bissaro B, Streit B, Isaksen I, et al. Molecular mechanism of the chitinolytic peroxygenase reaction. Proc Natl Acad Sci. 2020. https://doi.org/10.1073/pnas.1904889117.
54. Phillips CM, Iavarone AT, Marletta MA. Quantitative proteomic approach for cellulose degradation by *Neurospora crassa*. J Proteome Res. 2011;10:4177–85. https://doi.org/10.1021/pr200329b.
55. Sygmund C, Kracher D, Scheiblbrandner S, et al. Characterization of the two *Neurospora crassa* cellobiose dehydrogenases and their connection to oxidative cellulose degradation. Appl Environ Microbiol. 2012;78:6161–71. https://doi.org/10.1128/AEM.01503-12.
56. Beers RF, Sizer IW. A spectrophotometric method for measuring the breakdown of hydrogen peroxide by catalase. J Biol Chem. 1952;195:133–40.

Publisher's Note

Springer Nature remains neutral with regard to jurisdictional claims in published maps and institutional affiliations.

Ready to submit your research? Choose BMC and benefit from:

- fast, convenient online submission
- thorough peer review by experienced researchers in your field
- rapid publication on acceptance
- support for research data, including large and complex data types
- gold Open Access which fosters wider collaboration and increased citations
- maximum visibility for your research: over 100M website views per year

At BMC, research is always in progress.

Learn more biomedcentral.com/submissions

ARTICLE III

Felice A.K.G., Schuster C., Kadek, A., Filandr F., Laurent, C.V.F.P., Scheiblbrandner, S., Schwaiger, L., Schachinger, F., Kracher, D., Sygmund, C., Man, P., Halada, P., Oostenbrink, C. & Ludwig, R.

Chimeric cellobiose dehydrogenases reveal the function of cytochrome domain mobility for the electron transfer to lytic polysaccharide monooxygenase

ACS Catal., ***under review.***

My contribution: *conducting experiments (HDX-MS), data analysis & interpretation, figure design*

Chimeric cellobiose dehydrogenases reveal the function of cytochrome domain mobility for the electron transfer to lytic polysaccharide monooxygenase

Alfons K.G. Felice[1], Christian Schuster[1], Alan Kadek[2,3], Frantisek Filandr[2,3], Christophe V.F.P. Laurent[1,4], Stefan Scheiblbrandner[1], Lorenz Schwaiger[1], Franziska Schachinger[1], Daniel Kracher[1], Christoph Sygmund[1], Petr Man[2,3], Petr Halada[2], Chris Oostenbrink[4] and Roland Ludwig[1]

[1] Biocatalysis and Biosensing Research Group, Department of Food Science and Technology, BOKU – University of Natural Resources and Life Sciences, Muthgasse 18, 1190 Vienna, Austria

[2] BIOCEV - Institute of Microbiology, The Czech Academy of Sciences, Prumyslova 595, 252 50 Vestec, Czech Republic

[3] Department of Biochemistry, Faculty of Science, Charles University in Prague, Hlavova 8, 128 43 Prague, Czech Republic

[4] Department of Material Sciences and Process Engineering, BOKU – University of Natural Resources and Life Sciences, Muthgasse 18, 1190 Vienna, Austria

Keywords: cellobiose dehydrogenase, chimeric enzyme, domain swapping, electron transfer, lytic polysaccharide monooxygenase

ABSTRACT

The natural function of cellobiose dehydrogenase (CDH) to donate electrons from its catalytic flavodehydrogenase (DH) domain via its cytochrome (CYT) domain to lytic polysaccharide monooxygenase (LPMO) is an example of a highly efficient extracellular electron transfer chain. To investigate the function of CYT domain movement in the two occurring electron transfer steps, two CDHs from the ascomycete *Neurospora crassa* (*Nc*CDHIIA and *Nc*CDHIIB) and four chimeric CDH enzymes created by domain swapping were studied in combination with the fungus' own LPMOs (*Nc*LPMO9C and *Nc*LPMO9F). Kinetic and electrochemical methods as well as hydrogen/deuterium exchange mass spectrometry were used to study the domain movement, interaction and electron transfer kinetics. Molecular docking provided insight into the protein-protein interface, orientation of domains and binding energies. We find that the first, interdomain electron transfer step (IDET) from the catalytic site in the DH domain to the CYT domain depends on steric and electrostatic interface complementarity and the length of the protein linker between both domains, but not on the redox potential difference between the FAD and heme *b* cofactors. After CYT reduction, a conformational change of CDH from its closed-state to an open-state allows the second, interprotein electron transfer step (IPET) from CYT to LPMO to occur by direct interaction of the *b*-type heme and the type-2 copper center. Chimeric CDH enzymes favor the open-state and achieve higher IPET rates by presenting the heme *b* cofactor to LPMO. The IPET, which is influenced by interface complementarity and the heme *b* redox potential, is very efficient with bimolecular rates between 2.9 – 8.8 10^5 M^{-1} s^{-1}.

INTRODUCTION

The catalytic activity of LPMO and its interaction with CDH has been reported to increase the rate of hydrolysis of cellulose from recalcitrant biomass and to increase the overall efficiency of enzymatic cocktails [1–4]. Compared with electron donating, low molecular weight reductants of LPMO such as gallate or ascorbate, CDH is specific for LPMO and shows a fast electron transfer at physiological concentrations [5,6]. CDH is an extracellular flavocytochrome and contains FAD and a *b*-type heme in the DH and CYT domains, respectively, which are connected via a flexible linker. The electron transfer between the domains is pH-dependent and has been studied by Igarashi and coworkers in detail [7]. Recently, the structure of the full length protein has been elucidated and two conformations (closed- and open-state) of the CYT domain were observed, which are supposed to play a role in IDET and IPET [8].

LPMO activation by CDH comprises three steps: (i) catalytic cellobiose oxidation in the DH active-site leads to the formation of the reduced $FADH_2$ cofactor, (ii) interaction of CYT with DH in the closed-state results in the subsequent one-electron IDET, and (iii) interaction of CYT in the open-state with LPMO results in the one electron IPET. In the closed-state of CDH the FAD and heme *b* cofactors are in close proximity (~9 Å), which should favor IDET, whereas IPET depends on the interaction of the heme *b* with LPMO [8], which should be favored in the open-state. The structure of the linker in the open- or closed-state could not be fully determined in crystal structures, which indicates its high flexibility.

The two CDHs encoded in the genome of *N. crassa* provide a good basis to study the influence of the CYT mobility on electron transfer due to several reasons. First, the structure of *Nc*CDHIIA has been elucidated (PDB ID: 4QI7) and second, a comparison of the steady-state kinetic constants of the two CDHs in a previous study found a 3.5-fold faster IDET rate for *Nc*CDHIIA at pH 6.0 compared to *Nc*CDHIIB despite the ~50 mV lower redox potential of its heme *b* cofactor than in *Nc*CDHIIB. The independence of the IDET rate from the

driving force suggests a different function of both enzymes' CYT domains, possibly an adaptation to the copper center redox potentials of different LPMOs [6]. Structural features of the domains and surface charge distribution have been shown to influence the CDH domain interaction kinetics [9,10]. SAXS and SANS studies showed that the oxidized form of CDH populates a variety of conformational states between closed- and fully open state and that pH, presence of divalent cations and the presence of LPMO modulate occupation of the closed- and open-state [11,12]. Fast scanning AFM studies showed a preference of the open-state in the reduced form of CDH [13]. These observations raise the question of how CYT interacts with either DH or LPMO and which structural and kinetic determinants govern the interaction.

Based on sequence alignment and the elucidated crystal structures we created chimeric CDH enzymes by exchanging linker, CYT, and DH domains of the two *Nc*CDHs to study the role of the CYT-DH interface, the effect of different cofactor redox potentials, and the influence of the linker length on the protein-protein interaction and IDET. CYT-LPMO interaction was also studied by hydrogen/deuterium exchange mass spectrometry (HDX-MS) measurements and transient-state kinetics to determine the interaction site of CDH-LPMO and evaluate its structural and kinetic determinants to verify recent results obtained by Courtade et al. who showed binding of CDH and CYT to the LPMO active-site by means of ^{15}N-HSQC and ^{13}C-aromatic-HSQC [14] and of Laurent et al. who modelled the interaction between both enzymes [15].

To study the effect of (i) the surface complementarity at the protein-protein interface, (ii) differences in the redox potentials of the cofactors, and (iii) the linker length on the domain interaction and the electron transfer rate, a domain swapping strategy was applied to create chimeric enzymes of the two *N. crassa* CDHs by exchanging CYT and linkers with different structural and physical properties. Chimeric CDHs were studied by steady-state and

presteady-state kinetics, electrochemical methods and molecular modelling in combination with two *N. crassa* LPMOs.

RESULTS

Construction and properties of chimeric CDH variants—

A domain swapping strategy was applied to exchange linkers and CYT domains of the two *N. crassa* CDHs (**Fig. 1A**). The sequence alignment of *Nc*CDHIIA (UniProt: Q7RXM0) with *Nc*CDHIIB (UniProt: Q7S0Y1) gives a sequence identity of 53% and was used together with the crystal structure of *Nc*CDHIIA (PBD: 4QI7) and a homology model of *Nc*CDHIIB to define the individual CDH domains. The end of the N-terminal CYT domain is defined by a cysteine residue forming a disulfide bond (CYT_A: Q1–C211, CYT_B: Q1–C216, for brevity we denote the domains and the linker of *Nc*CDHIIA by $_A$ and *Nc*CDHIIB by $_B$). This disulfide bond in CYT is found in several CDHs and possibly evolved to stabilize the C-terminus from mechanical stress exerted by the linker. After this cysteine the linker sequence follows ($Linker_A$: S212–S229, $Linker_B$: S217–T250). The DH domain starts with the first amino acid firmly connected with DH and ends with the C-terminus (DH_A: F230–V772, DH_B: Y251–R805). The C-terminus of *Nc*CDHIIA features an additional family 1 carbohydrate binding module (P773–V806), which is not present in *Nc*CDHIIB. The sequence identities of individual linkers, CYT and DH domains deviate considerably from the global sequence identity (**Fig. 1B**). The catalytically active DH domains are most conserved, the linkers least. The linkers of both enzymes are rich in serine, threonine, and proline, but differ substantially in length. $Linker_A$ consists of 18 amino acids, while $Linker_B$ is twice as long and consists of 34 amino acids. The evolutionary divergence of the CYT domains and linkers points towards different mechanistic properties, physiological functions, and interacting LPMOs.

Production and purification of enzymes—

Wild-type *N. crassa* CDHs (*Nc*CDHIIA denoted as CDH_{AAA} and *Nc*CDHIIB denoted as CDH_{BBB}) and four chimeric CDHs (CDH_{AAB}, CDH_{ABB}, CDH_{BBA}, and CDH_{BAA}) were recombinantly produced in *Pichia pastoris* and chromatographically purified (**Fig. S1, Table S1**). LPMO9F and LPMO9F from *N. crassa* were also produced in *P. pastoris* and chromatographically purified. The molecular weight of the individual domains and linkers can be calculated from the amino acid sequence and summed up to obtain molecular weights for full-length CDHs (**Fig. 1C**). Close molecular weights for the two wild-type enzymes CDH_{AAA} and CDH_{BBB} are predicted and also between the smallest and biggest chimeric enzymes (CDH_{AAB} and CDH_{BBA}, respectively) the mass difference is only 4484 Da. The molecular weights of the six purified CDHs determined by SDS-PAGE differ from the calculated values. The observed molecular weights are 12–39% larger and a result of posttranslational N-glycosylation [16] and O-glycosylation[38] . Considerable differences in the glycosylation, even between closely composed chimeric CDH_{BBA} and CDH_{BAA}, point towards batch-to-batch variations between fermentations or differences in the post-translational processing of the chimeric CDHs. UV-Vis spectra of the oxidized and reduced chimeric CDHs reveal that the FAD and heme *b* cofactors are properly incorporated (**Fig. S2**).

Catalytic performance of DH domains in chimeric CDH—

In the reductive half-reaction, the oxidation of cellobiose in the active site of the DH domain results in the formation of cellobiono-δ-lactone and the reduced cofactor. In the oxidative half-reaction, the two electrons stored at the $FADH_2$ are then transferred to the heme *b* cofactor in the CYT domain in two separate, one-electron transfer steps to provide

electrons for LPMO reduction[6]. Alternatively, the electrons can be transferred from $FADH_2$ to a two-electron acceptor such as 2,6-dichloroindophenol, which allows the assessment of catalysis without contribution of the subsequent electron transfer step to the CYT domain. To investigate if the exchange of the CYT domain influences catalysis in the DH domain, we determined the pH optima, steady-state catalytic constants, and presteady-state rates for the two wild-type CDHs and the four chimeric CDHs. The pH optimum of the catalytic reaction with cellobiose and 2,6-dichloroindophenol resulted in bell-shaped pH profiles with optima between 4.5–5.5 (**Figs. 2A,B**). In comparison with the wild-type enzymes, the chimeric CDHs show a slight shift of the pH optimum, narrower peaks, and a reduced activity above pH 7. The presence of CYT_B in chimeric enzymes based on DH_A lowers the pH optimum, whereas the presence of CYT_A increases the pH optimum of DH_B-based chimeric enzymes. The catalytic constants and presteady-state rates were determined at pH 6.0 (**Fig. 2C, Table 1**). At this pH optimal CDH-LPMO interaction was observed [5], which is important for later experiments. The determined K_M and k_{cat} of CDH_{AAA} for cellobiose are both about four times higher than that of CDH_{BBB}, which results in the same catalytic efficiency. In the presence of CYT_B the K_M and k_{cat} of DH_A are slightly lower compared to CDH_{AAA}, whereas the presence of CYT_A has no significant effect on the K_M and k_{cat} of DH_B compared to CDH_{BBB}. The catalytic efficiencies at pH 6.0 are similar for all wild-type and chimeric CDHs, which renders this pH suitable for studying the subsequent IDET and IPET steps. The presteady-state reduction rates of FAD at 449 nm (**Fig. 2C**, k_{obs}^{449}) and the thereof extrapolated limiting rates for infinite substrate concentration (**Table 1**, k_{lim}^{449}) show that enzymes with a DH_A domain oxidized cellobiose ~2.5 times faster than enzymes with a DH_B domain, but no influence of the swapped CYT domains is observed. The k_{obs}^{449} plotted vs. the cellobiose concentration indicates a higher substrate affinity of the DH_B active site, which is in agreement with the results from steady-state analysis. The performed experiments show that

the reductive-half reaction of DH is not affected by a swap in the cytochrome domain, but in the oxidative-half reaction the activity with the electron acceptor 2,6-dichloroindophenol is slightly influenced by the swap of the CYT domain.

Cofactor redox potentials in chimeric CDH—

The FAD and heme *b* cofactor in CDH make close contact (~9 Å edge-to-edge distance) in the enzyme's closed-state. To determine if a domain swap influences the cofactor redox potentials the midpoint redox potentials of FAD (**Table 1**) and heme *b* (**Table 2**) for the wild-type and chimeric CDHs were determined to identify possible differences, which could influence IDET and IPET rates. However, no significant change was found. The midpoint redox potentials of FAD in all CDHs were between 24–43 mV vs. . standard hydrogen electrode (SHE). The spectroelectrochemical measurement of the relatively low FAD absorbance in the presence of the strong CYT Soret-band resulted in bigger errors for enzyme solutions with a lower enzyme concentration. The low amount of purified CDH_{AAB} did not allow the determination of its FAD redox potential. In contrast to the similar redox potential of FAD in DH_A and DH_B, the heme *b* redox potential in the CYT domains differs by about 60 mV. While CYT_A showed little modulation of its redox potential in wild-type and chimeric CDHs (~97–103 mV vs. SHE), the CYT_B redox potentials were slightly increased (169 and 172 mV vs. SHE) in the chimeric CDHs compared to wild-type CDH_{BBB} (158 mV vs. SHE).

Interdomain electron transfer in chimeric CDHs—

Cellobiose oxidation in the DH domain is followed by IDET from the $FADH_2$ or $FADH^{\bullet}$ semiquinone to the oxidized heme *b*. Steady-state kinetic measurements with cellobiose and the one-electron acceptor cytochrome *c,* which interacts only with CYT but not with the DH domain, were used to compare wild-type and chimeric CDHs (**Fig. 3A, Table 2**). The

cytochrome *c* turnover number (TN) of CDH_{AAA} was about 3.5-fold higher than that of CDH_{BBB}, which corresponds to the faster catalytic turnover found for DH_A. All chimeric CDHs exhibit lower cytochrome *c* TNs than the wild-type CDHs, but it is surprising that for three out of the four the reduction is only 4–12-fold and not an almost complete shut-down of the IDET (~150-fold reduction) as for CDH_{BBA}. This indicates two points: (i) a relatively good compatibility of the unfamiliar CYT domain despite their low sequence identity of 42% and (ii) the influence of the linker on the CYT-DH interaction, which is demonstrated by the reduced IDET of chimeric CDHs featuring the longer $Linker_B$. The pH optimum of the IDET was partially influenced by domain swapping. The wild-type CDH_{BBB} has a lower pH optimum (4.5) than CDH_{AAA}, but exhibits a plateau until pH 8.0. The pH optimum of chimeric CDHs is identical or close to that of the respective DH domain, which can be explained by the isoelectric points of CYT and DH domains in CDH. The CYT domain in CDHs has typically a very low pI of ~3, whereas the DH domains have a pI of ~5 [43]. The deprotonation of acidic amino acid residues on the DH domain close to the CYT-DH interface generates electrostatic repulsion of the strongly negatively charged CYT domain. Interestingly, the for CDH_{BBB} observed plateau of IDET is also found in CDH_{BBA} and CDH_{BAA} and thus seems to be a feature of CYT_B.

Although the interprotein electron transfer (IPET) between CYT and cytochrome *c* is very fast [17–19], it could still influence the observed IDET rate. Therefore, we measured also the transient reduction rate of the heme *b* cofactor to avoid a possibly rate-limiting step. This direct measurement of IDET in CDH was performed by stopped-flow spectrophotometry at 563 nm to observe the reduction of the heme *b* α-peak (**Figs. 3B, 3C, Table 2**). The observed transient rates show exactly the same trends as the steady-state rates ensuring that the cytochrome *c* assay provides a good estimation for the IDET rate in CDH. As expected, the IDET rate (k_{obs}^{563}) of all CDHs is slower than the respective FAD reduction rate (k_{obs}^{449}).

However, in case of CDH_{AAA}, k_{obs}^{563} is 50 s^{-1} and very close to k_{obs}^{449} (80 s^{-1}). In this case a limitation of the IDET at low cellobiose concentrations (<1 mM) was observed. For CDH_{BBB} and all chimeric CDHs a much slower IDET was observed and therefore limitation was found for substrate concentrations down to 50 µM. Taking into account that the redox potential difference between CYT_A and DH_A (~102 mV) is lower than for CYT_B and DH_A or DH_B (~158 mV), the thermodynamic driving force between the cofactors obviously plays no role for the IDET rate. This exciting observation was further investigated by calculating of the electron transfer rate based on the Marcus theory of electron tunneling. A modified version used by Dutton and coworkers [20,21] was applied using reported maximum, average, and minimum values for the quantum mechanical constants (λ, B, E) for the calculation of the corresponding distance-dependent electron transfer rates. The edge-to-edge distance between the FAD and the heme *b* propionate A in docking models of CDH_{AAA} and CDH_{BBB} is 0.8 and 0.9 nm, respectively (**Fig. 4**). This corresponds to theoretical IDET rates in the order of 10^5–10^6 s^{-1}, which are at least four orders of magnitude faster than the measured IDET rates.

Considering the observed mobility of the linker and CYT domain in CDH we postulate that this large difference between the calculated and the measured rates is due conformational changes: the transition between the open- and closed-state of the CYT domain. The optimal, closest possible distance between the FAD and heme *b* cofactors depends on the correct orientation of the CYT domain at its DH domain interface. The open-state distance between the cofactors can easily exceed 1.5 nm and shut-down IDET. With IDET depending on the closed-state, or at least a very close proximity between DH and CYT, a steric mismatch between the domain surfaces, repulsive electrostatic interactions, or a linker that provides too much mobility will reduce IDET. This is verified by inspection of the k_{obs}^{563} rates for both evolved wild-type CDHs and the chimeric CDHs (**Table 2**). The IPET for the constructed

chimeric enzymes decreased by one order of magnitude for CDH_{AAB}, CDH_{ABB}, and CDH_{BAA} and two orders of magnitude for CDH_{BBA}.

Based on the steady-state catalytic constants and k_{obs}^{563}, a limiting substrate concentration above which the IDET limits the catalytic rate can be calculated. For the naturally occurring *Nc*CDH_{AAA} and *Nc*CDH_{BBB} already low cellobiose concentrations (55 and 35 μM, respectively) ensure that both CDHs reach their maximum IDET rate, which is the prerequisite of efficient LPMO reduction.

Evaluation of the DH-CYT interaction site by docking—

The program HADDOCK [22,23] was used to determine the interface of the four possible CYT-DH combinations found in the wild-type and chimeric enzymes by ambiguous restraint driven docking. A sample size of 200 docking poses for each CYT-DH pair was used for analysis. A "rotation" angle is used to define the rotation of CYT around a defined interdomain axis (**Fig. 5A, Table S2**) in regard to DH, relative to the corresponding angle observed in the closed-state *Myriococcum thermophilum* CDH structure (PDB: 4QI6). Similarly, we used the terms "declination" to describe the vertical offset angle, and "inclination" to describe the horizontal offset angle of the docked CYT domain relative to the DH domain. The feasibility of docking poses was further assessed by considering the maximal extension of $Linker_A$ and $Linker_B$, which was estimated to be 6 and 11 nm, respectively. By using the distance field reaction coordinate as implemented in the GROMOS++ software [24,25], the shortest curved distance between the C-terminus of the CYT domain and the N-terminus of the DH domain, not passing through the protein was computed. Docking poses in which this distance was longer than the maximal extension of the linker were excluded from subsequent analysis (**Fig. 5B**, grey squares). The pH dependent surface charges of the domains were calculated from pH 4–8 (**Fig. S3**) and the protonation

states corresponding to pH 6.0 were used for the docking. For this pH, the contribution of the van-der-Waals energy to the protein-protein interaction (-158.14 ± 62.2 kJ.mol^{-1}) is generally 4–5 times higher than the electrostatic energy (-36.79 ± 20.9 kJ.mol^{-1}), which indicates the importance of structurally complementary domain surfaces. A comparison of CDH_{AAA} and CDH_{BBB} shows that the declination and inclination angles of the 200 docking positions are narrower for CDH_{AAA} which is indicative of a sterically more defined CYT-DH interaction. In CDH_{AAA} the CYT rotation around the rotation axis is well-defined by two groups with angles at -5 ± 15° and 25 ± 15°. The rotational position at 19.5° is preferred, since it exhibits the strongest van-der-Waals and electrostatic interaction energies. In CDH_{BBB} the docked rotational positions fall further apart (40±50°, 110±20°) indicating a less directed interaction and a lower complementarity of the domain surfaces. The interaction energies are less favorable than in CDH_{AAA}. Interestingly, the energetically most favorable docking position of CYT and DH at in CDH_{BBB} is not feasible due to the restricting length of the linker. This particular position with a rotation angle of –144.5° corresponds to an almost 180° rotation of the allowed rotational position with the second lowest van-der-Waals energy.

In chimeric CDHs the linker plays an important role. The shorter $Linker_A$ restricts the angular CYT orientation in CDH_{BAA} and CDH_{AAB} much more than the longer $Linker_B$ in CDH_{BBA} and CDH_{ABB}. Only one angular orientation at 45±25° is allowed by the length of $Linker_A$, while the longer $Linker_B$ allows for rotational positions between 45±25° and 110±40°. In case of CDH_{BBA} (k_{obs}^{563} = 0.04 s^{-1}), the rotational orientation of CYT_B against DH_A at 126.3° is strongly preferred in terms of interaction energies (E_{vdW}: -300.7 kJ.mol^{-1}; E_{Elec} -40.4 kJ.mol^{-1}) over rotational position at 32.7° (which is the IDET competent orientation in CDH_{BAA}), which has less favorable interaction energies (E_{vdW}: -176.8 kJ.mol^{-1}; E_{Elec}: -22.8 kJ.mol^{-1}). The steric restriction provided by $Linker_A$ prevents the CYT in CDH_{BAA} to bind in a noncompetent position and thereby increases IDET (k_{obs}^{563} = 0.4 s^{-1}).

The average contact surface area for all possible complexes was calculated and averaged for each CYT-DH combination as well as the binding affinity, which was calculated with PRODIGY [26–28] (**Table S3**). The averaged contact surface areas correspond to ~4% of the total DH surface area and ~9% of the total CYT surface area. The small interaction site and low calculated affinities of the CYT-DH complexes (K_D = 3.2–47 µM) suggest a relatively transient and reversible interaction when compared to other redox proteins [29].

Interaction site of CYT with LPMO—

Two interaction sites CDH's CYT domain with LPMO have been proposed in literature based on computational docking. One potential interaction site has been proposed to be opposite to LPMO's type-2 copper center around a conserved Pro-Gly-Pro patch, which requires long range electron transfer through LPMO, but would allow the reduction of the substrate bound LPMO. Another study suggested a direct interaction of heme *b* in CYT with the copper center of LPMO, which would necessitate the desorption of LPMO from its polymeric substrate. This mode would require no long range electron transfer through the LPMO molecule [8]. To experimentally determine the protein-protein interaction site of CDH and LPMO in solution, hydrogen/deuterium exchange kinetics were followed by mass spectrometry for CDH_{AAA} and *N. crassa* LPMO9F. This particular LPMO is well suited for such an analysis since it is a small LPMO (24.8 kDa) lacking N-glycosylation, a C-terminal CBM1, and linker region which is often heavily O-glycosylated [30].

Both proteins alone or in a mixture were subjected to H/D exchange followed by online digestion with pepsin and the resulting fragments were analyzed as described previously[29]. No detectable difference in the deuteration was observed on CDH_{AAA}. This could be caused by a combination of several factors: (i) a very short-lived or weak interaction of both enzymes, (ii) the protruding heme propionate-A group being the most prominent interaction

partner leading to little involvement of other CYT residues, or (iii) the subsequent CYT-DH interaction interfering with the CYT deuteration.

For LPMO9F on the other hand, protein backbone deprotection was observed in several peptide fragments when CDH was present in the solution. Visualization on the crystal structure (4QI8)[8] shows that the perturbed protein regions occur in three loops surrounding the active site copper center (**Fig. 6**). Although deprotection by interaction is not the most common scenario in hydrogen/deuterium exchange, it has been recognized as one of the possible biologically relevant outcomes [31–33]. In the case of CDH-LPMO interaction it likely reflects the transient nature of the complex, where a short-lived interaction with the heme *b* in CYT leads to the local loosening of the structure around the copper center of LPMO and/or destabilization of the hydrogen bonding network in this region. Finally, no deuteration changes of any kind were observed around the conserved patch ^{207}Pro-Gly-Pro^{209} (**Fig. 6**) close to the C-terminus.

Heterogenous electron transfer–

CDH is recognized for its ability to directly transfer electrons to electrode surfaces via its CYT domain [34]. The heterogeneous electron transfer of wild-type and chimeric CDHs to a self-assembled monolayer (SAM) of thioglycerol on gold electrodes [6] was investigated for two reasons: (i) to verify that all produced enzymes and their domains are in their native, electron transfer competent conformation and (ii) to study the effect of swapped linkers and CYT domains on the direct electron transfer to an electrode. Unfortunately, CDH_{BBA} was not available in sufficient amounts for these experiments. In presence of 20 mM cellobiose catalytic currents were observed for all variants (**Fig. S4**). The onset potentials of the anodic waves correlate well with the corresponding, spectroelectrochemically determined CYT redox potentials. Current densities were extracted at an overpotential of 200 mV above the

midpoint potential of the CYT domain (CYT_A at 300 mV, CYT_B at 360 mV vs. SHE) and a scan rate of 15 mV s^{-1}. The highest current density was found for CDH_{AAA} (11.3 ± 1.8 µA cm^{-2}), followed by CDH_{ABB} (3.7 ± 1.5 µA cm^{-2}), CDH_{BBB} (2.6 ± 1.7 µA cm^{-2}), $CDHB_{BAA}$ (1.9 ± 0.3 µA cm^{-2}), and CDH_{AAB} (1.2 ± 1.0 µA cm^{-2}). Every CDH clearly showed direct electron transfer to the electrode and thereby verified the integrity of the electron transfer route.

Anodic and cathodic peak currents were obtained for all CDHs over a range of scan rates (3–150 mV s^{-1}). The plot of the peak currents vs. the square root of the scan rates is linear for all enzymes and indicate a freely diffusing redox species and no adsorption onto the electrode (**Fig. S5)**. The peak separation of the anodic and cathodic peak increased with increasing scan-rates (**Fig. S6**). The heterogeneous electron transfer is reversible at very low scan rates and quasi-reversible at scan rates above 5 mV s^{-1} pointing towards a fast electron transfer compared to mass transport. This allows the calculation of the heterogeneous electron transfer constant (k_0) according to the method of Nicholson and Shain for the quasi-reversible electron transfer regime [35]. All wild-type and chimeric CDHs show a similar k_0 between 2.6–5.2 10^{-4} cm s^{-1} at the most relevant scan speed for comparison (50 mV s^{-1}, **Fig. 7**), which demonstrates that there is no restrained interaction of any CYT with the thioglycerol monolayer on the gold electrode and all CDHs are functional. This is comparable with an k_0 of ca. 10^{-3}–10^{-4} for cytochrome *c* on gold electrodes [36]. CDH_{BBB} with the lowest k_0 has the least efficient electron transfer of its CYT domain with the electrode.

Interprotein electron transfer kinetics—

After verifying that the wild-type and chimeric CDHs are all similarly electron transfer competent we investigated the final electron transfer from CYT to LPMO (IPET). In sequential stopped-flow experiments, CDHs were pre-reduced by a stoichiometric amount of

cellobiose. After 90 s in the aging loop, oxygen had fully reoxidized $FADH_2$, which was necessary to prevent any interfering IDET to CYT. Then the CDH with the reduced CYT was shot against an equimolar, 3, 10, and 50-fold molar ratio of *Nc*LPMO9C to measure the IPET rate. A linear dependence of k_{obs}^{563} on LPMO concentrations was found (**Fig. 8**), which indicates that the electron transfer between both enzymes is fast enough to show no saturation even for the highest measured LPMO concentration [18]. The bimolecular IPET rate was calculated from the slope of k_{obs}^{563} versus the LPMO concentration. The determined rates are all within the same order of magnitude, which indicates that the interaction mechanism is not evolved to recognize and favor specific CDH/LPMO combinations, but is based on a universal recognition mechanism which depends little on surface complementarity. Nevertheless, significant differences in IPET were observed. CYT_B, which is present in three measured CDHs, generally exhibits a two-times faster bimolecular rate with *Nc*LPMO9C (7.4–8.8 10^5 M^{-1} s^{-1}) than CDHs with CYT_A (2.9–5.1 10^5 M^{-1} s^{-1}). CDH_{AAA} with the fastest IDET exhibits the slowest IPET, because of a preferentially closed-state conformation. CDH_{BBA}, which cannot easily achieve an IDET competent closed-state conformation exhibits the fasted IPET, because of a preferential open-state conformation.

The redox potential difference between the cofactors correlates negatively with the IPET rate. CYT_B with its higher midpoint potential compared to CYT_A has a comparatively lower driving force for electron transfer between the heme *b* and the type-2 copper, but shows the higher IPET rates. This indicates that CYT/DH combinations of poor surface complementarity or with an unsuitable linker preferably populate the IPET competent open-state conformation. We conclude that the closed- and open-state distribution of CDH populations define the electron transfer rates of CYT in IDET and IPET.

DISCUSSION

The two-domain structure of CDH has been recognized soon after its discovery by observing the spectral features of its two cofactors, proteolytic cleavage into the separated domains, and distinct catalytic properties of the full-length CDH and its DH domain. The domain organization became evident with the first isolated CDH sequence of *Phanerochaete chrysosporium* [37], but the purpose of the CYT domain remained unknown. Crystallization experiments in which only the separated, proteolytically generated CYT and DH domains formed crystals indicated the high mobility of the linker and CYT domain [38,39]. At the same time Igarashi et al. investigated the pH-dependence of the IDET between the DH and CYT domain of *P. chrysosporium* CDH in a presteady-state kinetic study and determined the redox potential of the heme *b* and FAD cofactor, which is the driving force of IDET [9].

However, the physiological function of the CYT domain and the highly variable length of the linker in CDHs (16–40 amino acids) remained enigmatic. Also the considerable length of $Linker_B$ in comparison to other flavocytochromes, e.g. flavocytochrome *b2*'s hinge (linker) region consists of only of 15 amino acids [40], is unusual. In the two CDHs from *N. crassa* $Linker_B$ is almost twice as long as $Linker_A$ and both have the lowest sequence identity (29%) of CDH's structural elements despite sharing two common features: a high percentage of serine, threonine and proline residues and a conserved Pro-Val-Pro motif. Likewise, the sequence identity of the CYT domain (43%) is low compared to that of the DH domains (60%). This higher diversity of linker and CYT sequences is observed for all CDHs and suggests an evolutionary adaptation to contact redox partner proteins while the DH domain serves as a source of electrons.

With the discovery of LPMO in 2010 [4], the physiological redox partner of CDH was finally discovered, which gives us the opportunity to study the CYT domain's IDET and IPET mechanism as part of a natural, extracellular electron transfer chain. This framework supports

the testing of hypotheses on CDH's molecular, catalytic, and electron transfer properties. Swapping domains between the structurally, catalytically and electrochemically different CDHs of one organism was chosen to differentiate the function of the involved domains and linker in the electron transfer route from CDH's $FADH_2$ to LPMO's type-2 copper center. Fortunately, all wild-type and chimeric CDHs could be recombinantly expressed in *P. pastoris* and all enzymes except CDH_{AAB} could be produced in sufficient quantity. The determined specific activities of the purified chimeric enzymes and their absorption spectra exhibit a similar activity and spectral properties compared to the wild-type CDHs and are therefore properly folded. However, a difference in the extent of glycosylation of the wild-type and chimeric CDHs was found. This variation is inevitable with the chosen yeast expression system, which is known to produce various glycoforms. However, the N-glycosylation sites are not located at the DH-CYT interface and thus should not affect the performed experiments. O-glycosylation of the linker was previously reported [41], but we lacked the resources to determine if this minor fraction of glycosides varied between the produced CDHs. The determined heterogeneous electron transfer rates for all CDHs were relatively similar and indicated no significant influence of the glycosylation on the interaction with the thioglycerol-modified gold electrode.

Kinetic studies of the catalytic reaction of the DH domain showed no change in the reductive half-reaction in chimeric CDHs, but showed an effect of the swapped CYT domains on the oxidative half-reaction by shifting the pH optima for the two-electron acceptor 2,6-dichloroindophenol. Since the pH optimum of the catalytic reaction in CDH depends on the electron acceptor [42,43] this clearly indicates the CYT domain's influence on the oxidative catalytic half-reaction. The pH optima of CDH_{AAA} and CDH_{BBB} are identical to previous data [6]. These results support the previously observed effect of the CYT domain influencing on the catalytic step in the DH domain of *M. thermophilum* CDH [10]. At pH 6.0, which is also the pH

optimum of the CDH-LPMO interaction [5], only small differences between the catalytic efficiency were observed between the wild-type and chimeric CDHs. This pH turned out to be suitable to study the subsequent electron transfer steps. The presteady-state reduction rates of FAD by cellobiose at 449 nm (k_{obs}^{449}) show a clear separation between enzymes with a DH_A domain (80–82 s^{-1}) and a DH_B domain (30–33 s^{-1}), but no effect on a CYT swap on the rate of the reductive-half reaction.

While the effects of the domain swap on the catalysis of the chimeric enzymes was moderate, the IDET between DH and CYT was strongly affected. Steady-state experiments showed different pH optima and a 4–12 times (with the exception of CDH_{BBA}) reduced TN of the chimeric CDHs with cytochrome *c*. These findings were corroborated by transient-state findings. The highest IDET rates were measured by stopped-flow spectroscopy for wild-type enzymes, which had a 125 times (CDH_{AAA}) or 10 times (CDH_{BBB}) higher IDET rate than the successive chimeric enzyme. Modelling studies showed the importance of surface complementarity and the degree of orientational freedom provided by the linker. Given the length of $Linker_A$ (7 nm) and $Linker_B$ (11 nm) it can be expected that in the open-state the distance limit for a reasonable fast electron transfer (~1.5 nm) between CYT and DH is often exceeded. It was also found that the redox potential difference between CYT and DH is not the dominant driving force for IDET, since CDHs with a CYT_A have a lower ΔE (64–104 mV) between the cofactors than CYT_B carrying CDHs (158–172 mV), but similar or faster IDET rates. The reason is the close edge-to-edge distance between the FAD and heme. For the typical distance of ~0.9 nm in *N. crassa* CDH's closed-state, the electron transfer rates are 10^5 times higher than the measured rates. This means that the mobility of the CYT domain between closed- and open-state conformation is the rate-limiting factor of IDET and not the electron transfer event itself. A shorter linker ($Linker_A$) and a higher complementarity at the CYT-DH interface increases IDET by supporting the closed-state of the CDH.

The efficiency of the subsequent electron transfer step from CYT to LPMO, the IPET, is most important for the overall rate of the process and determines the rate of the oxidative depolymerization of polysaccharides. A specific and fast IPET saves valuable resources for the metabolism of the cellulolytic organism (less enzymatic consumption of cellobiose, less secreted CDH needed) and prevents futile electron transfer to other molecules which reduces not only the efficiency of the extracellular electron transfer system, but could also produce degradation products detrimental to the organism's growth. The performed HDX-MS experiments also indicated the interaction of CYT and LPMO to happen via a direct contact between their active centers. The observed interaction is relatively weak and brief, underlining a flexible and transient complex formation, which fits well with the necessity of LPMO to detach and reattach to cellulose in order to get reduced. The apparent transient interaction also complements all previous findings hinting at a very dynamic system which depends on interplay between electrostatic forces of cofactors and thermodynamic forces governing domain movements.

The IPET rates all have the same order of magnitude, which indicates that the interaction mechanism is not evolved to recognize and favor specific CDH/LPMO combinations, but is based on a universal recognition mechanism between the heme *b* propionate A and the copper center, which depends little on surface complementarity [15]. This is corroborated by reports on the interaction of different CDHs and LPMOs from *N. crassa* [5], CDH and LPMO from different fungi [1,2] and even from fungal CDH to bacterial LPMOs [44]. The measured bimolecular rates for the final electron transfer step from CYT to LPMO were found to be very fast with values between 2.9–8.8 10^5 M^{-1} s^{-1}. A similar rates was also found for the very fast CYT-cytochrome *c* interaction (10^6 M^{-1} s^{-1})[18]. We can conclude that the rate determining driving force for IPET is not the redox potential difference between LPMO and CYT, since CDHs with a CYT_B have a lower ΔE to LPMO but exhibit higher rates. The linker length

plays also no detectable role. However, the higher IPET rates obtained for all CDHs with a CYT_B (1.5–3 times faster than CYT_A rates) suggest that it is better adapted for the interaction with NcLPMO9C than CYT_A although only a very small surface area of the proteins is involved in the interaction [15]. The higher IPET of the chimeric CDHs over the wild-type CDHs points towards a higher preference of the open-state conformation.

EXPERIMENTAL PROCEDURES

Molecular biology, expression and purification

Genetic constructs of *cdhIIA* (NCU00206) and *cdhIIB* (NCU05923) were described previously [6] and used for this study. A silent mutation (C456T) was introduced to the gene NCU05923 to delete the BstBI (Bsp119I) restriction site. Alignments using MEGA 6 [45] applying the BLOSSOM 62 algorithm together with 3D structure analysis of NCU00206 (PDB 4QIU7) were applied to define exact borders of the individual domains (**Table S4**). Fragments of the individual domains were generated and joined to generate four chimeric constructs by overlap extension PCR. The genetic integrity of the amplicons encoding chimeric CDHs was checked by DNA sequencing at Microsynth (Wolfurt, Austria). Following established methods [46] the constructs were expressed in a *Pichia pastoris* expression system (KM71H, Invitrogen). Best producing variants were preselected (Weis et al.) cultivated in 500 mL scale fermentation (**Fig. S1**) and purified by hydrophobic interaction (PHE-Sepharose Fast Flow, GE Healthcare) and anion exchange chromatography (Qsource15, GE Healthcare). Two chimeric CDHs (CDH_{AAB} and CDH_{BBA}), still containing minor impurities after these two steps, were subjected to additional size exclusion chromatography (Superdex 75). SDS-PAGE analysis of all preparations used in this study is displayed in **Fig. 1**.

Enzyme activity assays and protein quantitation

The activity of CDHs was determined in 1 mL assays by following the reduction of either 0.3 mM 2,6-dichloroindophenol (DCIP, ε_{520} = 6.8 mM^{-1} cm^{-1}) or 50 µM cytochrome *c* from equine heart (ε_{550} = 19.6 mM^{-1} cm^{-1}). Assays were buffered with 100 mM sodium citrate-phosphate buffer according to [47] at the indicated pH. The pH dependent activity was

measured with 30 mM lactose as saturating substrate. Assay reactions were monitored for 180 s at 30 °C at the indicated absorption maxima wavelengths in a Lambda 35 UV-visible (UV-Vis) spectrophotometer equipped with a temperature-controlled 8-cell changer (Perkin-Elmer). The protein concentration of wild-type and chimeric CDHs was determined via the absorbance at 280 nm and the theoretical molar absorption coefficient ε_{280} calculated with the Expasy Prot-Param program (http://web.expasy.org/protparam/) using the mature amino acid sequence.

Spectroelectrochemistry

Spectroelectrochemical experiments were done using 500 µL samples containing around 50 µM wild-type or chimeric CDH, 100 mM KCl, 100 mM potassium phosphate buffer pH 6.0, and a redox mediator mixture comprising anthraquinone-1,5-disulfonate, 2-hydroxy-1,4-naphtoquinone, indigo carmine, indigotrisulfonate, duroquinone, methylene blue, phenazine methosulfate, 1,2-naphtoquinone and N,N,N',N'-tetramethyl-*p*-phenylenediamine (all 3 µM), and methyl viologen (150 µM). All experiments were carried out under anaerobic conditions at 30 °C in a thin layer (d = 0.05 mm) spectroelectrochemical cell (BASi, West Lafayette, IN; USA) with a standard three – electrode setup comprising a Ag|AgCl – reference electrode (BASi), a platinum gauze (Goodfellow Cambridge Ltd., Huntington, England, UK) as working electrode, and a platinum wire (Goodfellow Cambridge Ltd.) as auxiliary electrode. A Whitley DG 250 Anaerobic Workstation (Don Whitley Scientific Ltd., Shipley, England, UK) was used to work under oxygen free conditions. The reference electrode was calibrated against a saturated calomel electrode. All potentials are reported relative to the standard hydrogen electrode (SHE). Nernst plots consisted of at least 5 data points, showed linear behavior and were consistent with a one-electron redox process in case of the heme *b*, and a two-electron process in case of the FAD.

Voltammetry

Preparation of enzyme modified electrodes started with the cleaning of gold disk-electrodes (d = 1.6 mm, BASi, West Lafayette, IN, USA) by dipping in acidic Piranha solution (H_2SO_4:H_2O_2 = 3:1 (V/V)) for 5 min, cycling in 0.1 M NaOH (-0.205 to -1.205 V vs. Ag|AgCl, 10 cycles, 100 mV s^{-1}), polishing to mirror finish with aqueous alumina particles (0.05 µm) on a MicroCloth (Buehler, Lake Bluff, IL, USA), ultrasonication to get rid of residual polishing particles and cycling in 0.5 M H_2SO_4 (-0.205 to +1.705 V vs. Ag|AgCl, 20 cycles, 200 mV s^{-1}). After rinsing with ultrapure water and drying with nitrogen gas the electrodes were immersed overnight in 10 mM 1-thioglycerol dissolved in absolute ethanol for SAM formation. The electrodes were then washed with 20% ethanol to remove unbound thioglycerol, ultrapure water and dried over a stream of nitrogen gas. A custom-made Teflon holder was put over the electrode surface, leaving a cylindrical cavity with a volume of ~20 µL above the thioglycerol-modified gold surface. Then, a 100 µM CDH solution in 100 mM McIlvaine buffer, pH 6.0, was applied to the cavity. The assembly was covered with a dialysis membrane (45 kDa cut-off) held in place via a rubber O-ring.

Electrochemical experiments were carried out using a PGSTAT204 potentiostat/galvanostat (Metrohm Inula GmbH, Vienna, Austria) with a standard three-electrode setup comprising the enzyme-modified gold electrode as working electrode, a platinum wire as counter electrode, and an Ag|AgCl electrode as reference electrode. The 100 mM McIlvaine buffer, pH 6.0 contained 0.1 M KCl as supporting electrolyte. A typical set of experiments comprised cyclic voltammetry of the thioglycerol-modified electrode (blank), the enzyme-modified thioglycerol-electrode, the enzyme-modified thioglycerol-electrode in presence of 20 mM cellobiose, and the enzyme-modified thioglycerol-electrode in presence of 20 mM cellobiose

and 50 µM ferrocenemethanol. The applied potential window ranged from 5–550 mV vs. SHE. Scan rates were varied from 3–500 mV s^{-1}. Before the start of the experiment the electrochemical cell containing buffer and the electrode setup was deoxygenated by purging with argon gas for 15 min. The bulk solution was not agitated during the measurement which was performed at 30 °C.

Cyclic voltammograms were analyzed using the NOVA software (Metrohm) and Microsoft Excel. The evaluation whether freely diffusing or adsorbed CDH species dominate the electrochemical process was done by assessing the linearity of plots of peak current vs. the square root of the scan rate. Reversibility, quasi-reversibility, or irreversibility of the electron transfer process was assessed by the shape of the voltammograms and the peak-to-peak separation. Standard heterogeneous electron transfer rate constants k_0 were calculated using the model for quasi-reversible processes described by [48] Nicholson & Shain and [49] Matsuda & Ayabe with a transfer coefficient of $\alpha = 0.5$ and interpolated values ($\Psi = 1/(-2.46+0.041*dEp)$) of the kinetic parameter Ψ for the scan rate dependent peak potential separation. Diffusion coefficients for CDH were calculated from the slope of the linear correlation of the anodic or cathodic peak currents, the square root of the scan rate, the active electrode surface area ($A = 0.0177$ cm^2), and an enzyme concentration of 100 µM (10^{-7} mol cm^{-3}) applying the Randles-Sevcik equation [50,51]. Peak currents were assessed by applying Nicholson's empiric equation $Ipa/Ipc = (Ipa)0/Ipc+0.485(Isp)0/Ipc+0.086$ [35].

Presteady-state kinetic studies

The rapid spectral changes induced by substrate oxidation and resulting change of redox state of the CDH cofactors were followed with an SX 20 stopped-flow instrument (Applied Photophysics, Leatherhead, UK) equipped with a photomultiplier tube (AP/PMT.R928). The

redox state of the FAD cofactor was monitored at the appropriate isosbestic point (449 nm) of the heme cofactor which itself was monitored at 563 nm. Observed rates (k_{obs}) for the indicated cellobiose concentrations were estimated by fitting the data to a single exponential curve. The reduction of *Nc*LPMO9C by CDH was studied using a UV-Vis photodiode array detector (AP/SXPDAUV) and sequential mixing mode. CDH was reduced in a first step by mixing with an appropriate concentration of cellobiose. Upon depletion of electrons from the FAD by means of oxygen reactivity, in a sequential step, CDH was rapidly mixed with *Nc*LPMO9C. The observed rates of transfer were estimated by following the redox state of the cytochrome domain of CDH and fitting the data of A_{563} to a single exponential curve. All presteady-state experiments were performed in 100 mM sodium citrate-phosphate buffer, pH 6.0 at 30 °C.

Modelling of CDH chimeras

SWISS-MODEL [52–54] was used to generate homology models for the cytochrome (CYT) and dehydrogenase (DH) domains of *Nc*CDHIIB (ORF: NCU05923), considering the crystal structure of *Nc*CDHIIA (PDB: 4QI7) [55] as template. Steepest descent energy minimization with 2500 steps (initial step size of 0.1 nm) was performed with the GROMOS software package for molecular simulation [56] using the 54a7 force field [57,58] as a further refinement for the resulting homology models. Subsequently, the complexes CYT_A-DH_A, CYT_A-DH_B, CYT_B-DH_A, and CYT_B-DH_B have been modelled using HADDOCK 2.2 [22,23] with interaction restraints between heme *b* and the Arg697 and Arg719 for *Nc*CDHIIA and *Nc*CDHIIB, respectively. The number of starting structures was set to 1000 and refined to 200 structures. Non-bonded energy values (i.e. van der Waals and electrostatic energies) were taken from the HADDOCK output and the angles of the CYT domain relative to the DH domain around three axes defined by two (virtual) atoms j and k, was measured by computing the dihedral

angle i – j – k – l, with the (virtual) atoms defined in **Table S2**. The distance-field reaction coordinate [25] was used to estimate the shortest distance between the linker anchor points, along a path that does not pass through the protein domains. Electrostatic surface representations as well as protonation states were computed with PROPKA 3.1 [59,60], PDB2PQR [61] and the PyMOL APBS plug-in [62–66]. Binding affinities were predicted with PRODIGY [67–69].

Hydrogen/deuterium exchange mass spectrometry

Prior to the mass spectrometric analyses, *Nc*CDHIIA was deglycosylated under non-denaturing conditions as utilized previously for the analyses of CDH from *M. thermophilum* [31]. CDH was incubated overnight with 15 U Endo Hf (New England Biolabs, USA) per 1 µg protein at 37 °C in 50 mM sodium acetate buffer pH 5.75 to detach the N-glycans. The deglycosylated CDH was preincubated alone or in a mixture with *Nc*LPMO9F (1:3 and 3:1 molar ratios) in H_2O-based 50 mM sodium acetate buffer pH 5.75 for 30 minutes. After preincubation, the deuterium labeling was started by a 10-fold dilution of the protein samples into deuterated buffer (50 mM sodium acetate pD 5.75). The final protein concentration during the labeling was 5 µM for the examined protein and 15 µM for the interaction partner. The deuteration reaction proceeded at 21 °C and 50 µl aliquots were removed after 0.33, 1, 3, 10, 30, 60, 180 and 300 minutes. The rest of the HDX-MS workflow including the stopping of the exchange in the aliquots, denaturation of samples and their online enzymatic digestion by immobilized porcine pepsin, LC-MS analysis by Fourier transform ion cyclotron resonance mass spectrometer and data processing was performed exactly as optimized for *M. thermophilum* CDH and described elsewhere [31].

ACKNOWLEDGMENTS

CONFLICT OF INTEREST

The authors declare that they have no conflicts of interest with the contents of this article.

AUTHOR INFORMATION

Corresponding Author

To whom correspondence should be addressed: Roland Ludwig (E-mail: roland.ludwig@boku.ac.at; Telephone: +431 47654 75216)

Author contributions

A.K.G.F. wrote the first draft of the manuscript and performed together with C.S. and C.Syg. the production and purification of chimeric CDHs and steady-state kinetic measurements. C.V.F.P. and C.O. performed and interpreted docking and modelling studies. A.K., F.F., P.M. and P.H. performed and analysed H/D exchange experiments, D.K. performed and analyzed fast-kinetic experiments, S.Sch., L.S. and F.S. performed and analyzed electrochemical experiments. R.L. initiated the study, designed experiments, evaluated and interpreted data, and wrote the final draft of the manuscript together with C.O, P.M. and P.H.

Funding Sources

This work was funded by the Austrian Science Fund (project I2385-N28) and the Czech Science Foundation (projects 16-34818L). A.K.G.F. was supported by a scholarship of the Austrian Academy of Sciences (DOC scholarship), S.S. by the Austrian-Singapore Graduate School programme and C.V.F.P.L., L.S., F.S. and D.K. by the doctoral programme BioToP (W1224) funded by the Austrian Science Fund. A.K.G.F. was supported by a Doc fellowship

of the Austrian Academy of Science. Access to the MS facility was enabled by MEYS CR (CZ.1.05/1.1.00/02.0109, LQ1604 and LM2015043 CIISB) funding.

REFERENCES

(1) Langston, J. A.; Shaghasi, T.; Abbate, E.; Xu, F.; Vlasenko, E.; Sweeney, M. D. Oxidoreductive Cellulose Depolymerization by the Enzymes Cellobiose Dehydrogenase and Glycoside Hydrolase 61. *Appl Env. Microbiol* **2011**, *77* (19), 7007–7015. https://doi.org/10.1128/AEM.05815-11.

(2) Phillips, C. M.; Beeson, W. T.; Cate, J. H.; Marletta, M. A. Cellobiose Dehydrogenase and a Copper-Dependent Polysaccharide Monooxygenase Potentiate Cellulose Degradation by *Neurospora crassa*. *ACS Chem. Biol.* **2011**, *6* (12), 1399–1406. https://doi.org/10.1021/cb200351y.

(3) Phillips, C. M.; Iavarone, A. T.; Marletta, M. A. Quantitative Proteomic Approach for Cellulose Degradation by *Neurospora crassa*. *J. Proteome Res.* **2011**, *10* (9), 4177–4185. https://doi.org/10.1021/pr200329b.

(4) Harris, P. V.; Welner, D.; McFarland, K. C.; Re, E.; Navarro Poulsen, J.-C.; Brown, K.; Salbo, R.; Ding, H.; Vlasenko, E.; Merino, S.; et al. Stimulation of Lignocellulosic Biomass Hydrolysis by Proteins of Glycoside Hydrolase Family 61: Structure and Function of a Large, Enigmatic Family. *Biochemistry* **2010**, *49* (15), 3305–3316. https://doi.org/10.1021/bi100009p.

(5) Kracher, D.; Scheiblbrandner, S.; Felice, A. K. G.; Breslmayr, E.; Preims, M.; Ludwicka, K.; Haltrich, D.; Eijsink, V. G. H.; Ludwig, R. Extracellular Electron Transfer Systems Fuel Cellulose Oxidative Degradation. *Science* **2016**, *352* (6289), 1098–1101. https://doi.org/10.1126/science.aaf3165.

(6) Sygmund, C.; Kracher, D.; Scheiblbrandner, S.; Zahma, K.; Felice, A. K. G.; Harreither, W.; Kittl, R.; Ludwig, R. Characterization of the Two *Neurospora crassa* Cellobiose Dehydrogenases and Their Connection to Oxidative Cellulose Degradation. *Appl. Environ. Microbiol.* **2012**, *78* (17), 6161–6171. https://doi.org/10.1128/AEM.01503-12.

(7) Igarashi, K.; Yoshida, M.; Matsumura, H.; Nakamura, N.; Ohno, H.; Samejima, M.; Nishino, T. Electron Transfer Chain Reaction of the Extracellular Flavocytochrome Cellobiose Dehydrogenase from the Basidiomycete *Phanerochaete chrysosporium*. *FEBS J.* **2005**, *272* (11), 2869–2877.

(8) Tan, T.-C.; Kracher, D.; Gandini, R.; Sygmund, C.; Kittl, R.; Haltrich, D.; Hällberg, B. M.; Ludwig, R.; Divne, C. Structural Basis for Cellobiose Dehydrogenase Action during Oxidative Cellulose Degradation. *Nat. Commun.* **2015**, *6*. https://doi.org/10.1038/ncomms8542.

(9) Igarashi, K.; Momohara, I.; Nishino, T.; Samejima, M. Kinetics of Inter-Domain Electron Transfer in Flavocytochrome Cellobiose Dehydrogenase from the White-Rot Fungus *Phanerochaete chrysosporium*. *Biochem. J.* **2002**, *365* (Pt 2), 521.

(10) Kracher, D.; Zahma, K.; Schulz, C.; Sygmund, C.; Gorton, L.; Ludwig, R. Inter-Domain Electron Transfer in Cellobiose Dehydrogenase: Modulation by pH and Divalent Cations. *FEBS J.* **2015**, *282* (16), 3136–3148. https://doi.org/10.1111/febs.13310.

(11) Bodenheimer, A. M.; O'Dell, W. B.; Oliver, R. C.; Qian, S.; Stanley, C. B.; Meilleur, F. Structural Investigation of Cellobiose Dehydrogenase IIA: Insights from Small Angle Scattering into Intra- and Intermolecular Electron Transfer Mechanisms. *Biochim. Biophys. Acta Gen. Subj.* **2018**, *1862* (4), 1031–1039. https://doi.org/10.1016/j.bbagen.2018.01.016.

(12) Bodenheimer, A. M.; O'Dell, W. B.; Stanley, C. B.; Meilleur, F. Structural Studies of *Neurospora crassa* LPMO9D and Redox Partner CDHIIA Using Neutron Crystallography and Small-Angle Scattering. *Carbohydr. Res.* **2017**, *448*, 200–204. https://doi.org/10.1016/j.carres.2017.03.001.

(13) Harada, H.; Onoda, A.; Uchihashi, T.; Watanabe, H.; Sunagawa, N.; Samejima, M.; Igarashi, K.; Hayashi, T. Interdomain Flip-Flop Motion Visualized in Flavocytochrome Cellobiose Dehydrogenase Using High-Speed Atomic Force Microscopy during Catalysis. *Chem. Sci.* **2017**, *8* (9), 6561–6565. https://doi.org/10.1039/C7SC01672G.

(14) Courtade, G.; Wimmer, R.; Røhr, Å. K.; Preims, M.; Felice, A. K. G.; Dimarogona, M.; Vaaje-Kolstad, G.; Sørlie, M.; Sandgren, M.; Ludwig, R.; et al. Interactions of a Fungal Lytic Polysaccharide Monooxygenase with β-Glucan Substrates and Cellobiose Dehydrogenase. *Proc. Natl. Acad. Sci.* **2016**, *113* (21), 5922–5927. https://doi.org/10.1073/pnas.1602566113.

(15) Laurent, C. V. F. P.; Breslmayr, E.; Tunega, D.; Ludwig, R.; Oostenbrink, C. Interaction between Cellobiose Dehydrogenase and Lytic Polysaccharide Monooxygenase. *Biochemistry* **2019**, *58* (9), 1226–1235. https://doi.org/10.1021/acs.biochem.8b01178.

(16) Ortiz, R.; Matsumura, H.; Tasca, F.; Zahma, K.; Samejima, M.; Igarashi, K.; Ludwig, R.; Gorton, L. Effect of Deglycosylation of Cellobiose Dehydrogenases on the Enhancement of Direct Electron Transfer with Electrodes. *Anal. Chem.* **2012**, *84* (23), 10315–10323. https://doi.org/10.1021/ac3022899.

(17) Mason, M. G.; Wilson, M. T.; Ball, A.; Nicholls, P. Oxygen Reduction by Cellobiose Oxidoreductase: The Role of the Haem Group. *FEBS Lett.* **2002**, *518* (1–3), 29–32. https://doi.org/10.1016/S0014-5793(02)02633-9.

(18) Mason, M. G.; Nicholls, P.; Divne, C.; Hallberg, B. M.; Henriksson, G.; Wilson, M. T. The Heme Domain of Cellobiose Oxidoreductase: A One-Electron Reducing System. *Biochim. Biophys. Acta BBA - Bioenerg.* **2003**, *1604* (1), 47–54. https://doi.org/10.1016/S0005-2728(03)00023-9.

(19) Samejima, M.; Phillips, R. S.; Eriksson, K.-E. L. Cellobiose Oxidase from *Phanerochaete chrysosporium* Stopped-Flow Spectrophotometric Analysis of PH-Dependent Reduction. *FEBS Lett.* **1992**, *306* (2–3), 165–168. https://doi.org/10.1016/0014-5793(92)80991-O.

(20) Moser, C. C.; Keske, J. M.; Warncke, K.; Farid, R. S.; Dutton, P. L. Nature of Biological Electron Transfer. *Nature* **1992**, *355* (6363), 796–802. https://doi.org/10.1038/355796a0.

(21) Page, C. C.; Moser, C. C.; Chen, X.; Dutton, P. L. Natural Engineering Principles of Electron Tunnelling in Biological Oxidation–Reduction. *Nature* **1999**, *402* (6757), 47–52. https://doi.org/10.1038/46972.

(22) Dominguez, C.; Boelens, R.; Bonvin, A. M. J. J. HADDOCK: A Protein−Protein Docking Approach Based on Biochemical or Biophysical Information. *J. Am. Chem. Soc.* **2003**, *125* (7), 1731–1737. https://doi.org/10.1021/ja026939x.

(23) de Vries, S. J.; van Dijk, A. D. J.; Krzeminski, M.; van Dijk, M.; Thureau, A.; Hsu, V.; Wassenaar, T.; Bonvin, A. M. J. J. HADDOCK versus HADDOCK: New Features and Performance of HADDOCK2.0 on the CAPRI Targets. *Proteins Struct. Funct. Bioinforma.* **2007**, *69* (4), 726–733. https://doi.org/10.1002/prot.21723.

(24) Eichenberger, A. P.; Allison, J. R.; Dolenc, J.; Geerke, D. P.; Horta, B. A. C.; Meier, K.; Oostenbrink, C.; Schmid, N.; Steiner, D.; Wang, D.; et al. GROMOS++ Software for the Analysis of Biomolecular Simulation Trajectories. *J. Chem. Theory Comput.* **2011**, *7* (10), 3379–3390. https://doi.org/10.1021/ct2003622.

(25) de Ruiter, A.; Oostenbrink, C. Protein–Ligand Binding from Distancefield Distances and Hamiltonian Replica Exchange Simulations. *J. Chem. Theory Comput.* **2013**, *9* (2), 883–892. https://doi.org/10.1021/ct300967a.

(26) Xue, L. C.; Rodrigues, J. P.; Kastritis, P. L.; Bonvin, A. M.; Vangone, A. PRODIGY: A Web Server for Predicting the Binding Affinity of Protein-Protein Complexes. *Bioinforma. Oxf. Engl.* **2016**, *32* (23), 3676–3678. https://doi.org/10.1093/bioinformatics/btw514.

(27) Kastritis, P. L.; Rodrigues, J. P. G. L. M.; Folkers, G. E.; Boelens, R.; Bonvin, A. M. J. J. Proteins Feel More Than They See: Fine-Tuning of Binding Affinity by Properties of the Non-Interacting Surface. *J. Mol. Biol.* **2014**, *426* (14), 2632–2652. https://doi.org/10.1016/j.jmb.2014.04.017.

(28) Vangone, A.; Bonvin, A. M. J. J. Contacts-Based Prediction of Binding Affinity in Protein-Protein Complexes. *eLife* **2015**, *4*, e07454. https://doi.org/10.7554/eLife.07454.

(29) Janin, J.; Bahadur, R. P.; Chakrabarti, P. Protein–Protein Interaction and Quaternary Structure. *Q. Rev. Biophys.* **2008**, *41* (2), 133–180. https://doi.org/10.1017/S0033583508004708.

(30) Kittl, R.; Kracher, D.; Burgstaller, D.; Haltrich, D.; Ludwig, R. Production of Four *Neurospora crassa* Lytic Polysaccharide Monooxygenases in *Pichia pastoris* Monitored by a Fluorimetric Assay. *Biotechnol. Biofuels* **2012**, *5* (1), 79. https://doi.org/10.1186/1754-6834-5-79.

(31) Kadek, A.; Kavan, D.; Felice, A. K. G.; Ludwig, R.; Halada, P.; Man, P. Structural Insight into the Calcium Ion Modulated Interdomain Electron Transfer in Cellobiose Dehydrogenase. *FEBS Lett.* **2015**, *589* (11), 1194–1199. https://doi.org/10.1016/j.febslet.2015.03.029.

(32) Konermann, L.; Vahidi, S.; Sowole, M. A. Mass Spectrometry Methods for Studying Structure and Dynamics of Biological Macromolecules. *Anal. Chem.* **2014**, *86* (1), 213–232. https://doi.org/10.1021/ac4039306.

(33) Sowole, M. A.; Konermann, L. Effects of Protein–Ligand Interactions on Hydrogen/Deuterium Exchange Kinetics: Canonical and Noncanonical Scenarios. *Anal. Chem.* **2014**, *86* (13), 6715–6722. https://doi.org/10.1021/ac501849n.

(34) Lindgren, A.; Larsson, T.; Ruzgas, T.; Gorton, L. Direct Electron Transfer between the Heme of Cellobiose Dehydrogenase and Thiol Modified Gold Electrodes. *J. Electroanal. Chem.* **2000**, *494* (2), 105–113. https://doi.org/10.1016/S0022-0728(00)00326-0.

(35) Nicholson, R. S. Theory and Application of Cyclic Voltammetry for Measurement of Electrode Reaction Kinetics. *Anal. Chem.* **1965**, *37* (11), 1351–1355.

(36) Bowden, E. F.; Hawkridge, F. M.; Blount, H. N. Interfacial Electrochemistry of Cytochrome c at Tin Oxide, Indium Oxide, Gold, and Platinum Electrodes. *J. Electroanal. Chem. Interfacial Electrochem.* **1984**, *161* (2), 355–376. https://doi.org/10.1016/S0022-0728(84)80193-X.

(37) Raices, M.; Paifer, E.; Cremata, J.; Montesino, R.; Stahlberg, J.; Divne, C.; Szabó, I. J.; Henriksson, G.; Johansson, G.; Pettersson, G. Cloning and Characterization of a CDNA Encoding a Cellobiose Dehydrogenase from the White Rot Fungus *Phanerochaete chrysosporium*. *FEBS Lett.* **1995**, *369* (2–3), 233–238. https://doi.org/10.1016/0014-5793(95)00758-2.

(38) Hallberg, B.; Henriksson, G.; Pettersson, G.; Divne, C. Crystal Structure of the Flavoprotein Domain of the Extracellular Flavocytochrome Cellobiose Dehydrogenase. *J. Mol. Biol.* **2002**, *315* (3), 421–434. https://doi.org/10.1006/jmbi.2001.5246.

(39) Hallberg, B. M.; Bergfors, T.; B\äckbro, K.; Pettersson, G.; Henriksson, G.; Divne, C. A New Scaffold for Binding Haem in the Cytochrome Domain of the Extracellular Flavocytochrome Cellobiose Dehydrogenase. *Structure* **2000**, *8* (1), 79–88.

(40) Diêp Lê, K. H.; Lederer, F.; Golinelli-Pimpaneau, B. Structural Evidence for the Functional Importance of the Heme Domain Mobility in Flavocytochrome B2. *J. Mol. Biol.* **2010**, *400* (3), 518–530. https://doi.org/16/j.jmb.2010.05.035.

(41) Kadek, A.; Kavan, D.; Marcoux, J.; Stojko, J.; Felice, A. K. G.; Cianférani, S.; Ludwig, R.; Halada, P.; Man, P. Interdomain Electron Transfer in Cellobiose Dehydrogenase Is Governed by Surface Electrostatics. *Biochim. Biophys. Acta BBA - Gen. Subj.* **2017**, *1861* (2), 157–167. https://doi.org/10.1016/j.bbagen.2016.11.016.

(42) Harreither, W.; Sygmund, C.; Augustin, M.; Narciso, M.; Rabinovich, M. L.; Gorton, L.; Haltrich, D.; Ludwig, R. Catalytic Properties and Classification of Cellobiose Dehydrogenases from Ascomycetes. *Appl Env. Microbiol* **2011**, *77* (5), 1804–1815. https://doi.org/ 10.1128/AEM.02052-10 .

(43) Zamocky, M.; Ludwig, R.; Peterbauer, C.; Hallberg, B. M.; Divne, C.; Nicholls, P.; Haltrich, D. Cellobiose Dehydrogenase-a Flavocytochrome from Wood-Degrading, Phytopathogenic and Saprotropic Fungi. *Curr. Protein Pept. Sci.* **2006**, *7* (3), 255–280.

(44) Loose, J. S. M.; Forsberg, Z.; Kracher, D.; Scheiblbrandner, S.; Ludwig, R.; Eijsink, V. G. H.; Vaaje-Kolstad, G. Activation of Bacterial Lytic Polysaccharide Monooxygenases with Cellobiose Dehydrogenase. *Protein Sci.* **2016**, *25* (12), 2175–2186. https://doi.org/10.1002/pro.3043.

(45) Tamura, K.; Stecher, G.; Peterson, D.; Filipski, A.; Kumar, S. MEGA6: Molecular Evolutionary Genetics Analysis Version 6.0. *Mol. Biol. Evol.* **2013**, *30* (12), 2725–2729. https://doi.org/10.1093/molbev/mst197.

(46) Harreither, W.; Felice, A. K. G.; Paukner, R.; Gorton, L.; Ludwig, R.; Sygmund, C. Recombinantly Produced Cellobiose Dehydrogenase from *Corynascus thermophilus* for Glucose Biosensors and Biofuel Cells. *Biotechnol. J.* **2012**, 1359–1366. https://doi.org/10.1002/biot.201200049.

(47) McIlvaine, T. C. A Buffer Solution for Colorimetric Comparison. *J. Biol. Chem.* **1921**, *49* (1), 183.

(48) Nicholson, R. S.; Shain, Irving. Theory of Stationary Electrode Polarography. Single Scan and Cyclic Methods Applied to Reversible, Irreversible, and Kinetic Systems. *Anal. Chem.* **1964**, *36* (4), 706–723. https://doi.org/10.1021/ac60210a007.

(49) Matsuda, H. Zur Theorie der Wechselspannungs-Polarographie. *Z. Für Elektrochem. Berichte Bunsenges. Für Phys. Chem.* **1958**, *62* (9), 977–989. https://doi.org/10.1002/bbpc.19580620909.

(50) Ševčík, A. Oscillographic Polarography with Periodical Triangular Voltage. *Collect. Czechoslov. Chem. Commun.* **1948**, *13*, 349–377. https://doi.org/10.1135/cccc19480349.

(51) Randles, J. E. B. A Cathode Ray Polarograph. Part II.—The Current-Voltage Curves. *Trans. Faraday Soc.* **1948**, *44* (0), 327–338. https://doi.org/10.1039/TF9484400327.

(52) Arnold, K.; Bordoli, L.; Kopp, J.; Schwede, T. The SWISS-MODEL Workspace: A Web-Based Environment for Protein Structure Homology Modelling. *Bioinformatics* **2006**, *22* (2), 195–201. https://doi.org/10.1093/bioinformatics/bti770.

(53) Benkert, P.; Biasini, M.; Schwede, T. Toward the Estimation of the Absolute Quality of Individual Protein Structure Models. *Bioinformatics* **2011**, *27* (3), 343–350. https://doi.org/10.1093/bioinformatics/btq662.

(54) Biasini, M.; Bienert, S.; Waterhouse, A.; Arnold, K.; Studer, G.; Schmidt, T.; Kiefer, F.; Cassarino, T. G.; Bertoni, M.; Bordoli, L.; et al. SWISS-MODEL: Modelling Protein Tertiary and Quaternary Structure Using Evolutionary Information. *Nucleic Acids Res.* **2014**, *42* (W1), W252–W258. https://doi.org/10.1093/nar/gku340.

(55) Tan, T.-C.; Kracher, D.; Gandini, R.; Sygmund, C.; Kittl, R.; Haltrich, D.; Hällberg, B. M.; Ludwig, R.; Divne, C. Structural Basis for Cellobiose Dehydrogenase Action during Oxidative Cellulose Degradation. *Nat. Commun.* **2015**, *6*, 7542.

(56) Schmid, N.; Christ, C. D.; Christen, M.; Eichenberger, A. P.; van Gunsteren, W. F. Architecture, Implementation and Parallelisation of the GROMOS Software for Biomolecular Simulation. *Comput. Phys. Commun.* **2012**, *183* (4), 890–903. https://doi.org/10.1016/j.cpc.2011.12.014.

(57) Schmid, N.; Eichenberger, A. P.; Choutko, A.; Riniker, S.; Winger, M.; Mark, A. E.; van Gunsteren, W. F. Definition and Testing of the GROMOS Force-Field Versions 54A7 and 54B7. *Eur. Biophys. J.* **2011**, *40* (7), 843–856. https://doi.org/10.1007/s00249-011-0700-9.

(58) Poger, D.; Van Gunsteren, W. F.; Mark, A. E. A New Force Field for Simulating Phosphatidylcholine Bilayers. *J. Comput. Chem.* **2010**, *31* (6), 1117–1125. https://doi.org/10.1002/jcc.21396.

(59) Olsson, M. H. M.; Søndergaard, C. R.; Rostkowski, M.; Jensen, J. H. PROPKA3: Consistent Treatment of Internal and Surface Residues in Empirical p K_a Predictions. *J. Chem. Theory Comput.* **2011**, *7* (2), 525–537. https://doi.org/10.1021/ct100578z.

(60) Søndergaard, C. R.; Olsson, M. H. M.; Rostkowski, M.; Jensen, J. H. Improved Treatment of Ligands and Coupling Effects in Empirical Calculation and Rationalization of PKa Values. *J. Chem. Theory Comput.* **2011**, *7* (7), 2284–2295. https://doi.org/10.1021/ct200133y.

(61) Dolinsky, T. J.; Nielsen, J. E.; McCammon, J. A.; Baker, N. A. PDB2PQR: An Automated Pipeline for the Setup of Poisson–Boltzmann Electrostatics Calculations. *Nucleic Acids Res.* **2004**, *32* (suppl_2), W665–W667. https://doi.org/10.1093/nar/gkh381.

(62) Baker, N. A.; Sept, D.; Joseph, S.; Holst, M. J.; McCammon, J. A. Electrostatics of Nanosystems: Application to Microtubules and the Ribosome. *Proc. Natl. Acad. Sci.* **2001**, *98* (18), 10037–10041. https://doi.org/10.1073/pnas.181342398.

(63) Bank, R.; Holst, M. A New Paradigm for Parallel Adaptive Meshing Algorithms. *SIAM Rev.* **2003**, *45* (2), 291–323. https://doi.org/10.1137/S003614450342061.

(64) Holst, M. Adaptive Numerical Treatment of Elliptic Systems on Manifolds. *Adv. Comput. Math.* **2001**, *15* (1–4), 139–191. https://doi.org/10.1023/A:1014246117321.

(65) Holst, M.; Saied, F. Multigrid Solution of the Poisson—Boltzmann Equation. *J. Comput. Chem.* **1993**, *14* (1), 105–113. https://doi.org/10.1002/jcc.540140114.

(66) Holst, M. J.; Saied, F. Numerical Solution of the Nonlinear Poisson–Boltzmann Equation: Developing More Robust and Efficient Methods. *J. Comput. Chem.* **1995**, *16* (3), 337–364. https://doi.org/10.1002/jcc.540160308.

(67) Kastritis, P. L.; Rodrigues, J. P. G. L. M.; Folkers, G. E.; Boelens, R.; Bonvin, A. M. J. J. Proteins Feel More Than They See: Fine-Tuning of Binding Affinity by Properties of the Non-Interacting Surface. *J. Mol. Biol.* **2014**, *426* (14), 2632–2652. https://doi.org/10.1016/j.jmb.2014.04.017.

(68) Vangone, A.; Bonvin, A. M. Contacts-Based Prediction of Binding Affinity in Protein–Protein Complexes. *eLife* **2015**, *4*, e07454. https://doi.org/10.7554/eLife.07454.
(69) Xue, L. C.; Rodrigues, J. P.; Kastritis, P. L.; Bonvin, A. M.; Vangone, A. PRODIGY: A Web Server for Predicting the Binding Affinity of Protein–Protein Complexes. *Bioinformatics* **2016**, *32* (23), 3676–3678. https://doi.org/10.1093/bioinformatics/btw514.

ABBREVIATIONS

The following abbreviations are used: AFM, atomic force microscopy; CDH, cellobiose dehydrogenase; CYT, cytochrome domain; DCIP, 2,6-dichloroindophenol; DH, dehydrogenase domain; FAD, flavin adenine dinucleotide; HDX, hydrogen/deuterium exchange; IDET, interdomain electron transfer; IPET, interprotein electron transfer; LPMO, lytic polysaccharide monooxygenase; MS, mass spectrometry; SAM, self-assembled monolayer; SANS, small-angle neutron scattering; SAXS, small-angle X-ray scattering; SHE, standard hydrogen electrode; TN, turnover number

FIGURES

FIGURE 1. Properties of chimeric enzymes. *A*, Domain architecture. The two *N. crassa* wild-type CDHs (CDHIIA denoted as CDH_{AAA} and CDHIIB denoted as CDH_{BBB}) consist of an N-terminal CYT domain, C-terminal DH domain and protein linker connecting the two domains. Four chimeric CDHs (CDH_{BBA}, CDH_{BAA}, CDH_{AAB}, and CDH_{ABB}) were created by domain swapping. *B*, Linker sequence and position in CDH. The alignment shows sequence identities and the N- and C-terminal ends of the linkers. *C*, Purified wild-type and chimeric CDHs. The measured and calculated molecular weights differ due to glycosylation.

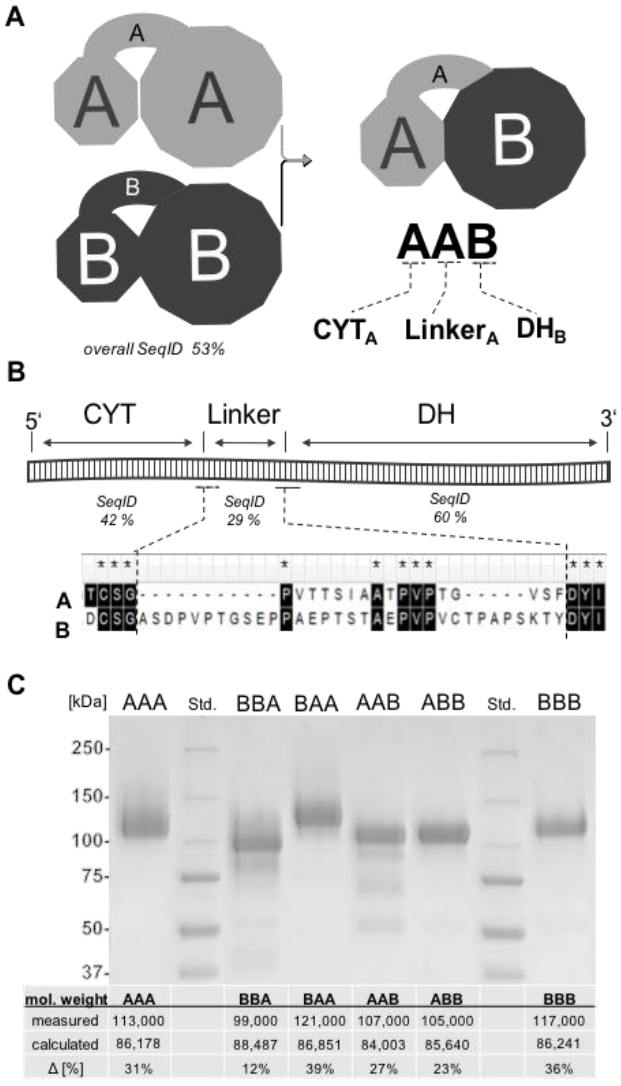

mol. weight	AAA	BBA	BAA	AAB	ABB	BBB
measured	113,000	99,000	121,000	107,000	105,000	117,000
calculated	86,178	88,487	86,851	84,003	85,640	86,241
Δ [%]	31%	12%	39%	27%	23%	36%

FIGURE 2. Effects of domain swapping on catalytic rates in the DH domain. *A*, pH Optima of cellobiose conversion in CDHs with a DH_A when using the two-electron acceptor 2,6-dichloroindophenol. *B*, pH Optima of CDHs with a DH_B using the same substrate and cosubstrate as in (A). *C*, FAD reduction rate in all CDHs measured at 449 nm (k_{obs}^{449}) for increasing cellobiose concentrations.

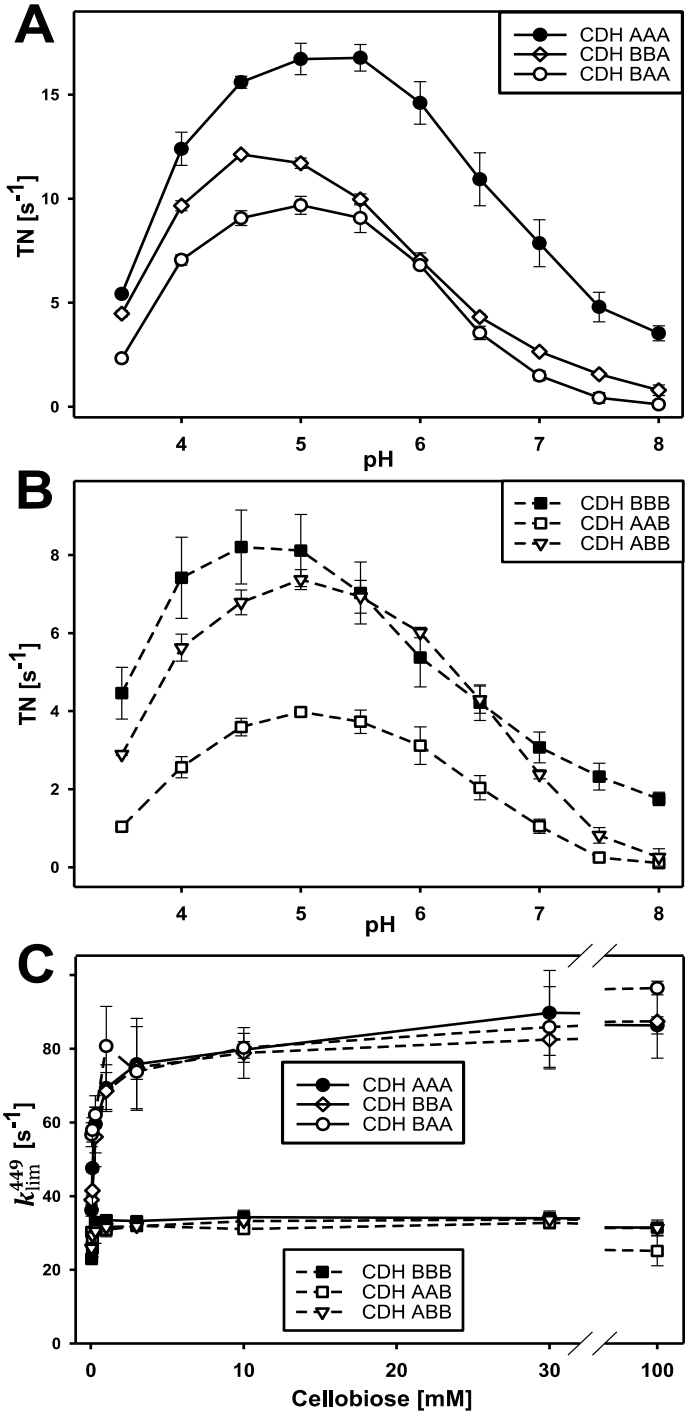

FIGURE 3. Effects of domain swapping on IDET. *A*, pH optima of cytochrome *c* turnover numbers for wild-type and chimeric CDHs. *B*, IDET rates (k_{obs}^{563}) of DH_A to different CYT domains measured for increasing cellobiose concentrations. *C*, IDET rates of DH_B to different CYT domains measured for increasing cellobiose concentrations.

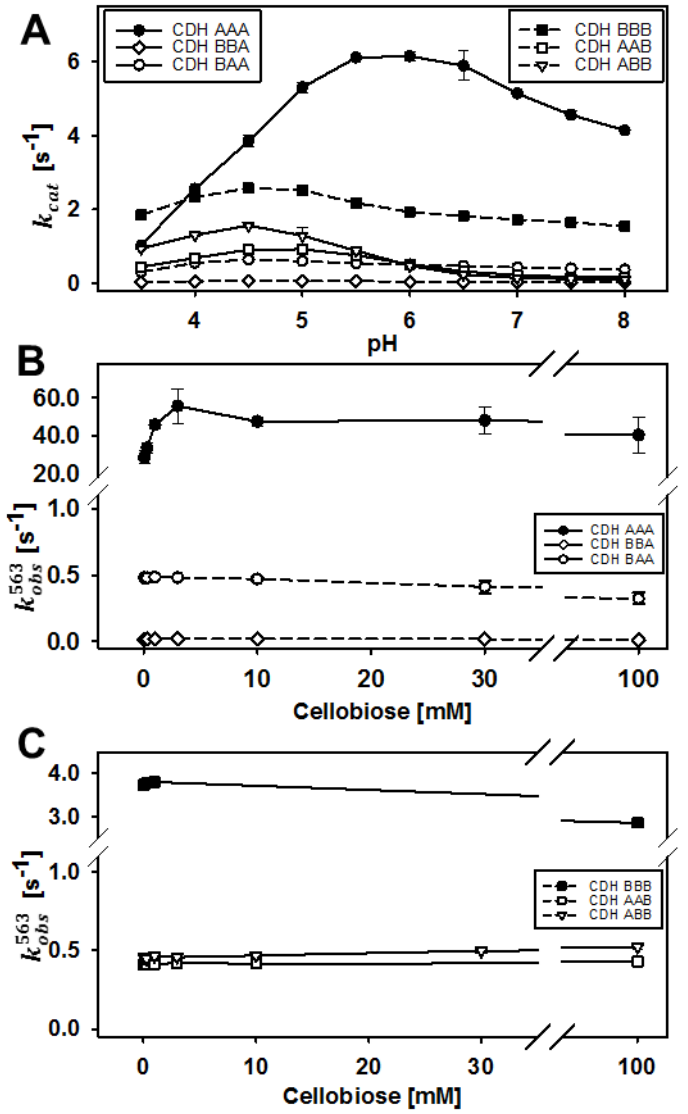

FIGURE 4. Electron transfer in CDH (IDET). *A*, Detail of the crystal structure of *Mt*CDHIIA (PDB:4QI6) featuring the closed-state conformation. The edge-to-edge distance between the FAD and heme cofactors is 0.9 nm. *B*, The electron transfer rate plotted against cofactor distance for CDH (lower and upper limit, solid lines; most probable parameters, dashed line). The bars at the bottom indicate the observed IDET rates and edge-to-edge distances for CDH_{AAA} and CDH_{BBB} in docking calculations.

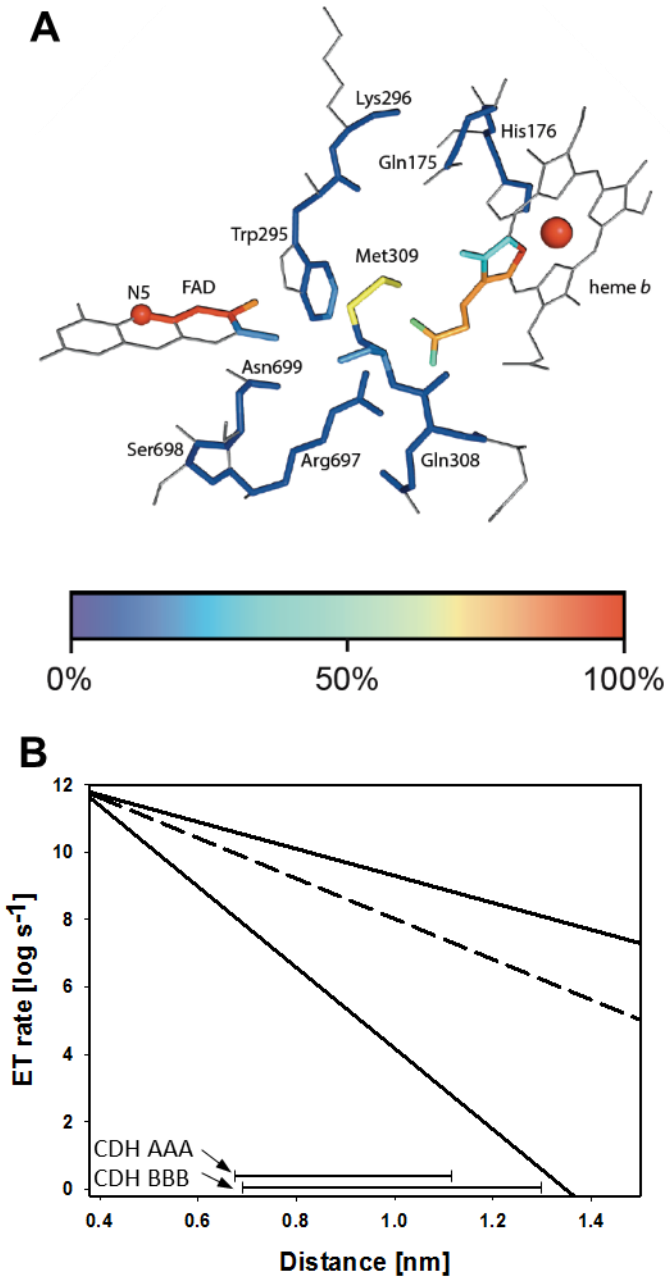

FIGURE 5. Orientation of CYT to DH in docking poses. From a total of 200 docking poses for each CYT-linker-DH pair the angle of rotation, declination and inclination were measured in regard to its deviation from the crystal structure of the closed-state conformation of *M. thermophilum* CDH (PDB: 4QI6). The electrostatic (red) and van-der-Waals (blue) binding energies for each pose are given in kJ mol^{-1}. *A*, docking poses in wild-type CDH_{AAA}. *B*, docking poses in wild-type CDH_{BBB}. *C*, docking poses in wild-type CDH_{BAA}. *D*, docking poses in wild-type CDH_{ABB}. *E*, docking poses in wild-type CDH_{BBA}. F, docking poses in wild-type CDH_{AAB}.

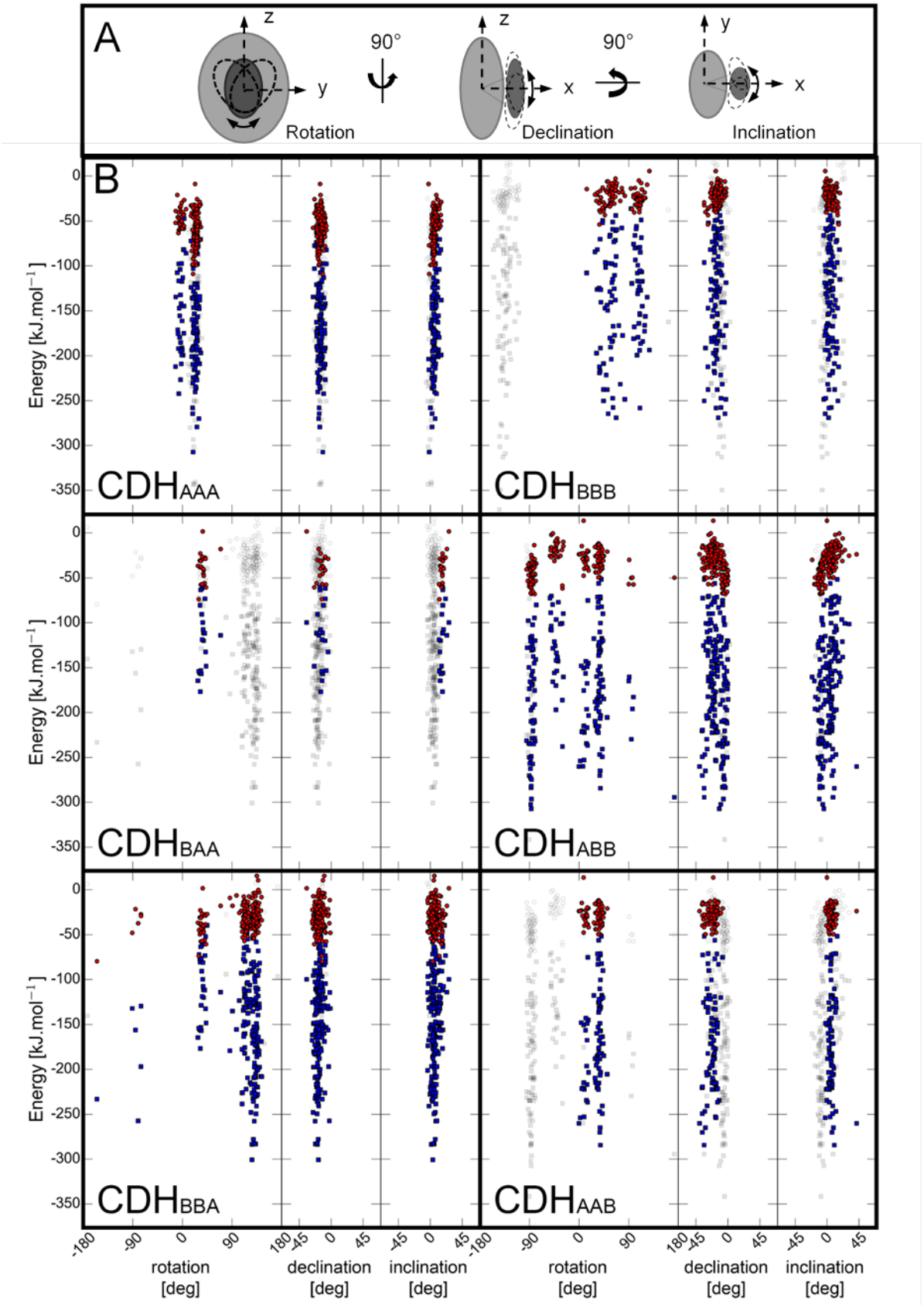
A
z
y
Rotation
90°
z
x
Declination
90°
y
x
Inclination
B
CDHAAA
CDHBBB
CDHBAA
CDHABB
CDHBBA
CDHAAB
Energy [kJ.mol−1]
0
-50
-100
-150
-200
-250
-300
-350
-180
-90
0
90
180
-45
0
45
rotation [deg]
declination [deg]
inclination [deg]

FIGURE 6. Structure changes arising from *N. crassa* LPMO9f and CDH_{AAA} interaction detected by H/D exchange. Structural differences between free LPMO and LPMO in the presence of CDH_{AAA} were visualized using difference heat map (A) (http://peterslab.org/MSTools/). Deuteration levels of the protein alone were subtracted from those observed for the protein in the presence of CDH_{AAA}. Increased deuteration (deprotection) upon interaction is shown by red colors while protection is in blue (scale bar is at the bottom of the panel). Secondary structure elements, loops and copper coordinating residues (green) and ProGlyPro patch (orange) are depicted above the heat map. Individual exchange times are show on the right. Two selected time points (30m and 3 h, indicated by arrowhead) were visualized on the LPMO structure (PDB: 4QI8) (B). The coloring scale follows the one in panel A. The central copper atom is shown in green and the side chains of the histidine brace residues and Pro-Gly-Pro patch are shown as sticks. Structure on the left visualizes histidine brace (green) and Pro-Gly-Pro patch (orange) residues.

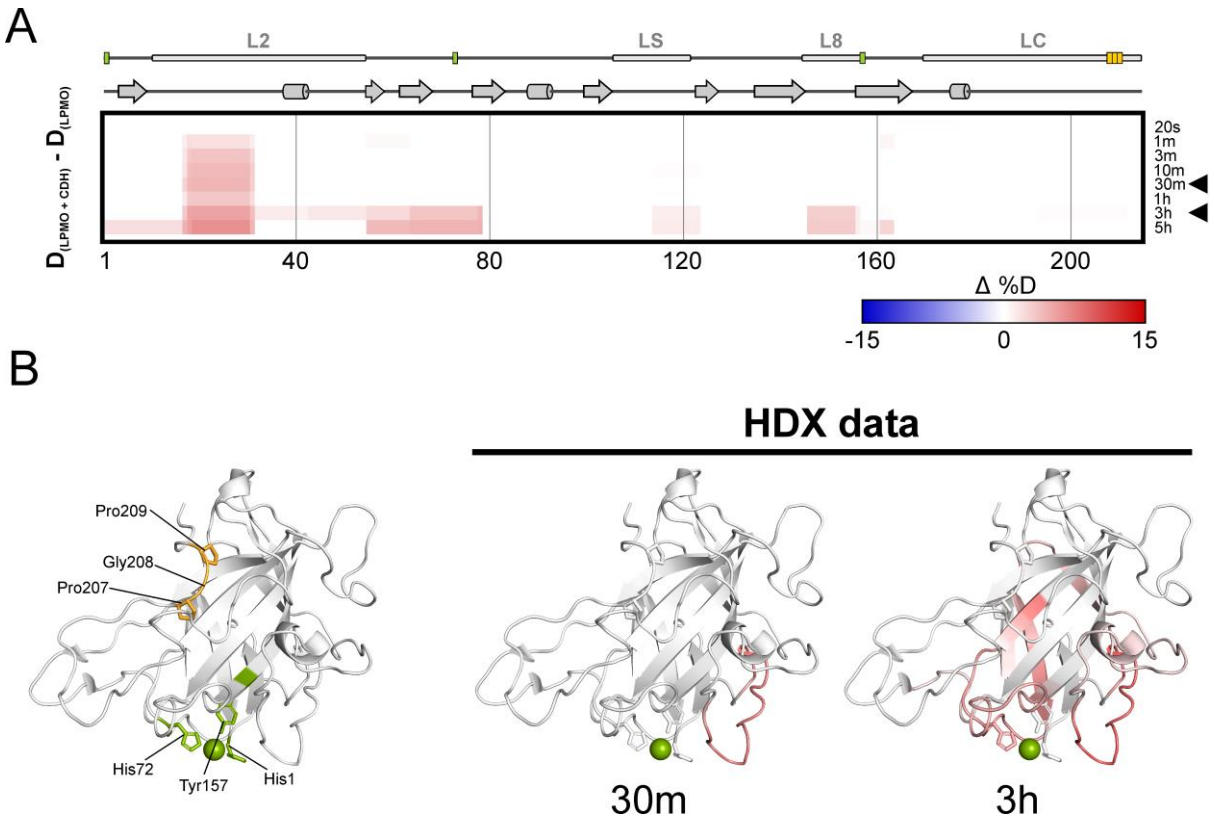

FIGURE 7. Heterologous electron transfer rates (k_0). k_0 was calculated from the peak separation of the anodic and cathodic wave observed from cyclic voltammograms measured at different scan-rates (3–50 mV s^{-1}) according to Nicholson-Shain. Data from scan-rates above 50 mV s^{-1} could not be used, because the increased capacitive current did not allow the exact determination of the peak maxima. The data (peak separation vs. scan rate) are given in Fig. S6.

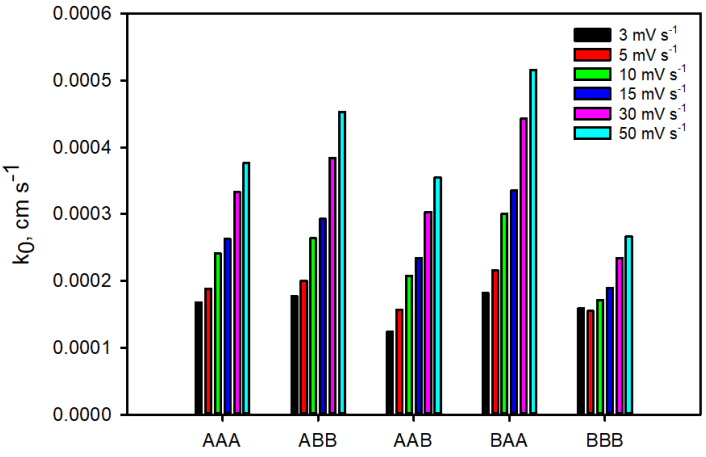

FIGURE 8. Effects of domain swapping on IPET. Stopped-flow measurements of the electron transfer from pre-reduced CYT to LPMO at 563 nm at for increasing LPMO concentrations show a linear relation from which bimolecular rates were calculated.

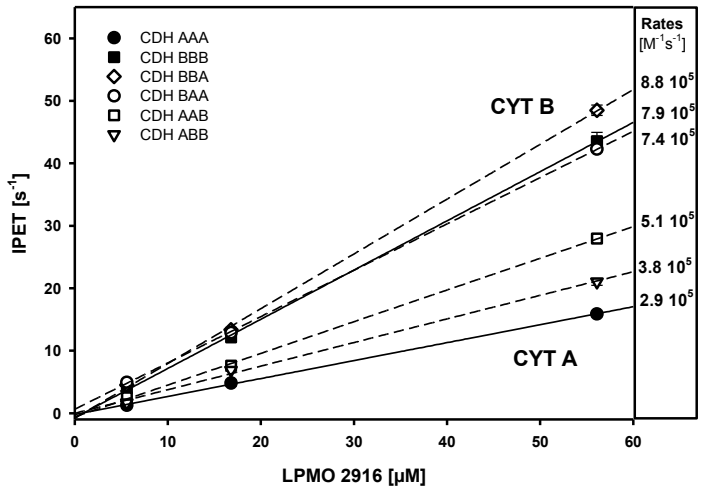

Table 1: Catalytic constants, transient rates and FAD redox potentials of CDHs.

The steady-state catalytic constants of the DH domains in wild-type and chimeric CDHs were determined for cellobiose as substrate and 2,6-dichloroindophenol as saturating cosubstrate. Transient FAD reduction rates (k_{obs}^{449}) measured in a stopped-flow spectrophotometer at different cellobiose concentrations were used to extrapolate the maximal reduction rate of FAD in presence of an infinite cellobiose concentration (k_{lim}^{449}). The midpoint redox potentials ($E^{1/2}$) of the FAD cofactor in regard to the standard hydrogen electrode (SHE) was determined in a spectroelectrochemical cell is given in the last column. All measurements were performed at pH 6.0. n.d.: not determined

Enzyme	k_{cat} [s^{-1}]	K_M [mM]	k_{cat}/K_M [M^{-1} s^{-1}]	k_{lim}^{449} [s^{-1}]	*E* vs. SHE [mV]
CDH AAA	17.8 ± 0.4	0.105 ± 0.003	1.7 10^5	81.8 ± 2.2	33 ± 5
CDH BAA	9.0 ± 0.3	0.057 ± 0.006	1.6 10^5	82.2 ± 2.6	24 ± 5
CDH BBA	14.2 ± 0.4	0.075 ± 0.005	1.9 10^5	79.8 ± 2.4	31 ± 1
CDH BBB	4.6 ± 0.1	0.027 ± 0.002	1.7 10^5	33.5 ± 0.4	43 ± 15
CDH ABB	5.0 ± 0.1	0.026 ± 0.003	1.9 10^5	32.3 ± 0.4	33 ± 23
CDH AAB	4.5 ± 0.2	0.046 ± 0.003	1.0 10^5	30.4 ± 0.6	n.d.

Table 2: Steady-state and transient-state IDET rates and heme *b* redox potentials.

Comparison of cytochrome *c* reduction rates given as turnover numbers (TN) as an indicator of IDET with transient k_{obs}^{563} rates. The heme *b* midpoint redox potentials and the potential difference to the FAD in the wild-type DH domain is given. All measurements were performed at pH 6.0.

Enzyme	pH Opt	TN @ pH 6 [s^{-1}]	IDET [s^{-1}]	E vs. SHE [mV]	ΔE [mV]
CDH AAA	6.0	6.14 ± 0.12	50.00 ± 0.10	102 ± 4	69
CDH BAA	6.0	0.50 ± 0.03	0.40 ± 0.02	172 ± 5	148
CDH BBA	5.0	0.04 ± 0.01	0.02 ± 0.02	169 ± 5	138
CDH BBB	4.5	1.93 ± 0.03	4.00 ± 0.01	158 ± 2	115
CDH ABB	4.5	0.48 ± 0.01	0.40 ± 0.01	97 ± 4	64
CDH AAB	5.0	0.52 ± 0.01	0.40 ± 0.02	103 ± 4	104

ARTICLE IV

Petrenčáková, M., Filandr, F., Hovan, A., Yassaghi, G., Man, P., Kožár, T., Schwer, M. S., Jancura, D., Plückthun, A., Novák, P., Miškovský, P., Bánó, G. & Sedlák, E.

Photoinduced damage of *As*LOV2 domain is accompanied by increased singlet oxygen production due to flavin dissociation.

Sci. Rep. **10**, 1–15 (2020)

My contribution: *conducting experiments (LC-MS/MS analysis of oxidative modifications), data analysis & interpretation, figure design*

SCIENTIFIC REPORTS
nature research

OPEN

Photoinduced damage of AsLOV2 domain is accompanied by increased singlet oxygen production due to flavin dissociation

Martina Petrenčáková[1,6], František Filandr[2,6], Andrej Hovan[1,6], Ghazaleh Yassaghi[2], Petr Man[2], Tibor Kožár[3], Marc-Simon Schwer[4], Daniel Jancura[1,3], Andreas Plückthun[4], Petr Novák[2], Pavol Miškovský[3,5], Gregor Bánó[1,3*] & Erik Sedlák[3*]

Flavin mononucleotide (FMN) belongs to the group of very efficient endogenous photosensitizers producing singlet oxygen, $^1O_2$, but with limited ability to be targeted. On the other hand, in genetically-encoded photosensitizers, which can be targeted by means of various tags, the efficiency of FMN to produce $^1O_2$ is significantly diminished due to its interactions with surrounding amino acid residues. Recently, an increase of $^1O_2$ production yield by FMN buried in a protein matrix was achieved by a decrease of quenching of the cofactor excited states by weakening of the protein-FMN interactions while still forming a complex. Here, we suggest an alternative approach which relies on the blue light irradiation-induced dissociation of FMN to solvent. This dissociation unlocks the full capacity of FMN as $^1O_2$ producer. Our suggestion is based on the study of an irradiation effect on two variants of the LOV2 domain from *Avena sativa*; wild type, AsLOV2 wt, and the variant with a replaced cysteine residue, AsLOV2 C450A. We detected irradiation-induced conformational changes as well as oxidation of several amino acids in both AsLOV2 variants. Detailed analysis of these observations indicates that irradiation-induced increase in $^1O_2$ production is caused by a release of FMN from the protein. Moreover, an increased FMN dissociation from AsLOV2 wt in comparison with AsLOV2 C450A points to a role of C450 oxidation in repelling the cofactor from the protein.

Flavin mononucleotide (FMN) belongs to a group of efficient endogenous photosensitizers in cells with rather high singlet oxygen, $^1O_2$, quantum yield (Φ_Δ) within the range 0.51–0.65[1,2]. Depending on FMN concentrations and concentrations of available oxygen, the flavin(s) can be even more effective $^1O_2$ generators than exogenous porphyrins used for cell killing in photodynamic therapy (PDT). To minimize the potential deleterious effect of flavins to cells, the isoalloxazine moiety of flavin cofactors is typically deeply buried in the protein core of flavo-enzymes[3] or storage proteins[4].

Singlet oxygen, the lowest energy excited electronic state of molecular oxygen, belongs to the group of reactive oxygen species (ROS), which includes superoxide anion ($O_2^{\bullet-}$), hydrogen peroxide (H_2O_2), and hydroxyl radical ($HO^\bullet$), enabling to oxidize and/or oxygenate many biologically relevant molecules[5,6]. Singlet oxygen can be produced in a variety of ways by physical mechanisms, including energy transfer from the excited triplet states of particular chromophores to molecular oxygen[7], or by chemical mechanisms as one of the products of peroxidase enzymes[8]. In biological systems, $^1O_2$ is usually generated by electronic energy transfer from an excited state of a photosensitive molecule, so-called photosensitizer (PS), to ground state O_2[6]. The high reactivity of singlet oxygen towards biological molecules is relevant in the context of PDT[9] and chromophore-assisted laser inactivation (CALI) of proteins and cells[10,11].

[1]Department of Biophysics, Faculty of Science, P.J. Šafárik University, Jesenná 5, 041 54, Košice, Slovakia. [2]BioCeV - Institute of Microbiology, Průmyslová 595, 252 50, Vestec, Czech Republic. [3]Center for Interdisciplinary Biosciences, Technology and Innovation Park, P.J. Šafárik University, Jesenná 5, 041 54, Košice, Slovakia. [4]Department of Biochemistry, University of Zürich, Winterthurerstrasse 190, CH-, 8057, Zurich, Switzerland. [5]SAFTRA photonics Ltd, Jesenná 5, 041 54, Košice, Slovakia. [6]These authors contributed equally: Martina Petrenčáková, František Filandr, and Andrej Hovan. *email: gregor.bano@upjs.sk; erik.sedlak@upjs.sk

Studies addressing the behavior and action of $^1O_2$ have been performed for decades, but there is still a limited knowledge on the spatially- and temporally-dependent $^1O_2$-induced cell signaling processes[12,13]. An encapsulation of a photosensitizer in a protein matrix, thus forming a genetically-encoded photosensitizer, facilitates ROS production with (i) molecular level spatial control via protein targeting, and (ii) temporal and dose control by the incident light[2,13,14].

On the other hand, the improved control regarding $^1O_2$ production by using genetically-encoded photosensitizers leads to attempts to utilize them as antimicrobial agents[15,16] or in PDT[17]. Up to now, more than 400 individual compounds have been recognized as possible candidates for use as PSs[9]. However, a large fraction of the small organic PSs has unsuitable physico-chemical properties such as low solubility and stability in aqueous solvents, and inherent low specificity for targeted diseased tissue. Consequently, such compounds exhibit a certain toxicity to other, healthy tissues[18,19]. Alternatively, the use of proteins as genetically encoded $^1O_2$ generators offers new ways of designing, synthesizing, and targeting of biomacromolecules containing PS[20].

Recently, significant efforts have been invested into the design of protein PSs containing FMN due to its high value of Φ_Δ[15,21–23]. On the other hand, genetically encoded fluorescent tags have inherently very low efficiency of $^1O_2$ production ($\Phi_\Delta < 0.09$)[15,20,24,25]. These observations point to a strong effect of the surrounding protein matrix on $^1O_2$ production efficiency by the chromophore[21].

Two major ways how the protein environment diminishes the yield of $^1O_2$ production have been identified: (i) inefficient diffusion of molecular oxygen through the protein scaffold to the site of PS localization and (ii) quenching of the excited state of PS, e.g. FMN triplet state, by the protein environment[23]. In fact, efficiency of the $^1O_2$ production in miniSOG (mini-singlet oxygen generator; $\Phi_\Delta = 0.03–0.05$)[21,26], engineered from the FMN-containing LOV2 domain of *Arabidopsis thaliana* phototropin 2[27], upon chemical denaturation increased over 10-fold in comparison with its native form[21]. Consequently, these observations led to efforts to develop protein PSs with improved $^1O_2$ production, such as SOPP (singlet oxygen photosensitizing protein; $\Phi_\Delta = 0.19–0.26$)[26] and particularly SOPP3 with $\Phi_\Delta = 0.60$, comparable to that of free FMN[23]. These improved variants of miniSOG were obtained by identification and replacement of amino acids responsible for: (i) steric barriers for oxygen diffusion toward the PS, (ii) quenching of FMN triplet state by electron transfer, and (iii) quenching of produced $^1O_2$ by chemical reactions[23,26].

In line with these observations is a finding of ~10-fold increase of the Φ_Δ value in miniSOG after its irradiation[23]. This finding was explained as the result of progressive photoinactivation of certain amino acids, such as His, Met, Phe, Trp, and Tyr, that are responsible for $^1O_2$ quenching[5,8,28] and/or the buildup of FMN photoproducts[21]. Indeed, very recently Torra *et al.*[29] showed that the irradiation of miniSOG leads not only to oxidation of several residues, which are possible electron donors to FMN, but also to phototransformation of FMN to lumichrome, which results in facilitation of the access of molecular oxygen to the isoalloxazine ring of FMN.

In this work, we present detailed analysis of cumulative irradiation of two forms of LOV2 domain of phototropin 1 from *Avena sativa* (AsLOV2), wild type (wt) and its variant with replaced cysteine 450 (the numbering correspond to the original sequence of the LOV domain in phototropin 1) for alanine (C450A). These two variants differ by an ability of light-induced conformational change, which is induced by covalent bond forming between the thiol group of C450 and C(4a) on the isoalloxazine ring. While AsLOV2 is able of photoswitching, the variant C450A, due to removing of the thiol, has lost this property. The AsLOV2 primary structure is more than 80% identical with miniSOG. Our results clearly show different kinetics of FMN triplet states of the AsLOV2 and its variant, increased efficiency of $^1O_2$ production as a function of irradiation time as well as oxidative modification of both proteins. Based on these observations, we conclude that the irradiation-induced increase of $^1O_2$ production in the AsLOV2 variants is due to a release of FMN to solvent as a result of oxidative modification of certain amino acids in the AsLOV2 structure. Our results suggest a new approach towards designing an efficient protein photosensitizer as a carrier of a chromophore that can be subsequently released by irradiation of the protein at the site of its action.

Experimental methods

Cloning, expression and purification of the AsLOV2 domain. Wild type AsLOV2 as well as variant AsLOV2-C450A were expressed in *E. coli* strain BL21(DE3). The bacterial cells were grown at 37 °C in ampicillin containing (100 µg/ml) TB medium until they reached OD_{600} ~0.6–0.8. Protein expression was induced by adding isopropyl β-D-galactopyranoside (100 µM final concentration) following a temperature downshift from 37 °C to 25 °C. Expression was carried out in darkness overnight at 25 °C. The proteins were purified using metal ion affinity chromatography (Ni-NTA Superflow, Qiagen). The sequence of the final construct of AsLOV2 contains an N-terminal His_{10}-tag, followed by amino acids 404–547 of AsLOV2 according the original numbering of phototropin 1. After IMAC purification they were run on a Superdex 75 Increase, 10/300 GL, size exclusion column and concentrated in 20 mM TrisHCl buffer, pH 7.8. All steps were performed in darkness. The ratio of absorbance at 280 nm/477 nm of the final protein was ~2.5, suggesting the absence of AsLOV2 apoform[30].

Sample irradiation (by laser) and singlet oxygen phosphorescence. Samples (1.2 ml) containing 25 µM protein were placed in a 10 × 10 × 40 mm quartz cuvette equipped with an overhead-type glass stirrer and kept at ~30 °C. A laser system consisting of a pulsed optical parametric oscillator (OPO) (GWU basiScan-M) pumped with the third harmonic of a Nd:YAG laser (Spectra-Physics, Quanta-Ray, INDI-HG-10S) was used to excite the samples. The OPO wavelength was tuned to 475 nm matching the absorption maximum of the AsLOV2 protein. The repetition rate of the 5–7 ns long laser pulses was set to 10 Hz. The 3 mm diameter laser beam was focused to the cuvette by means of a 200 mm lens. The average laser power on the sample was 0.9 mW. The phosphorescence signal of singlet oxygen passed through a 1250–1300 nm band-pass filter and was detected with a photomultiplier tube (Hamamatsu H10330A-75) operated in photon counting mode. A multichannel scaler PCI card (Becker & Hickl, MSA-300) was used to acquire the phosphorescence time course. In order to suppress the

background signal originating from the optical components, the emission signal was measured with two additional band-pass filters, in the 1200–1250 nm and the 1300–1350 nm spectral regions. The background signal was assumed to have a slowly varying wavelength dependence in the covered spectral range. The resulting singlet oxygen phosphorescence was calculated by subtracting the average of the two auxiliary measurements (acquired in the adjacent spectral regions) from the signal measured in the 1250–1300 nm spectral range. The background was efficiently suppressed this way. Throughout the experiments an average of 2500 laser pulses was detected with each filter consecutively. The time needed for a single measurement set (three band-pass filters) was 12.5 min. The total irradiation time was 75 min.

Measurements of FMN triplet state lifetime. An additional 633 nm cw laser was added to the optical setup to monitor the FMN triplet state lifetime in a flash-photolysis experiment[31]. The polarization of the cw laser was oriented at the magic angle with respect to the excitation beam polarization. The laser beam was passing through the sample area excited with the pulsed laser. The time-resolved absorption at 633 nm was measured with an avalanche photodiode (Thorlabs, APD110A2) connected to a digitizing oscilloscope (Tektronix, DPO 7254). The average signal of 2500 laser pulses was acquired consecutively throughout the irradiation experiment. Eighteen decay curves were measured during the 75 minutes interval. The protein concentration was 25 µM.

Determination of a light-induced released of FMN. Relative amounts of released FMN from AsLOV2 wt and AsLOV C450A were determined by FMN fluorescence after filtration using 10 kDa cut-off filter tubes. Each sample, i.e. non-illuminated and illuminated AsLOV2 wt and AsLOV2 C450A, 900 µl of 10 µM protein, was loaded into Amicon Ultra Centrifugal filter tube and centrifuged for 5 min at 7500 *g*. After the spin, the collected flow-through of each sample was measured for FMN fluorescence.

Spectral analysis. Different spectroscopic techniques have been used to follow the structural changes of AsLOV2 wild type and variant C450A after irradiation with blue light. All spectra were recorded at room temperature.

Ultraviolet and visible absorption spectra were obtained with a UV-2401PC UV-Vis spectrophotometer (Shimadzu). Protein concentrations were calculated by using an extinction coefficient of $\varepsilon_{447} = 13800\ M^{-1}{\cdot}cm^{-1}$ for oxidized FMN[32]. The measurements were performed in quartz cuvettes with 1 cm pathlength. The protein concentration was 25 µM.

Fluorescence emission spectra were recorded with a RF-5301PC spectrofluorophoto-meter (Shimadzu). The emission spectra of FMN and tryptophan were measured by using excitation wavelengths at 445 nm and 295 nm, respectively. For obtaining fluorescence spectra, a protein concentration of 10 µM was used.

Circular dichroism spectra measurements were performed by Jasco 810 (Jasco). The protein concentration used in CD measurements was 10 µM. The measurements in the far-UV and the near-UV spectral regions were performed in quartz cuvette with 1 mm and 1 cm pathlengths, respectively.

Adduct decay kinetics measurements. For light-induced adduct formation accompanied by absorbance changes in the spectral region 425–520 nm, we used a photographic flash (Canon) as a light source. Adduct decay kinetics were measured by following absorbance at 447 nm in quartz cuvettes with 1 cm pathlength. A UV-2401PC UV-Vis recording spectrophotometer (Shimadzu) was used. In all measurements, the protein concentration was 25 µM.

Molecular modeling. The Maestro/Desmond[33,34] combination of programs has been used for model building, energy minimization, MD simulations and analysis of simulation results. The OPLS-2005 force field (the up-to-date version of the OPLS force field family[35–42]) was used to carry out the simulation studies. The two AsLOV2 protein structures (PDB ID: 2v0u and 2v0w) were downloaded from the Protein Data Bank, updated in Maestro using the "Protein Preparation Wizard". The proteins were solvated (SPC water model[43]; the water molecules were added within 1 nm buffer around the protein, creating thus a $6 \times 6 \times 7$ nm sized solvent box) and the resulting structures were then minimized. The final structures were equilibrated and submitted for 5 ns NPT (pressure at 1.01325 bar) simulations with the Desmond program at 300 K. Molecular geometries resulting from simulations were saved at 0.5 ps intervals and were visualized within the Maestro and VMD[44] programs and were used for further analysis. The cystine thiol of C450 of AsLOV wt (PDB ID: 2v0u) was oxidized to SOO^- and the resulting structures were also solvated, and NPT simulated for 5 ns in Desmond as described above. Comparative simulations were then performed for the C450A-mutated AsLOV2 domain.

The Caver 3.0 program[45] has been used for analysis of possible transport tunnels in all protein structures downloaded from the RCSB protein database as well as all structures saved from MD simulations.

The BIOVIA Discovery Studio[46] visualizer was also used for complementary visualization and analysis of the modeled molecular structures.

Top-down mass spectrometry. Proteins were desalted off-line on a Protein OptiTrap (Optimize Technologies, Oregon City, USA) with 0.1% formic acid (FA) in water and eluted with 80% acetonitrile/0.1% FA. Protein concentration were adjusted to 5 µM with water and the proteins were loaded into a quartz capillary ESI tip and mounted onto a home-built nESI source. Data were acquired in a broad band mode (m/z 200–3000) or in a CASI mode (Continuous Acquisition of Selected Ions) where selected charged states (19+, 20+, 21+ and 22+) of the protein were analyzed and fragmented simultaneously. Protein fragmentation was done through collision-induced dissociation in the quadrupole (front end) of 15 T FT-ICR MS (solariX XR, Bruker Daltonics, Bremen, Germany). Data were interpreted by a software tool developed in the laboratory and validated manually in Data Analysis 4.1 (Bruker Daltonics).

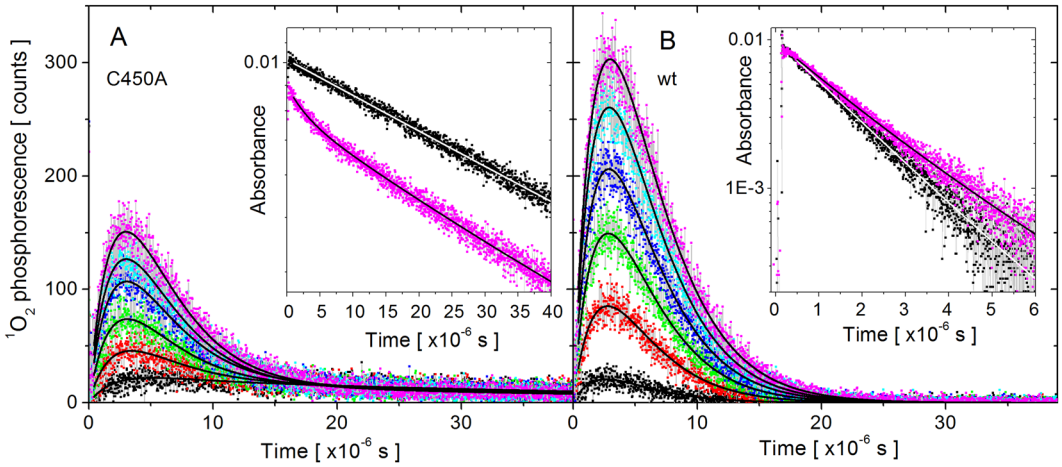

Figure 1. The time-course of the singlet oxygen phosphorescence signal for AsLOV2 C450A (**A**) and AsLOV2 wt (**B**) at different irradiation levels. The six curves were fitted in a global fitting procedure; the lines represent the fitted results. Insets: The decay of the FMN triplet state absorbance at 633 nm following the excitation laser pulse as measured for AsLOV2 C450A and AsLOV2 wt. Black and magenta points correspond to low and high irradiation, respectively.

Bottom-up mass spectrometry. Samples (10 µg) of each wild-type and C450A AsLOV2, both irradiated and non-irradiated, were digested using trypsin or Asp-N in 100 mM Tris-HCl pH 8.5 at 37 °C overnight. Subsequently, the samples were analyzed using LC-MS/MS. Peptides were injected on a reversed phase trap column (Zorbax 300SB-C18 5 µm, 0.3 × 5 mm, Agilent Technologies, USA) and desalted by 0.1% FA in water for 3 min at flow rate of 20 µL/min. Next, the peptides were eluted and separated on an analytical column (ZORBAX 300SB-C18, 0.3 × 150 mm, 3.5 µm, Agilent, USA) using a linear acetonitrile gradient from 5 to 35% of solvent B. Solvents were as follows: A: 0.1% FA in water, B: 0.1% FA, 95% ACN in water. The flow on the analytical column was 10 µL/min and the temperature was held at 50 °C. Eluting peptides were analyzed online with ESI-FT-ICR MS (15 T solariX XR, Bruker Daltonics, Germany) operating in data-dependent mode. The data were processed by DataAnalysis 4.1 (Bruker Daltonics, USA) and then searched by MASCOT in ProteinScape 4 (Bruker Daltonics, USA) against a database containing the AsLOV2 wt and C450A sequences. Various oxidative modifications of Met, Phe, His, Trp, Tyr, Pro and Cys were set as a variable. Parallel analysis in PEAKS X Studio was also conducted with automatic search for possible modifications present in the Unimod database. All found oxidized peptides and their non-oxidized variants were then manually searched in the data and their extracted ion chromatograms and highest intensity monoisotopic peaks were compared to estimate the level of oxidation. Assignment of oxidative modification to specific amino acids was done based on the fragment ions in the MS/MS spectra.

Results

In this work, singlet oxygen is generated through the interaction of triplet state FMN (^{3}FMN) with molecular oxygen. The kinetics of the ^{3}FMN transient absorption signals and $^1O_2$ phosphorescence were analyzed considering two assumptions. First, the small size of the studied AsLOV2 proteins (~3.5 nm diameter) suggests that $^1O_2$ diffuses out of the protein matrix relatively fast. Due to this fact, $^1O_2$ spends most of its lifetime in the water environment. The justification of this assumption is given in the Supporting information.

The second assumption is related to the fact that the FMN molecule is released from the protein to solvent due to oxidative modifications of the protein. The FMN released to water leads to an increase of $^1O_2$ production outside of the protein. The presence of FMN in the aqueous environment was also observed in the work of Westberg *et al.*[23] at low irradiation. In this work, we found evidence that FMN is present in the aqueous environment and its amount in the solution increases with irradiation of the sample.

Determination of ^{3}FMN lifetime. The time-resolved ^{3}FMN absorbance at 633 nm of the AsLOV2 C450A and the AsLOV2 wt are shown in insets of Fig. 1. The obtained ^{3}FMN lifetime values for both AsLOV2 variants are summarized in Table 1. The black points belong to low irradiation (obtained during the first 12.5 min of the irradiation), while the data taken after extensive irradiation (75 min) of the samples are shown in magenta.

Singlet oxygen phosphorescence. The experimental time-courses of the $^1O_2$ phosphorescence signals are shown in Fig. 1A,B for the AsLOV2 C450A and the AsLOV2 wt, respectively. The phosphorescence kinetics changes dramatically upon prolonged irradiation of the samples. For both AsLOV2 variants, the intensity of the phosphorescence signal increased significantly after 75 min of irradiation, indicating enhanced $^1O_2$ production. Analysis of the $^1O_2$ phosphorescence signals relies on the ^{3}FMN lifetime values, $\tau_{T,i}$, determined in the flash photolysis experiments. For all the six irradiation levels, the time-dependence of singlet oxygen phosphorescence $P(t)$ was assumed to consist of independent contributions, which correspond to different ^{3}FMN groups:

	AsLOV2 C450A		AsLOV2 wt	
	low irradiation (12.5 min)	high irradiation (75 min)	low irradiation (12.5 min)	high irradiation (75 min)
τ_T^{prot} [μs]	57 ± 2		1.5 ± 0.01	
τ_T^{prot*} [μs]	32 ± 7	23 ± 3	—	—
τ_T^{water} [μs]	2.7[F]		2.7[F]	
τ_Δ [μs]	2.7 ± 0.2	3.0 ± 0.2	2.6 ± 0.2	3.3 ± 0.2

Table 1. The lifetime values of ^{3}FMN and $^1O_2$ as determined by fitting the time-resolved absorbance and phosphorescence data. [F]fixed value, not varied during the fitting procedure.

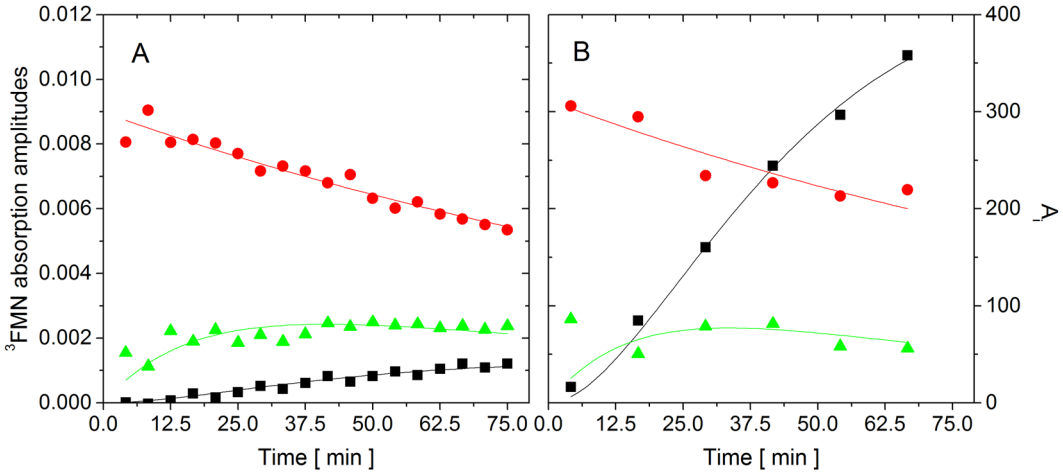

Figure 2. The amplitudes of the exponential ^{3}FMN absorption decays, Abs_i^0 (**A**) and the amplitudes A_i of the different ^{3}FMN group contributions to the $^1O_2$ phosphorescence signal (see Eq. 1) (**B**) in intact protein (red circles), in oxidized protein (green triangles), and in water (black squares) as a function of the irradiation time of AsLOV2 C450A. The solid lines represent the results of the fitting procedures.

$$P(t) = \sum_i \left[\frac{A_i \tau_\Delta}{\tau_\Delta - \tau_{T,i}} \left(e^{-\frac{t}{\tau_\Delta}} - e^{-\frac{t}{\tau_{T,i}}} \right) \right] \quad (1)$$

where A_i is amplitude of the phosphorescence and τ_Δ is the lifetime of the $^1O_2$ molecule.

In agreement with the assumption that singlet oxygen, wherever being produced, spends most of its lifetime in the aqueous environment, only a single lifetime of singlet oxygen, τ_Δ, was assigned to all the different contributions. It is noted that this approximation holds true due to the relatively short singlet oxygen lifetime in water environment and low protein concentration.

In the following sections, detailed analyses of ^{3}FMN lifetimes and $^1O_2$ phosphorescence are presented for the AsLOV2 C450A and AsLOV2 wt.

AsLOV2 C450A. The ^{3}FMN lifetime. Based on the transient absorption signals measured with the AsLOV2 C450A, we concluded that three different FMN groups are present in the system. These groups were assigned to the FMN inside the intact protein, the FMN inside the oxidized protein and the FMN in the water environment. The corresponding ^{3}FMN lifetimes (τ_T^{prot}, τ_T^{prot*}, and τ_T^{water}) were determined by fitting all the 18 decay curves with triple-exponential decays using the following constrictions: τ_T^{prot} - a single fitting parameter used for all the decay curves; τ_T^{prot*} - no restrictions, this lifetime was allowed to evolve during the irradiation; τ_T^{water} - not fitted, fixed to 2.7 μs - the lifetime measured by our apparatus in aqueous solution of FMN, which is in agreement with previously reported value[2].

The ^{3}FMN lifetime values obtained for AsLOV2 C450A can be summarized as follows: $\tau_T^{prot} = 57 \pm 2$ μs; τ_T^{prot*} - gradually decreases from 32 ± 7 μs (at low-irradiation) to 23 ± 3 μs (at high-irradiation) (Figure S1). The decreasing τ_T^{prot*} lifetime is likely caused by the gradually increasing accessibility of the protein interior to oxygen due to by the irradiation-induced oxidation. The ^{3}FMN lifetime determined for AsLOV2 C450A, $\tau_T^{prot} = 57$ μs, is in accordance with the corresponding lifetime values previously reported for the C450A variant, i.e. 72 μs[31] and 98 μs[47], and also with the lifetimes found in miniSOG, $\tau_T^{prot} = 28$ μs, and SOPP, $\tau_T^{prot} = 79$ μs at 30 °C[26].

Additional information can be derived from the amplitudes Abs_i^0 of the triple-exponential decay curves ($\Sigma_i Abs_i^0 \exp(-t/\tau_{Ti})$), which represents ^{3}FMN absorption right after the excitation laser pulse (Fig. 2A). The direct comparison of the initial absorption amplitudes is difficult because of the unknown extinction coefficients for all three different ^{3}FMN groups. Despite this drawback, the absorption amplitudes provide an important information about the kinetics of the system evolution.

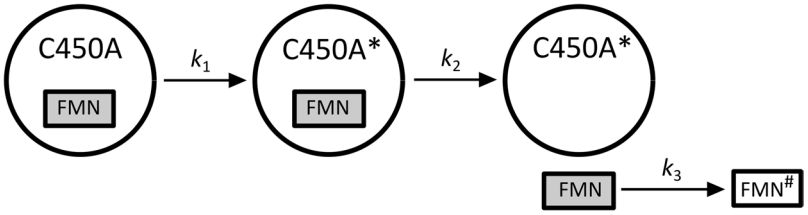

Scheme 1. The scheme of the irradiation-induced changes in AsLOV2 C450A and FMN dissociation. C450A and C450A* represent the intact and the oxidized protein, respectively. FMN and FMN# represent the intact and the bleached flavin cofactor, respectively.

Based on the experimental observation, we proposed a model that schematically describes irradiation-induced changes in AsLOV2 C450A accompanied by FMN release (Scheme 1).

The protein oxidation is characterized by the unimolecular rate constant k_1. The constant k_2 represents the rate constant of the FMN release from the oxidized protein. For the sake of simplicity, only a single unimolecular rate constant k_2 was used for all the proteins with different level of oxidation. Finally, the bleaching of FMN in the water environment (rate constant k_3) was taken into account in the model. Precise description of the model by differential equations and the corresponding analytical solutions for different FMN groups' concentrations $[FMN]_i$ are shown in Supporting information. It is noted that the values of k_1, k_2, and k_3 depend on the irradiation conditions and are specific for the present experiment.

To determine the rate constant of FMN bleaching, k_3, in the solution, we performed separate experiments. For this purpose, 25 µM FMN was mixed with 25 µM apoAsLOV2, which was prepared according to the procedure of Dürr *et al.*[48] and was irradiated in the same way as both AsLOV2 variants. Noteworthy, upon admixture of apoAsLOV2 and FMN, formation of holoAsLOV2 was not detected based on UV-Vis absorbance measurement. The apoAsLOV2 wt was used to mimic the presence of the protein in the solution. As expected, significant bleaching of FMN was observed and both the production of singlet oxygen and the initial absorbance values Abs^0_{water} of ^{3}FMN decreased exponentially. The rate of the bleaching was determined as $1/k_3 = 3260$ s, which reflects both the decay of $^1O_2$ production, and the decay of the ^{3}FMN absorption amplitudes (Abs^0_{water}). The ^{3}FMN lifetime remained unaffected, 2.7 ± 0.1 µs, during the irradiation experiment.

The obtained kinetics of ^{3}FMN absorption amplitudes (Fig. 2A) for AsLOV2 C450A were fitted according to the model shown in Scheme 1 (assuming proportionality between: (i) the concentration of FMN, (ii) the amount of ^{3}FMN produced and (iii) the ^{3}FMN absorption signal Abs_i^0 in each group, throughout the irradiation experiment). The data points of Abs^0_{prot} were fitted by the single exponential decay (Eq. S1), from which the characteristic time, $1/k_1 = 9000$ s was obtained for the rate of protein oxidation in our system. The value of k_2 was determined by fitting the ^{3}FMN absorption in the oxidized protein Abs^0_{prot*} and in the solution Abs^0_{water} with the corresponding time-dependences (Eqs. S2 and S3), using the previous values of k_1 and k_3. The best match of the experimental data and the analytical curves was obtained for $1/k_2 = 1000$ s. Based on the fits shown in Fig. 2A, we can conclude that the experimental data are well described by the model.

AsLOV2 C450A. Singlet oxygen phosphorescence. The ^{3}FMN lifetime values (τ_T^{prot}, τ_T^{prot*}, and τ_T^{water}) were utilized to analyze the $^1O_2$ phosphorescence data. The phosphorescence amplitudes A_{prot}, A_{prot*} and A_{water} and the lifetime of singlet oxygen τ_Δ were determined in a global fit (using all the measured curves shown in Fig. 1A). The lifetime of $^1O_2$ was allowed to evolve during the irradiation. The fitted curves and the obtained amplitudes are shown in Figs. 1A and 2B, respectively. The evolutions of A_{water} and A_{prot} were fitted with the corresponding time-dependences of $[FMN]_{water}$ and $[FMN]_{prot}$, respectively. The general shape of these curves reproduces the experimental data very well. Based on the proposed model, the proportionality factors of the two curves (black and red line in Fig. 2B) can be used to calculate the quantum yield of singlet oxygen production in the intact AsLOV2 C450A, using the quantum yield of $^1O_2$ production by FMN in the solution ($\Phi_{\Delta\,water} = 0.57$)[2] as a reference. Taking into account the different absorbance of the two FMN groups at the excitation wavelength (475 nm) (Figure S2), the Φ_Δ value for the intact AsLOV2 C450A equals to 0.07. The analogous quantitative analysis of the A_{prot*} data is not feasible due to the changing level of oxidation during the experiment.

AsLOV2 wt. The ^{3}FMN lifetime. The kinetics of ^{3}FMN transient absorption in the AsLOV2 wt (inset Fig. 1B), were analyzed in analogous way as for the AsLOV2 C450A variant. In the case of the AsLOV2 wt, only two triplet state lifetime components were identified. Based on this observation, we concluded that FMN is released from the oxidized AsLOV2 wt very fast. This is in agreement with our results from molecular dynamics studies, which indicate a steric clash between the oxidized Cys450 and FMN (see below). The ^{3}FMN absorption decays were fitted with two lifetime values (τ_T^{prot}, τ_T^{water}), assuming that these lifetimes do not change during the irradiation: τ_T^{prot} - a single fitting parameter used for all the decay curves; τ_T^{water} - not fitted, fixed to 2.7 µs, which is the lifetime measured in pure FMN solution. The global fit resulted in a value of $\tau_T^{prot} = 1.50 \pm 0.01$ µs. The low error indicates high-quality fits.

The obtained lifetime of the ^{3}FMN state in AsLOV2 wt is in good agreement with the results of Swartz *et al.*, $\tau_T^{prot} = 2$ µs[31] and Song *et al.*, $\tau_T^{prot} = 2.2$ µs[49], but differs from the triplet state decay time reported by Gil *et al.*, $\tau_T^{prot} = 9.5$ µs[47].

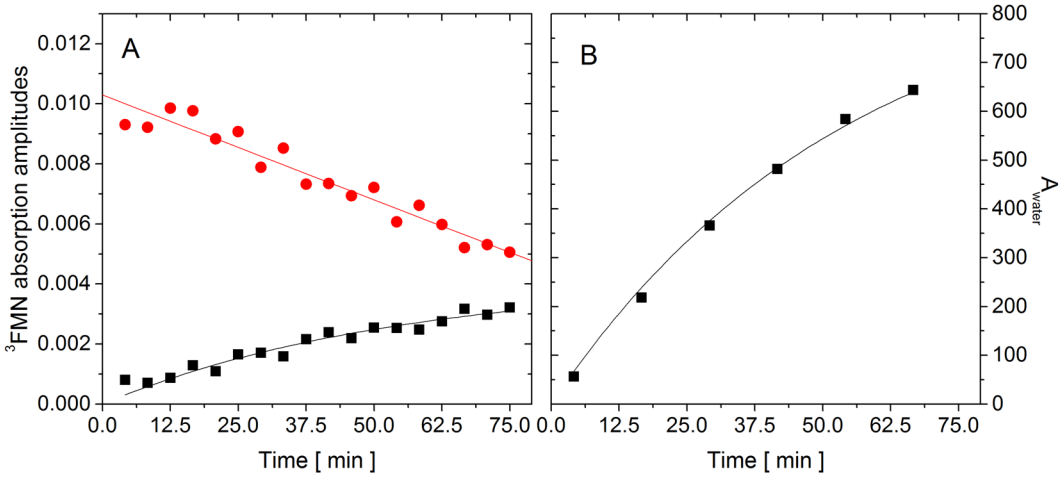

Figure 3. The amplitudes of the exponential ^{3}FMN absorption decays, Abs_i^0 (**A**) and the amplitudes A_i of the different ^{3}FMN group contributions to the $^1O_2$ phosphorescence signal (see Eq. 1) (**B**) in intact protein (red circles) and in water (black squares) as a function of the irradiation time of AsLOV2 wt. The solid lines represent the results of the fitting procedures.

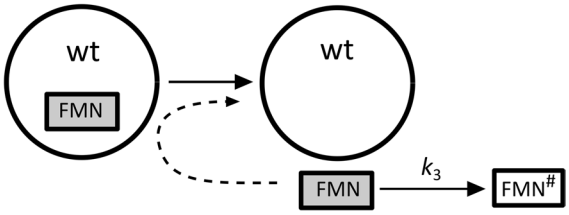

Scheme 2. The scheme of the irradiation-induced changes in AsLOV2 wt and FMN dissociation. FMN and FMN# represent the intact and the bleached flavin cofactor, respectively.

The amplitude of the ^{3}FMN absorption Abs^0_{prot} indicates that the amount of ^{3}FMN produced in the intact protein (Fig. 3A, red points) decreased by 50%. At the same time, there is no evidence of slowing the decrease down towards longer irradiations. In this case, the experimental data are better fitted with a linear decrease than with an exponential decay. This behavior is consistent with the assumption of the fast FMN release from the protein and can be rationalized as follows: the quantum yield of $^1O_2$ production is very low for the FMN inside the AsLOV2 wt. Once the FMN is released from the protein, the rate of $^1O_2$ production increases, which in turn enhances the rate of the protein oxidation and the rate of FMN release. In principle, the FMN release acts as an auto-catalyzed reaction, which explains the unusual (quasi-linear) decrease of Abs^0_{prot}. Scheme 2 shows a model of irradiation-induced changes in the AsLOV wt accompanied by FMN release.

The mathematical description of this model is shown in the Supporting information. This model was used to fit the Abs_i^0 values in Fig. 3A. The curvature of the Abs_{water} (black squares), reflecting the bleaching effect, is well described by the rate constant k_3.

AsLOV2 wt. Singlet oxygen phosphorescence. The procedure of the analysis of $^1O_2$ phosphorescence data of the AsLOV2 wt were analogous as in the case of AsLOV2 C450A, taking into account the different model of irradiation-induced changes in the protein. Based on the fitting results, we conclude that the observed phosphorescence signal in AsLOV2 wt can be fully explained by $^1O_2$ production in the solution and the contribution of the FMN_{prot} group can be considered as negligible. The results of the phosphorescence global fits and the obtained amplitudes A_{water} are shown in Figs. 1B and 3B, respectively. The A_{water} values are well fitted with the $[FMN]_{water}$ time-dependence using the same value of $1/k_3 = 3260$ s.

The global fit (based on the developed model) allowed us to determine the dependence of $^1O_2$ lifetime on irradiation time (Fig. 4). The results show than in both AsLOV2 variants the lifetime of $^1O_2$ increases with irradiation time very likely as a result of progressive proteins oxidation.

Changes in AsLOV2 optical spectra induced by irradiation. *UV-VIS absorption spectroscopy.* UV-VIS absorption spectra of the wild type and the C450A variant of AsLOV2 are almost identical in the spectral range 300–550 nm and correspond to the absorption of FMN (Figure S2). Both variants exhibit major absorption peaks at 447 nm, 473 nm, and a shoulder at ~425 nm. The difference between these two forms in the region 300–400 nm reflects the replacement of cysteine for alanine in position 450[31,32]. After blue light irradiation, a small spectral change in the region 400–500 nm is observed in both AsLOV2 forms, corresponding to ~12% and

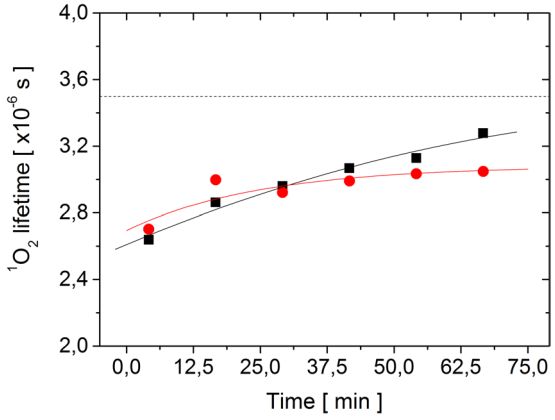

Figure 4. Dependence of the $^1O_2$ lifetime on irradiation time in AsLOV2 C450A (red circles) and AsLOV2 wt (black square). The estimated error of individual data points is ±0.2 μs. The solid lines serves as an eye lead. The dashed line is the $^1O_2$ lifetime in pure water[70].

~22% decrease in the absorbance at 447 nm for AsLOV2 C450A and AsLOV2 wt, respectively (Figure S3). The observed decrease is usually attributed to chromophore bleaching. The small increase in the absorbance in the region 300–400 nm has been previously interpreted as a result of tryptophan oxygenation to kynurenine[50], which is in accordance with the results obtained by mass spectrometry (see below).

Circular dichroism. Structural changes in AsLOV2 proteins induced by irradiation were also followed by circular dichroism (CD) spectroscopy in the far- and near- UV regions (Figure S4). In the far-UV region, the CD spectra show that both variants of AsLOV2 contain similar fractions of α-helical (~13 ± 3%) and β-sheet (32 ± 3%) structures (for the analysis we used two different web servers: DICHROWEB[51,52] and BeStSel[53]). Small changes in the secondary structure in both variants of AsLOV2 are noticeable after the extensive laser irradiation (Figures S4A,C), corresponding to ~13% and ~25% decrease in ellipticity at 222 nm for AsLOV2 C450A and AsLOV2 wt, respectively. The extent of the changes is similar both in the far-UV and the near-UV regions to those observed in the corresponding UV-VIS absorption spectra. The observed changes can be attributed to a direct effect of ROS or can be of a secondary nature as a result of the chromophore oxygenation and/or its release[54].

Fluorescence. AsLOV2 contains two intrinsic fluorescent probes, FMN chromophore and one tryptophan residue, Trp491. Comparison of the fluorescence emission spectra of the flavin chromophore located in the AsLOV2 wt and its variant AsLOV2 C450A clearly shows significantly lower intensity of the fluorescence in the AsLOV2 wt (Fig. 5). This is due to light-induced formation of covalent bond between flavin chromophore and the reactive cysteine in the AsLOV2 wt. The fluorescence maximum of the wild-type protein after irradiation is moved to higher wavelengths, corresponding to the peak of free FMN at 520 nm (Fig. 5A). These results suggest that part of the flavin chromophores are released from the binding pocket into the solvent. In fact, we fitted the fluorescence spectrum of AsLOV2 wt after irradiation as a combination of the fluorescence spectra of protein bound FMN and free FMN. The obtained fit consists of two fractions combining ~45% of the free FMN and ~55% protein-bound FMN (Fig. 5A). In the case of AsLOV2 C450A, the irradiation induces ~23% decrease in fluorescence intensity measured at 500 nm (Fig. 5B). An analogous fit for AsLOV2 C450A (Fig. 5B) led to fractions of free and protein-bound FMN equal to ~25% and ~75%, respectively. On the other hand, the intrinsic tryptophan fluorescence of AsLOV2 C450A before irradiation is ~20% higher than the fluorescence of AsLOV2 wt (insets Fig. 5). The irradiation induces ~1.6-fold and ~2.6-fold increase in fluorescence intensity of AsLOV2 C450A and AsLOV2 wt, respectively. The absence of a shift in the maximum of the tryptophan fluorescence suggests that the observed irradiation-induced increase is not due to a conformational change in the proteins, but rather due to decreased fluorescence quenching by the flavin cofactor.

To address the possibility of FMN dissociation from the protein, we performed simple filtration experiments in which the released cofactor passes through the filter, while the protein is retained. The outcome of these experiments showed that before irradiation there was no free FMN detected in the filtrate. The irradiation-induced changes in the proteins led to release of FMN from both types of proteins (Fig. 6). Although this method does not allow quantitative determination of released FMN, it does allow a relative comparison: irradiation induced a release of ~1.8-fold more FMN in the case AsLOV2 wt in comparison with AsLOV2 C450A variant (Fig. 6), which corresponds to the ratio of dissociated FMN from AsLOV2 wt and AsLOV2 C450A obtained from the analysis of the fluorescence spectra in Fig. 5.

Another way to assess the fraction of retained FMN in the protein after irradiation is to compare the amplitude of the cysteinyl-FMN adduct formation in the AsLOV2 wt measured by flash-induced absorbance changes at 447 nm[55] using samples before and after the extensive (75 min) irradiation by laser (Fig. 7). The obtained results suggest that after irradiation only ~40% of FMN is able to form the adduct.

Determination of irradiation-induced changes in primary structures of AsLOV2. Light-induced production of $^1O_2$ by FMN is accompanied by covalent modification of amino acids in AsLOV2, which

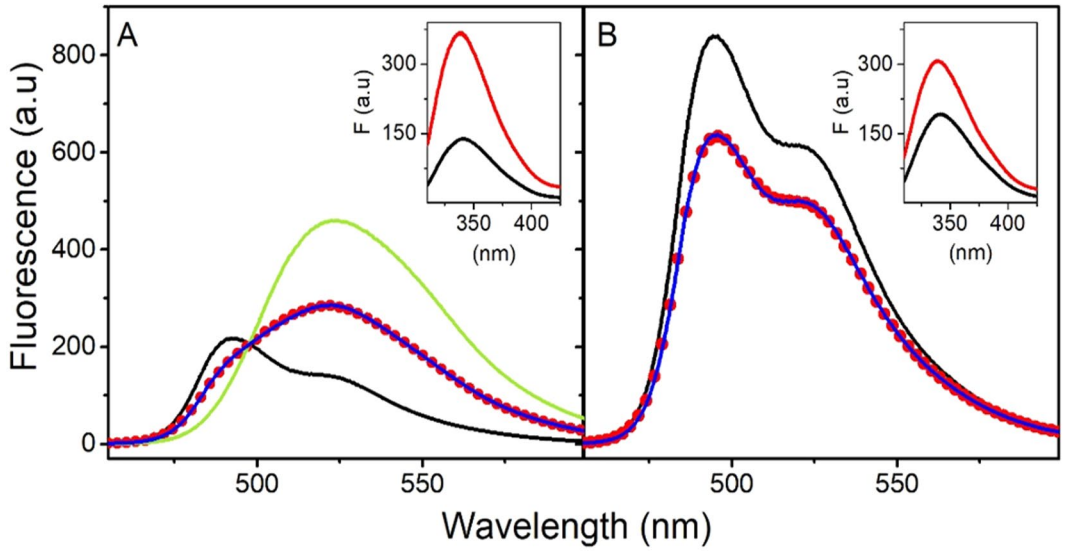

Figure 5. Fluorescence emission spectra of FMN and intrinsic tryptophan in AsLOV2 wt and AsLOV C450A. The fluorescence of FMN in AsLOV2 wt (**A**) and in AsLOV2 C450A (**B**) before (black line) and after (red dots) illumination and the fluorescence of free FMN (green). The blue line shows the fit to FMN fluorescence after the illumination. The fits (blue line) consist of two fractions of fluorescence: protein-bound and free FMN. Insets: Intrinsic tryptophan fluorescence of the corresponding forms of AsLOV2 before (black line) and after illumination (red line). The concentrations of proteins and the free FMN were 10 µM in 20 mM Tris-HCl, pH 7.8.

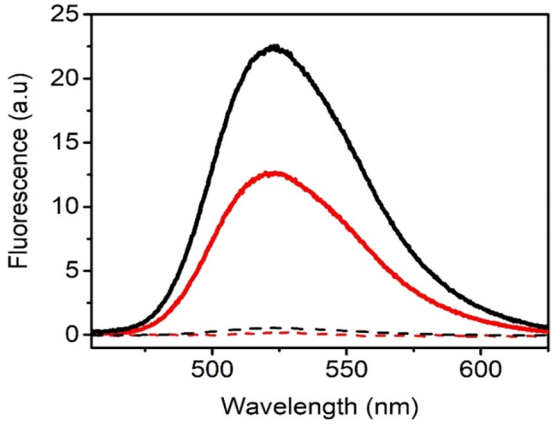

Figure 6. Analysis of a release of FMN from AsLOV2 wt and AsLOV2 C450A induced by blue light irradiation. FMN fluorescence indicates a release of FMN from its binding pocket to the bulk solvent. FMN fluorescence of non-irradiated AsLOV2 wt (black dashed), AsLOV2 C450A (red dashed) and irradiated AsLOV2 wt (black solid) and AsLOV2 C450A (red solid).

localization and nature of the modification were determined. First, we measured the intact mass to verify the protein state and possible fragmentation. Based on these data (Figure S5A), we concluded that the irradiated proteins are intact, no significant fragmentation occurred but they differ in the extent of oxidative modifications, with C450A form being significantly more affected upon irradiation (Figure S5B).

In the bottom-up approach, the protein was digested in solution, analyzed by LC-MS/MS and the generated peptides were identified by database searching and automated *de novo* sequencing. This yielded a list of modified residues and allowed a direct comparison between the different AsLOV2 states regarding the extent of oxidation of individual amino acids (Fig. 8). By this approach, 97% coverage was achieved and only five residues (460–464) were missed (Figure S6). Observed oxidation of the His-tag sequence (N-terminal Met and histidines) are not listed among the modified residues in Fig. 8, as this part of the sequence (the first 31 amino acids) is unnatural for AsLOV2 (Figure S6).

In the AsLOV2 wt, di- and tri- oxidation of Cys450, (but not single oxidation) were found to be very prominent modifications. While the bottom-up method targeted the whole bulk of protein populations, the top-down approach allowed the selection of the "first-hit"/singly oxidized species, and their subsequent fragmentation and assignment of modified residues based on the protein MS/MS spectra. The selection of singly oxidized protein forms had also another benefit as it "filtered-out" the Cys450 modification, which occurred as double and triple

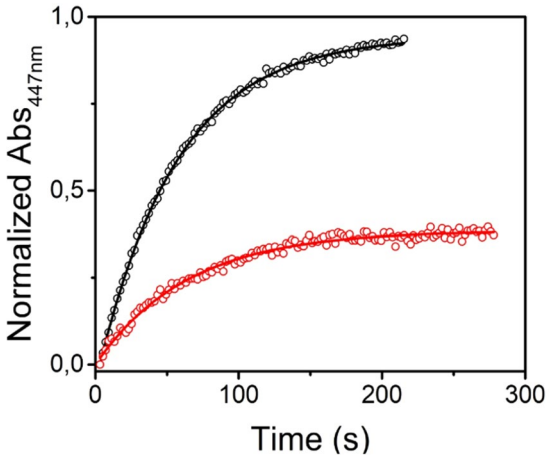

Figure 7. Dark state recovery kinetics of non-irradiated (black) and irradiated (red) AsLOV2 wt. Experimental data are shown as circles and the solid lines show fits of the data by single exponential functions.

	Mod.	wt-N [%]	mut-N [%]	wt-I [%]	mut-I [%]	mut-I - mut-N / wt-I - wt-N
F415:	+O1	0.0	0.0	2.8	3.8	1.4
P420	-C1O1	0.0	0.0	19.3	19.8	1.0
P423/426	-C1O1	0.0	0.3	11.1	14.7	1.3
F429	+O1	0.0	1.0	19.0	21.5	1.1
C450	+O2/+O3	-	-	82.5	-	*
F452/P456	+O1	0.0	0.0	0.1	0.2	2.0
P456	-C1O1	0.0	0.0	0.3	1.0	3.0
Y483	+O1	0.0	0.0	3.5	3.7	1.1
F490/W491	+O1	1.1	1.6	18.4	16.3	0.9
W491	-C1O1	0.0	0.0	7.9	7.4	0.9
M499	+O1	10.0	9.8	29.5	44.0	1.8
Y508	+O1	0.0	0.2	1.2	1.0	0.7
M530	+O1	0.6	0.0	6.1	11.7	2.1

Figure 8. List of oxidation products and their extent of oxidation (intensity of oxidatively modified peptide) in all studied protein forms – wild-type (wt) and C450A (mut) before (N) and after (I) irradiation. Column Mod shows the elemental composition of the modification (oxidation: +O1, +O2 or +O3; Trp to kynurenin: -C1+O1; Pro to pyrrolidone: -C1O1). When it was not possible to clearly assign oxidation to one specific residue, two possibly affected residues are listed in the first column. The last column highlights the fold change in oxidation between C450A and wt forms. In case of C450 oxidation (marked in the last column with an asterisk) such comparisons were not possible due to generation of different peptides upon oxidation and due to mutation. The intensity of oxidized form was indirectly deduced from intensity decrease of the intact, unoxidized Asp-N generated peptide.

oxidation and allowed us to focus on other residues. Unfortunately, the gas-phase fragmentation of AsLOV2 proved to be quite inefficient as we missed fragmentation in the middle of the protein (Figure S7A). Nonetheless, we obtained the information supporting and complementing our bottom-up data. Based on the oxidation increase between the N-terminal fragment ions b26 and b47 together with the same trend observed from the opposite site (C-terminal fragment ions y127 and y151) we can point on Phe415 as an oxidation-sensitive amino acid. Furthermore, we can also conclude (based on fragment ion y36, Figure S7B), that the sequence spanning from Gly511 to the C-terminus is not affected by oxidative events in any of the analyzed AsLOV2 forms. This is at first in apparent contrast with the bottom-up data, where Met530 was found to be oxidized and where the data point to a significant difference between wt and C450A forms (Fig. 8). However, one should keep in mind that the top-down fragmentation was aimed at the first-hit oxidation and thus we can assume that Met530 oxidation is a secondary event. Finally, we can state that the remaining primary oxidation sites are localized between amino acids 420 and 511 where the majority of significantly oxidized residues were found by the bottom-up approach.

Altogether, based on the MS data it can be concluded that: (i) the modifications occurring in AsLOV2 upon irradiation consist of various products of amino acid side chain oxidations, (ii) the modifications are light-dependent as the overall extent of the oxidative modifications is much higher in irradiated samples of both

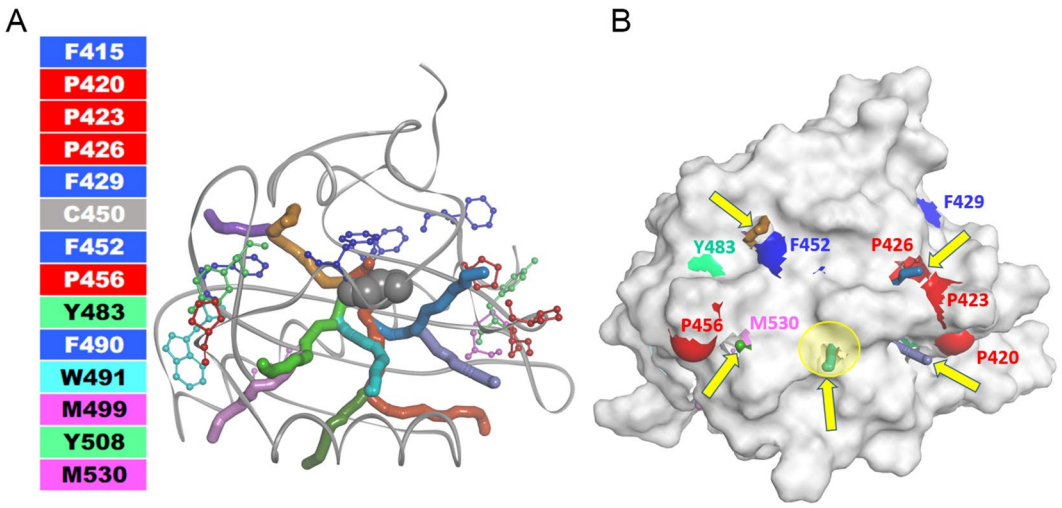

Figure 9. Discovery Studio visualization of Caver-calculated tunnels of minimized PDB ID: 2v0u structure. (**A**) Ribbon representation of the protein with color-coded amino acids (summarized in Fig. 6) shown in ball and stick representation. C450 is shown in grey CPK representation. The color coding of the tunnels represented as CPK does not correspond to the color coding of the amino acids and is for their distinction only. (**B**) Surface representation of the protein with color coding of the amino acids of interest on the surface. The yellow arrows highlight the tunnels reaching the protein surface. The ribityl chain of FMN structure (not shown) overlaps with the circled tunnel 1 (yellow semitransparent circle). Detailed information from 5 ns MD simulations is summarized in Figure S9.

AsLOV2 wt and the AsLOV2 C450A variant, (iii) generally the same amino acids are oxidized in both AsLOV2 variants, (iv) the extent of some oxidative modification is higher in AsLOV2 C450A compared to AsLOV2 wt.

Detection of tunnels in the structure of AsLOV2. The unusual modification of proline residues (highlighted in red in Figs. 9 and S8, illustrating that P420, P423 and P426 form a cluster on the right side of the protein) led us to an assumption that in this part of the protein exit channel(s) may exist, connecting the source of the production of $^1O_2$ with the protein surface. As a result, even prolines, which are usually resistant to redox reactions, are oxidized by reactive oxygen species created by FMN. Indeed, the Caver 3.0[45] tunnel analysis of AsLOV2 wt crystal structure (PDB ID: 2v0u) detected the presence of several tunnels. We have analyzed several AsLOV2-related protein structures: at first we considered their optimized geometries and then their geometries resulting from 5 ns MD simulation in water environment: (i) dark state of AsLOV2 wt (PDB ID: 2v0u), i.e. without covalent bond between C450 and C4(a) of the isoalloxazine ring (Figure S8A), (ii) *in silico* SOO^- substitution on C450 Sulphur (Figure S8B), (iii) light state of AsLOV2 wt (PDB ID: 2v0w), i.e. with covalent bond between C450 and C4(a) of the isoalloxazine ring (Figure S8C), and (iv) *in silico* mutated AsLOV2 C450A (Figure S8D). The presence of tunnels was detected in all the protein geometries (Figures S8A–D). However, the number of tunnel clusters, as indicated on the pie chart on Figure S8 slightly differs, related to the C450 modifications/FMN binding. Several tunnel clusters (channels) (Figs. 9 and S8) are believed to be lined by the above mentioned P420, P423 and P426 amino acids. Several other channels, as illustrated in Figs. 9 and S8 terminate in the proximity of the highlighted amino acids listed in Fig. 8 and are shown as CPK representation in Figure S8. Interestingly, the comparison of a number of channels observed in MD simulations in AsLOV2 wt and AsLOV2 C450A suggests that C450A exhibits slightly more tunnels and could thus suffer a larger damage by oxygen than AsLOV2 wt. The highest number of calculated tunnels was found in 2v0u-SOO^-, which in the light of our results might point to increased dynamics of the protein matrix explaining thus more efficient release of FMN from the protein.

Discussion

The protein matrix surrounding FMN can efficiently decrease the Φ_Δ value by quenching the excited triplet state of FMN and by restriction of oxygen diffusion towards the isoalloxazine ring[56]. This, on one side, may have a protective role for the photosensitizers close surrounding by preventing unwanted production of ROS but on the other hand, significantly limits the ROS effect on the site of an intendent action. Here, we argue that genetically-encoded photosensitizers may be used as a carrier of the reactive cofactor, and the release of the cofactor can be modulated by an irradiation or possibly other perturbation of the protein matrix.

Primary structure modification of AsLOV2 upon irradiation. As can be deduced from the fine structure of FMN absorption spectrum in the wavelength range 400–500 nm, the cofactor has no extensive contacts with solvent molecules[57]. This is also in accordance with the crystal structures of the closely related flavoproteins SOPP and miniSOG[2]. On the other hand, our *in silico* analysis of the AsLOV2 crystal structure[58] suggests the existence of several channels in the protein structure, connecting the reactive site C(4a) on the isoalloxazine ring with the protein surface (Fig. 9). This connection becomes even more obvious after molecular dynamics simulation (Figure S8). The presence of channels was also identified by molecular dynamics

simulation in the case of miniSOG[59]. If the channels play an active role as a traffic route of molecular oxygen to the FMN binding site and diffusion of the $^1O_2$ and possibly other ROS out to the protein surface, one can expect oxidatively modified amino acids localized close to these channels. Indeed, the localization of three modified prolines, Pro420, Pro423, and Pro426, at the orifice of a cluster of several channels provide an explanation of unexpected modification of this otherwise very oxidation-resistant amino acid (Fig. 9). Our results strongly support the ability of reactive oxygen species to react with proline[60,61]. Because some reports conclude that proline does not interact with $^1O_2$ our observations suggest a production of other ROS than $^1O_2$ by FMN when encapsulated in AsLOV2[62–64].

ROS effectively react with aromatic amino acids such as Trp and Tyr. One surprising observation regarding oxidative modification of amino acids in AsLOV2 was that none of the three tyrosine residues, present in AsLOV2, were modified by ROS produced by FMN. There are two ROS species that can be produced by FMN, $O_2^{\bullet-}$ and $^1O_2$. While $O_2^{\bullet-}$ is relatively unreactive and directly reacts only at a few specific protein sites[65], $^1O_2$ reacts efficiently with five common and functionally important amino acids (Cys, His, Met, Trp, Tyr)[5,8,66]. However, our findings show that ROS produced by AsLOV2 variants, surprisingly, do not oxidize the tyrosine residues of AsLOV2. Noteworthy, the absence of modification of tyrosine residues by $^1O_2$ was also noticed in the case of two unrelated proteins such as cytochrome *c* (containing 4 Tyr residues)[67] and lysozyme (containing 3 Tyr residues)[68].

The absence of the irradiation-induced modification of electron rich amino acids such as Tyr and Phe in both variants of AsLOV2 is unexpected on chemical grounds. Kiselar *et al.*[69] speculated that some of the oxidative modification of aromatic residues in general can be "transferred" to Met by radical transfer. This suggestion could help explain the rather significant increase in Met oxidation, but only low Tyr and Phe oxidation in C450A.

A higher number of oxidative modifications of amino acids detected in our work in comparison with a very recent paper by Torra *et al.*[29] can be attributed to the differences in the solution irradiation (wavelength, power, etc.) and partially also to the higher sensitivity and resolution obtained by our LC-MS/MS analysis on FT-ICR MS and combination of proteomics approaches directed at localization of the modification sites. Our approach truly analyzes all protein states present in the sample and, in addition, the top-down analysis allows the identification of the first-hit residues. In contrast, Torra *et al.*[29] identified the oxidized residues in the crystal structure, hence the possibility that they observed just the crystallization-capable population cannot be excluded.

Approaches to increase singlet oxygen production by LOV domains. The models based on our data demonstrate the fact that irradiation of both AsLOV2 variants is accompanied by FMN dissociation from the protein matrix. However, the dissociation as well as the production of $^1O_2$ is more efficient in AsLOV2 wt than in AsLOV2 C450A. The observed increase in $^1O_2$ yield is thus rather the consequence of FMN release than of the protein oxidation.

In several previous studies, the authors assumed that an increase in $^1O_2$ production was due to blocking concurrent reactions by electron transfer from redox-active amino acids such as Tyr, Phe, Met, Trp, and Cys, which quench the triplet state of FMN and may thus lead to formation of $O_2^{\bullet-}$[29]. In fact, this assumption led to efforts to rationally design genetically encoded efficient flavoproteins by replacing amino acids responsible for quenching of the FMN triplet state[23,26], allowing thus increased production of $^1O_2$. These efforts indeed led to an increased Φ_Δ value attained in miniSOG and SOPP without detecting a dissociation of FMN[21,26]. These observations suggest that $^1O_2$ production in genetically-encoded photosensitizers can be achieved also without a release of the cofactor from the protein matrix.

Impact of mutation C450A on FMN release. The combined analyses of the data obtained from ^{3}FMN absorption experiments (Fig. 3A), from the analytical models as well as from fitting of irradiation-induced FMN fluorescence of the free and protein-bound FMN (Fig. 5) point to the release of approximately $48 \pm 3\%$ and $28 \pm 4\%$ of FMN from AsLOV2 wt and AsLOV2 C450A, respectively, after irradiation of the proteins. About 1.8-fold higher release of FMN from AsLOV2 wt in comparison with AsLOV2 C450A was documented by direct determination of relative amount of FMN released from the irradiated proteins (Fig. 6). All these results suggest that AsLOV2 wt is more affected by irradiation than its variant C450A. Strikingly, the amplitude of irradiation-induced changes in absorbance and ellipticity (Figures S3 and S4) as well as the extent of changes detected by mass spectrometry analysis (Figure S7) clearly show the opposite, i.e. that the variant C450A is more perturbed than AsLOV2 wt. In fact, the analysis of the total (integrated) $^1O_2$ phosphorence signal in both variants clearly shows that AsLOV C450A produced significantly higher amount of $^1O_2$ (Figure S10) and likely also other ROS during irradiation, which explains the higher oxidation damage of AsLOV2 C450A in our experiments.

To reconcile our observations, we hypothesize that more efficient release of FMN from AsLOV2 wt than from its Ala-containing variant is due to irradiation-induced oxidation of Cys450. As illustrated in Figure S9, the "brute force" superposition of C450 and (per)oxidized C450 results in a steric clash of modified Cys450 and FMN. Molecular geometry optimization and the subsequent MD simulations can easily eliminate such inappropriate molecular contacts, but in real structures such intermolecular conflicts could facilitate the release of FMN from AsLOV2.

Conclusions

We show that an irradiation-induced increase of $^1O_2$ production in the AsLOV2 variants is due to a release of FMN to solvent as a result of oxidative modification of certain amino acids, predominantly the reactive cysteine 450, localized nearby the isoalloxazine ring in the AsLOV2 structure. Our findings may be utilized to design more efficient genetically encoded photosensitizers based on LOV domains. The protein scaffold can serve merely as a targetable carrier while the reactive cofactor would be released at the site of action by a suitable perturbation of the protein structure. In principle, intensive blue light irradiation or combined approach including both

irradiation and thermogenesis could be applied. The irradiation can be more efficient in releasing FMN, if the binding site of isoalloxazine ring becomes repulsive upon irradiation, either through steric clashes or through charge repulsion. Enhanced effect, might be achieved by placing suitable amino acids close to the isoalloxazine ring. These amino acids, such as cysteine or methionine, upon irradiation-induced oxidation increase their volumes and form steric clashes, thereby repelling the flavin cofactor. Local thermogenesis could be an alternative approach that would increase FMN dissociation from AsLOV2, due to the increased dynamics of polypeptide chain and consequently the increase of the Φ_Δ value[2].

Received: 13 September 2019; Accepted: 13 February 2020;
Published online: 05 March 2020

References

1. Baier, J. *et al.* Singlet oxygen generation by UVA light exposure of endogenous photosensitizers. *Biophys. J.* **91**, 1452–1459, https://doi.org/10.1529/biophysj.106.082388 (2006).
2. Westberg, M., Bregnhoj, M., Etzerodt, M. & Ogilby, P. R. Temperature Sensitive Singlet Oxygen Photosensitization by LOV-Derived Fluorescent Flavoproteins. *The journal of physical chemistry. B* **121**, 2561–2574, https://doi.org/10.1021/acs.jpcb.7b00561 (2017).
3. Baron, R. *et al.* Multiple pathways guide oxygen diffusion into flavoenzyme active sites. *Proceedings of the National Academy of Sciences of the United States of America* **106**, 10603–10608, https://doi.org/10.1073/pnas.0903809106 (2009).
4. Meissner, B., Schleicher, E., Weber, S. & Essen, L. O. The dodecin from Thermus thermophilus, a bifunctional cofactor storage protein. *The Journal of biological chemistry* **282**, 33142–33154, https://doi.org/10.1074/jbc.M704951200 (2007).
5. Davies, M. J. Singlet oxygen-mediated damage to proteins and its consequences. *Biochem. Biophys. Res. Commun.* **305**, 761–770, https://doi.org/10.1016/s0006-291x(03)00817-9 (2003).
6. Ogilby, P. R. Singlet oxygen: there is indeed something new under the sun. *Chem. Soc. Rev.* **39**, 3181–3209, https://doi.org/10.1039/b926014p (2010).
7. Schweitzer, C. & Schmidt, R. Physical mechanisms of generation and deactivation of singlet oxygen. *Chem Rev* **103**, 1685–1757, https://doi.org/10.1021/cr010371d (2003).
8. Davies, M. J. Reactive species formed on proteins exposed to singlet oxygen. *Photochemical & photobiological sciences: Official journal of the European Photochemistry Association and the European Society for Photobiology* **3**, 17–25, https://doi.org/10.1039/b307576c (2004).
9. Mansoori, B. *et al.* Photodynamic therapy for cancer: role of natural products. *Photodiagnosis Photodyn Ther* **26**, 395–404, https://doi.org/10.1016/j.pdpdt.2019.04.033 (2019).
10. McLean, M. A. *et al.* Mechanism of chromophore assisted laser inactivation employing fluorescent proteins. *Anal. Chem.* **81**, 1755–1761, https://doi.org/10.1021/ac801663y (2009).
11. Riani, Y. D., Matsuda, T., Takemoto, K. & Nagai, T. Green monomeric photosensitizing fluorescent protein for photo-inducible protein inactivation and cell ablation. *BMC Biol.* **16**, 50, https://doi.org/10.1186/s12915-018-0514-7 (2018).
12. Redmond, R. W. & Kochevar, I. E. Spatially resolved cellular responses to singlet oxygen. *Photochem Photobiio* **82**, 1178–1186, https://doi.org/10.1562/2006-04-14-IR-874 (2006).
13. Wojtovich, A. P. & Foster, T. H. Optogenetic control of ROS production. *Redox Biol* **2**, 368–376, https://doi.org/10.1016/j.redox.2014.01.019 (2014).
14. Westberg, M. *et al.* Exerting better control and specificity with singlet oxygen experiments in live mammalian cells. *Methods* **109**, 81–91, https://doi.org/10.1016/j.ymeth.2016.07.001 (2016).
15. Endres, S. *et al.* An optogenetic toolbox of LOV-based photosensitizers for light-driven killing of bacteria. *Sci Rep* **8**, 15021, https://doi.org/10.1038/s41598-018-33291-4 (2018).
16. Hilgers, F. *et al.* Genetically Encoded Photosensitizers as Light-Triggered Antimicrobial Agents. *Int J Mol Sci* **20**, 4608, https://doi.org/10.3390/ijms20184608 (2019).
17. Shirmanova, M. *et al.* Towards PDT with Genetically Encoded Photosensitizer KillerRed: A Comparison of Continuous and Pulsed Laser Regimens in an Animal Tumor Model. *PLoS ONE* **10**, e0144617, https://doi.org/10.1371/journal.pone.0144617 (2015).
18. Norman, R. A. Past and future: porphyria and porphyrins. *Skinmed* **4**, 287–292, https://doi.org/10.1111/j.1540-9740.2005.03706.x (2005).
19. Xiong, Y., Tian, X. & Ai, H. W. Molecular Tools to Generate Reactive Oxygen Species in Biological Systems. *Bioconjug Chem* **30**, 1297–1303, https://doi.org/10.1021/acs.bioconjchem.9b00191 (2019).
20. Jiang, H. N., Li, Y. & Cui, Z. J. Photodynamic Physiology-Photonanomanipulations in Cellular Physiology with Protein Photosensitizers. *Front Physiol* **8**, 191, https://doi.org/10.3389/fphys.2017.00191 (2017).
21. Ruiz-Gonzalez, R. *et al.* Singlet oxygen generation by the genetically encoded tag miniSOG. *J. Am. Chem. Soc.* **135**, 9564–9567, https://doi.org/10.1021/ja4020524 (2013).
22. Rodriguez-Pulido, A. *et al.* Correction: Assessing the potential of photosensitizing flavoproteins as tags for correlative microscopy. *Chem Commun (Camb)* **52**, 9300, https://doi.org/10.1039/c6cc90313d (2016).
23. Westberg, M., Bregnhoj, M., Etzerodt, M. & Ogilby, P. R. No Photon Wasted: An Efficient and Selective Singlet Oxygen Photosensitizing Protein. *The journal of physical chemistry. B* **121**, 9366–9371, https://doi.org/10.1021/acs.jpcb.7b07831 (2017).
24. Jimenez-Banzo, A. *et al.* Singlet oxygen photosensitisation by GFP mutants: oxygen accessibility to the chromophore. *Photochemical & photobiological sciences: Official journal of the European Photochemistry Association and the European Society for Photobiology* **9**, 1336–1341, https://doi.org/10.1039/c0pp00125b (2010).
25. Ragas, X., Cooper, L. P., White, J. H., Nonell, S. & Flors, C. Quantification of photosensitized singlet oxygen production by a fluorescent protein. *ChemPhysChem* **12**, 161–165, https://doi.org/10.1002/cphc.201000919 (2011).
26. Westberg, M., Holmegaard, L., Pimenta, F. M., Etzerodt, M. & Ogilby, P. R. Rational design of an efficient, genetically encodable, protein-encased singlet oxygen photosensitizer. *J. Am. Chem. Soc.* **137**, 1632–1642, https://doi.org/10.1021/ja511940j (2015).
27. Shu, X. *et al.* A genetically encoded tag for correlated light and electron microscopy of intact cells, tissues, and organisms. *PLoS biology* **9**, e1001041, https://doi.org/10.1371/journal.pbio.1001041 (2011).
28. Jensen, R. L., Arnbjerg, J. & Ogilby, P. R. Reaction of singlet oxygen with tryptophan in proteins: a pronounced effect of the local environment on the reaction rate. *J. Am. Chem. Soc.* **134**, 9820–9826, https://doi.org/10.1021/ja303710m (2012).
29. Torra, J. *et al.* Tailing miniSOG: structural bases of the complex photophysics of a flavin-binding singlet oxygen photosensitizing protein. *Sci Rep* **9**, 2428, https://doi.org/10.1038/s41598-019-38955-3 (2019).
30. Zayner, J. P., Antoniou, C. & Sosnick, T. R. The amino-terminal helix modulates light-activated conformational changes in AsLOV2. *J. Mol. Biol.* **419**, 61–74, https://doi.org/10.1016/j.jmb.2012.02.037 (2012).
31. Swartz, T. E. *et al.* The photocycle of a flavin-binding domain of the blue light photoreceptor phototropin. *The Journal of biological chemistry* **276**, 36493–36500, https://doi.org/10.1074/jbc.M103114200 (2001).
32. Salomon, M., Christie, J. M., Knieb, E., Lempert, U. & Briggs, W. R. Photochemical and mutational analysis of the FMN-binding domains of the plant blue light receptor, phototropin. *Biochemistry* **39**, 9401–9410 (2000).

33. Desmond Molecular Dynamics System. Schrödinger Maestro 2019-2; Desmond Molecular Dynamics System; Schrödinger Inc. & D. E. Shaw Research; New York, NY (2019).
34. Bowers, K. J. *et al*. in Proceedings of the 2006 ACM/IEEE conference on Supercomputing - SC '06 (ACM Press, 2006).
35. Jorgensen, W. L. & Tirado-Rives, J. The OPLS [optimized potentials for liquid simulations] potential functions for proteins, energy minimizations for crystals of cyclic peptides and crambin. *J. Am. Chem. Soc.* **110**, 1657–1666, https://doi.org/10.1021/ja00214a001 (1988).
36. Jorgensen, W. L., Maxwell, D. S. & TiradoRives, J. Development and testing of the OPLS all-atom force field on conformational energetics and properties of organic liquids. *J. Am. Chem. Soc.* **118**, 11225–11236, https://doi.org/10.1021/Ja9621760 (1996).
37. Damm, W., Frontera, A., TiradoRives, J. & Jorgensen, W. L. OPLS all-atom force field for carbohydrates. *J. Comput. Chem.* **18**, 1955–1970, 10.1002/(Sici)1096-987x(199712)18:16<1955::Aid-Jcc1>3.3.Co;2-A (1997).
38. McDonald, N. A. & Jorgensen, W. L. Development of an all-atom force field for heterocycles. *Properties of liquid pyrrole, furan, diazoles, and oxazoles. J. Phys. Chem. B* **102**, 8049–8059, https://doi.org/10.1021/Jp981200o (1998).
39. Jorgensen, W. L. & McDonald, N. A. Development of an all-atom force field for heterocycles. *Properties of liquid pyridine and diazenes. Theochem-Journal of Molecular Structure* **424**, 145–155, https://doi.org/10.1016/s0166-1280(97)00237-6 (1998).
40. Rizzo, R. C. & Jorgensen, W. L. OPLS All-Atom Model for Amines: Resolution of the Amine Hydration Problem. *J. Am. Chem. Soc.* **121**, 4827–4836, https://doi.org/10.1021/ja984106u (1999).
41. Kaminski, G. A., Friesner, R. A., Tirado-Rives, J. & Jorgensen, W. L. Evaluation and Reparametrization of the OPLS-AA Force Field for Proteins via Comparison with Accurate Quantum Chemical Calculations on Peptides†. *The Journal of Physical Chemistry B* **105**, 6474–6487, https://doi.org/10.1021/jp003919d (2001).
42. Watkins, E. K. & Jorgensen, W. L. Perfluoroalkanes: Conformational Analysis and Liquid-State Properties from ab Initio and Monte Carlo Calculations. *The Journal of Physical Chemistry A* **105**, 4118–4125, https://doi.org/10.1021/jp004071w (2001).
43. Berendsen, H. J. C., Grigera, J. R. & Straatsma, T. P. The Missing Term in Effective Pair Potentials. *J. Phys. Chem.-Us* **91**, 6269–6271, https://doi.org/10.1021/J100308a038 (1987).
44. Humphrey, W., Dalke, A. & Schulten, K. VMD: visual molecular dynamics. *J. Mol. Graph.* **14**(33-38), 27–38 (1996).
45. Chovancova, E. *et al*. CAVER 3.0: a tool for the analysis of transport pathways in dynamic protein structures. *PLoS Comput. Biol.* **8**, e1002708, https://doi.org/10.1371/journal.pcbi.1002708 (2012).
46. Dassault Systemes BIOVIA; Discovery Studio Client; San Diego, USA. Dassault Systemes BIOVIA; Discovery Studio 2019 Client; San Diego, USA (2019).
47. Gil, A. A. *et al*. Femtosecond to Millisecond Dynamics of Light Induced Allostery in the Avena sativa LOV Domain. *The journal of physical chemistry. B* **121**, 1010–1019, https://doi.org/10.1021/acs.jpcb.7b00088 (2017).
48. Durr, H., Salomon, M. & Rudiger, W. Chromophore exchange in the LOV2 domain of the plant photoreceptor phototropin1 from oat. *Biochemistry* **44**, 3050–3055, https://doi.org/10.1021/bi0478897 (2005).
49. Song, S. H. *et al*. Modulating LOV domain photodynamics with a residue alteration outside the chromophore binding site. *Biochemistry* **50**, 2411–2423, https://doi.org/10.1021/bi200198x (2011).
50. Fukunaga, Y., Katsuragi, Y., Izumi, T. & Sakiyama, F. Fluorescence characteristics of kynurenine and N'-formylkynurenine. *Their use as reporters of the environment of tryptophan 62 in hen egg-white lysozyme. Journal of biochemistry* **92**, 129–141, https://doi.org/10.1093/oxfordjournals.jbchem.a133909 (1982).
51. Lobley, A., Whitmore, L. & Wallace, B. A. DICHROWEB: an interactive website for the analysis of protein secondary structure from circular dichroism spectra. *Bioinformatics* **18**, 211–212 (2002).
52. Sreerama, N. & Woody, R. W. Estimation of protein secondary structure from circular dichroism spectra: comparison of CONTIN, SELCON, and CDSSTR methods with an expanded reference set. *Anal. Biochem.* **287**, 252–260, https://doi.org/10.1006/abio.2000.4880 (2000).
53. Micsonai, A. *et al*. BeStSel: a web server for accurate protein secondary structure prediction and fold recognition from the circular dichroism spectra. *Nucleic Acids Res.* **46**, W315–W322, https://doi.org/10.1093/nar/gky497 (2018).
54. Tomasková, N., Varinska, L. & Sedlak, E. Rate of oxidative modification of cytochrome c by hydrogen peroxide is modulated by Hofmeister anions. *General Physiology and Biophysics* **29**, 255–265, https://doi.org/10.4149/gpb_2010_03_255 (2010).
55. Zayner, J. P. & Sosnick, T. R. Factors that control the chemistry of the LOV domain photocycle. *PLoS ONE* **9**, e87074, https://doi.org/10.1371/journal.pone.0087074 (2014).
56. Leferink, N. G. *et al*. Identification of a gatekeeper residue that prevents dehydrogenases from acting as oxidases. *The Journal of biological chemistry* **284**, 4392–4397, https://doi.org/10.1074/jbc.M808202200 (2009).
57. Yagi, K., Ohishi, N., Nishimoto, K., Choi, J. D. & Song, P. S. Effect of hydrogen bonding on electronic spectra and reactivity of flavins. *Biochemistry* **19**, 1553–1557, https://doi.org/10.1021/bi00549a003 (1980).
58. Halavaty, A. S. & Moffat, K. N- and C-terminal flanking regions modulate light-induced signal transduction in the LOV2 domain of the blue light sensor phototropin 1 from Avena sativa. *Biochemistry* **46**, 14001–14009, https://doi.org/10.1021/bi701543e (2007).
59. Pietra, F. Molecular dynamics simulation of dioxygen pathways through mini singlet oxygen generator (miniSOG), a genetically encoded marker and killer protein. *Chem. Biodivers.* **11**, 1883–1891, https://doi.org/10.1002/cbdv.201400125 (2014).
60. Alia, A., Mohanty, P. & Matysik, J. Effect of proline on the production of singlet oxygen. *Amino Acids* **21**, 195–200, https://doi.org/10.1007/s007260170026 (2001).
61. Matysik, J., Alia, A., Bhalu, B. & Mohanty, P. Molecular mechanisms of quenching of reactive oxygen species by proline under stress in plants. *Current Science* **82**, 525–532 (2002).
62. Signorelli, S., Arellano, J. B., Melo, T. B., Borsani, O. & Monza, J. Proline does not quench singlet oxygen: evidence to reconsider its protective role in plants. *Plant physiology and biochemistry: PPB* **64**, 80–83, https://doi.org/10.1016/j.plaphy.2012.12.017 (2013).
63. Pimenta, F. M., Jensen, R. L., Breitenbach, T., Etzerodt, M. & Ogilby, P. R. Oxygen-dependent photochemistry and photophysics of "miniSOG," a protein-encased flavin. *Photochemistry and Photobiology* **89**, 1116–1126, https://doi.org/10.1111/php.12111 (2013).
64. Barnett, M. E., Baran, T. M., Foster, T. H. & Wojtovich, A. P. Quantification of light-induced miniSOG superoxide production using the selective marker, 2-hydroxyethidium. Free radical biology &. *medicine* **116**, 134–140, https://doi.org/10.1016/j.freeradbiomed.2018.01.014 (2018).
65. Winterbourn, C. C. Reconciling the chemistry and biology of reactive oxygen species. *Nat. Chem. Biol.* **4**, 278–286, https://doi.org/10.1038/nchembio.85 (2008).
66. Di Mascio, P. *et al*. Singlet Molecular Oxygen Reactions with Nucleic Acids, Lipids, and Proteins. *Chem Rev* **119**, 2043–2086, https://doi.org/10.1021/acs.chemrev.8b00554 (2019).
67. Kim, J. *et al*. Oxidative modification of cytochrome c by singlet oxygen. *Free radical biology & medicine* **44**, 1700–1711, https://doi.org/10.1016/j.freeradbiomed.2007.12.031 (2008).
68. Marques, E. F., Medeiros, M. H. G. & Di Mascio, P. Lysozyme oxidation by singlet molecular oxygen: Peptide characterization using [(18) O]-labeling oxygen and nLC-MS/MS. *Journal of mass spectrometry: JMS* **52**, 739–751, https://doi.org/10.1002/jms.3983 (2017).
69. Kiselar, J. G., Maleknia, S. D., Sullivan, M., Downard, K. M. & Chance, M. R. Hydroxyl radical probe of protein surfaces using synchrotron X-ray radiolysis and mass spectrometry. *International journal of radiation biology* **78**, 101–114, https://doi.org/10.1080/09553000110094805 (2002).
70. Jensen, R. L., Arnbjerg, J. & Ogilby, P. R. Temperature effects on the solvent-dependent deactivation of singlet oxygen. J. Am. Chem. Soc. 132, 8098–8105, https://doi.org/10.1021/ja101753n (2010).

Acknowledgements
This work was supported by the research grants provided by Slovak research and development agency (APVV-15-0069 and APVV-15-0485) and by the research grant VEGA 1/0557/20. Instrument access for mass spectrometry analysis was enabled through EU_FT-ICR_MS network funded by the EU Horizon 2020 grant 731077. IMIC group acknowledges support from CSF 19-16084 S and infrastructure funding CZ.1.05/1.1.00/02.0109, LQ1604 and LM2015043 CIISB. Dr. Anna Kozarova (University of Windsor, Windsor, Ontario, Canada) is acknowledged for critical reading of the manuscript. This work forms a part of PhD study of M.P.

Author contributions
M.P., P.Mi., D.J., P.N., P.Ma., G.B. and E.S. designed the research, M.P., F.F., A.H., G.Y., T.K., M.-S.S. and G.B. performed experiments and analyzed data, P.Ma., A.P., D.J., G.B. and E.S. wrote the manuscript.

Competing interests
The authors declare no competing interests.

Additional information
Supplementary information is available for this paper at https://doi.org/10.1038/s41598-020-60861-2.

Correspondence and requests for materials should be addressed to G.B. or E.S.

Reprints and permissions information is available at www.nature.com/reprints.

Publisher's note Springer Nature remains neutral with regard to jurisdictional claims in published maps and institutional affiliations.

Open Access This article is licensed under a Creative Commons Attribution 4.0 International License, which permits use, sharing, adaptation, distribution and reproduction in any medium or format, as long as you give appropriate credit to the original author(s) and the source, provide a link to the Creative Commons license, and indicate if changes were made. The images or other third party material in this article are included in the article's Creative Commons license, unless indicated otherwise in a credit line to the material. If material is not included in the article's Creative Commons license and your intended use is not permitted by statutory regulation or exceeds the permitted use, you will need to obtain permission directly from the copyright holder. To view a copy of this license, visit http://creativecommons.org/licenses/by/4.0/.

© The Author(s) 2020